UAB
Universitat Autònoma de Barcelona

MODIFICATION STRATEGIES BASED ON HYBRID NANOMATERIALS OF CARBON COMPOSITE SENSORS FOR ELECTROANALYSIS. ENVIRONMENTAL AND CLINICAL APPLICATIONS

Laia López Fernandez

ADVERTIMENT. L'accés als continguts d'aquesta tesi queda condicionat a l'acceptació de les condicions d'ús establertes per la següent llicència Creative Commons:  https://creativecommons.org/licenses/?lang=ca

ADVERTENCIA. El acceso a los contenidos de esta tesis queda condicionado a la aceptación de las condiciones de uso establecidas por la siguiente licencia Creative Commons:  https://creativecommons.org/licenses/?lang=es

WARNING. The access to the contents of this doctoral thesis it is limited to the acceptance of the use conditions set by the following Creative Commons license:  https://creativecommons.org/licenses/?lang=en

UAB
Universitat Autònoma
de Barcelona

MODIFICATION STRATEGIES BASED ON HYBRID NANOMATERIALS OF CARBON COMPOSITE SENSORS FOR ELECTROANALYSIS.

ENVIRONMENTAL AND CLINICAL APPLICATIONS

Laia López Fernández

Doctoral Thesis

Doctoral Studies in Chemistry

Supervisors:

Dr. María del Mar Baeza Labat

Dr. Cristina Palet Ballús

Department of Chemistry

Faculty of Science

Bellaterra, 2024

UAB
Universitat Autònoma
de Barcelona

MODIFICATION STRATEGIES BASED ON HYBRID NANOMATERIALS OF CARBON COMPOSITE SENSORS FOR ELECTROANALYSIS.

ENVIRONMENTAL AND CLINICAL APPLICATIONS

Memoria para optar al grado de Doctor Internacional presentada por:
Laia López Fernández

Research Group on Biological Treatment and Valorisation of Liquid and Gaseous Effluents
ENOCOV

GTS
GRUP DE TÈCNIQUES DE SEPARACIÓ EN QUÍMICA

Dr. María del Mar Baeza

Dr. Cristina Palet

This work has been possible thanks to the personal grant awarded from *Universitat Autònoma de Barcelona* in *Personal Investigador en Formació* (PIF) fellowship program. This work has been executed within Research Group on Biological Treatment and Valorisation of Liquid and Gaseous Effluents (GENOCOV) and *Grup de Tècniques de Separació* (GTS) to whom I have gratitude, without them this work has not been possible.

I would like to acknowledge the support obtained from Erasmus + Traineeships 2020-2021 fellowship. Also, to Dr. Dietmar Appelhans and Dr. Silvia Moreno for receiving me in Bioactive and Responsive Polymers department from the *Leibniz-Institut für Polymerforschung Dresden e.V.* during the 6 months research stay, which help me to enhance my scientific knowledge and the research included in this PhD Thesis.

« Logic will take you from A to B.

Imagination will take you everywhere. »

Albert Einstein

Index

Summaries

Nowadays, analytical chemistry has an important role in society. This part of the chemistry is present in a lot of fields, for example in industry, in medicine, or it helps in the environmental monitoring of some contaminants, such as metals. Among some techniques to use in metals determination with low detection limit (DL), such as inductively coupled plasma–atomic emission spectrometry (ICP-AES), inductively coupled plasma–mass spectrometry (ICP-MS), and atomic absorption spectrometry (AAS), electrochemical techniques are a complementary strategy due to their characteristics: no time-consuming sample pretreatment, no specialize personnel is required, cost-effective and can be portable. In the last years, the use of composite materials based on different carbon allotropes has been an interesting option to customize the electrochemical sensors used in these techniques and achieve a better performance. For the fabrication of these composite electrodes, an isolating matrix and carbon materials are used. As carbon materials: graphite, carbon nanotubes, graphene, and glassy carbon, are viable alternatives because of their electrical properties. Considering all these carbon materials, in this thesis they were tested in cadmium (Cd), lead (Pb) and copper (Cu) determination using square wave anodic stripping voltammetry (SWASV).

Time ago, the electrochemical determination of metals was done using polarography, and as a working electrode one made of mercury was used. Mercury has some interesting properties, for example the affinity with some metals leading to the formation of amalgams with them. That decreases the reduction potential of this metal ion analyte, that can improve the electrochemical detection. Even though the use of mercury electrodes is not environmentally friendly, some alternatives can be found to exploit its properties while reducing related risks. For that reason, in this thesis the superficial modification of the composite electrode was performed with two type of mercury nanoparticles (HgNPs). And the performance of these modifications was evaluated analysing Cd, Pb and Cu using SWASV in spiked tap water, Mar Menor water and more complex samples (as from the acid digestion of vineyards residues).

Another property of the carbon materials is that they can have biocompatibility, for that reason a new surface modification to explore this property was proposed in this thesis. The polymersomes (Psomes), which are polymeric vesicles able to react to some external stimulus (pH, magnetic field, temperature, change in temperature, etc.) are used to develop biosensors. Psomes were loaded with Glucose Oxidase (GOx), which is a natural enzyme that can catalyse the transformation of glucose in H_2O_2 and gluconic acid, and the hydrogen peroxide was detected electrochemically, using chronoamperometry.

Furthermore, a cascade reaction was proposed to evaluate the communication between different loaded vesicles (compartmentalization). Using the GOx loaded Psomes to produce H_2O_2 and then the consumption of hydrogen peroxide was tested using two different loaded Psomes: on one hand, Psomes loaded with a natural enzyme, Catalase (CAT), and on the other hand, Hemin Chloride loaded Psomes, which is a nanozyme.

Hoy en día, la química analítica desempeña un papel importante en la sociedad. Esta parte de la química está presente en muchos campos, por ejemplo, en la industria, en la medicina, o ayuda en la monitorización medioambiental de algunos contaminantes, como los metales. Hay algunas técnicas que se utilizan en la determinación de metales que tienen un bajo límite de detección (DL), como la espectrometría de emisión atómica con plasma acoplado inductivamente (ICP-AES), la espectrometría de masas con plasma acoplado inductivamente (ICP-MS) y la espectrometría de absorción atómica (AAS) pero las técnicas electroquímicas son una buena opción debido a sus características: no requieren pretratamiento de la muestra, no necesitan personal especializado, son económicas y pueden ser portátiles. En los últimos años, el uso de materiales compuestos basados en distintos alótropos de carbono ha sido una opción interesante para personalizar los sensores electroquímicos utilizados en dichas técnicas y conseguir un mejor rendimiento y adaptabilidad. Para la fabricación de estos electrodos compuestos, se han utilizado una matriz aislante y materiales de carbono. Como materiales de carbono se han usado grafito, nanotubos de carbono, grafeno, carbono vítreo, ya que son una alternativa viable debido a sus propiedades eléctricas. Considerando todos estos materiales de carbono, en esta tesis se probaron en la determinación de cadmio (Cd), plomo (Pb) y cobre (Cu) mediante voltamperometría de redisolución anódica de onda cuadrada (SWASV).

Tiempo atrás, la determinación electroquímica de metales se realizaba utilizando polarografía, y en esta técnica como electrodo de trabajo se empleaba uno de mercurio. El mercurio tiene algunas propiedades interesantes, por ejemplo, la afinidad con algunos metales que lleva a la formación de amalgamas con ellos. Eso disminuye el potencial de reducción de iones metálicos de interés, lo que puede mejorar la detección electroquímica. Aunque el uso de electrodos de mercurio no es respetuoso con el medio ambiente, se pueden encontrar algunas alternativas para aprovechar sus propiedades reduciendo los riesgos asociados. Por ello, en esta tesis se realizó la modificación superficial del electrodo compuesto con dos tipos de nanopartículas de mercurio (HgNPs). Y se evaluó el rendimiento de estas modificaciones analizando Cd, Pb y Cu utilizando SWASV en agua del grifo dopada, agua del Mar Menor y muestras más complejas (por ejemplo, procedentes de la digestión ácida de residuos de los viñedos).

Otra propiedad de los materiales de carbono es que pueden ser biocompatibles, por ello en esta tesis se propuso una nueva modificación superficial para explorar esta propiedad. Los *polymersomes* (*Psomes*), que son vesículas poliméricas capaces de reaccionar a estímulos externos (como pH, campo magnético, temperatura, cambio de temperatura, etc.) se utilizaron para desarrollar biosensores. Los *Psomes* se cargaron con Glucosa Oxidasa (GOx),

que es una enzima natural capaz de catalizar la transformación de glucosa en acido glucónico y H_2O_2, y este último se detectó electroquímicamente, utilizando la técnica de cronoamperometría.

Además, se propuso una reacción en cascada para evaluar la comunicación entre las diferentes vesículas cargadas (compartimentación). El uso de los *Psomes* cargadas con GOx para producir H_2O_2 y el consumo de este se probó utilizando dos *Psomes* con carga diferente: por un lado, *Psomes* cargados con una enzima natural, Catalasa (CAT), y por otro, *Psomes* cargados con Cloruro de Hemin, que es una nanozima.

Avui dia, la química analítica exerceix un paper important en la societat. Aquesta part de la química és present en molts camps, per exemple, en la indústria, en la medicina, o ajuda en el monitoratge mediambiental d'alguns contaminants, com els metalls. Hi ha algunes tècniques que s'utilitzen en la determinació de metalls que tenen un límit de detecció (DL) baix, com l'espectrometria d'emissió atòmica amb plasma acoblat inductivament (ICP-AES), l'espectrometria de masses amb plasma acoblat inductivament (ICP-MS), i l'espectrometria d'absorció atòmica (AAS) però les tècniques electroquímiques són una bona opció a causa de les seves característiques: no requereixen pretractament de la mostra, no necessiten personal especialitzat, són econòmiques i poden ser portàtils. En els últims anys, l'ús de materials compostos basats en diferents formes al·lotròpiques de carboni ha estat una opció interessant per a personalitzar els sensors electroquímics utilitzats en aquestes tècniques i aconseguir un millor rendiment i adaptabilitat. Per a la fabricació d'aquests elèctrodes compostos s'empra una matriu aïllant i materials de carboni. Com a materials de carboni s'han emprat: grafit, nanotubs de carboni, grafè, carboni vitri, ja que són una alternativa viable a causa de les seves propietats elèctriques. Considerant tots aquests materials de carboni, en aquesta tesi es van provar en la determinació de cadmi (Cd), plom (Pb) i coure (Cu) mitjançant voltamperometria de redissolució anòdica d'ona quadrada (SWASV).

Temps enrere, la determinació electroquímica de metalls es realitzava utilitzant polarografia, i en aquesta tècnica com a elèctrode de treball s'emprava un de mercuri. El mercuri (Hg) té algunes propietats interessants, per exemple, l'afinitat amb alguns metalls que porta a la formació d'amalgames amb ells. Això disminueix el potencial de reducció d'ions metàl·lics d'interès, la qual cosa permet a la millora de la detecció electroquímica. Encara que l'ús d'elèctrodes de mercuri no és respectuós amb el medi ambient, es poden trobar algunes alternatives per a aprofitar les seves propietats reduint els riscos associats. Per això, en aquesta tesi es va realitzar la modificació superficial de l'elèctrode compost amb dos tipus de nanopartícules de mercuri (HgNPs). I es va avaluar el rendiment d'aquestes modificacions analitzant Cd, Pb i Cu utilitzant SWASV en aigua de l'aixeta dopada, aigua de la Mar Menor i mostres més complexes (com per exemple, procedents de la digestió àcida de residus de les vinyes).

Una altra propietat dels materials de carboni és que poden ser biocompatibles, per això en aquesta tesi es va proposar una nova modificació superficial per a explorar aquesta propietat. Els *polymersomes* (*Psomes*), que són vesícules polimèriques capaces de reaccionar a estímuls externs (com a pH, camps magnètics, canvi de temperatura, etc.) s'han emprat per a desenvolupar biosensors. Els *Psomes* es van carregar amb Glucosa Oxidasa (GOx), que és un enzim natural capaç de catalitzar la transformació de glucosa en àcid glucònic H_2O_2, i

aquesta últim es va detectar electroquímicament, utilitzant la tècnica de cronoamperometria.

A més, es va proposar una reacció en cascada per a avaluar la comunicació entre les diferents vesícules carregades (compartimentació). L'ús dels *Psomes* carregats amb GOx per a produir H_2O_2 i el consum d'aquest es va provar utilitzant dos *Psomes* amb càrrega diferent: d'una banda, *Psomes* carregats amb un enzim natural, Catalasa (CAT), i per un altre, *Psomes* carregats amb Clorur de Hemin, que és una nanozima.

Abbreviations & symbols

Acronym	Meaning
A	Electroactive area
a	Statistical parameter related to the fitting of the Gaussian curve
AAS	Atomic Absorption Spectroscopy
AES	Atomic Emission Spectroscopy
AL	Alginate
ASV	Anodic Stripping Voltammetry
AuNPs	Gold NanoParticles
BCP	Block CoPolymer
BODIPY	4,4-difluoro-4-bora-3a,4a-diaza-s-indacene
bpy	Bypyridiyl
C	Capacitor
[C]	Concentration
CAT	Catalase Peroxidase
CDs	Carbon Dots
CE	Counter Electrode
CNFs	Carbon NanoFibers
CNOs	Carbon Nano-Onions
CNTs	Carbon NanoTubes
CPE	Constant Phase Element
Cryo-TEM	Cryogenic Transmission Electron Microscopy
CV	Cyclic Voltammetry
CVD	Chemical Vapor Deposition
C_α	Electroactive specie concentration
DAB	1,2-diaminobenzene
DEAEM	2-(diethylamino)ethyl methacrylate
DL	Detection Limit
DLS	Dynamic Light Scattering
DME	Dropping Mercury Electrode
DMSO	Dimethylsulfoxid

DPASV	Differential Pulse Anodic Stripping Voltammetry
DPV	Differential Pulse Voltammetry
D_{α}	Diffusion coefficient of the electroactive species
E	Potential
e	Electrons
E_{ap}	Anodic peak potential
E_{app}	Potential applied
E_{cp}	Cathodic peak potential
E_{MW}	Potential at maximum width
SCE	Saturated Calomel Electrode
EDX	Energy-Dispersive X-rays
EIS	Electrochemical Impedance Spectroscopy
F	Faraday constant (96485 C·mol^{-1})
FITC-CAT	Catalase peroxidase labelled with fluorescein isothiocyanate
FITC-GOx	Glucose oxidase labelled with fluorescein isothiocyanate
FRET	Fluorescence Resonance Energy Transference
G	Gerischer impedance
GCE	Glassy Carbon Electrode
GO	Graphene Oxide
GOx	Glucose Oxidase
GrO	Graphite Oxide
HBPO	Poly(3-ethyl-3-oxetanemethanol)
Hemin	Hemin Chloride
HFF	Hollow Fiber Filtration
HgNPs	Mercury NanoParticles
His	Histidine
H-NMR	Proton-Nuclear Magnetic Resonance
HRP	Horseradish Peroxidase
I/i	Current
I_{MW}	Current maximum width.

i_0	Exchange current
i_{ap}	Anodic peak current
i_{cp}	Cathodic peak current
ICP	Inductively Coupled Plasma
IPE	Inkjet Printed Electrodes
IR	Infrared spectroscopy
ISE	Ion Selective Electrodes
i_t	Current generated at time t
LE	Loading Efficiency
LPO	LactoPerOxidase
LR	Linear Range
LSASV	Linear Swap Anodic Stripping Voltammetry:
m	Slope
MALS	MultiAngle Light Scattering
min	Minutes
MS	Mass Spectroscopy
Myo	Myoglobin
MWCNTs	Multiwall Carbon NanoTubes
n	Number of electrons
N	Mols of the analyte oxidized or reduced
NDs	NanoDiamonds
NPs	NanoParticles
OES	Optical Emission Spectroscpy
PANAM	Poly(amidoamine) dendrimer
PANI	Polyaniline
PAT	Phosphinothricin acetyltransferase
PBS	Phosphate Buffer saline
PCL	Poly(ε-caprolactone)
PDA	Polydiacetylene
PDDA	Poly(diallyldimethylammonium chloride)

PdI	Polydispersion Index
PDMS	poly(dimethylsiloxane)
PDPA	2-(diisopropylamino)ethyl methacrylate)
PEG	Poly(ethylene glycol)
PEO	Poly(ethylene oxide)
pH*	pH star
PMBT	Poly(2-mercaptobenzothiazole)
PMOXA	Poly(2-methyl-2-oxazoline)
PMPC	Poly(2-(methacryloyloxy)ethyl phosphorylcholine
Psomes	Polymersomes
PVA	Polyvinyl Alcohol
PVP	Poly(4-vinylpyridine)
Q	Charge
QL	Quantification Limit
R	Resistance
R_{CT}	Charge Transfer Resistance
RE	Reference Electrode
R	Universal ideal gas constant (8.3145 $J \cdot K^{-1} \cdot mol^{-1}$)
rGO	reduced Graphene Oxide
ROS	Reactive Oxigen Species
R_{Ω}	Ohmic Resistance
s	Seconds
S	Signal
sd	Standard deviation
SEC	Size Exclusion Chromatography
SEM	Scanning Electron Microscopy
SOD	SuperOxide Dismutase
SPE	Screen Printed Electrodes
SWASV	Square-Wave Anodic Stripping Voltammetry
T	Temperature

t	Time
t_{bm}	Time between measurements
TEM	Transmission Electron Microscopy
TMP	TransMembrane Preasure
UV-Vis	Ultraviolet-Visible range
W	Warburg impedance
WE	Working Electrode
x_0	Mean diameter
XPS	X-Ray Photoemission Spectroscopy
XRD	X-Ray Diffraction
Z	Electrical impedance
Z_{imag}	Imaginary part of the impedance
Z_{real}	Real part of the impedance
α	Transference coefficient
β-CD	β-cyclodextrin
β-CD-SH	Heptakis-(6-deoxy-mercapto)-β-cyclodextrin
ΔE	Equilibrium potential
ζ	Zeta Potential
Θ	Coefficient of the Constant Phase Element
λ	Wavelenght
ν	Scan rate
π	Number pi (3.1416)
φ	Phase shift
ω	Angular frequency

Figures, schemes & tables

Figures

Schemes

Tables

Chapter I

Introduction

Nowadays, analytical chemistry has a wide impact in the world. Analytical chemistry can be defined as the science of obtaining, processing, and communicating information about the composition and structure of the matter [1]. This branch of the chemistry is widely used in several fields, for example in industry, medicine, or environmental analysis.

One of the purposes of analytical chemistry is to detect and quantify some persistent contaminant agents that can affect living beings' health and environment. Some metals are one of these pollutants. They are usually characterized by their high atomic weight, high density, and their metallic character, as examples lead (Pb), cadmium (Cd), chromium (Cr), mercury (Hg), arsenic (As), etc. Due to their potential environmental and health risks, the study and regulation of metals is an important affair. For that reason, several instrumental techniques have been developed, for example: Inductively Coupled Plasma (ICP) coupled to detectors based on different detection systems as Mass Spectroscopy (MS) or Optical Emission Spectroscopy (OES), also, Atomic Absorption or Emission Spectroscopy (AAS or AES) and electrochemical techniques.

Some of these techniques require high-cost equipment, specialized knowledge of them, extensive sample preparation and analysis and they are not portable. On the contrary, electrochemical techniques can solve some of these inconveniences with cost-effective equipment and tools needed and in addition they can be portable. For example, the models EmStat or Palmsens (from Palmsens B.V, Houten, The Netherlands), both are portable and can perform a lot of electrochemical techniques. The sample preparation and the time of analysis could be both relatively short and easy compared to the other mentioned techniques, even depending on the matrix.

1.1. What is a sensor?

A sensor is a device which detects or respond to some type of input from the environment and this input is translated into human-readable property. The main parts of a sensor are presented in **Scheme 1**. The receptor recognises the input, the analyte reacts with the receptor, which is the information of the sample component and generate a response that is called primary signal. The transducer processes the signal, usually by amplifying and transforming it into the secondary signal, that usually is an electrical one. The secondary signal measured is proportional to the analyte concentration.

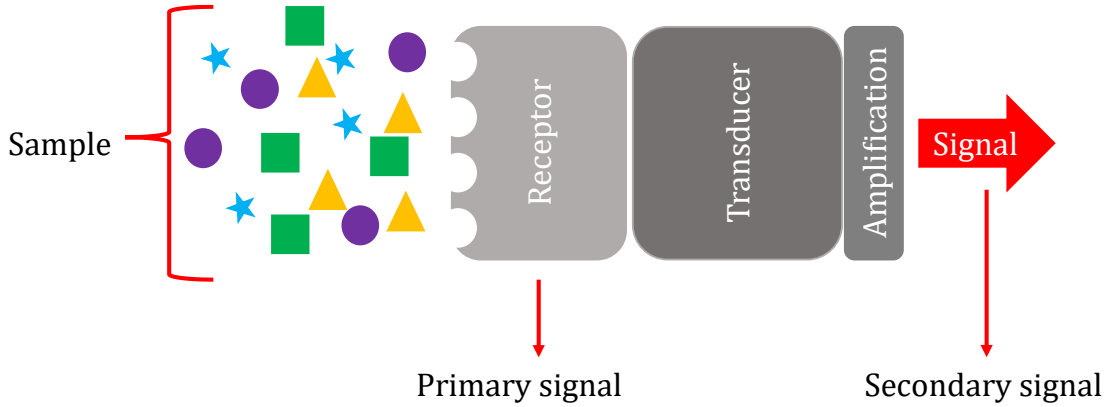

Scheme 1. Sensor scheme response. Only one element of the sample is recognised by the receptor. The transducer converts the signal associated with the process (primary signal) into an electrical one which is amplified and processed (secondary signal).

There are several classifications for sensors, one of which is that they can be divided in active and passive sensors. The active ones require a power signal, otherwise the passive does not require power signal to produce a response. Other classifications are related to the type of receptor and to the type of transducer [2].

Depending on the nature of the signal that the receptor identifies, there are mainly two types of receptors:

- **Physical**: there are not chemical reactions involved in the detection (e.g. change in the mass, change in the temperature, among others)
- **Chemical**: there is a chemical reaction involved (e.g. as chelate compounds, redox reactions, etc.)

When the receptor has biological nature (enzyme, antibodies, AND, cells, etc.) it is known as a biosensor.

One of the most used classifications is based on the transducer, depending on it there are several types. The transducer converts the primary signal into a secondary one. Depending on the changes that the analyte produces in the receptor, the operating principle of the transducer can be:

- **Electrochemical**: changes in electric current generated by the interaction of the analyte and the electrode. There are possible electrochemical sensors, as follows:
  - **Voltametric sensors**: current is measured.
  - **Potentiometric sensors**: potential is measured.
- **Electrical**: no electrochemical processes take place, but the signal arises caused by the interaction of the analyte.

- **Magnetic**: changes in the magnetic properties can be induced by the adsorption of the analyte in the receptor surface.
- **Thermal**: thermal effect can be generated by a chemical reaction occurred by the analyte and the receptor.
- **Mass**: induced by the adsorption of analyte on the surface of the sensor.
  - **Piezoelectric sensors**: measurement of the frequency change caused by adsorption of a mass of the analyte at the oscillator.
  - **Surface acoustic wave devices**: modification of the propagation velocity of a generated acoustical wave.
- **Optical**: changes in the optical properties of the receptor.
  - **Absorbance**: caused by the absorptivity of the analyte or by the chromophore used.
  - **Reflectance**: measured in non-transparent media.
  - **Luminescence**: caused by the intensity of light emitted by a chemical reaction.
  - **Fluorescence**: measured as the emission effect caused by irradiation.
  - **Refractive index**: measured as the result of a change in the solution composition.
  - **Optothermal effect**: measurement of the thermal effect caused by light absorption.
  - **Light Scattering**: based on effects caused by particles of definite size present in the sample.

1.1.1. Electrochemical sensors

This work focuses specifically on electrochemistry, which is a multidisciplinary science based on chemical phenomena associated with the charge separation. The separation of charge is often associated with charge transference, which can occur either in the solution or on the electrode surface [3].

Electrochemical sensors can be classified according to the type of signal used for measurements. Being one the potentiometry, that measures the variation of potential generated between a reference electrode and a working electrode, for example this is the case of the ion selective electrode (ISE). Another one, the electrochemical impedance measurements that provide information about the physicochemical processes occurring in an electrochemical cell. And finally, voltammetric methods measure the current intensity that it is generated by the application of a potential on the working electrode. This applied potential is fixed respect to the reference electrode, and it can be constant over time, or it can vary [4]. This cell is formed by three electrodes: working electrode, reference electrode and counter electrode immersed in a solution containing the analyte or the generated electroactive species (see **Scheme 2**).

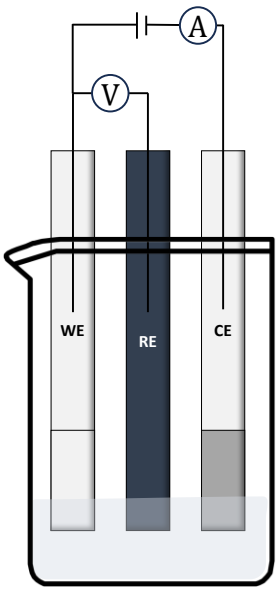

Scheme 2. Three electrode cell used in voltammetric techniques.

- **Working electrode** (**WE**): its potential is varied according to the technique used and the electrochemical reaction occurs on its surface.
- **Reference electrode** (**RE**): its potential remains constant thought the experiment.
- **Counter electrode** (**CE**): it closes the circuit between the WE, the solution, and the electrical source.

There are several techniques in voltammetry and can be classified according to the excitation wave applied (see **Table 1**).

Table 1. Classification of voltammetric techniques according to the potential excitation signals applied [5].

Excitation signal		Technique
Lineal	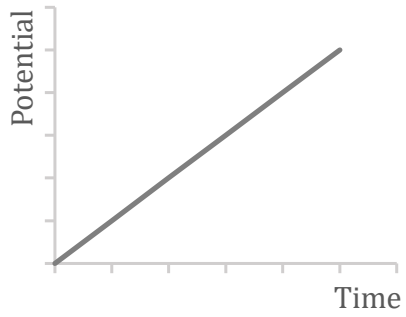	Polarography Hydrodynamic voltammetry
Differential pulse	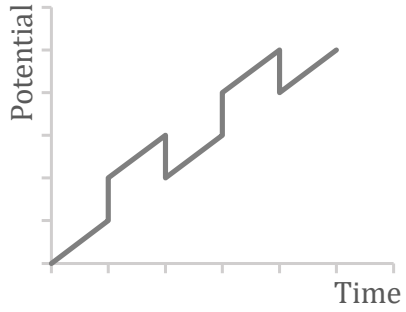	Differential pulse polarography
Square wave	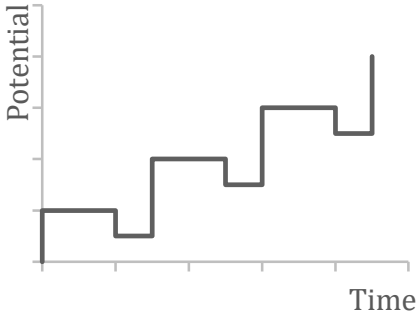	Square wave voltammetry
Triangular	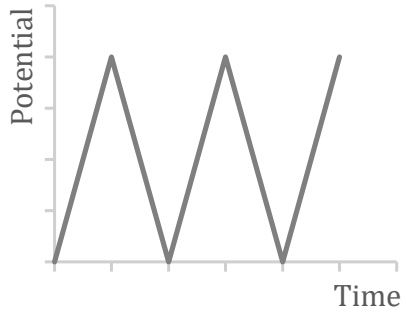	Cyclic voltammetry

The amperometric technique is a voltametric technique in which a constant potential is applied to the working electrode. This potential is sufficient to produce the electrochemical reaction of the analyte or electroactive species at the electrode surface. In amperometry the quantification of the analyte is possible because of the current generated is proportional to

the number of species oxidized or reduced at the surface of the electrode and it is defined by the Faraday's law (**Equation 1**) [6]:

$$i_t = {}^{dQ}/_{dt} = nF\,{}^{dN}/_{dt} \qquad \textbf{(Equation 1)}$$

Where:

i_t: current generated at time t

t: time (s)

Q: charge (C)

n: mols of electrons transferred per mol of analyte.

F: Faraday constant (96485 C· mol^{-1})

N: mols of the analyte oxidized or reduced

So, *dQ/dt* correspond to the oxidation or reduction speed (C·s^{-1}) and depend on several factors: the electron transference speed between the electrode and the electrochemical species; the electrode characteristics (electroactive area); the mass transport that can be migration, convection, and/or diffusion. Migration current is due the electrical gradient and can be controlled by adding a supporting analyte to the electrochemical cell. Convection current is due the stirring of the solution and can be minimized not applying stir or by applying a controlled stirring. The diffusion current arises from the concentration gradient that is formed between the electrode surface and the solution as a consequence of the applied potential and the subsequent electrochemical reaction.

The main disadvantage of the amperometric technique is the low specificity, which means that all the species in the sample that have redox behaviour as the analyte at an applied potential can interfere in the measurements of such analyte of interest. Even though, this inconvenient can be solved by adding some elements to our sensor that can be selective to the target analyte.

The development of novel materials and the modification of the known ones open a new world of possibilities to enhance the performance of the sensors used in electrochemistry. Moreover, the manufacture of the electrodes can be done by different way, so there are different types of them such as composite electrodes, 3D printed electrodes, inkjet printed electrodes (IPE), and screen-printed electrodes (SPE) (see **Figure 1**). This versatility on production process can facilitate the adaptation of the type of manufacture to the needs of the final application and the analyte to be detected.

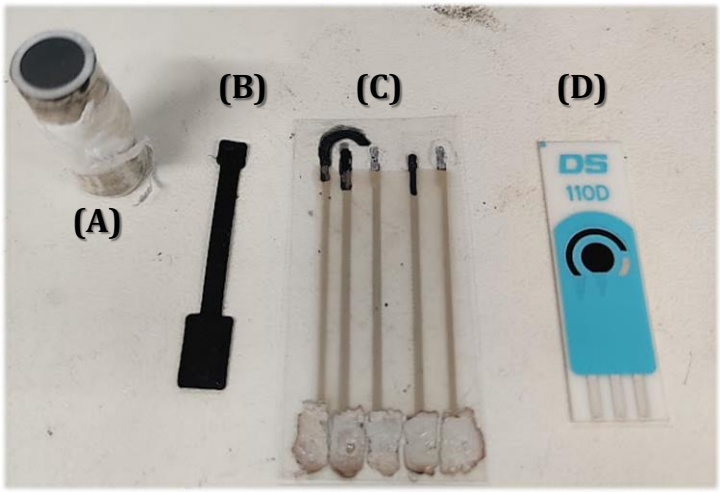

Figure 1. Different types of electrodes depending on the fabrication technique used for their manufacture (from left to right): homemade (A) composite electrode,(B) 3D printed electrode, (C) inkjet printed electrode and (C) commercial screen printed electrode.

Composite electrodes based on different allotropic forms of carbon and epoxy resin were used in this work. A composite is defined as the combination of two dissimilar materials. Each individual component keeps its original nature while giving the composite distinctive chemical, mechanical and physical qualities, different from those shown by the individual components. If any of its parts are conductor, the resultant composite become conductor and such property confer it a suitable feature to be used as electrochemical sensor.

Depending on the composition and distribution of the conductive particles on the electrode surface and the electroactive area there are different behaviours as macroelectrodes and microelectrodes. Microelectrodes presents advantages, such as higher signal/noise ratio, lower detection limits compared to the macroelectrodes, but they present an inconvenience that is the intensity they generate is low and must be amplified. To solve that, these microelectrodes can be collected in an insulating matrix and create an array leading to the

Edge effect[1] and to a composite material[7]. When the microelectrodes are collected, the diffusion of the electroactive species can be radial or linear (see **Figure 2**) depending on the charge and the dispersion of the conductor. The signal of the linear diffusion is the sum of the individual currents generated by each microelectrode. So, at the end, by dispersing a conductor material in an insulating matrix, there is a sensor with a signal as strong as that of a macroelectrode but showing the signal-to-noise ratio of a microelectrode [8] [9].

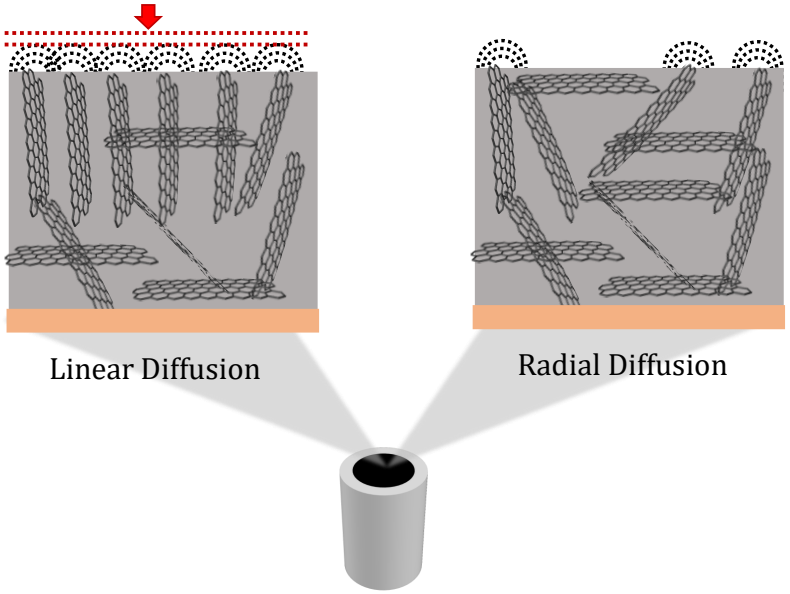

Figure 2. Influence of composite material composition on surface matter diffusion processes: linear and radial.

So, the electrical property of the composite material depends on the nature of each different component, which are carbon material and polymer, on their relative quantities, or ratios and consequently, onto its final's distribution. That affects to the resistivity of the composite material and therefore its electrochemical behaviour.

A composite material has the main advantage that offers a flexible design that allows to reach characteristics that the individual constituent cannot give and tailor the material to the specifications of an optimum design for the required application [10].

The percolation theory was developed by Broadbent and Hammersley in 1957 [11], but it was used years before to interpret the conductivity behaviour of composite materials. The obtained percolation curves can help to optimize the composition of the composite material used in the electrode manufacture under the criterion of analytical signal improvement.

[1] Edge effects are an increase in the experimental current compared to what would be expected, because of the concentration gradients are originated near the edges of the conductor material [7].

A percolation curve has three main regions as is shown in **Figure 3**: low, medium, and high resistivity composition zones. The top one, at a low percentage of conductive material (high resistivity composition), acts like a bad conductor or even insulating. As the amount of conductor material increases still there are high resistivity zones in medium and high composition zones (percolation composition). This is because the conductive particles are closer to each other, improving the conductivity but not enough. Near percolation composition is where the material improves its conductivity and decrease the resistance to the current to flow. The low resistivity composition is the composition where the conductivity is maximum. As a result, the percolation curve provides the data to find a compromise between the percentage of conductive material and the relation signal/noise, considering that the larger the signal-to-noise ratio, the smallest the detection limit (DL) achieved.

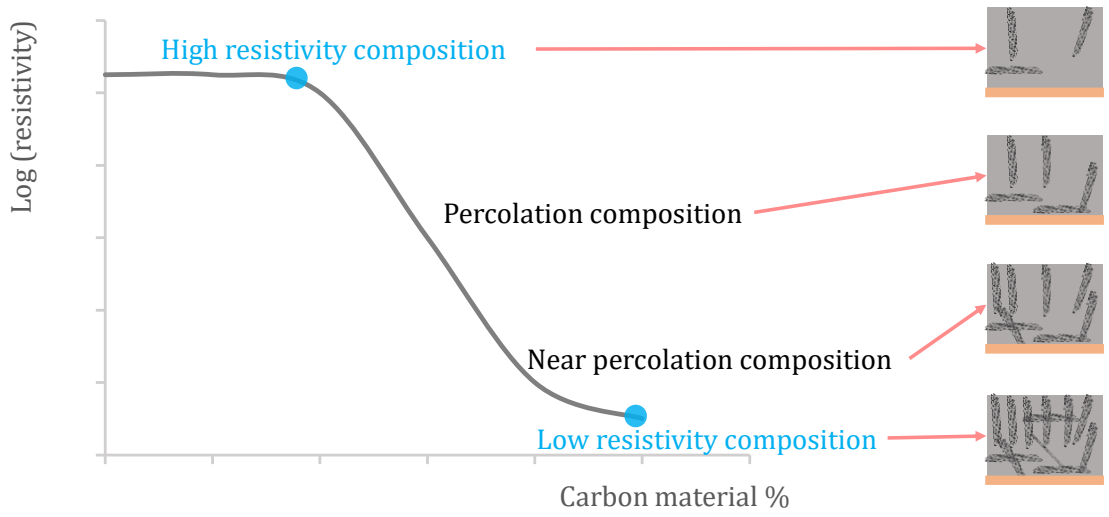

Figure 3. Percolation curve for composite based on carbon materials and epoxy resin. Resistivity of the composite material is related to the ratio of the conductive material used.

Composites based on conductive phases dispersed in polymeric matrices has led to important advances in analytical electrochemistry. Although the same type of polymeric matrices is used in the production of the electrodes, depending on the kind of conductive phase (graphite, carbon nanotubes (CNTs) or graphene) and their different characteristics, the percolation curve may change. For example, using CNTs as conductor materials and the resin Epotek H77 as isolating material, the percolation curve will be different depending on the characteristics of the CNTs used (length and diameter) and therefore their optimum and maximum percentage will also vary [12]. On one hand, the optimum percentage is where the electrode presents the best performance (improved signal-to-noise-ratio and can

achieve lower LD). On the other hand, the maximum percentage is the maximum material that the polymeric resin admits, so this electrode will present more conductor points.

1.1.2. Functionalization of the electrode

The modification of the electrodes could be done by modifying the composite material previous at the fabrication of the composite electrode, or just modifying the surface of the composite electrode. Between both, surface modification present interesting advantages, such as: easy surface renewal, low background current that can be translated in an improvement of the DL, increase of the selectivity, wide range of linear response among others [13].

Additionally, modifying the composite electrode surface can be done easily and three types of processes can be followed [14]:

- **Chemical modification**: an electroactive centre is immobilized onto electrode surface by a chemical reaction.
- **Electro-adsorption**: electroactive species in the solution are adsorbed onto the electrode surface by applying a potential.
- **Deposition**: applying the modifier onto the electrode surface by drop-casting technique or dipping the electrode surface into the modifier.

Among these possibilities, in this thesis the selected modification technique is the deposition by drop-casting. That means a drop of the modifier solution is placed over the composite electrode surface [9].

These modifiers can have different natures, such as: nanomaterials, polymers, biological structures, among others. The selection of one or another will depend on the targeted analyte.

- **Nanomaterials**

In Greek the prefix "*nano*" means really small (10^{-9} m), and nanoscience is the science that study the structures and molecules at this scale, between 1 to 100 nm, and nanotechnology is the practical application of them. The concept of nanotechnology was introduced by the Nobel prize laureated Richard Feynman in 1959. In 1974, Norio Taniguchi coined the term "*nanotechnology*" and defined it as "the processing of separation, consolidation, and deformation of materials by one atom or one molecule" [15].

The manufacturing methods to obtain nanomaterials have two main approaches (see **Scheme 3**) [16]:

- **Top-down**: consist in breaking the bulk material to get nanosized particles, for example chemical etching or mechanical milling.
- **Bottom-up**: consist in building-up of the nanostructures from the bottom: atom-by-atom or molecules-by-molecules by physical and/or chemical methods, for example nucleation and growth or laser pyrolysis.

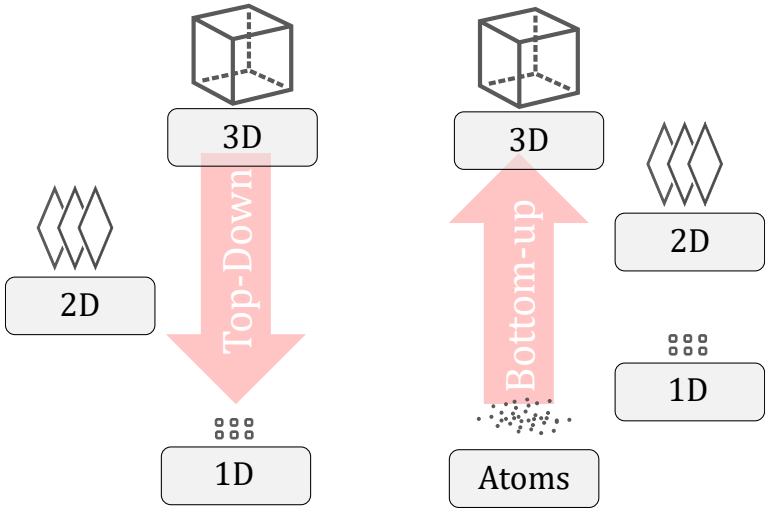

Scheme 3. Different approaches of the nanomaterials manufacturing methods. Top-down and Bttom-Up.

Furthermore, depending on the type of method used there are physical, chemical, and biological synthetic approaches [17].

The properties of the nanomaterials are not the same that the corresponding bulk material. Their special properties (chemical and physical) are related to their nanoscale size (quantum confinement[2]) such as large surface area, mechanically strong, optically active, and chemically reactive. Due to these same features, it made them a potential hazard [16].

The structure based on carbon atoms can take many physical forms. This phenomenon is known as allotropic carbon moieties. Allotropy is a phenomenon that affects many metals and nanometals Depending on the structure of these allotropic materials, they can be 0D,

[2] The quantum confinement effect is observed when the size of the particle is too small to be comparable to the wavelength of the electron.

1D, 2D and 3D. As an example, in **Figure 4**, different allotropy carbon form and their different structure are shown.

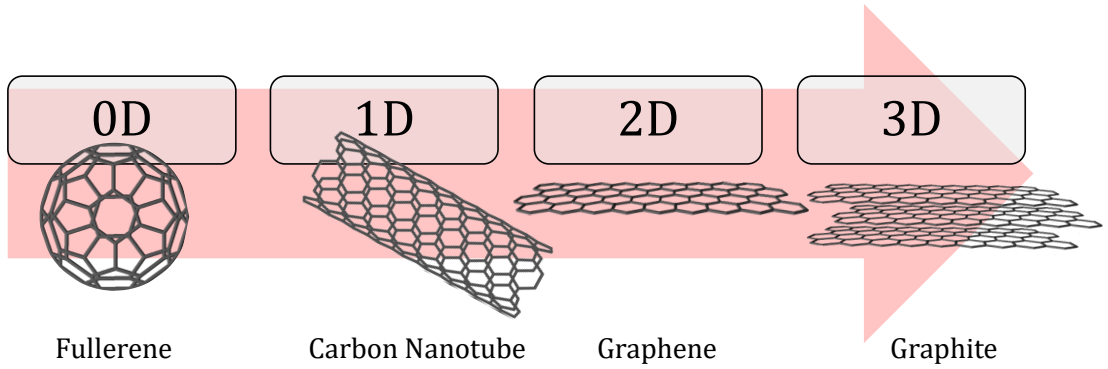

Figure 4. Dimension of the different carbon allotropes nanostructures and graphite.

Carbon shows different orbital hybridization heading to the capability to generate different bonds with different orientations. For this reason, carbon has different allotropic forms and can generate different nanostructures. Graphene (2D), which is a single graphite layer (3D), was isolated in 2010 by the Nobel-prized Geim and Novoselov. In 1991, Iijima discovered carbon nanotubes (CNTs), which is a graphene layer rolled-up (1D). Also, carbon nanofibers (CNFs) are 1D, and they were discovered by Edison in 1879. In 1985, Kroto and Smalley, discovered the fullerenes, which are spherical nanocages formed by pentagonal and hexagonal rings (0D). Carbon nano-onions (CNOs) were discovered by Ugarte in 1992. They are cages with spherical or polyhedral shape formed by several fullerene-like overlapped carbon shells that are defective and disordered to a certain degree. Carbon dots (CDs) are nanoparticles where graphitic and amorphous carbon phases coexist (0D). In 1963, nanodiamonds (NDs) were discovered and they present sp^3 hybridization leading to the formation of hexagonal or cubic diamond lattice (0D) [18], [19], [20].

The different organization of the C atoms provides different properties and the quantum confinement imposed by the nanoscale, make the carbon material a suitable option for a sensing platform. Carbon materials are widely used in several fields like biology, engineering, material science, etc. There are a lot of publications using the key word "*carbon material*", and they increase every year for the last 10 years, as in shown in **Figure 5**. In

addition, the number of publications of these materials applied for sensing applications, and concretely, as electrochemical sensing platforms have increase in the last decade, too.

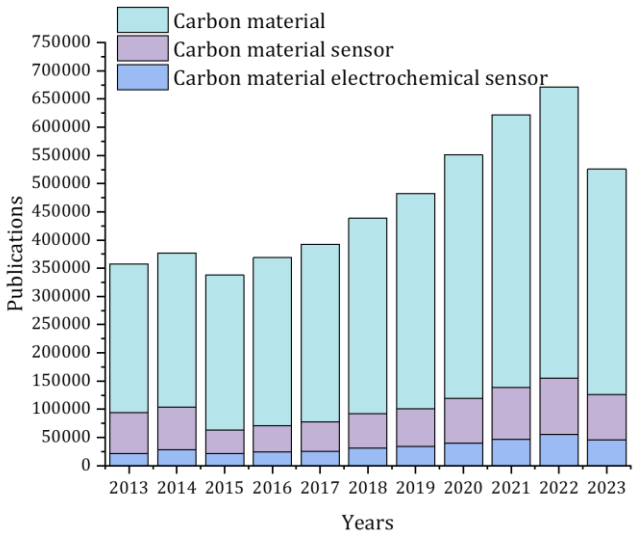

Figure 5. Publications of the last 10 years (January 2013- september 2023). The keywords used in the search (carbon material, carbon material sensor and carbon material electrochemical sensor) (Data from: app.dimensions.ai).

These different carbon materials have both advantages and disadvantages to be used for sensing applications.

In the case of graphite, which is one of the oldest carbon materials used, it is used as precursor of some synthetic routes to obtain other carbon nanostructures, even is also used as it is. Graphite presents good electrical and thermal conductivity, dimensional and thermal stability, low cost, and acceptable corrosion resistance.

To enhance the applicability of these carbon nanomaterials and to overcome some problems that can be derivate from their structure, such as their high hydrophobicity, the carbon nanomaterials can be properly modified. The modification can be divided in two types, either covalent (the hybridization can be affected) or non-covalent (the hybridization is not affected) procedures.

The covalent modification of carbon nanotubes involves several chemical steps (i.e. oxidation, fluorination, among others) and the result is a covalent bond of the functionalization group and the CNTs. Covalent functionalization has high variety of synthetic routes. However, there are some disadvantages such as, the loss of aromaticity [21] or the increase of the defects, which can change the properties of the CNTs (mechanical and electrical). For that reason, the non-covalent modification could be a good choice to avoid these difficulties. The non-covalent modifications are based on supramolecular complexation made by hydrogen bonds, by adsorption based on Van der Waals forces,

electrostatic forces, and π-stacking interactions. All non-covalent interactions are based on π-π interactions between aromatic groups [18], which are weak interactions so their stability can be low.

Graphene's chemistry resembles the graphite one, due to the sp^2 hybridization. Both, the oxidation and the reduction of graphene have been widely studied and it has been demonstrated that the oxidation level depends on the nature of the oxidant agent and the quality of the graphite used [22], [23]. Graphene oxide (GO) has a high concentration of polar groups, that makes it hydrophilic and allows its modification with different functional groups (by derivatization, Williamson reaction, Wittig reaction, nanoparticles and/or quantum dots as modifiers, among others such as Prussian blue, metal hydroxides, porphyrins, aromatic dyes, cyclodextrins, etc.)[18].

Besides the problem of hydrophobicity of both carbon materials, that can be solved, as mentioned, by modifying them, graphene presents higher biocompatibility than CNTs [24].

- **Polymers**

Since long time polymers were known, but the term "*polymer*" was coined by Jöns Jakob Berzelius in 1833, which means "*poly*" as many (whereas "*mono*" means single) and "*mer*" parts in Greek [25]. Polymers are natural or synthetic large molecules composed by monomers, that could be the same structure repeated n times or different structures that are repeated. Some natural polymers are proteins (monomers: amino acid), cellulose (monomers: sugar molecules) or rubber (monomer: isoprene). Some synthetic polymers are polyethylene (monomer: ethylene), polyvinyl chloride (monomer: vinyl chloride) or vinyl acetate (monomers: ethylene and acetic acid).

The chains can grow in different forms and depending on that they have different physicochemical properties [26]:

- **Linear**: they are soluble and melt.
- **Branched**: they are soluble and melt.
- **Crosslinking**: consist in the reaction of different monomers with more than two functional groups with a suitable stoichiometry of these functional groups resulting in a 3D network. This network is insoluble and unable to melt.

Over the years, these polymers have been modified to attend the society requirements. Some examples of polymers modifications are as follows: vulcanizing rubbers to avoid melting at high temperatures, development of polymer as biocides (in general, biocidal polymers

comprise quaternary ammonium, phosphonium, tertiary sulfonium, and guanidinium ions), in textile (e.g. Gore-Tex and Nylon), as drug carriers or to mimic the cells [27]. The versatility that they offer, allow us to use them in different fields like industry, medicine, or engineering.

Polymersomes (Psomes) are considered the structural analogues of liposomes. They are artificial hollow vesicles enclosed by bilayer membranes composed of amphiphilic block copolymers, so they can be nanoscale. They present high stability, robustness, surface functionalization, and stimuli responsive membrane [27]. **Figure 6** shows different stimuli that can produce changes in the Psomes, such as change in the pH, redox reactions, thermal, enzymatic reactions, electricity, or magnetism [28].

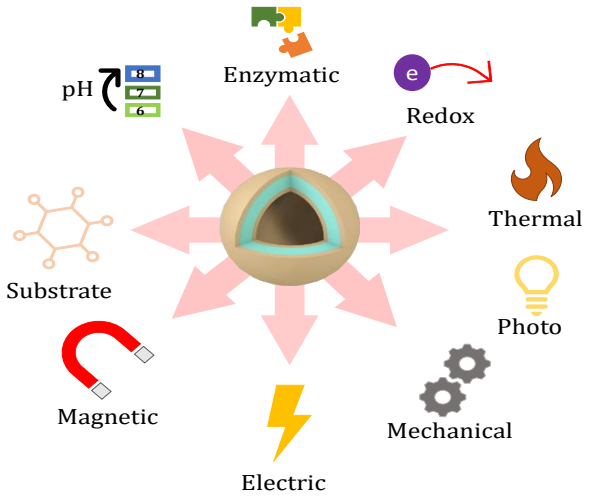

Figure 6. Stimuli response of Psomes.

These vesicles can be loaded with drugs to allow their controlled release [29], [30], [31], with enzymes[32], [33], [34], or with organelles to simulate the cells[35].

Due to its response to external stimuli and the properties of the polymers used in the assembly of the Psomes, they are a novel strategy to be used in sensing platforms [36], [37]. In **Table 2**, there are some examples of loaded Psomes with different cargos used for sensing optical approaches based on different detection instrumental techniques. However, its limited application in electrochemical sensors is surprising.

Table 2. Some examples of the use of Psomes for sensing approaches using spectrophotometric techniques.

Polymer	Encapsulated	Analyte	Technique	Ref.
Poly(ethyleneglycol)-b-poly(ε-caprolactone)(PEG-PCL)	BODIPY [3]	pH response	Colorimetric	[38]
Azobenzene	Polydiacetylene (PDA)	temperature	Fluorescence (enhance by adding β-cyclodextrine)	[39]
Mix of phospholipids and polydiacetylenes	Fluorescent benzoxazole	pH response	Fluorescent Resonance energy transference (FRET)	[40]
Poly(2-methyl-2-oxazoline)-block- poly(dimethylsiloxane)-block poly(2-methyl-2-oxazoline) (PMOXA-b-PDMS-b-PMOXA)	Horseradish Peroxidase (HRP)	pH response	Fluorescence (Amplex™ Red reaction)	[41]
poly(2-(methacryloyloxy)ethyl phosphorylcholine-block-2-(diisopropylamino)ethyl methacrylate) (PMPC-PDPA)	Nile blue	pH response	Colorimetric	[42]
Azobenzene	PDA	α-cyclodextrin	Colorimetric	[43]
PDA	BODIPY	Organic amine, triethylamine	Fluorescence	[44]
PDA	Probe DNA	Targeted DNA	Colorimetric	[45]

[3] 4,4-difluoro-4-bora-3a,4a-diaza-s-indacene it is a family of dyes.

Table 2 (continue). Some examples of the use of Psomes for sensing approaches using spectrophotometric techniques.

Polymer	Encapsulated	Analyte	Technique	Ref.
PDA	phenylboronic acid	H_2O_2	Colorimetric	[46]
Poly(3-ethyl-3-oxetanemethanol) and poly(ethylene oxide) (HBPO-PEO) terminated in tertiary alkanolamines	Cresol red	SO_2	Colorimetric	[47]
PDA	Anti-PAT	Phosphinothricin cetyltransferase (PAT)	Colorimetric (Immunoreaction)	[48]
poly-(e-caprolactone)-b-(poly[2-(diethylamino)-ethyl methacrylate]-b-poly- (ethylene glycol)) (PCL-b-PDEAEMA-b-PEG)	Rhodamine	CO_2	Fluorescence	[37]
Poly(2-methyl-2-oxazoline)-block-poly(dimethylsiloxane)-block poly(2-methyl-2-oxazoline) (PMOXA-b-PDMS-b-PMOXA)	Superoxide dismutase (SOD)	H_2O_2	Fluorescence (Amplex™ Red reaction)	[37]
Poly(2-methyl-2-oxazoline)-block poly(dimethylsiloxane)-block poly(2-methyl-2-oxazoline) (PMOXA-b-PDMS-b-PMOXA)	Superoxide dismutase (SOD) and lactoperoxidase (LPO)	O_2 and H_2O_2	Fluorescence (Amplex™ Red reaction)	[37]

1.2. Targeted analytes

So, at the end, the modification of the electrode depends on the targeted analyte. In this work the first targeted analytes evaluated were "heavy metals", such as cadmium (Cd), copper (Cu) and lead (Pb). The other measured analyte is glucose ($C_6H_{12}O_6$), determined indirectly as hydrogen peroxide (H_2O_2) previous enzymatic reaction with the enzyme Glucose Oxidase (GOx).

1.2.1. Metals

Usually, "*heavy*" is related to high density and "metal" is used to refer to the pure element or an alloy with high metal content. The term "*heavy metal*" is often used for metals and semimetals indistinctly, that have been associated with contamination and potential toxicity or ecotoxicity. But the IUPAC define a metal as: *"elements which conduct electricity, have a metallic lustre, are malleable and ductile, form cations, and have basic oxides"* [49], so the term is wide.

Besides its toxicity, some metals have important role in the metabolism and without them the organism can become affected by specific symptoms [50]. This type of metals is commonly called essential metals and for human beings these are copper (Cu), iron (Fe), zinc (Zn), cobalt (Co), chromium (Cr), manganese (Mn), molybdenum (Mo) and nickel (Ni). Essential metals are involved in biological functions, including catalytic action, stabilization of proteins, movement of electrons, prevention of damage by Reactive Oxygen Species (ROS[4]) among others [51].

There are some other metals that do not have any role in the human metabolism and are dangerous for environment and health, for example cadmium (Cd), lead (Pb) and mercury (Hg), among others.

Some of the sources of all these metals (Cu, Fe, Cd, Pb, etc.) are either naturals (lixiviation, volcanism) or anthropogenic (mining, industry, urbanism, etc.). Since we are exposed to them, the legislation must register a maximum authorized value, which for drinking water are listed in **Table 3**.

[4] Reactive oxygen species (ROS) can damage the DNA or the cell.

Table 3. Maximum concentration of Cd, Cu, Pb and Hg allowed in drinking water by World Health Organization (WHO) and the European Union.

Metal	Cd [μg·L^{-1}]	Cu [μg·L^{-1}]	Pb [μg·L^{-1}]	Hg [μg·L^{-1}]	Ref
WHO	3	2000	10	6	[52]
European Union	5	2000	5	1	[53]

The main problems of these metals (besides their toxicity) are the persistence in the ecosystems and the capability of bioaccumulation in the organisms leading to biomagnification in the trophic chain. For those reasons, the concentration of this metals must be monitored. In **Table 4**, there are some examples of modified carbon electrodes used to monitor these metals [54].

Table 4. Summary of different modified bare carbon electrodes used for, metal analysis. The type of electrode, metals and the kind of matrix analyzed, and the electrochemical technique applied are here listed.

Electrode	Metal	Matrix	Technique	Ref.
SnO_2/rGO	Cd^{2+}, Pb^{2+}, Cu^{2+} and Hg^{2+}	Synthetic samples	SWASV	[55]
Nafion/ionic liquid/Graphene composite SPE	Zn^{2+}, Pb^{2+} and Cd^{2+}	Bottled water	SWASV	[56]
Modified Carbon nanofibers SPE	Zn^{2+}, In^{3+}, Bi^{3+}, Cd^{2+}, Tl^{3+} and Pb^{2+}	Tap water	DPASV	[57]
Graphite felt	Zn^{2+}	Tap water and food supplement	LSASV	[58]
Graphite felt	Pb^{2+}	Synthetic samples	LSASV	[59]
CNTs/Poly(1,2-DAB)[5] composite modified GC electrode	Cd^{2+} and Cu^{2+}	Metallurgic wastewater	SWASV	[60]
CNT/(H_2pyrabza) ligand and its modification on paraffin-impregnated graphite electrode	Pb^{2+} and Hg^{2+}	Sea, lake and well water	SWASV	[61]
CNTs microelectrode	Cd^{2+}, Pb^{2+} and Cu^{2+}	Tap water	SWASV	[62]
Hg(II)-imprinted PMBT[6]/AuNPs/ SWCNTs/GCE	Hg^{2+}	River and Tap water	DPASV	[63]
MWCNT-β-CD/SPE	Pb^{2+}	Bottle, lake and tap water	DPASV	[64]
N-doped Graphene modified GCE	Cd^{2+}, Pb^{2+}, Hg^{2+} and Cu^{2+}	Tap water	DPASV	[65]

[5] 1,2-diaminobenzene
[6] Poly(2-mercaptobenzothiazole)

Table 4 (continue). Summary of different modified bare carbon electrodes used for, metal analysis. The type of electrode, metals and the kind of matrix analyzed, and the electrochemical technique applied are here listed.

Electrode	Metal	Matrix	Technique	Ref.
PANI[7]-GO hydrogel/ GCE	Pb^{2+}	Tap water, industrial influent, and environmental water	SWASV	[66]
$[Ru(bpy^{8})_3]^{2+}$-GO/ Au	Cd^{2+}, Pb^{2+}, Hg^{2+} and As^{3+}	Tap water, and Cauvery River water	DPV	[67]
GO-Fe_3O_4-PAMAM[9]/ GCE	$Cd^{2+}$and Pb^{2+}	Lake and river water	SWASV	[68]
Graphene/CeO_2/GCE	Cd^{2+}, Pb^{2+}, Hg^{2+} and Cu^{2+}	Synthetic samples	DPASV	[69]
ZnO@Graphene/carbon SPE	$Cd^{2+}$and Pb^{2+}	Wastewater	ASV	[70]

SWASV: Square-wave Anodic Stripping Voltammetry

DPASV: Differential Pulse Anodic Stripping Voltammetry

LSASV: Linear Swap Anodic Stripping Voltammetry

DPV: Differential Pulse Voltammetry

ASV: Anodic Stripping Voltammetry

[7] Polyaniline
[8] Bipyrididyl
[9] Poly(amidoamine) dendrimer

1.2.2. Glucose

As was mentioned before, metals have several functions, along them avoiding Reactive Oxygen Species (ROS) damaging to DNA cells. ROS are a group of molecules that include highly reactive free oxygen radicals, for example superoxide anion ($O_2^{\cdot-}$) and the hydroxyl radical ($OH^{\cdot-}$) and non-radical oxidant hydrogen peroxide (H_2O_2) [71]. H_2O_2 is an inorganic compound with oxidizing properties, which make it unstable. A general decomposition reaction appears in (**Equation 2**). The decomposition reaction by oxidation is utilized in many electrochemical sensors, particularly in amperometric ones [72] .

$$a\ H_2O_2 \rightleftarrows b\ H_2O + c\ O_2 \qquad \textbf{(Equation 2)}$$

Where:

a,b,c: are the stoichiometric values

These stoichiometric values and the reaction itself depend on the presence of H_2, the material used for sensing and the pH of the media. The use of carbon materials contributes to the sensing of this analyte, on the contrary for the polymers' materials that, usually are not electroactive [72].

It is well known that the common glucose sensor detects H_2O_2, an electroactive specie that is generated enzymatically from glucose and by using Glucose Oxidase enzyme (GOx) as catalyser. But it was not until 1962 that Clark and Lyons report the first enzyme-based sensor for glucose, based on immobilized GOx, (EC 1.1.3.4). In 1975, the first glucose analyser based on amperometric detection of hydrogen peroxide was launched, and the principle of how it works is shown in **Scheme 4** . The GOx oxidise the glucose into gluconic acid and H_2O_2. The H_2O_2 is detected by the electrode at the oxidation potential applied. In the first generation of glucose sensors, this electrode was made of platinum, so they were quite expensive. The second generation of glucose biosensors used synthetic electron acceptors in the form of redox couples or dyes. They use them as a mediator that can transfer electrons between the

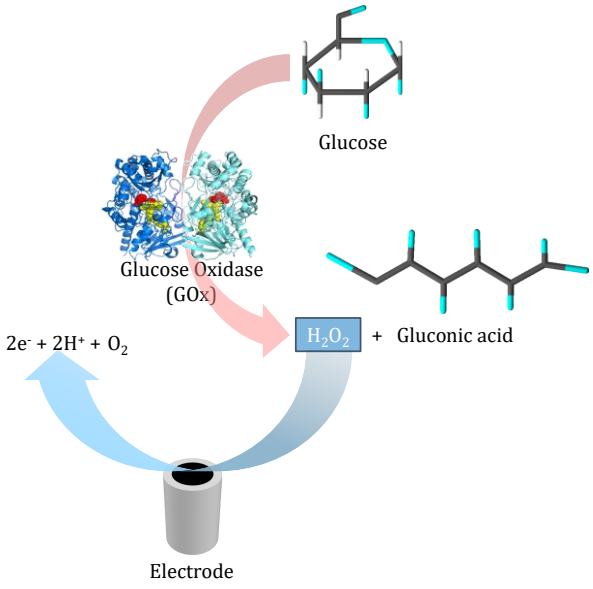

Scheme 4. Operational method of a first generation enzymatic electrochemical glucose sensor.

active site of the enzyme and the surface of the electrode. Due to the toxicity and relative solubility of this redox pairs and dyes, a new generation of glucose sensors were born. So, in this sense, the use of screen-printed electrodes was a step forward by using a long flexible poly(4-vinylpyridine) (PVP) or osmium dopped poly(vinylimidazole) polymer support that can shorten the distance between the active site of the GOx and the electrode surface to improve the electron transfer [73].

The operating method of GOx is a Ping-Pong Bi Bi mechanism, using the cofactor Flavin Adenin Dinucleotide (FAD) and Histidine (His) [74] (**Scheme 5**). As a Ping-Pong mechanism, the oxidation of D-glucose to gluconic acid in oxygen presence and the formation of hydrogen peroxide occurs in two main steps, where the enzyme has an intermediate state. First, the GOx enzyme interacts with the substrate (D-glucose) and the FAD oxidizes the D-glucose to glucono-δ- lactone and FAD is reduced to $FADH_2$. The enzyme is left in a reduced form (intermediate state, **Scheme 5**. **C**). It is followed by an electron transference to O_2 to form H_2O_2 and the enzyme returns to its original form. The glucono-δ-lactone hydrolyses in aqueous media and for gluconic acid [75].

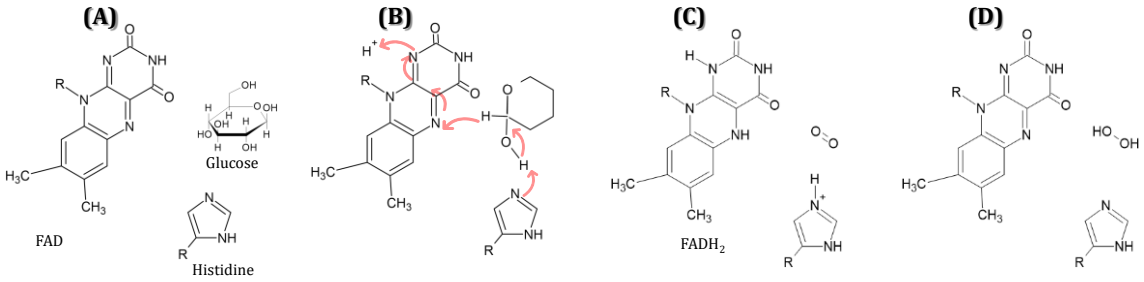

Scheme 5. GOx operating system where (A) GOx interacts with the substrate, (B) the most likely mechanism of GOx reduction, (C) GOx-O_2 complex and (D) GOx-H_2O_2 complex. His is considered the basic group of the enzyme [75].

Nowadays, some other approaches using the glucose sensor as example have been developed, for example the use of metallic or metal oxides nanoparticles (such as AuNPs, Fe_3O_4), modified carbon materials (poly(L-arginine) film onto MWCNTs-modified@Glassy Carbon Electrode (GCE), MWCNTs, modified with avidin and RuNPs onto GCE, among others), etc. [73], [76], [77], [78] .

Nanozyme is a recent term, coin in 2004 by Pasquato and Scrimin, to describe the gold nanoparticle-based transphosphorylation mimics process, which results on a proper onto the surface of gold nanoparticles [79]. Later, this Nanozyme term was used to denominate nanomaterials that have enzyme-like characteristics [80]. There are several differences between a natural enzyme and a nanozyme, which are summarized in **Table 5**.

Table 5. Principal differences between natural enzymes and nanozymes [81].

Natural Enzymes		Nanozymes	
Pros	**Cons**	**Pros**	**Cons**
High catalytic efficiency	Low stability	Low cost	Size (shape, structure, composition) dependent properties
High substrate specificity		Tuneable activity	
High enantio-selectivity		Self-assembly	
Tuneable activity		High stability (long-term storage, robustness to harsh environments)	
Wide range of catalytic reactions		Easy for mass production and further modification (such as bioconjugation)	
Good biocompatibility		Smart response to external stimuli	
Rational design via protein engineering and computation		Multifunction	

There are some other enzymes or nanozyme that, instead of producing H_2O_2, can consume it. For example, it is well known that Fe-porphyrins as nanozyme can catalyse the decomposition of H_2O_2, like the enzyme Catalase Peroxidase (CAT, EC 1.11.1.21) (see **Scheme 6**) [82].

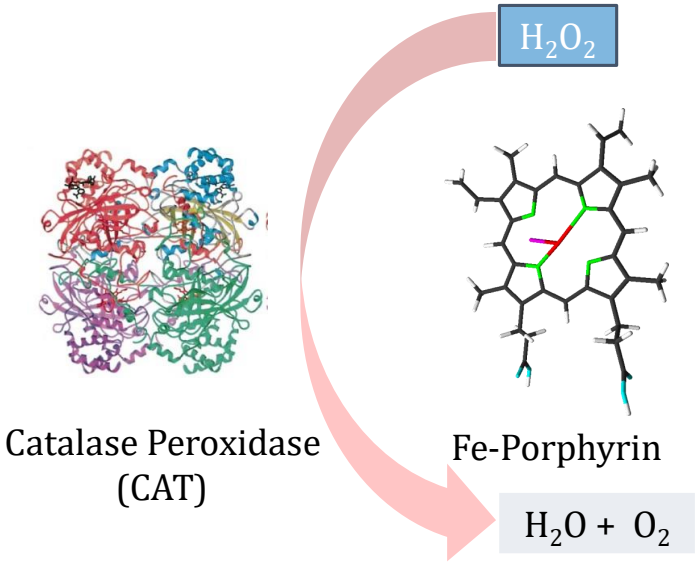

Scheme 6. General reaction of the decomposition og H_2O_2 catalyzed by enzyme CAT and nanozyme Fe-prophyrin.

CAT is a metalloenzyme, that contains iron. There are two possible mechanisms used by the CAT enzyme, one using a His and the direct one without His (as it is shown in **Scheme 7**). His unit plays an active role is the mechanism as an acid-base catalyst to mediate the transference of a proton (**Scheme 7.A**). Additionally, this reaction can be also followed directly, in absence of His (**Scheme 7.B**) [83].

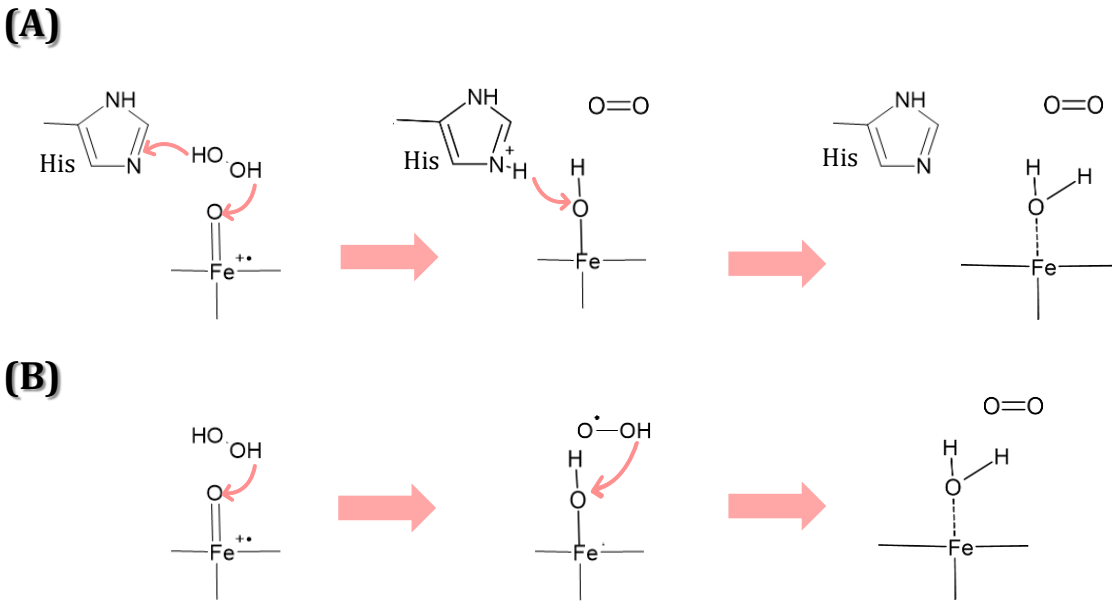

Scheme 7. CAT mechanism reaction (A) mediated His and (B) directly.

The mechanism of the Fe-Porphyrins is based on the Fenton reaction [84]. Originally, in this reaction Fe^{2+} was used that is oxidized into Fe^{3+} by H_2O_2 and forming OH^- (hydroxide) and $OH\cdot$ (hydroxide radical). This Fe^{3+} is reduced to Fe^{2+} by H_2O_2 forming $OOH\cdot$ (hydroperoxyl radical) and H^+ (proton). The total effect is the disproportionation of the H_2O_2 in H_2O and O_2.

This thesis explores the use of composite electrodes based on different allotropic forms of carbon modified with metal nanoparticles and loaded polymersomes with enzymes and/or nanozyme as electrode surface modification strategies. This goal was implemented to analyse diverse target analytes,

Chapter II

Objectives & overview

2.1. General Objective

The general objective of this research work was to design and develop new surface modification for the composite electrodes optimized in our research group for environmental and clinical applications. The modifications could be inorganic or biological, and both were tested due to the different challenge that each one presents.

2.2. Specific objectives

As was mentioned the modifications tested were inorganic or biological, and each one presents several challenges.

For the inorganic modification the selected application was persistent pollutant analysis, such as metals and the corresponding specific objectives are:

1) To optimize of the carbon material used for the composite electrode construction based on previous research group works.
2) To optimize of the operation parameters for use SWASV technique.
3) Synthesis and characterization of the suitable nanoparticles for the electrode surface modification.
4) Characterization and comparison of the response of the proposed modified electrodes for metal analysis with different modifications.
5) Application of the optimized customized sensor to real samples from different origins and matrices.

For the biological modification, the polymersome (Psomes) approach was followed to exploit the advantages given by these vesicles. In this case, the 15% graphite electrode, which was previously optimized by the research group, was used.

1) Learn how to prepare empty and loaded Psomes and characterize them.
2) To optimize the surface modification of the bare electrode to anchor the Psomes.
3) Morphological characterization of the obtained hybrid material.
4) Optimization of the conditions to follow of the enzymatic reaction using chronoamperometry.
5) Use this approach to test vesicles with heterogeneous charge to generate cascade reactions taking advantage of Psomes characteristics.
6) Study the suitability of the Psomes for encapsulating nanozymes, and their synergy with natural enzymes.

2.3. Overview

Several tasks were performed to achieve the main objective and the specific ones. A summary of the accomplished tasks is shown in **Table 6.**

This thesis is based on previous research group information, so the optimization stage of the different carbon materials is not developed in here. In the first chapter where the results are presented, this information is used to test the different carbon materials to achieve the best determination of Cd^{2+}, Pb^{2+} and Cu^{2+} using Square-Wave Anodic Stripping Voltammetry.

The second part of the results is a continuation of the previous one. Therefore, the optimized carbon material electrode is used as a base for the modification followed by using mercury nanoparticles, and by using the optimized SWASV's parameters, as well. Due to the well-known properties of mercury, it is a good candidate for enhancing the response of the raw electrode towards metal analysis.

The electrode in the third part of the results was based on carbon material selected in the previous chapter, and by using the corresponding carbon material percentage as it was optimized for biosensors in previous works of the research group. The modification using Glucose Oxidase (GOx) and the Psomes developed in Dresden, as well as chronoamperometry parameters were optimized.

The fourth part of the results is a continuation of the previous one, adding the complexity of a heterogenous load of the vesicles used (Psomes). The challenge of this chapter was that the load was done using a natural enzyme (CAT) and a nanozyme (modified Hemin) This was done to demonstrate the versatility that can be gained by using Psomes as molecular encapsulation via vesicle-like mechanism.

This thesis presents two sensors: an inorganic one and a proof of concept of a hybrid nanomaterial for a biosensor.

Scheme 8 summarizes the main line of research of this work.

Table 6. Summary of the task performed to complete the stablished objectives.

Thesis chapter	Objective	Task performed	Extra info.
Composite electrodes based on carbon materials towards metal analysis	Optimization of the carbon composite material used for metal analysis using SWASV.	Characterization of the commercial carbon materials using TEM. Synthesis of rGO using Hummer's approach. Fabrication of the electrodes of each composite material and their electrochemical characterization (using CV and EIS). Optimization of the measurement conditions. Measurement of each metal individually.	Some of these results were presented in the 1st International Electronic Conference on Chemical Sensors and Analytical Chemistry (CSAC2021) and was published as a proceeding.
Composite electrodes modified with mercury nanoparticles	Enhance the performance of the bare electrode using the properties of mercury and the advantages of the nanoparticles to achieve a better sensing platform.	Synthesized mercury nanoparticles and characterize them using TEM and XPS. Optimization of the surface modification. Measurement of each metal individually and simultaneously. Analysis of real samples.	Some of these results were submitted as a paper.

Table 6 (continue). Summary of the task performed to complete the stablished objectives.

Composite electrodes modified using enzyme loaded polymersomes	Develop a novel hybrid material that enables the incorporation of the Psomes and the electrochemical monitoring of the enzymatic product.	Prepare empty and loaded Psomes. Characterization and verify the enzyme activity of the loaded Psomes. Develop a novel hybrid nanomaterial that allows the incorporation of the loaded vesicles. Optimize the electrochemical conditions of measurements and other parameters to follow the enzymatic reaction.	Some of this research was conducted in Dresden Leibniz-Institut für Polymerschung e.V. (Germany) as part of a collaboration and was continued in the Universitat Autònoma de Barcelona.
Cascade reaction over modified composite electrodes	Develop a novel hybrid material that enables the incorporation of heterogeneous loaded Psomes and the electrochemical monitoring of the enzymatic product.	Development of a hybrid material with heterogenous load for the electrode modification. Development of a protocol for the nanozymes loading. Check the cascade reaction using natural enzyme and nanozymes.	Some of this research was conducted in Dresden Leibniz-Institut für Polymerschung e.V. (Germany) as part of a collaboration and was continued in the Universitat Autònoma de Barcelona.

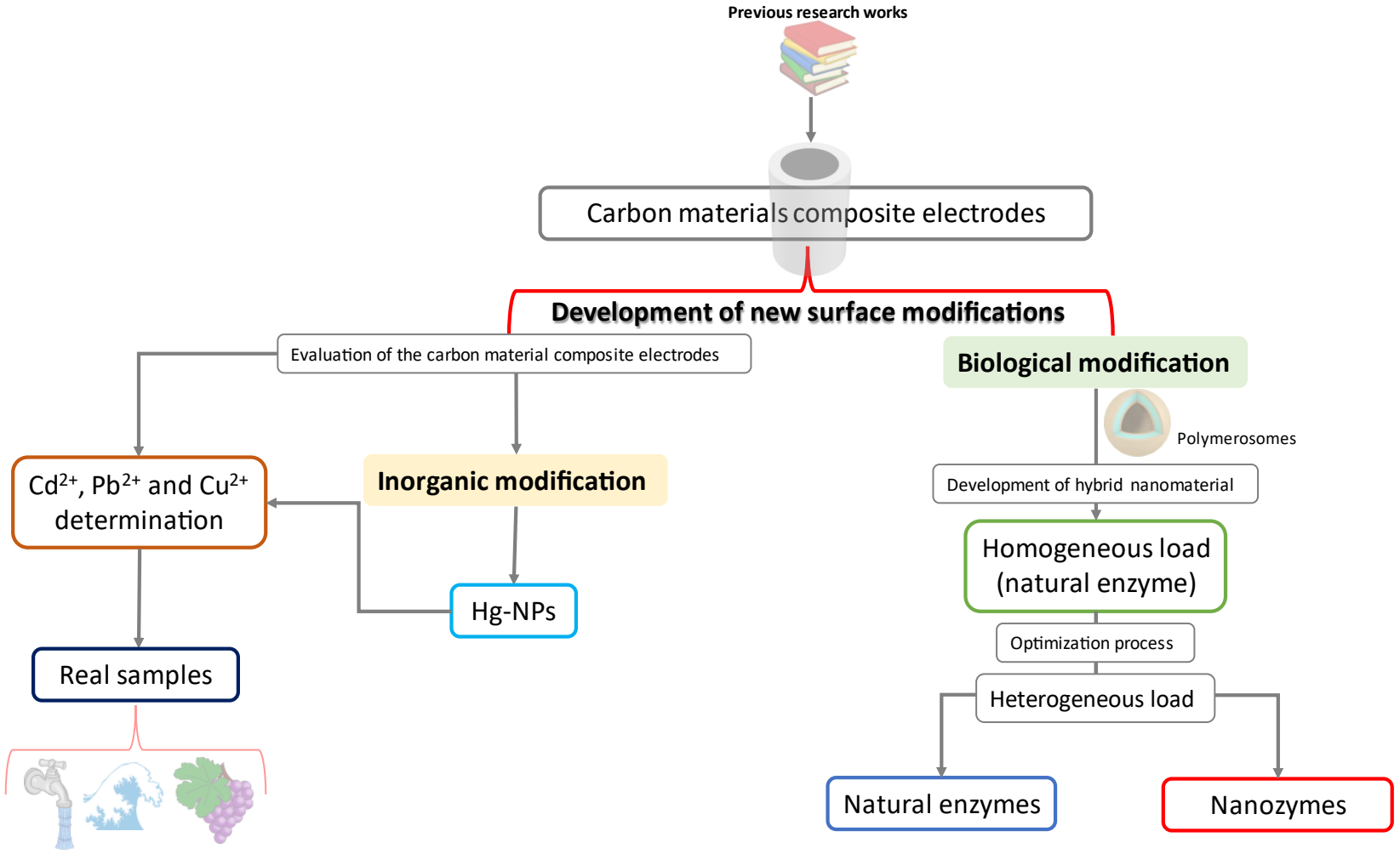

Scheme 8. Graphic outline of the content of this thesis.

Chapter III

Materials & Methods

In this part, it is presented the common methodologies used in this thesis. Specifically, the reagents and solutions used, minor equipment, the morphological and electrochemical characterization procedures, construction of the bare electrodes, and description of the electroanalytical measurements processes. Some of the reagents, equipment, synthesis, modifications of the electrodes and measurement techniques needed for the development of the experimental are presented in the chapter where it is required.

3.1. Apparatus and conditions

To pH measurements a pH meter: model HI 2211 pH/ORP meter (the equipment and the calibration solutions (pH: 4.0, 7.0 and 9.0) were from Hanna Instruments S.L, Eibar, Gipuzkoa, Spain).

Another minor equipment used:

- Ultrasound probe: model Vibracell VC50 from Sonics & Materials INC, (Newtown, CT, USA).
- Centrifuge (Digicen CE 07) using an angular rotor (RT 018) from ALRESA (Daganzo de Arriba, Madrid, Spain).
- Agate mortar from Labbox Labware, S.L. (Barcelona, Spain).
- Ultrasound bath from Labbox Labware, S.L. (Barcelona, Spain).
- Digital Microscope: model AM4815ZTL from DinoLite, (Almere, The Netherlands).
- Orbital Shake: model Unimax 1010; and incubator module: model Incubator 1000 from Heidolph Instruments GmbH & Co. KG (Schwabach, Germany)
- Hollow Fiber Filtration (HFF): model KrosFlo Research Iii System (SpectrumLabs, USA), equipped with a polysulfone-based separation module (MWCO: 500 kDa, SpectrumLabs, USA).

Ultrawave microwave digester from (Milestone Srl, Sorisole BG, Italy), was used to digest with concentrate HNO_3 the samples that will need it, previous ICP measurements. And as comparation method for the glucose determination the commercial Bioanalyzer YSI 2700 Select from Marshall Scientific (Hampton, NH, USA) was used.

3.2. Electrode fabrication and measurement system

3.2.1. Electrode fabrication

In this work, handmade composite electrodes based on carbon materials such as graphite, reduced graphene oxide or carbon nanotubes are used. In every chapter, the composite material used to prepare the electrode is indicated. However, the protocol to prepare

electrodes is the same independently of the carbon material, the time of mixing the materials to form the composite is not. In **Scheme 9**, the whole process is summarized. First, a copper sheet that has been clean with diluted HNO_3, is welded to a commercial connector (from Onda Radio S.A., Barcelona, Spain). After that, the connector is placed in a PVC tube (purchased in Servei Estació S.A., Barcelona, Spain), then filled with the selected composite material. In this work the composite material is formed by the selected carbon material and a polymeric matrix (Epotek H77A (epoxy) Epotek H77B (hardener) both from Epoxy Technology, Billerica, MA, USA). For graphite composite the mixing time is around half an hour, for CNTs is 1h and for rGO is around 2h. Then, it is cured for 2 days at 80 °C. Before used, the electrode is polished.

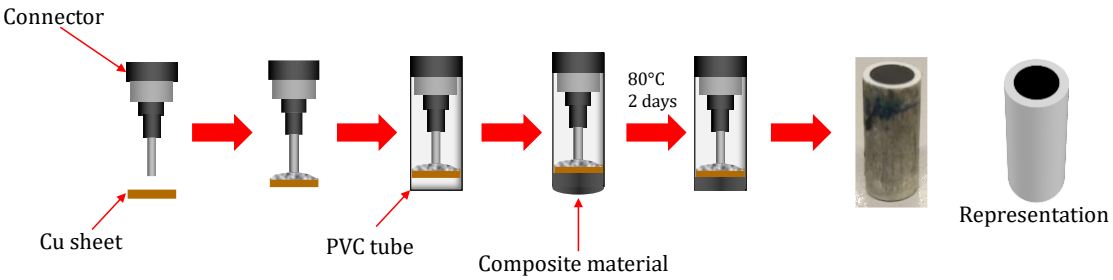

Scheme 9. Fabrication process of the composite electrode. On the right: image and representtaion of the electrode used in this work.

3.2.2. Electrochemical measurements

In all this work the analytical techniques used were chronoamperometry and anodic stripping voltammetry. Consequently, three electrode configurations were used: as counter electrode a platinum electrode 53-671 (Crison Instruments, Alella, Barcelona, Spain), as a reference electrode an Ag/AgCl Orion 900 single-junction electrode filled with a reference filling solution Orion 900001 (Thermo Electron Corporation, Beverly, MA, USA) and the composite electrodes were used as working electrodes. Furthermore, to characterize them a homemade Ag/AgCl electrode was used, due to the permeability of the porous frit of the commercial electrode to the $[Fe(CN)_6]^{3-}/[Fe(CN)_6]^{4-}$ redox probe solution.

Two measurement equipment were used depending on application: Multi AUTOLAB M101 (Eco Chemie, Utrecht, The Netherlands) and EMSTAT 4s (Palmsens B.V, Houten, The Netherlands), both computer controlled. The first one was used for the metal analysis and the second one was selected for the use of the enzyme modification electrodes due to its size and portability. The conditions of each analysis are detailed in the corresponding chapters.

3.3. Characterization techniques.

All the materials used were characterized by different means. In **Table 7**, there is a summary of what is analysed for each technique.

Table 7. Summary of the types of characterization, techniques, obtained information and sample where is used.

Type of characterization	Technique	Information	Sample
Morphological	Scanning electron Microscopy (SEM)	Information of the surface of the modified electrodes	Modified electrodes
	Transmission Electron Microscopy (TEM)	Information of the size of the nanomaterials.	Nanomaterials
	Dynamic Light Scattering (DLS)	Information about the size and polydispersity index (PdI)	Empty-Psomes and Loaded-Psomes
Chemical	X-Ray Photoelectron Spectroscopy (XPS)	Information about the oxidation state of the nanomaterials.	$HgNPs^{RouteA}$
	Inductively Coupled Plasma (ICP)	Quantification of metals (also as comparative method)	Metal reals samples and quantification of AuNPs@rGO and GOx-Psomes-β-CD-S-AuNPs@rGO
	Zeta potential (ζ potential)	Information about the stability of the nanomaterials	HgNPs

Table 7(continue). Summary of the types of characterization, techniques, obtained information and sample where is used.

Optical	UV-Vis	Absorbance	Porphyrins and control of the reaction of graphene oxide (GO) and reduced graphene oxide (rGO)
	Fluorescence	Fluorescence intensity	Amplex™ Red assay
Electrochemical	Cyclic Voltammetry (CV)	Electroactive area and Tafel diagrams	Raw electrodes and modified electrodes
	Electrochemical Impedance Spectroscopy (EIS)	Resistance to the current flow	Raw electrodes and modified electrodes

3.3.1. Morphological characterization

To have information about the morphology, size, distribution of the materials studied, several techniques were used.

⌘ **Scanning Electron Microscopy**

SEM produce the signal from interactions of the electron beam with atoms at various depths within the sample. SEM used: model MerlinFE-SEM from Carl Zeiss Microscopy, (GmbH, Oberkochen, Germany). And EDS used was Oxford LINCA X-Max detector from Jeol, (Peabody, MA, USA).

Various types of signals are produced depending on the sample or sensor evaluated that interacts with the beam: secondary electrons (SE) which is the standard analysis, back-scattered electrons (BSE) and energy-dispersive X-rays (EDX). SE can be used only to escape from the surface of the sample. BSE are beam electrons that are reflected from the sample by elastic scattering. Their energy is higher than the SE, they can emerge from deeper locations, but they lose resolution. Usually, BSE and X-rays spectra are used to characterize the material because they are related to the atomic number. Characteristic X-rays are emitted when the electron beam removes an electron from the shell, causing a higher-energy electron to replace it and release energy. These characteristic X-rays can be

measured by Energy-dispersive X-ray spectroscopy and used to identify and measure the abundance of elements in the sample and map their distribution [85].

⌘ **Transmission Electron Microscopy**

TEM, model JEM-2011, 200 kV from Jeol, (Peabody, MA, USA) equipped with a Complementary Metal Oxide Semiconductor device (CMOS) works like an optic microscope. First, a heated tungsten filament in the electron gun produces electrons that get focused on the sample by the condenser lenses. The magnetic lenses are used to focus the beam of electrons of the sample (the vacuum allows electrons to produce a clear image without collision with any air molecules). When the electrons hit the sample, it scatters them focusing them on the magnetic lenses forming a large clear image, and if it passes through a fluorescent screen, it forms a polychromatic image. So, the denser the specimen is, the higher number of electrons are scattered forming a darker image and more thinner and transparent specimens appear brighter [86].

Additionally, for the Cryogenic Transmission Electron Microscopy (Cryo-TEM) technique the sample preparation was done using Cryo-Plunging Leica EM GP (from Leica Biosystems, GmbH, Nussloch, Germany). To vitrify the samples, they were treated with ethanol or propanol and cooling, usually, with liquid N_2. The vitrification method is based in a very fast sample cooling that prevents the formation of crystalline ice. Another Cryo-TEM equipment was also used model Libra 120 microscope, 120 kV from Carl Zeiss Microscopy (GmbH, Oberkochen, Germany), equipped with a Charge Coupled Device (CCD) camera.

TEM and Cryo-TEM images were used to determine the particle size by measuring directly the images obtained using ImageJ software (1.52 P). The data obtained were treated using a data treatment software and adjusting the sizes obtained to a three-parameter Gaussian curve (see **Equation 3**).

$$y = ae^{\left[-\frac{1}{2}\left(\frac{x_0 - x}{sd}\right)^2\right]} \qquad \textbf{(Equation 3)}$$

Where:

a: statistical parameter related to the fitting.

x_0: mean diameter

sd: standard deviation.

⌘ **Dynamic Light Scattering**

DLS is a technique that can be used to determine the size distribution of small particles or polymers in suspension. When light hits small particles, the light scatters in all directions

(Rayleigh scattering[10]) if the particles are small compared to the wavelength. Even if the light source is a laser, and thus is monochromatic and coherent, the scattering intensity fluctuates over time. This fluctuation is due to small particles in suspension undergoing Brownian motion, and so the distance between the scatterers in the solution is constantly changing with time. This scattered light then undergoes either constructive or destructive interference by the surrounding particles, and within this intensity fluctuation, information is contained about the time scale of movement of the scatterers.

Such DLS measurements were used to analyse aqueous Psomes solution (≤ 1 mg mL^{-1}) that were done using a Zetasizer Nano-series with Dispersion Technology Software (version 5.00) (from Malvern Panalytical Ltd., Malvern, United Kingdom). The measurements were carried out at different pH at 20 °C. The equilibration time was 30 s and the acquisition time was 75 or 125 s (15 or 25 runs, 5 $s \cdot run^{-1}$) per three measurements. The data was collected using the NIBS (non-invasive backscatter) method using a Helium–Neon laser (4 mW, λ = 632.8 nm) and a fixed angle of 173°. The data was analysed using Malvern Software 7.11.

3.3.2. Chemical characterization.

This characterization can give information about the oxidation state of mercury, the amount of an element or the stability of the nanoparticles.

⌘ **X-Ray Photoelectron Spectroscopy**

XPS used: hemispherical Phoibos 150 EP MCD analyser (from SPECS, Berlin, Germany) that is a surface quantitative spectroscopic technique based on the photoelectric effect[11] that can give elemental composition, also the chemical state, and the overall electronic structure and density of the electronic states in the material. XPS not only shows what elements are present, but also what other elements they are bonded to. XPS belongs to the family of photoemission spectroscopies in which electron population spectra are obtained by irradiating a material with a beam of X-rays. Chemical states are inferred from the measurement of the kinetic energy and the number of the ejected electrons. When laboratory X-ray sources are used, XPS easily detects all elements except hydrogen and helium. A typical XPS spectrum is a plot of the number of electrons detected at a specific binding energy. Each element produces a set of characteristic XPS peaks. These peaks correspond to the configuration of the electrons within the atoms. XPS has the ability to

[10] Rayleigh scattering is mostly elastic scattering of light or other electromagnetic radiation by particles much smaller than the wavelength of the radiation.
[11] Photoelectric effect is the emission of electrons when electromagnetic radiations hit the material.

produce chemical state information. The local bonding environment is affected by the formal oxidation state, and the identity of its surrounding atoms.

⌘ **Inductively Coupled Plasma**

ICP-OES and ICP-MS are analytical techniques used to elemental analysis. ICPs are used to produce excited atoms and ions that emit electromagnetic radiation at a characteristic wavelength for each element. So, in the case of the Optical Emission Spectroscopy (OES) detector, the intensity of such emissions from various wavelengths of light are proportional to the concentrations of the elements within the sample. For the Mass Spectroscopy (MS) detector (often a quadrupole analyser), the ions are separated based on the relation mass-to- charge.

In this study, ICP-OES and ICP-MS model 7900 and model 5900, respectively, from Agilent (Santa Clara, CA, USA) were used.

⌘ **Zeta potential**

ζ is a term used to refers to the electrokinetic potential in colloidal dispersions. Zeta potential is the electric potential in the interfacial double layer (DL) at the location of the slipping plane relative to a point in the bulk fluid away from the interface. In other words, zeta potential is the potential difference between the dispersion medium and the stationary layer of fluid attached to the dispersed particle. The zeta potential is an important parameter and readily measurable indicator of the stability of colloidal dispersions. The magnitude of the zeta potential indicates the degree of electrostatic repulsion between adjacent, similarly charged particles in a dispersion. For molecules and particles that are small enough, a high zeta potential will confer stability. When the potential is small, attractive forces may exceed this repulsion and the dispersion may break and flocculate. So, colloids with high zeta potential (negative or positive) are electrically stabilized while colloids with low zeta potentials tend to coagulate or flocculate as outlined in the table.

ζ measurements were performed with Malvern Zetasizer® Nano Series Z instrument (from Malvern Panalytical Ltd., Malvern, United Kingdom). For the HgNPs analysis the ζ values were obtained using a 10mWred laser (632.8 nm) (Malvern Panalytical Ltd., Malvern, United Kingdom) and the values for the different synthesized HgNPs were obtained using 25 µL of each one and resuspended in 1 mL of deionized water. Each sample was equilibrated for 1 min at 25 °C before starting the ζ analysis, 30 runs per measurement were performed and the samples analyzed by triplicate.

3.3.3. Optical characterization

This characterization helps to follow the reduction reaction of the graphene oxide (GO) to reduced graphene oxide (rGO) by a change in the bands at 235 and 300 nm to one band at 267 nm. Also, the enzymatic reactions used a fluorescence component to characterize its activity.

⌘ **Ultraviolet-Visible and Fluorescence spectroscopy**

UV-Vis used was model UV2 from ATI Unicam (this company do no longer exist)) is a spectrophotometric technique that measure the absorption of electromagnetic radiation, as a function of frequency or wavelength, due to its interaction with a sample. The intensity of the absorption varies as a function of frequency, and this variation is the absorption spectrum.

Fluorescence spectroscopy involves using a beam of light, usually ultraviolet light, that excites the electrons in molecules of certain compounds and causes them to emit light; typically, but not necessarily, visible light. The instrument used was Microplate reader, model TECAN infinite PRO microplate reader equipped with I-control 1.10 software (from Tecan Group Ltd., Männedorf, Switzerland). Measurements to validate the H_2O_2 production or consumption were done by using Amplex Red Assay (λ_{Ex} = 534 nm, λ_{Em} = 580 nm, 1 h every 10 min).

The Amplex™ Red assay consist in an indirect assay of the H_2O_2, as is shown in **Figure 7**.

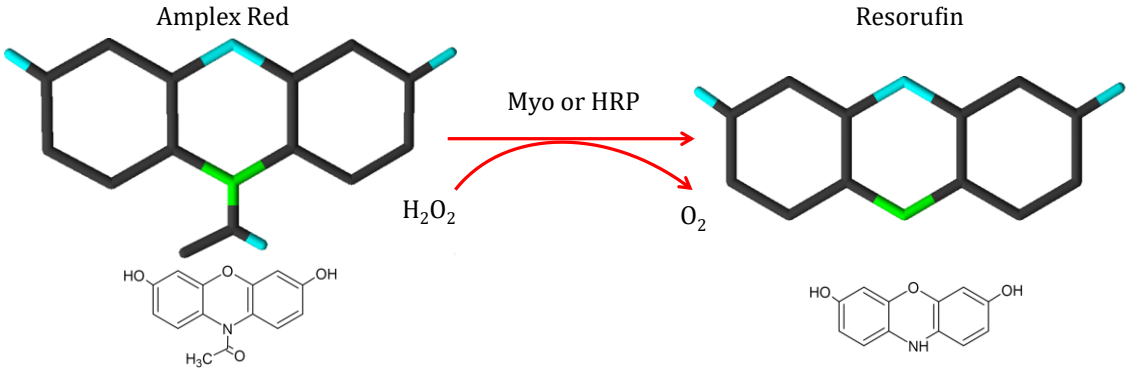

Figure 7. Amplex ™ Red reaction.

The H_2O_2 generated or consumed, depending on the enzyme o nanozyme used, reacts with the Myoglobin (Myo) or the Horseradish Peroxidase (HRP) and the Amplex™ Red (10-acetyl-3,7-dihydroxyphenoxazine, non-fluorescent) transforms into Resorufin (7-hydroxy-3H-phenoxazine-3-one), that is fluorescent.

Firstly, some stock solutions must be prepared, the concentration of the stock and the concentration of the solution (if it is required) are summarized in **Table 8**.

Table 8. Amplex™Red assay reagents and dilutions.

Reagent	Stock solution	Dilution concentration
Amplex™ Red	2.0 mg·mL^{-1} in DMSO (≥ 99.7%)	0.02 mg·mL^{-1} in Milli-Q water
H_2O_2 (30%, from Sigma Aldrich, St. Louise, MO, USA)	10 mM	4 μM
Myoglobin (Myo) from equine skeletal muscle, (95-100%, essentially salt-free, lyophilized powder)	1 mg·mL^{-1} of in PBS 1 mM	0.2 mg·mL^{-1}
D-(+)-Glucose	0.001 mg·mL^{-1} of in Milli-Q water	

All the reagents are from Sigma Aldrich, (St. Louise, MO, USA), except Amplex™ Red reagent was purchased from Life Technologies Corporation (Thermo Fisher, Eugene, USA).

The enzyme activity of the unpurified enzyme loaded Psomes was studied at two pH 7.4 and 6.0, so the same experiments were repeated for each pH. In, **Table 9** the Psomes solution used is called stock solution and it was estimated that 0.1 mg · mL^{-1} of unpurified enzyme loaded Psomes contains 0.01 mg · mL^{-1} of enzyme. Based on that the concentrations of the wells were calculated (Figure 8).

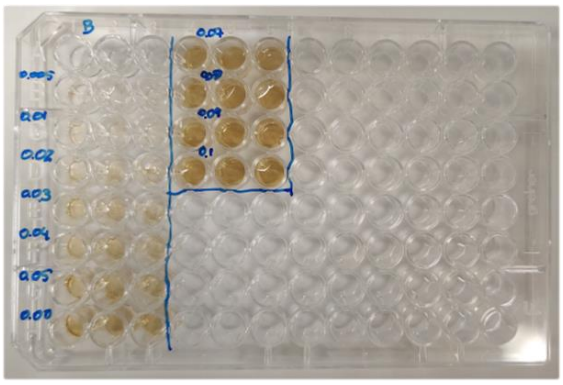

Figure 8. Preparation of standards to calibration procedure of Hemin chloride in a microplate containing 96 wells.

Table 9. Enzyme activity study: Concentration in the well and composition for GOx-Psomes and CAT-Psomes.

$[GOx]_{in\ the\ well}$	Dilution	$[CAT]_{in\ the\ well}$	Dilution
0 mg·mL^{-1}	100 µL PBS 1 mM	0 mg·mL^{-1}	100 µL PBS 1 mM
0.002 mg·mL^{-1}	10 µL stock solution + 90 µL PBS 1 mM	0.002 mg·mL^{-1}	10 µL stock solution + 90 µL PBS 1 mM
0.004 mg·mL^{-1}	20 µL stock solution + 80 µL PBS 1 mM	0.004 mg·mL^{-1}	20 µL stock solution + 80 µL PBS 1 mM
0.008 mg·mL^{-1}	40 µL stock solution + 60 µL PBS 1 mM	0.008 mg·mL^{-1}	40 µL stock solution + 60 µL PBS 1 mM
		0.015 mg·mL^{-1}	75 µL stock solution + 25 µL PBS 1 mM

Fresh working solution (WS) was prepared by mixing in proportion 1.5:1.5:6 Myo 0.2 mg·mL^{-1}, Amplex™ Red 0.02 mg·mL^{-1} and PBS 10 mM pH 7.4, respectively.

On one hand, to study the H_2O_2 production of the GOx-Psomes, 2.5 µL of glucose (0.001 mg·mL^{-1}) were added to each well and incubated for 30 min. On the other, to study the H_2O_2 consumption by CAT-Psomes, hence 20 µL H_2O_2 (4 µM) were added to each well and incubated for 30 min. When the incubation time has passed, 100 µL of WS were added to each well and the fluorescence intensity measurements were recorded for 1 h every 10 min (λ_{Ex}: 534 nm; λ_{Em}: 580 nm).

The study the purified enzyme-Psomes were carried out at two pH, 5 and 8. To perform the experiment, 300 µL of the purified enzyme-Psomes (0.25 mg·mL^{-1}) were added to an Eppendorf™. In the case of the GOx-Psomes 2.5 µL of glucose (0.01 mg·mL^{-1}) were added but in the case of the CAT-Psomes 5 µL of H_20_2 (20 µM) were added. The sample was stirred and incubated for 30 min. After this time, 300 µL of 10 mM PBS at pH 7.4 were added. Then 250 µL of the samples were added to a well, together with 3.4 µL of Amplex™ Red (0.02 mg·mL^{-1}), and 5 µL of Myo (0.2 mg·mL^{-1}). Finally, the fluorescence intensity measurements were recorded for 30 or 60 min every 10 min (λ_{Ex}: 534 nm; λ_{Em}: 585 nm).

3.3.4. Electrochemical characterization.

Beyond the electrochemical technique used to perform the analysis, there are two electrochemical techniques that must be remarked: Cyclic Voltammetry (CV) and Electrochemical Impedance Spectroscopy (EIS). They are the main techniques used for electrochemical characterization.

In both techniques the analysis was performed in an equimolar solution of 0.01 M $[Fe(CN)_6]^{3-}$ (99%)/$[Fe(CN)_6]^{4-}$ (≥99%) solution and 0.1 M KCl (99%). All these reagents were supplied by Sigma- Aldrich, (St. Louis, MO, USA) (see **Equation 4** for the oxidation reaction and **Equation 5** for the reduction reaction). This redox system is reversible.

$$[Fe(CN)_6]^{4-} \rightleftarrows [Fe(CN)_6]^{3-} + e^- \quad \textbf{(Equation 4)}$$

$$[Fe(CN)_6]^{3-} + e^- \rightleftarrows [Fe(CN)_6]^{4-} \quad \textbf{(Equation 5)}$$

⌘ **Cyclic voltammetry technique**

CV is a voltammetric technique that applies a linearly increasing potential at a constant scan rate, in a closed cycle. The excitation signal for this technique is triangular along time (see **Table 1** in **Chapter I**). Registering the current flowing through the electrode against the applied potential, sudden changes in the current correspond to electrochemical reactions. The peaks correspond to oxidation or reductio of the species in solution. If the potential changes towards positive values (anodic) the electrodes act like an oxidant agent, and if the potential changes towards negative values (cathodic) the electrode acts like a reducing agent. Hence, in one cycle, when the potential goes to positive values, the analyte over the electrode surface is oxidizing and reaching a maximum current, which is called anodic peak. When the potential goes towards negative values, due to the no stirring conditions, the oxidate analyte starts to reduce, generating the cathodic peak (with the corresponding minimum current).

If it is not notice otherwise, the scan rate (ν) selected was 10 $mV \cdot s^{-1}$, and the potential (E) went first to anodic values and then to cathodic. In **Figure 9**, the usual appearance of the CV for the reversible pair redox is shown. The result is a characteristic duck-shaped plot known as cyclic voltammogram.

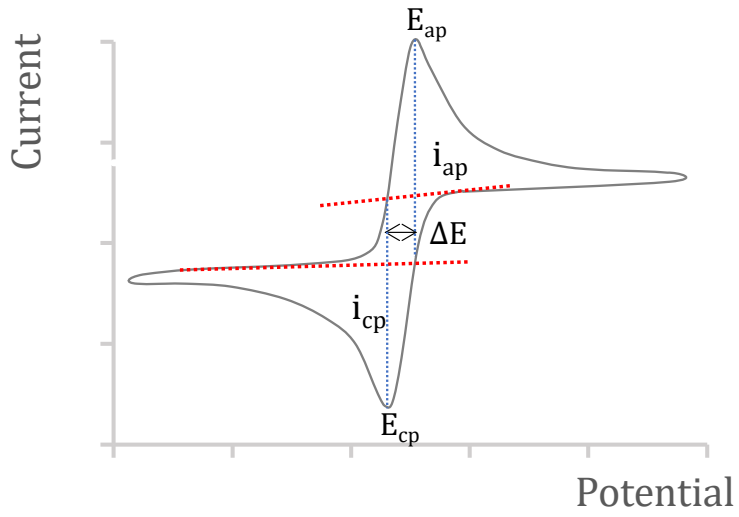

Figure 9. Cyclic voltammogram and relevant information obtained.

Several parameters can be extracted from this technique, as are indicated as follow:

- i_{ap}/E_{ap}: anodic peak current/ potential of the anodic peak (**Equation 4**)
- i_{cp}/E_{cp}: cathodic peak current/ potential of the cathodic peak (**Equation 5**)
- ΔE: equilibrium potential, where $|I_{cp}|= |I_{ap}|$. Also, in ideal conditions, $\Delta E = E_{ap}-E_{cp} = 0.059/n$.

Furthermore, the peak current can be related to the electroactive area (A) of the electrode, by the *Randles-Sevčik* equation (**Equation 6**) [87].

$$I_p = 3.01 \cdot 10^5 \cdot n^{3/2} \cdot (\alpha v D_{Red})^{1/2} \cdot A \cdot [C_a] \qquad \textbf{(Equation 6)}$$

Where:

n: number of electrons participating in the redox process (n=1)

α: transference coefficient, which is approximately 0.5.

D_{Red}: diffusion coefficient of the reduced species, $6.32 \cdot 10^{-6}$ $cm^2 \cdot s^{-1}$

v: scan rate is 0.01 $V \cdot s^{-1}$.

$[C_a]$: bulk concentration of the electroactive species (0.01 M).

Also, the logarithm of the current (log i) can be represented as a function of the applied potential, obtaining the Tafel diagrams (see **Figure 10**).

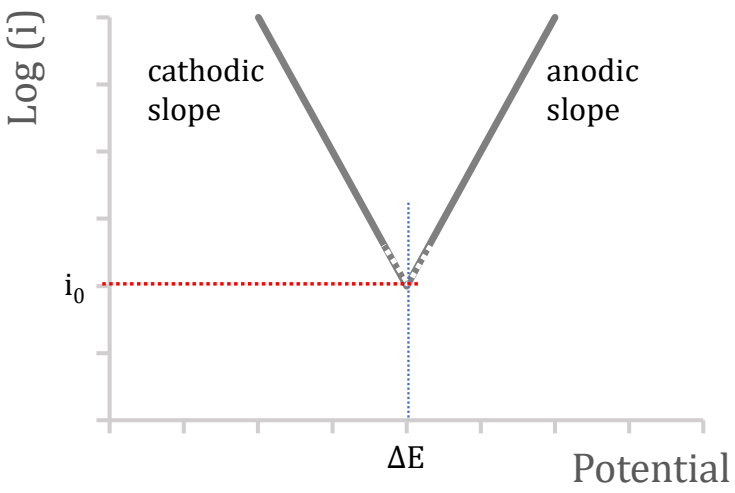

Figure 10. Tafel diagram example.

This diagram gives information about the exchange current (i_0), that is related to the reversibility of the process, and the charge transfer resistance can be calculated using (**Equation 7**).

$$i_0 = {RT}/{nFR_{CT}} \qquad \textbf{(Equation 7)}$$

Where:

R: universal ideal gas constant (8.3145 $J \cdot K^{-1} \cdot mol^{-1}$).

T: temperature (K).

n: number of exchanged electrons (*n*= 1)

F: Faraday constant (96485 $C \cdot mol^{-1}$)

R_{CT}: Charge transfer resistance

⌘ **Impedimetric measurements**

EIS was used to characterize the materials used and the surface process. To perform the measurements, by applying a small perturbation, the system must be in equilibrium or in a stationary state, and the resistance to the flow of electrons is recorded.

In the direct current (DC) system the resistance is given by the ohm law (**Equation 8**). Impedance is a term that describes the resistance when it is alternating current (AC) system (**Equation 9**).

$$E = IR \quad \textbf{(Equation 8)}$$

$$E = IZ \quad \textbf{(Equation 9)}$$

In both cases:

E: potential (V).

I: current (A).

R is the resistance (Ω) of the circuit for a DC current and Z is the impedance (Ω) of the circuit. Impedance depends on the frequency (f, units of Hz or s^{-1}). The sinusoidal potential (E(t)) can be express according to (**Equation 10**):

$$E(t) = E_{MW} \cdot \sin(\omega t) \quad \textbf{(Equation 10)}$$

Where:

E_{MW}: potential maximum width.

ω: angular frequency, $\omega = 2 \cdot \pi \cdot f$

In most of the cases, the current (i (t)) generated by a sinusoidal potential is also sinusoidal with the same angular frequency, but different phase and width to the potential (see **Figure 11**). That is described in (**Equation 11**).

$$i(t) = i_{MW} \cdot \sin(\omega t + \varphi) \quad \textbf{(Equation 11)}$$

Where:

i_{MW}: current maximum width.

ω: angular frequency, $\omega = 2 \cdot \pi \cdot f$

φ: phase shift of the current respect the potential.

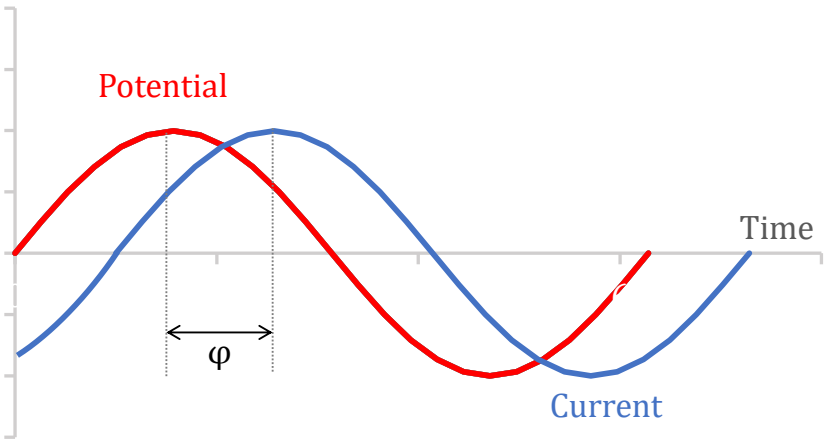

Figure 11. Sinusoidal excitation signal and the current generated shifted in phase.

So, if we isolate Z from (Equation 9), can be also expressed like (**Equation 12**).

$$Z = {E(t)}/{i\,(t)} = {E_{MW} \cdot \sin(\omega t)}/{i_{MW} \cdot \sin(\omega t + \varphi)} \qquad \textbf{(Equation 12)}$$

So, Z° can be defined as E_{MW}/ i_{MW} and a shift in phase φ. To simplify it, Euler identity ($e^{j\tau} = \cos\tau + j\sin\tau$) was applied to express the impedance (see **(Equation** 13).

$$Z = Z^{\circ}(\cos\varphi + \sin\varphi) = Z_{real} + jZ_{imag} \qquad \textbf{(Equation 13)}$$

Where:

Z_{real}: real part of the impedance

$j = \sqrt{-1}$

Z_{imag}: imaginary part of the impedance.

There are different ways of representing Z, but in this work the Nyquist plot is the main used to electrochemical proposes. In Nyquist plot the Z_{imag} is represented as function of the Z_{real}, and each point represents a frequency.

The data treatment is performed by adjusting the data to equivalent circuits. These circuits are formed by electric elements (resistance, capacitators, inductor, etc.) and other ones that are specifically electrochemical (constant phase element, Warburg, Gerischer, etc.). The combination of these elements allows to explain real process behaviour. In **Table 10**, there is a summary of common elements used in the equivalent circuits of this work.

Table 10. Common elements of EIS, their symbol and the impedance formula.

Element	Circuit symbol	Impedance
Resistance (R)		R
Capacitor (C)		$1/j\omega C$
Constant phase element (CPE or Q)		$1/Y_o(j\omega)^{\Theta}$
Warburg (W)		$1/Y_o\sqrt{j\omega}$
Gerischer (G)	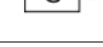	$1/Y_o\sqrt{k_a + j\omega}$

C: capacitance

$\mathbf{Y_o}$: admittance (Mho), $\mathbf{Y_o} = 1/\mathbf{Z_o}$

Θ: depending on this value CPE can act like R (Θ = 0), C (Θ = 1) or W (Θ = 0.5).

k_a: kinetic constant.

The easier equivalent circuit for an electrochemical system is shown in **Figure 12**. Consist in two resistances that can be related to the ohmic resistance (R_Ω) and the charge transfer resistance (R_{CT}). Here appears a Constant Phase Element (CPE), but in this case n = 1, so it acts like a Capacitor (C). This C gives information about the electrochemical double layer. There is no mass transference, for that reason no diffusion elements were needed. In the Randles circuit, there is a diffusion element. The Nyquist plot and the equivalent circuit are shown in **Figure 13.**

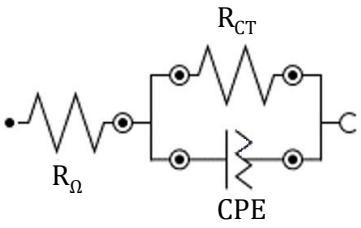

Figure 12. Simplest electrochemical equivalent circuit.

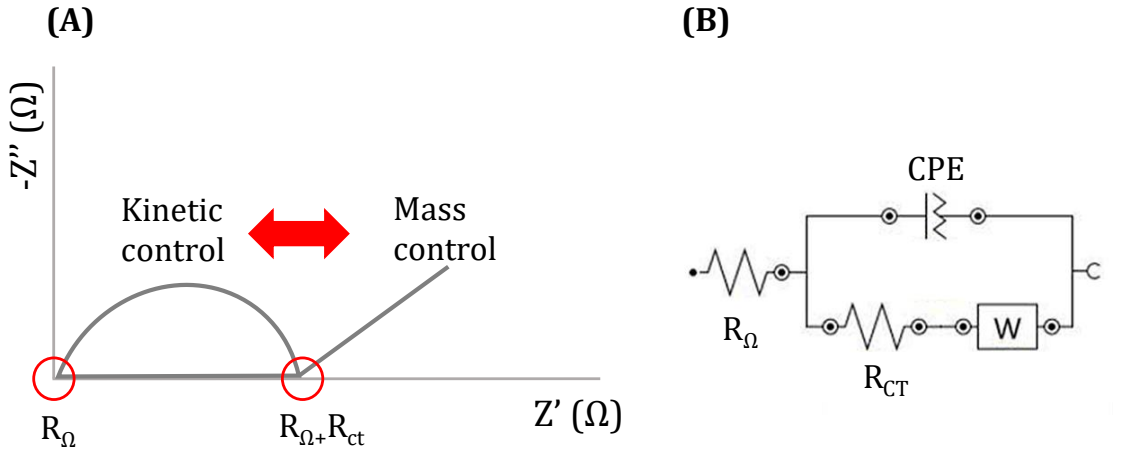

Figure 13. (A) Nyquist representation where the kinetic and mass control zones are highlighted, and (B) the equivalent circuit , called Randles circuit.

From the elements in **Table 10**, the purely mass control elements are Warburg (W) and Gerischer (G). CPE is a polyvalent element that can act differently depending on the Θ value. W is a diffusion element, but G can be related to the porosity of the material [88].

The range of the frequencies used for theses analysis are from 10^5 to 0.01 Hz and all the Nyquist plots were normalized to the minimum value obtained in each component, Z_{imag} and the Z_{real}, to compare them.

3.4. Analytical procedures

All the solutions were prepared in Milli-Q water (from Millipore, Billerica, MA, USA) if it is not indicated otherwise. And if it is not indicated otherwise, the solutions used to adjust the pH were 0.1 M NaOH (98% Alfa Aesar, by Thermo Fisher Scientific, Kandel, Germany) and 1 M HCl (37%, Sigma Aldrich St. Louis, MO, USA).

3.4.1. Metal analysis

The metal stock solutions prepared were: 20.5 mg·L^{-1} (0.18 mM) $Cd(NO_3)_2$ (99%, obtained from Panreac, Castellar del Vallès, Spain), 36.6 mg·L^{-1} (0.18 mM) $Pb(NO_3)_2$ (≥99%, supplied by Sigma-Aldrich, St. Louis, MO, USA) and 12.0 mg·L^{-1} (0.19 mM) $Cu(NO_3)_2$ (99.5%, purchased from Merck, Darmstadt, Germany) in HNO_3 1% (65% from VWR chemicals, Radnor, PA, USA). Then, to prepare a standard with all the metals together, they were diluted in 0.1 M acetic acid (CH_3COOH, 99.9% acquired from J. T. Baker, HPLC reagent, Radnor, PA, USA)/0.1 M ammonium acetate (NH_4CH_3COO, 97% purchased from Panreac, Castellar del Vallès, Spain) buffer at pH 4.6. And the concentration of each metal in this mixture was: 4.1 mg·L^{-1} for Cd^{2+}plus 3.7 mg·L^{-1} for Pb^{2+} and 4.8 mg·L^{-1} for Cu^{2+}.

Several analyses were performed. The first one for the optimization of the method, the second one for the interference studies and the third one for sample analysis. In all cases, the measured solutions are prepared in the acetic acid/acetate buffer.

⌘ **Solution for method optimization**

These analyses are performed by external calibration curves. The points of the calibration curves are prepared individually for each metal in a concentration range from $5.0 \cdot 10^{-3}$ to 1.0 mg·L^{-1} for Cd^{2+}, from $2.8 \cdot 10^{-2}$ to 1.0 mg·L^{-1} for Pb^{2+}, and from $5.7 \cdot 10^{-2}$ to 1.1 mg·L^{-1} for Cu^{2+}.

When the analysis is performed is for the measurement of the three metals simultaneously, an external calibration curve is also prepared. The concentration ranges go from $2.0 \cdot 10^{-3}$ to 1.0 mg·L^{-1} for Cd^{2+}, from $2.0 \cdot 10^{-3}$ to 1 mg·L^{-1} for Pb^{2+}, and from $1.0 \cdot 10^{-3}$ to 1.1 mg·L^{-1} for Cu^{2+}. Some of these concentrations are below the individual ones, these ones were selected to have the same amount of each metal at each point.

⌘ **Solutions for interference analysis**

Two solutions were initially prepared: one of 42 mg·L^{-1} of Fe^{2+} ($FeSO_4 \cdot 7H_2O$, ≥ 99%) and another one of 30 mg·L^{-1} of Fe^{3+} ($Fe(NO_3)_3 \cdot 9H_2O$, ≥ 98%,). Both are purchased from Sigma Aldrich (St. Louise, MO, USA). The organic matter interference analysis was performed by using and preparing a 125 mg·L^{-1} O_2 solution with glucose (D-(+)-glucose, ≥ 99.5%, from Sigma Aldrich, St. Louise, MO, USA), following the stoichiometric relation.

The analysis of interferences was performed first for Fe^{2+}, then Fe^{3+} and later with organic matter. In the Fe^{2+} and Fe^{3+} analysis the methodology used was the same. First a blank of acetic acid/acetate buffer was measured, and different additions of each Fe ion prepared solution were done. The final concentration ranges go from $8.0 \cdot 10^{-2}$ to $8.7 \cdot 10^{-1}$ mg·L^{-1} of Fe^{2+} and $7.0 \cdot 10^{-2}$ to $8.6 \cdot 10^{-1}$ mg·L^{-1} of Fe^{3+}. Once, the last addition was done, the metals of interest

were added, in a concentration of 0.1 $mg \cdot L^{-1}$ each one and measured, then their response is compared.

For the organic matter a solution of 125 $mg \cdot L^{-1}$ of O_2 was measured and the metals of interest were added in a concentration of 0.1 $mg \cdot L^{-1}$ each one. Then, this solution was measured.

⌘ **Approaches to real samples analysis**

In these cases, due to the complexity of some matrices the analysis was performed by standard addition. Which means that each sample was diluted according to the requirements in the acetic acid/acetate buffer. Each point of the calibration curve was prepared individually, by adding the stipulated volume of the sample and the volume of the metal mixture with known concentration. Then, the rest of the volume was filled with acetic acid/acetate buffer. The added concentrations of each metal go from 0 to 0.15 $mg \cdot L^{-1}$ of Cd^{2+}, Pb^{2+} and Cu^{2+}.

3.4.2. Glucose analysis

For glucose analysis, Phosphate Buffered Saline (PBS) tablets (from Sigma-Aldrich, St. Louise, MO, USA) were used to have a solution 10 mM at pH 7.4. The pH buffer was adjusted to other ones 5.0, 6.0, and 8.0 to perform the different tests. If it is not said otherwise, the pH used is 7.4.

Glucose Oxidase (GOx) from *Aspergillus niger* (essentially salt-free, lyophilized powder) was purchased from Sigma-Aldrich (St. Louise, MO, USA)

Catalase (CAT) was from bovine liver from Sigma-Aldrich (St. Louise, MO, USA)

Hemin Chloride (≥96%) was purchased from Cayman Chemicals, (MI, USA).

Using D-(+)-glucose a stock solution of 1 $mg \cdot mL^{-1}$ ($6 \cdot 10^{-3}$ M) was prepared.

Also, from this stock solution, the ones of $4 \cdot 10^{-5}$ M and $7 \cdot 10^{-5}$ M were prepared.

⌘ **Calibration curves procedure**

Calibration curves were done by performing additions to 25 mL of PBS. The concentration range of these additions from the stock solution was from $3.0 \cdot 10^{-5}$ to $3.5 \cdot 10^{-4}$ M of glucose.

⌘ Approaches to real samples

There were two different types of samples: the first one was an unknown glucose spiked sample in PBS 10 mM pH 7.4, This one was measured directly. The second one was a 40 % hypertonic glucose serum (Fresenius Kabi, Barcelona, Spain) and it was diluted in PBS 10 mM pH 7.4. First 2 mL of serum in 250 mL, to make the stock solution and then, from this stock solution 1 mL was taken and diluted in 100 mL of PBS 10 mM pH 7.4 and it was measured. The same range of concentration from $3.0 \cdot 10^{-5}$ to $3.5 \cdot 10^{-4}$ M of glucose was used. The measurements were performed by triplicated.

Chapter IV

Results

The results of this thesis are divided in four parts:

Part I: it will be explained the selection of the most suitable carbon material for metal analysis.

Part II: the synthesis and modification of the composite electrodes with HgNPs will be explained. Furthermore, the analytical performance and real sample analysis will be exposed.

Part III: the modification optimization using GOx-Psomes and the analytical conditions to perform the measurements of the H_2O_2 generation.

Part IV: using the optimized surface modification, the hybrid nanomaterial will contain heterogeneous charge: GOx and a consuming enzyme (CAT) or nanonzyme (Hemin chloride).

Additionally, in all the parts of this chapter, the terms bare and raw were used as synonyms. The inset of the images has the same unit as the main plot if it is not notice otherwise.

Part I

Composite electrodes based on carbon materials towards metal analysis

This chapter is a modification of the paper «Tunable electrochemical sensors based on carbon nanocomposite materials towards enhanced determination of cadmium, lead and copper in water» (https://doi.org/10.3390/CSAC2021-10456)

‡

4.1. Composite electrodes based on carbon materials

In nature we can find natural composite materials like bones; formed by apatite (that is the mineral matrix) and collagen fibres (that is a peptide). Also, wood, formed by cellulose fibres in a lignin matrix is also well-known [10]. Hence, composite materials are not a new idea, they have been used since long time ago; for example, Portland cement (which is a mixture of different oxides, sulphates, and water), sand in asphalt (to prevent degradation of the pavement, fulfil the holes, and increase traction) [89] and carbon black in non-conductive resin (to increase conductivity) [90]. These combinations of materials enhance the response, giving new properties that take advantage of some of the characteristics of the starting materials.

For electroanalytical applications, the use of composite materials for the construction of the electrodes is an attractive option due to their cost-effectiveness and smaller-size sensor, portability, reliability, and being easy-to-use devices. These electrochemical platforms are based on carbon allotropes (e.g., graphite, carbon nanotubes, graphene, and related materials) dispersed in an insulating polymeric matrix (such as epoxy, methacrylate, Teflon, etc.). They have led to important advances in the analytical electrochemistry field, especially in the design of sensors and biosensors devices. However, before using a composite material as electrochemical platform, it is important to optimize composition. One of the tools used for this purpose is percolation curves. The electric properties of the electrode depend on the material's inherent features, the amount used for electrode preparation and its distribution in the final composite electrode. The percolation theory was developed by Broadbent and Hammersley in 1957 [11], but it was used to interpret the conductivity behaviour of composite materials years before. A percolation curve has three main regions: low, medium, and high conductive zones. The top one, at a low percentage of conductive material, acts like a bad conductor or even insulating; as the amount of conductor material increases, the resistance decreases in medium and high composition zones. This is because the conductive particles are closer to each other, improving the conductivity. As a result, the percolation curve provides the data to find a compromise between the percentage of conductive material and the relation signal/noise ratio: the larger the signal-to-noise ratio, the smallest the detection limit achieved.

The study of the optimum composition of these carbon materials mixtures has been done in previous research group works (see **Table 11**).

Table 11. Optimum composition and maximum load of conductor material studied in the composite electrode by the group.

Material	Optimum [%]	Maximum [%]	Reference
Graphite	15	20	[91]
CNTs	10	20	[92]
rGO	15	16	[22]

4.1.1. Carbon materials

Carbon is in the group 14 of the element of the periodic table, and it has different structures depending on how its atoms are arranged, that is called allotropy. Diamond, graphite, graphene, and other forms of carbon have different properties depending on their allotropic forms. Most of the allotropic forms of carbon are not highly reactive, which is a fundamental characteristic of an electrode. Besides, the material chosen for the electrode must have low resistance to the charge transference and high ratio signal/noise. In this work, we use four of these forms of carbon: graphite, reduced graphene oxide (rGO), carbon nanotubes (CNTs) and glassy carbon.

4.1.1.1. Graphite

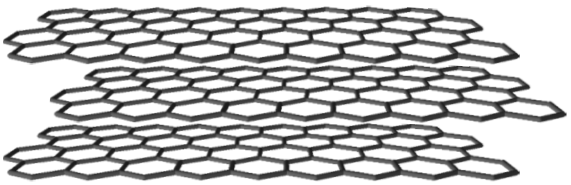

Figure 14. Graphite structure (3D).

Graphite is a greyish-black opaque substance, that can be found in nature, it is the most stable form of carbon. The atoms of carbon are arranged in hexagonal structure and by layers (graphene layers), as can be observed in **Figure 14**. The carbon has sp^2 hybridization and these atoms are joined by covalent bond, but between layers are attached by Van der Waals interactions [93]. This gives special properties to this material, one of the most important is that it is a good electrical conductor along the axis, but not between layers. This is due to the high conjugation of π electrons in the axis. Furthermore, as was said it can be considered chemically inert.

The graphite used for the composite electrode manufacturing was from Merck with a particle size 50 μm (Merck Millipore, Darmstadt, Germany).

4.1.1.2. Graphene

Graphene is a single layer of graphite, where carbon arranged hexagonally (**Figure 15**). The electrical conductivity of this material, like graphite is along the axis.

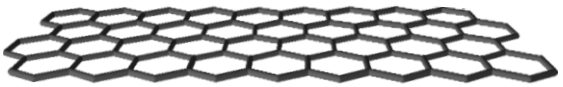

Figure 15. Graphene structure (2D).

To obtain the graphene sheet different methods have been used, including mechanical exfoliation of graphite layers, chemical vapor deposition (CVD), and the Staudenmaier-Brodie method, among others. In the previous works of the research group, Hummer's method was the selected to obtain this material [12], [22]. This method has three main steps: first the oxidation of the graphite using strong oxidizing agents, second the exfoliation of the graphite oixide (GrO) using ultrasounds to obtain graphene oxide (GO), and finally, the reduction of the GO to obtain reduced graphene oxide(rGO), using a mild reducing agent and temperature to recover structure. All these changes are schematically summarized in **Scheme 10.** The main difference between these compounds is the oxygen content, which is around 40-50% for GO and a lower oxygen percentage for rGO [94].

The application of graphite and its derivates (GrO, GO and rGO) are wide and diverse including: composites, anodes, sensors field, as biocides, in the energy area, etc.

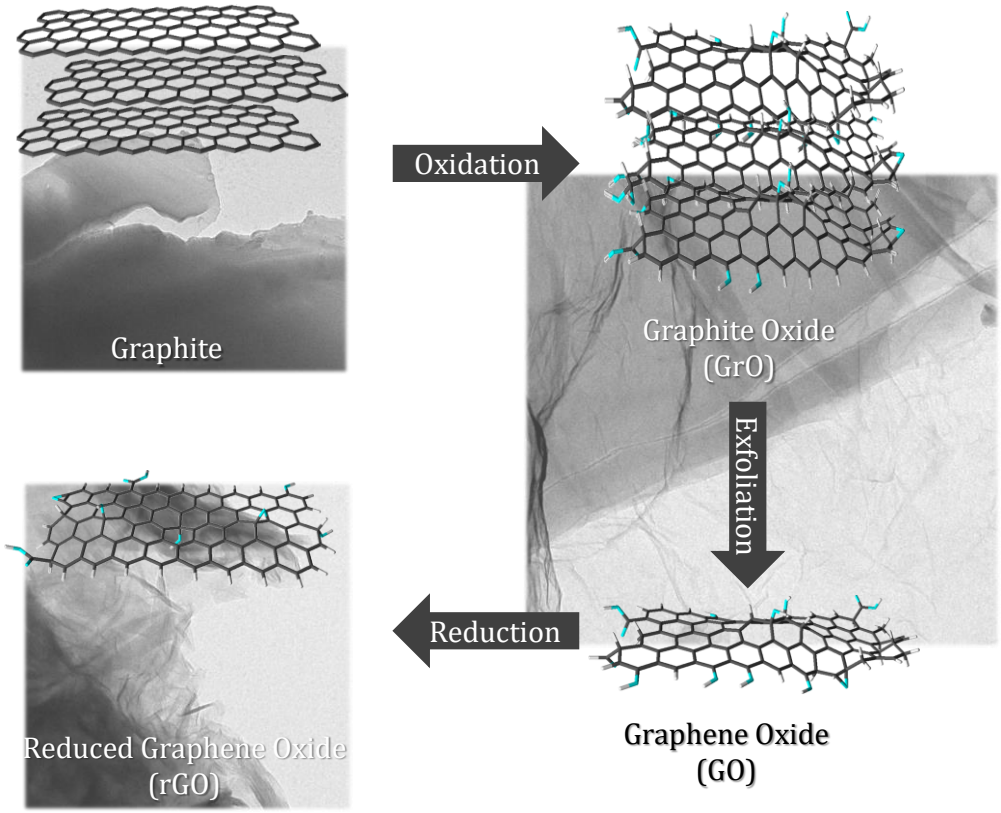

Scheme 10. Principal phases of the reduced Graphene Oxide synthesis. The images are from real TEM samples.

⌘ Synthesis of Graphene Oxide

Following Hummer's method, the first step of the synthesis is to use strong oxidizing agents to oxidize the graphite which leads to the formation of GrO. These reactions promote the appearance of carbonyl, epoxy, and hydroxyl groups which weaken the Van der Waals forces that hold the graphite layers together. Additionally, due to the presence of these groups this material presents hydrophilic behaviour and other alterations in the properties.

All the steps of the synthesis of GrO are summarized in **Scheme 11.**

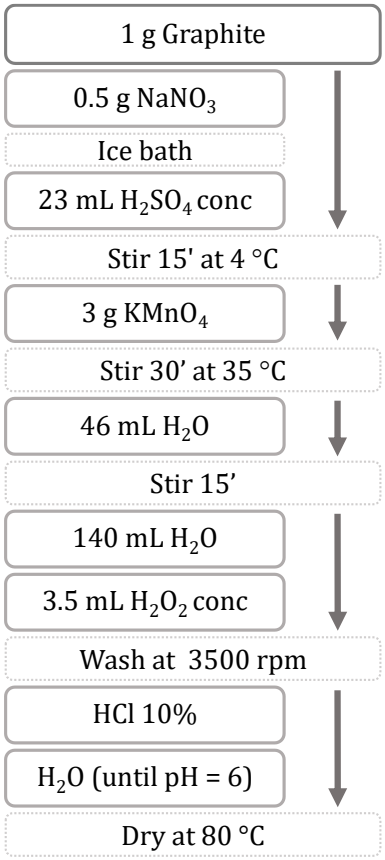

Scheme 11. GrO synthesis with summarized steps.

For the first step of the synthesis, 1 g of graphite powder (from Sigma Aldrich, St. Louis, MO, USA), 0.5 g of $NaNO_3$ (99%, from Labkem, Labbox Labware, S.L., Barcelona, Spain) and 23 mL of H_2SO_4 (95-97% from Scharlab S.L, Barcelona, Spain) were added in a 500 mL round bottom flask and stirred. Then, the flask was cooled down in an ice bath due to the exothermic reaction and stirred for 15 min. After that, 3 g of $KMnO_4$ (≥ 99.5%, from Labkem, Labbox Labware, S.L., Barcelona, Spain) were slowly added in flask and, subsequently, all the solution was heated up to 35 °C for 30 min, that helps the promotion of the oxidation. When the material was oxidized, the colour changed from black to dark brown. After cooling down the solution to room temperature, 46 mL of Milli-Q water was slowly added to reduce the acidity of the medium and stir for 15 min. Another 140 mL of Milli-Q water was added, and the solution was transferred to a beaker. Then, 3.5 mL of H_2O_2 (30% purchased from Merck KGaA, Darmstadt, Germany) were added to remove the excess MnO_2 formed. The solution was washed with HCl 10% and centrifuged at 3500 rpm as many times as necessary to remove a greenish viscous gel (MnO_2). The formed GrO and GO were washed with Milli-Q water and centrifuged until pH 6.0 is reached and dried at 80 °C. As a result, a black solid powder was obtained as a mixture of GrO/GO.

⌘ **Synthesis of Reduced Graphene Oxide**

A scheme of the steps followed is shown in **Scheme 12**.

The resulting dark solid was milled using an agate mortar and 1 mg·mL^{-1} solution of GrO/GO was prepared and sonicated for 1 h. After this step, the layers of GrO are separated, obtaining GO. Afterwards, the solution was heated at 95 °C in an oil bath. The pH was adjusted around 9.5 with NH_3 (25% w/w for analysis, Scharlab S.L, Barcelona, Spain). Gently add directly in the round bottom flask ascorbic acid (> 99.0%, from Panreac Química S.L.U., Barcelona, Spain), which is proposed as reducing agent, to have a concentration of 2 mM in the solution and stir for 15 min. The solution was then cooled at room temperature. Next, the solution was washed with Milli-Q water at 3500 rpm until pH 6.0 is reached, and rGO was dried at 80°C.

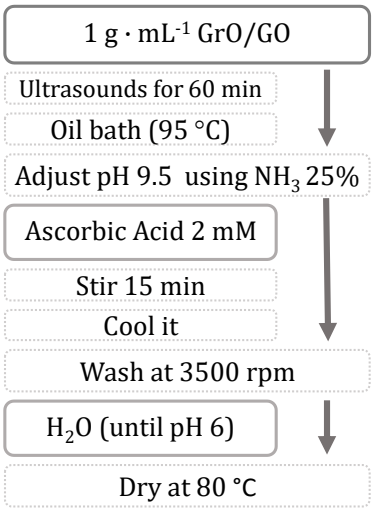

Scheme 12. rGO synthesis with summarized steps.

The reduction of the GO is characterized by the loss of O_2 in the structure and the recuperation of the hybridization sp^2 of the carbon atoms and, in this way, also, the properties.

4.1.1.3. Carbon Nanotubes

Carbon Nanotubes (CNTs) are graphene layers rolled up, getting a cylindrical form (**Figure 16**). Conduction is along the length of the tube. There are two types of nanotubes: single wall nanotubes (SWCNTs), which are made of a single rolled-up layer of graphene, and multiwall carbon nanotubes (MWCNTs), which are made of multiple concentric layers of graphene.

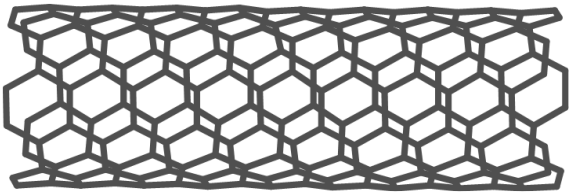

Figure 16. Carbon nanotube structure (1D).

CNTs were supplied from SES research (> 95%, Houston, TX, USA), with a diameter from 10 to 30 nm.

4.1.1.4. Glassy Carbon

Glassy carbon is non-graphitizable form of carbon, meaning that it cannot be converted into crystalline graphite. It is an amorphous allotropic form of carbon [95]. For a long time, the organization of the glassy carbon remains uncertain. Over the years, several models have been proposed to describe its structure, some of them collected in **Figure 17**. In 1972, Jenkin proposed a model, based on the data of Infrared Spectroscopy (IR), X-Ray Diffraction (XRD) and electron microscopy observations The model describes glassy carbon as a network of tangled graphitic ribbons (Jenkin's model). These ribbons were randomly oriented, twisted and with voids (due to the lower density of glassy carbon compared to graphite). Furthermore, to provide more crystallographic information the ribbons were characterized with the parameters of intraplanar microcrystalline length (L_a) and interplanar microcrystalline length (L_c) [95], [96]. In the 2000s, Harry proposed a model base on fullerenes. This model describes glassy carbon as curved fragments of carbon sheets, containing pentagons, hexagons, and heptagons, as well as a small number of closed structures [95], [97].

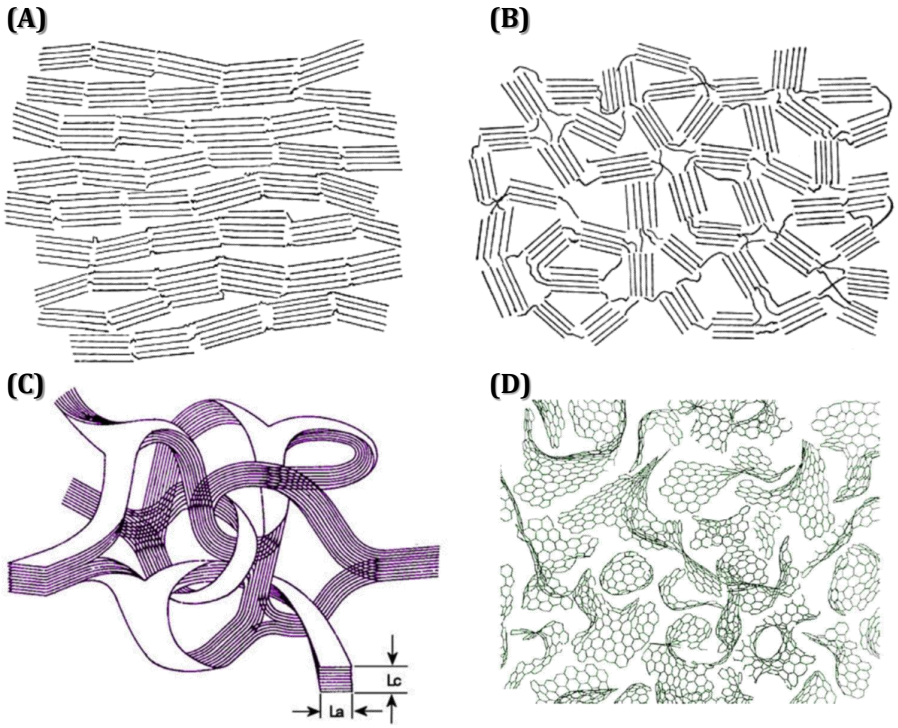

Figure 17. (A) Structure of graphitazing carbon, (B) Structure of non-graphitable carbon, (C) Jenkin's model and (D) Harry's model. Reprinted with permission from [95] under Creative Commons Attribution-NonCommercial-No Derivatives Licence.

In this work, the Glassy Carbon Electrode (GCE) was a handmade one, used in another previous research group work [92].

4.1.2. Morphological characterization

The morphological characterization was made by Transmission Electron Microscopy (TEM), except for the glassy carbon electrode, which cannot be treated to be adjusted to meet the requirements for TEM (see **Figure 18**).

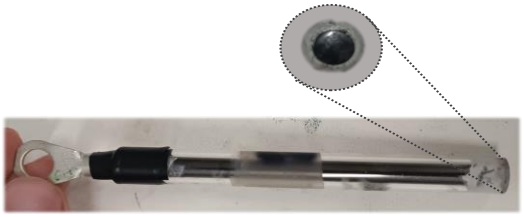

Figure 18. Glassy carbon electrode (GCE).

For the characterization, a dispersion of each carbon materials individually was previously ultrasonicated with an ultrasonic probe.

In **Figure 19.A**, the sheets of the graphite structure are observed. The more layers it has, opaquer it is, so the electron beam cannot pass through them. In **Figure 19.B**, a layer of rGO is observed, which is slightly folded. In **Figure 19.C**, CNTs are observed, which are randomly oriented.

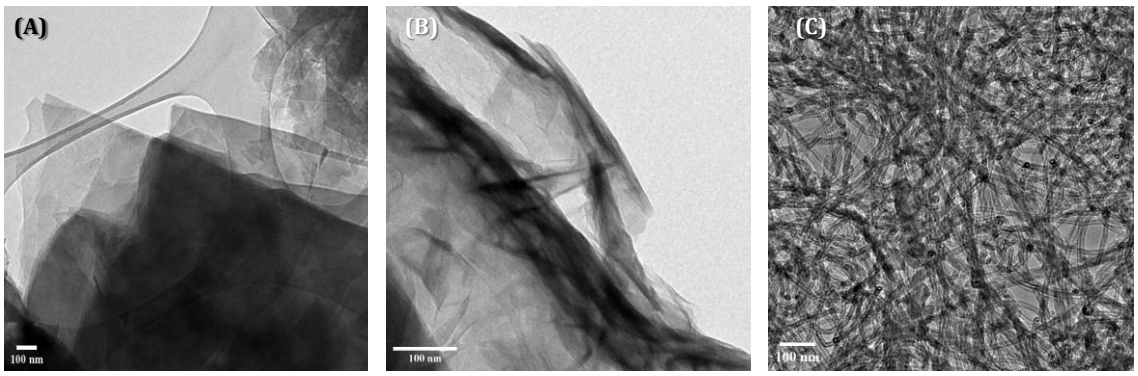

Figure 19. TEM characterization of: (A) graphite; (B) rGO and (C) CNTs.

In the case of CNTs, a diameter study was performed, to compare different batches, the new and the old ones, with a reference value from the supplier of 10-30 nm. Thirty measurements were done of old CNTs, and the size distribution is shown in **Figure 20.A**. The diameter obtained was 24 ± 5 nm. In **Figure 20.B**, seventy measurements were made to find the size distribution of the new CNTs. The size of the new CNTs was found to be 16 ± 5 nm. These values are in the range provided by the supplier, even they are slightly different between batches, so it will become relevant information during this thesis.

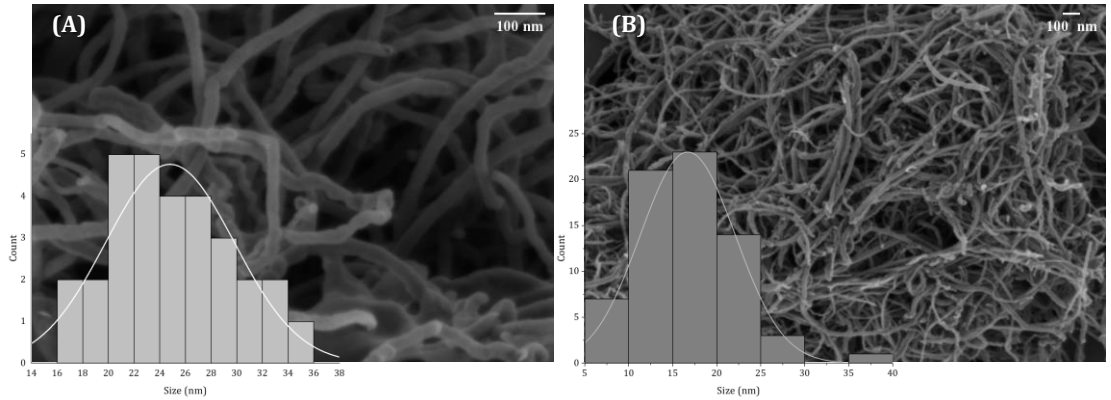

Figure 20. TEM(InLens detector) images and size distribution of (A) $CNTs_{old}$ and (B) $CNTs_{new}$.

4.1.3. Electrochemical characterization

The composite electrodes fabricated using the carbon materials previously described were, also, electrochemically characterized, by Cyclic Voltammetry (CV) and Electrochemical Impedance Spectroscopy (EIS) in an equimolar solution 0.01 M $[Fe(CN)_6]^{3-}/[Fe(CN)_6]^{4-}$ in 0.1 M KCl.

The optimum and the maximum conductive phase compositions were tested for all the materials (see **Table 11**). In all cases, the only component that can be reduced/oxidized is the studied pair Fe(III)/Fe(II) as redox probe.

The electroactive areas were calculated using the anodic current in Randles-Sevčik equation (see **(Equation** 6). Regarding the EIS analysis, the circuit that fit in all cases correspond to the one in **Figure 12**, except for the rGO, which also fit a Warburg element.

4.1.3.1. Graphite composite electrode

In **Figure 21.A**, CV results of composite electrode based on graphite as conductive phase at two different ratio graphite/epoxy resin are shown. The electroactive area of both electrodes was calculated: 0.37 cm^2 for the optimum composition (15% graphite) and 0.55 cm^2 for the maximum composition, 20% graphite. These differences in the electroactive area are due to the distribution of the conductive material (graphite) in the surface of the electrode. In **Figure 21.B**, the 15% graphite composite electrode presents higher resistance to the charge transfer (greater width of the semicircle) than the 20% graphite electrode.

These values obtained 5884 Ω for 15% and 1077 Ω for 20% (**Table 12**), are consistent with the theory of percolation curves and the previous works [91].

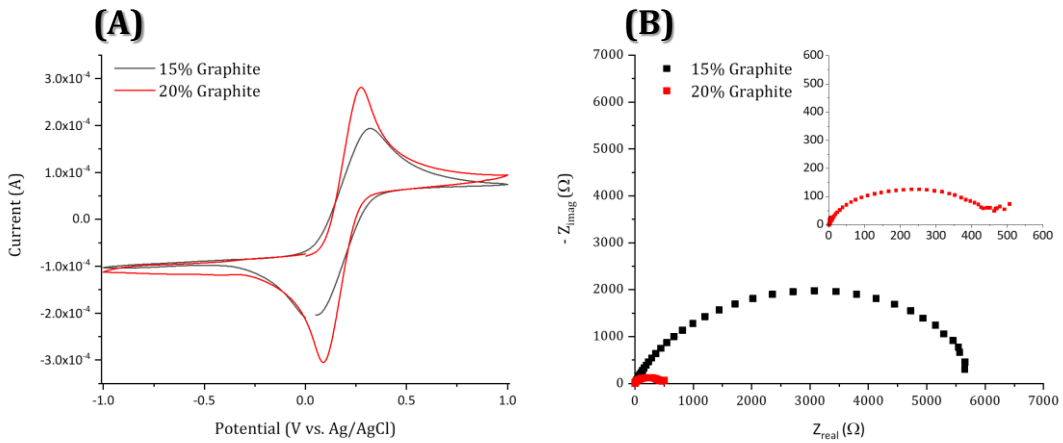

Figure 21. Electrochemical characterization of composite electrode based on graphite (A) CV (v: 10 mV·s^{-1}), and (B) EIS for 15% graphite electrode(black) and 20% graphite electrode (red). Inset of the EIS of the 20% graphite electrode.

4.1.3.2. Reduced graphene oxide composite electrode

As was explained before, the optimum composition was obtained for the synthesized rGO in the polymeric matrix Epotek H77. Depending on the starting material, in this case the graphite, the properties of the final material can change. The optimum composition of rGO (15%) was tested obtaining no peak, even changing the scan rate (see **Figure 22**). Usually, this change in the scan rate is used to test the electrochemical behaviour of the analyzed compounds. Neither oxidation nor reduction peaks were observed at any scan rate. The electrode has a microelectrode behaviour, which means a predominance of radial diffusion. As was said before, the electrical conductivity is through the axis, so rGO requires to be oriented.

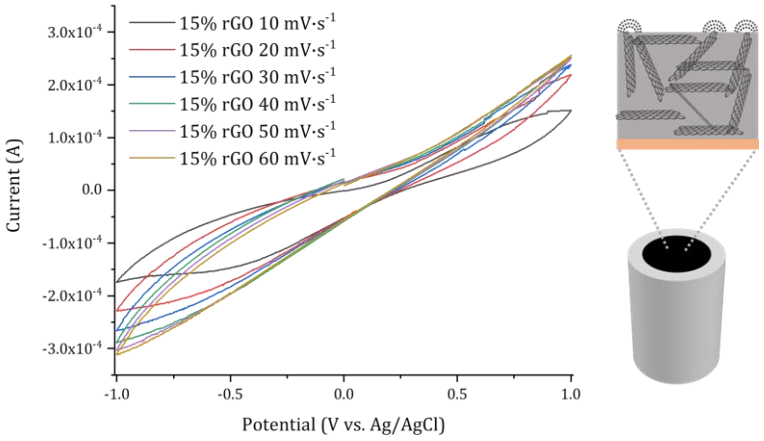

Figure 22. Electrochemical characterization of composite electrode based on rGO. CV of 15% rGO changing the scan rate from 10 mV·s^{-1} to 60 mV·s^{-1}. Radial difussion scheme.

To solve that problem, the rGO was doped with graphite, to enhance the conductivity, so the electrodes studied were 14% rGO and 1% graphite.

In **Figure 23.A**, on one hand, the peaks of the pair redox can be observed, so the calculated electroactive area is 0.27 cm^2. In **Figure 23.B**, on the other hand, the EIS seems to be controlled by mass transfer (diffusion zone).

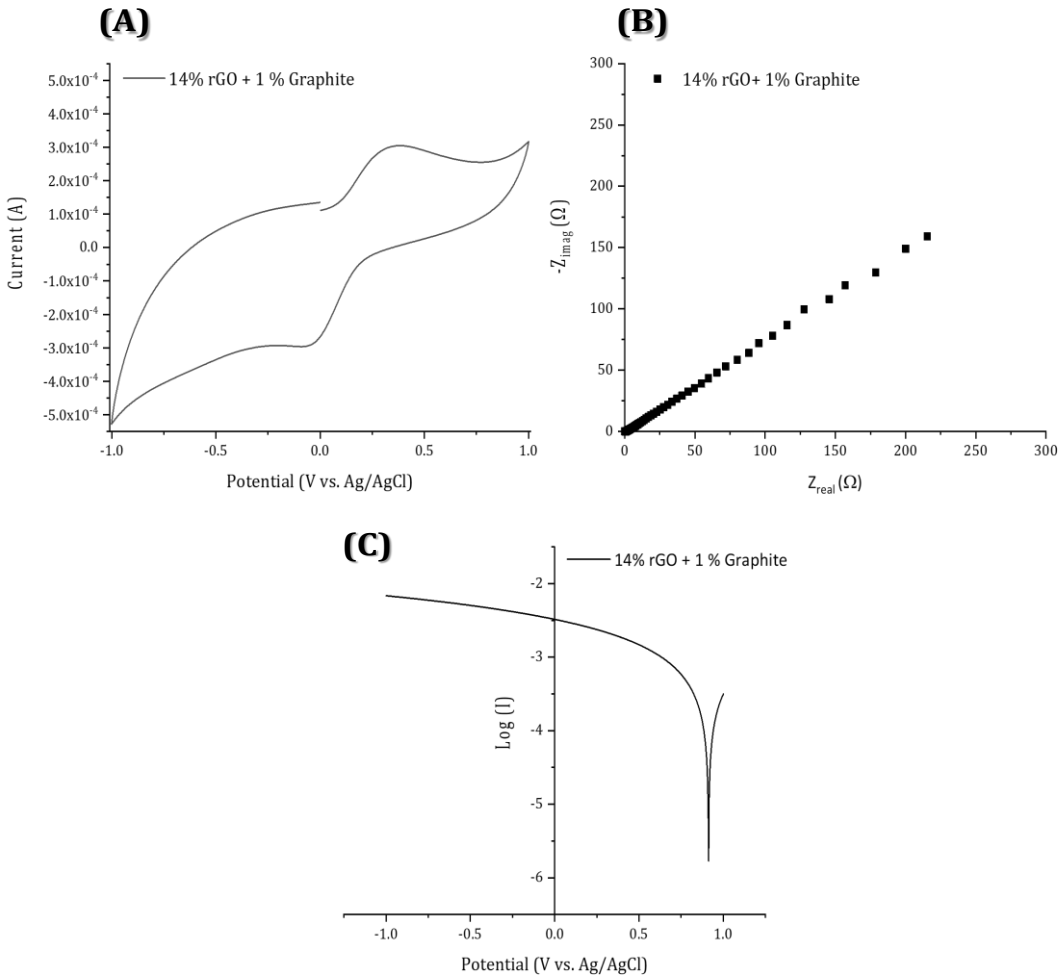

Figure 23. Electrochemical characterization of composite electrode sbased on rGO dopped with graphite. (A)CV (ν: 10 $mV \cdot s^{-1}$), (B) EIS and (C) Tafel diagram for 14% rGO+ 1% graphite electrode.

Using **Figure 23. C**, the Tafel diagram for the electrode, an approximation of the R_{CT} is calculated (57 Ω), and a low value compared to the other carbon materials was obtained (**Table 12**).

4.1.3.3. CNTs composite electrode

This section presents results of composite electrodes employing two different CNTs lots as the conductive phase an epoxy resin in the matrix material. As determined in the morphological characterization of CNTs, both new and old CNTs are within the size range established by the supplier. Therefore, the expected behaviour of the two studied CNTs was expected to be similar. In **Figure 24.A**, the electroactive area of the new CNTs is 0.26 cm^2 for the 7%, 0.35cm^2 for the 10%, and 0.39 cm^2 for the 15%. The mechanical stability of the 15% $CNTs_{new}$ was compromised, and the composite material was threshing. This shown in the CV as the big tail in the cationic part. The 10% $CNTs_{new}$ has also a small tail. The 10% $CNTs_{old}$ have an electroactive area of 0.21 cm^2.

Regarding to the **Figure 24.B**, the $CNTs_{old}$ exhibit the higher charge transfer resistance than the $CNTs_{new}$. In the case of $CNTs_{new}$, the increase of the R_{CT} (greater width of the semicircle) is inverse to the amount of conductor material: higher amount of $CNTs_{new}$ results in a lower R_{CT} (see **Table 12**). The values obtained for $CNTs_{new}$ are: 787.7 Ω, 18.0 Ω, 104.2 Ω for 7 %, 10 %, 15 %, respectively and for 10 % $CTNs_{old}$ is 988.5 Ω. Therefore, the electrochemical behaviour of the sensor can vary significantly depending on the specific batch of CNTs and their unique properties.

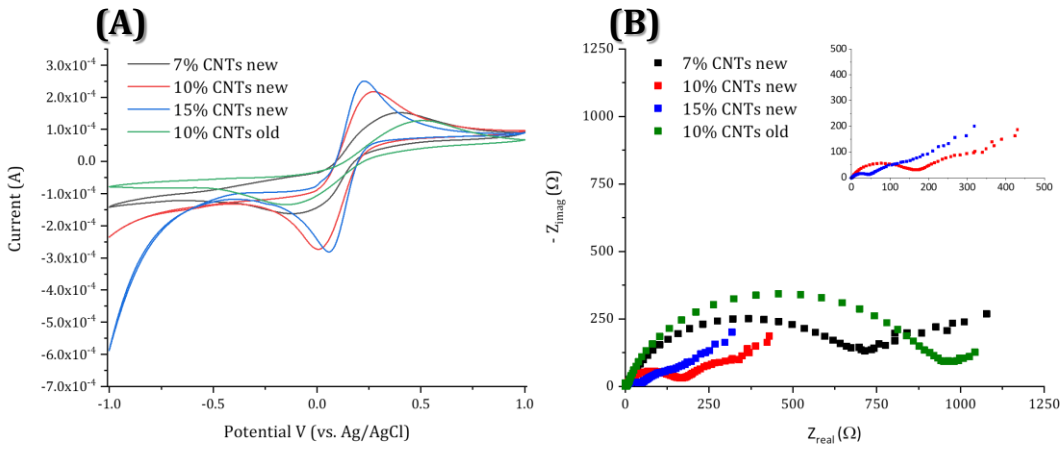

Figure 24. (A) CV and (B) EIS for 7% (black), 10% (red) and 15% (blue) $CNTs_{new}$ and 10% $CNTs_{old}$ (green). Inset: ampliation of 10% and 15% $CNTs_{new}$. ν: 10 $mV{\cdot}s^{-1}$.

These results highlight the impact of CNT morphology on the sensor's final electrochemical response, emphasizing its significance in the fabrication of composite sensors utilizing this allotropic carbon form as conductive phase.

4.1.3.4. Glassy carbon electrode

In **Figure 25.A**, CV results for the glassy carbon electrode are shown. The electroactive area for this electrode is 0.17 cm^2. This material (see **Table 12**) presents the highest R_{CT} (6789 Ω), as is shown in **Figure 25.B.** That can be related to its amorphous structure.

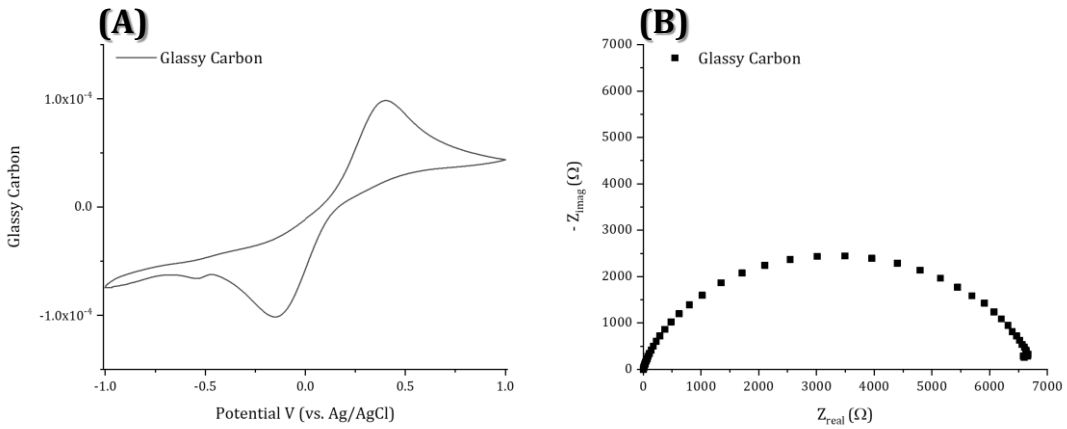

Figure 25. Electrochemical characterization of the glassy carbon electrode. (A) CV (ν: 10 $mV \cdot s^{-1}$), and (B) EIS.

The summary of all the parameters measured and calculated for each allotropic carbon form used to develop the composite electrode is shown in **Table 12**.

Table 12. Summary of the parameters obtained by the electrochemical characterization of studied composite electrodes and glassy crabon electrode: cathodic intensity (Ic), electroactive area (A), ohmnic resistance ($R_Ω$) and charge transfer resistance (R_{CT}).

Electrode	I_c [A]·10^4	A [cm^2]	$R_Ω$ [Ω]	R_{CT} [Ω]
15% Graphite	1.94	0.36	597	5884
20% Graphite	2.93	0.55	505	1077
14% rGO+1% graphite	1.43	0.27	-	57.00*
7% $CNTs_{new}$	1.39	0.26	36.5	787.7
10% $CNTs_{new}$	1.86	0.35	50.5	183.0
15% $CNTs_{new}$	2.08	0.39	54.2	104.2
10% $CNTs_{old}$	1.12	0.21	643	988.5
Glassy Carbon	0.930	0.17	32.9	6789

* This value was obtained using Tafel approach

The 20% graphite has the largest electroactive area of all the carbon materials. Adjusting the same equivalent circuit (Randles circuit, **Figure 13**), the 15% $CNTs_{new}$ presents the lower R_{CT}. However, as was mentioned before, the mechanical stability of the electrode was compromised. Furthermore, the behaviour of the $CNTs_{new}$ was not the same as the $CNTs_{old}$,

as the relatively different size range of the CNTs of each lot giving different electroactive area and different charge transfer resistance, so the new CNTs needs to be optimized. Thus, more compositions of this CNTs should be studied to determine the optimal composition. Therefore, the $CNTs_{old}$, which were fully optimized, were used for next studies.

4.1.4. Square wave anodic stripping voltammetry

To use the composite electrodes mentioned above, the selected technique was Square Wave Anodic Stripping Voltammetry (SWASV). In the past, this pulse technique was developed to enhance the sensitivity of the polarography and detection limits of 10^{-7} to 10^{-8} M were reported [98]. In **Figure 26** shows the excitation signal of this technique that is generated by adding the excitation signals of the staircase **Figure 26 A** and the pulse train signal **Figure 26 B**.

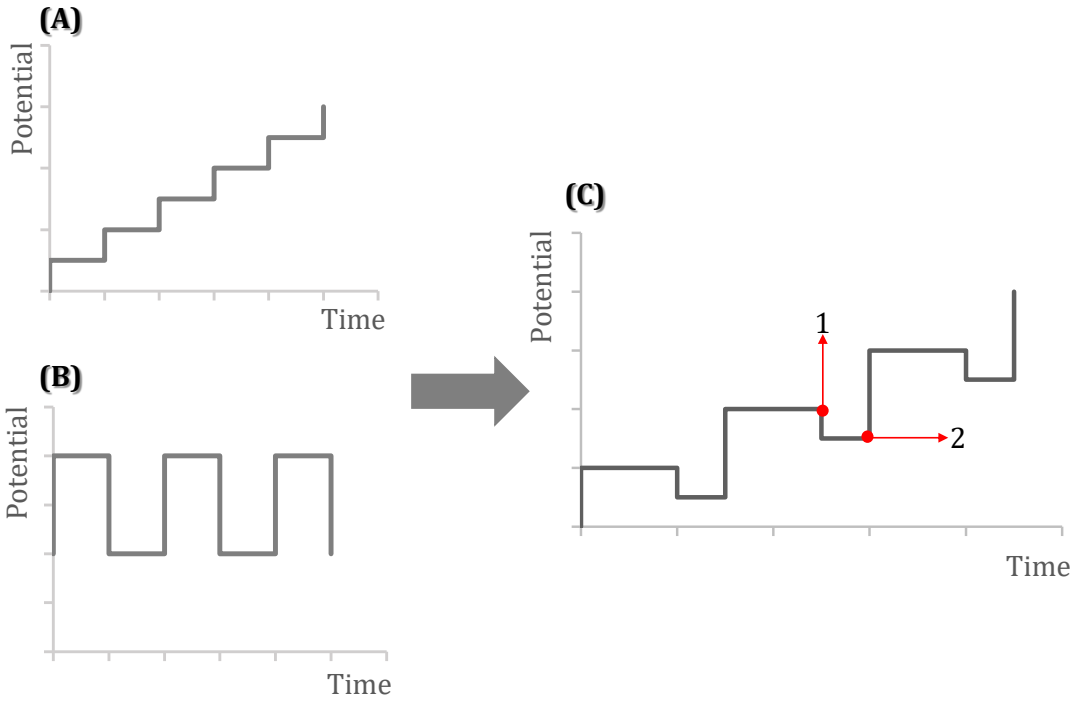

Figure 26. Excitation signal of (A) staircase, (B) pulse train, and (C) square wave, where the potential 1 and 2 are marked.

The current response (ΔI) of the square wave is measured using **Equation 14**.

$$\Delta i = i_1 - i_2 \qquad \textbf{(Equation 14)}$$

Where:

Δi: current response

i_1: current at the potential 1, which is the end of the forward pulse.

i_2: current at the potential 2, which is the end of the reversed pulse.

The SWASV technique has two main steps, that are summarized in **Figure 27**:

- **Preconcentration step:** during a specified time, with stirring and bubbling N_2, a potential of -1.4 V is applied [99]. On the surface of the electrode (it acts as a cathode), the cations of the solution are reduced.
- **Measurement step:** stirring is stopped, but the N_2 is still bubbling. This step consists in the application of a staircase potential from reducing potentials (negative) to oxidizing potentials (positive), and the current generated is recorded. On the surface of the electrode (it acts like an anode), the cations that were reduced in the previous step, now they are oxidized, giving a peak in the corresponding potential, so the electrode acts like an anode.

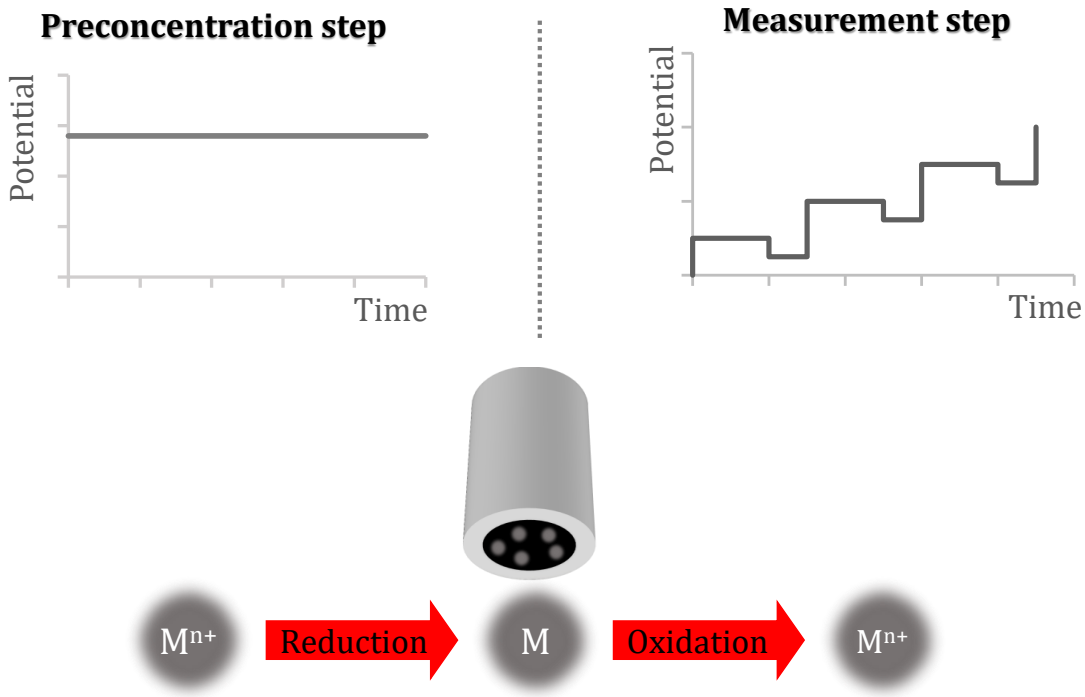

Figure 27. Summary of the excitation signal and what happen over the surface of the electrode in every step of the SWASV technique. M refers to any metal that can be in the solution.

4.1.4.1. Optimization of preconcentration time.

The first step performed was to optimize the preconcentration time for Cd^{2+}, Pb^{2+} and Cu^{2+}, using a 15% graphite electrode. That was for two reasons: it is the optimal composition of the graphite and the easy access of this material.

A mixture that containing 57 µg·L^{-1} Cu^{2+} and 90 µg·L^{-1} Pb^{2+} was measured changing at preconcentration times of 3, 5, 7, 10 and 15 min (**Figure 28.A**). Then, an individual solution of 100 µg·L^{-1} Cd^{2+} was analyzed using preconcentration times of 5, 7 and 10 min (**Figure 28.B**). **Figure 28.C** shows a graphical comparison of the results in terms of intensity measured. For Pb^{2+} and Cu^{2+}, there were no significant differences between 5 and 10 min just a 2% and 6%, respectively (less than 10%). But for Cd^{2+}, the difference in the signal between 5 and 10 mins is around 20%. However, if we compare these two values with the 7 min result, the difference is less than 10%. Therefore, the preconcentration time was set at 7 minutes.

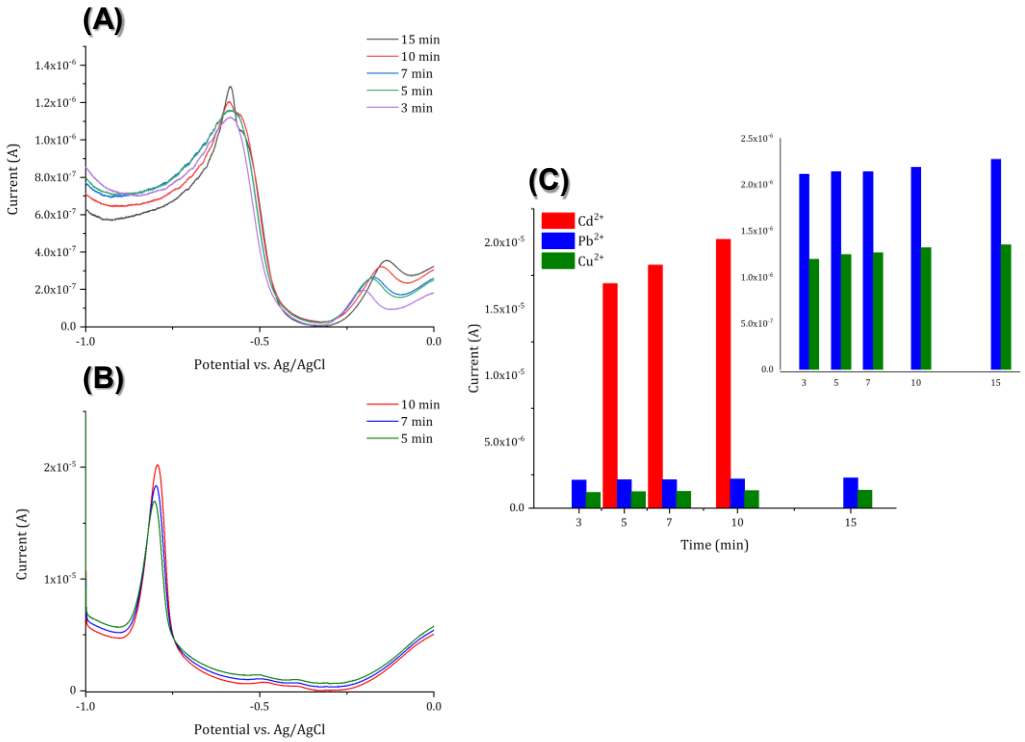

Figure 28. SWASV voltamograms of (A) Pb^{2+} and Cu^{2+} measured simultaneously and (B) Cd^{2+} for 15% graphite electrode. (C) comparison between the maximum of the metals measured previously separatelly, inset of the maximum of Pb $^{2+}$ and Cu^{2+}.

The optimal parameters of the analysis were:

- ⌘ Preconcentration step (7 minutes): 7 min at -1.4 V
- ⌘ Measurement step (~3 minutes): from -1.4 to 1 V; step: 0.0005 V;
- ⌘ Cleaning step (5 minutes): 5 min at 1 V

This additional final step of cleaning is added to ensure that the electrode surface is clean and ready to be used again.

In total, one analysis takes around 16 minutes.

4.1.5. Metal analysis

After previous studies with the optimal composition of graphite composite electrodes (15% graphite) in terms of S/N ratio, to follow the study and the optimization of the technique the response of other composite materials was studied. The performance of each kind of composite material and composition towards the metal analysis is going to be evaluated by individual performances of these materials using calibration curves for Cd^{2+}, Pb^{2+} and Cu^{2+}.

For Cd^{2+} analysis, **Figure 29** presents the calibration curves of each material.

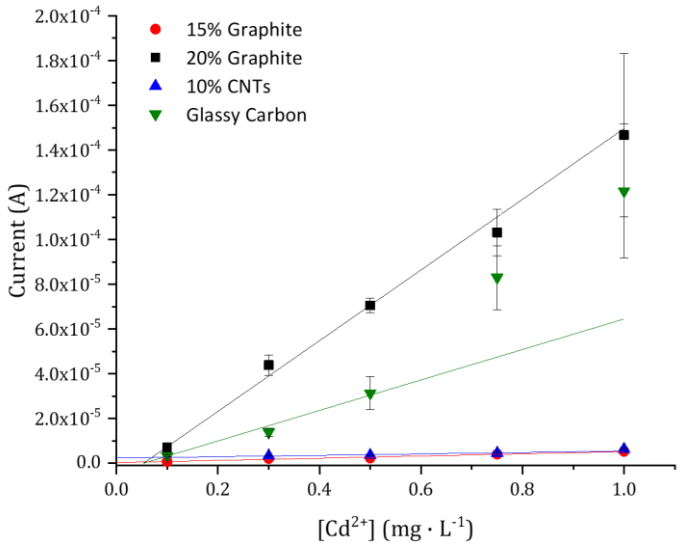

Figure 29. Calibration curves obtained for Cd^{2+} using different composite electrodes: ●15% Graphite, ■ 20% Graphite, ▲ 10% CNTs old and ▼ glassy carbon electrode. Experimental error is standard deviation (n= 3).

In **Table 13**, summarized the analytical information obtained.

Table 13. Analytical parameters of the calibration curves for Cd^{2+} with sensitivity, R^2 and linear range.

Electrode	Sensitivity [A·L·mg⁻¹]·10⁶	R^2 (n = 7)	Linear Range [mg·L⁻¹]
15% Graphite	(4.9 ± 0.4)	0.970	0.1 – 1
20% Graphite	(158 ± 6)	0.995	0.1 – 1
10% $CNTs_{old}$	(3.1 ± 0.7)	0.850 [x]	0.3 – 1
Glassy Carbon	(70 ± 20)	0.820	0.1 – 1

[x] n= 4

20% Graphite electrode presents the higher sensitivity, a R^2 near to 1 and a wide linear range. In this case, a larger number of conductive particles on the electrode surface enhances the sensor's sensitivity. However, this composition also initiates a reduction in the signal/noise ratio achieved for this graphite composition [91]. On the other hand, this fact does not impact in the final result because the analyte is pre-concentrated in the first step of analysis, effectively compensating for the reduction in S/N in the detection step. For that reasons, 20% graphite have the best response for this analysis.

For the Pb^{2+} analysis, **Figure 30** shows the calibration curves of each material.

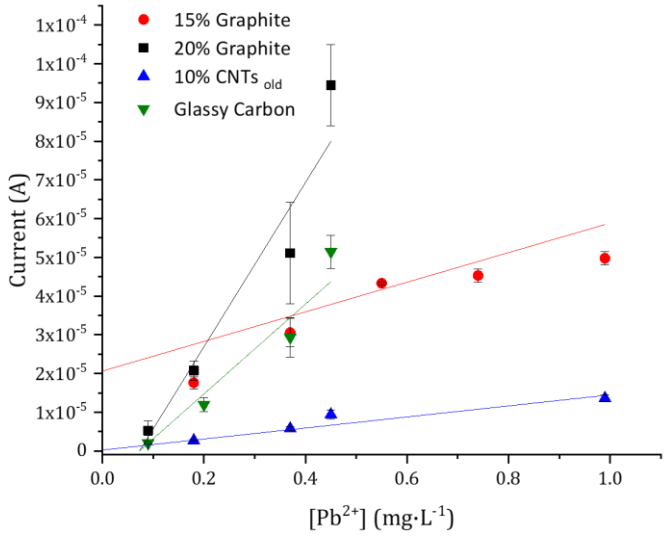

Figure 30. Calibration curves obtained for Pb^{2+} using different composite electrodes: ●15% Graphite, ■ 20% Graphite, ▲ 10% CNTs old and ▼ Glassy Carbon electrodes.

In **Table 14**, summarized the analytical information obtained.

Table 14. Analytical parameters of the calibration curves for Pb^{2+} with sensitivity, R^2 and linear range.

Electrode	Sensitivity $[A \cdot L \cdot mg^{-1}] \cdot 10^5$	R^2 (n = 5)	Linear Range $[mg \cdot L^{-1}]$
15% Graphite	(4 ± 2)	0.60	0.18 – 1
20% Graphite	(21 ± 3)	0.93[x]	0.09 – 0.45
10% $CNTs_{old}$	(1.4 ± 0.2)	0.96[x]	0.18 – 1
Glassy Carbon	(12 ± 2)	0.95 [x]	0.09 – 0.45

[x]n = 4

As for the other cationic metals, Cd^{2+} and Pb^{2+}, 20% graphite composite electrode presents the best response for the analysis, obtaining the highest sensitivity.

For the Cu^{2+} analysis **Figure 31** exhibits the calibration curves of each composite material.

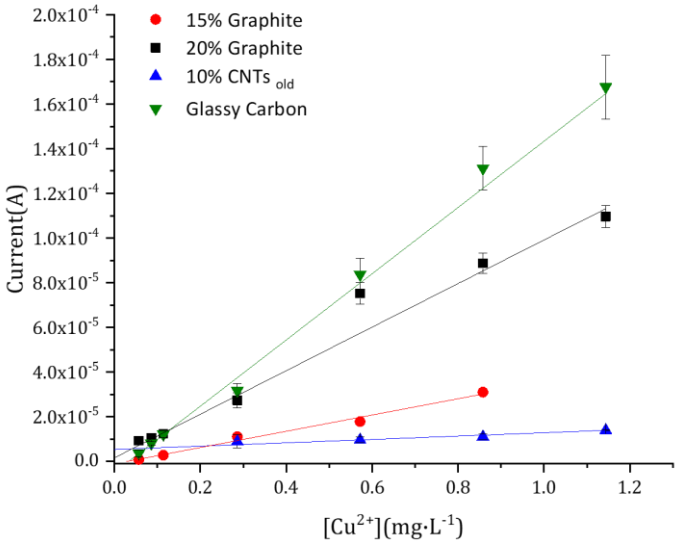

Figure 31. Calibration curves for Cu^{2+} using different composite electrodes: ●15% Graphite, ■ 20% graphite, ▲ 10% $CNTs_{old}$ and ▼ glassy carbon electrode.

In **Table 15**, summarized the analytical information obtained.

Table 15. Analytical parameters of the calibration curves for Cu^{2+}: sensitivity, R^2 and linear range.

Electrode	Sensitivity $[A \cdot L \cdot mg^{-1}] \cdot 10^5$	R^2 (n = 7)	Linear Range $[mg \cdot L^{-1}]$
15% Graphite	(4 ± 2)	0.98*	0.057 – 0.86
20% Graphite	(9.7 ± 0.7)	0.96	0.057 – 1.1
10% CNTs $_{old}$	(0.7 ± 0.09)	0.95^x	0.29 – 1.1
Glassy Carbon	(15 ± 0.7)	0.99	0.057 – 1.1

*n= 5; ^{x}n = 4

In this case, the best performance is for the glassy carbon electrode, with a wide linear range, R^2 near to 1 and the higher sensitivity. The second place is for the 20% graphite electrode.

Finally, the 14% rGO + 1% graphite electrode did not present defined peaks when Cu^{2+} was analyzed (see **Figure 32**), only at high concentrations (0.86 and 1.1 $mg \cdot L^{-1}$) were detected. For that reason, this composite electrode was dismissed, and the other metals were not tested.

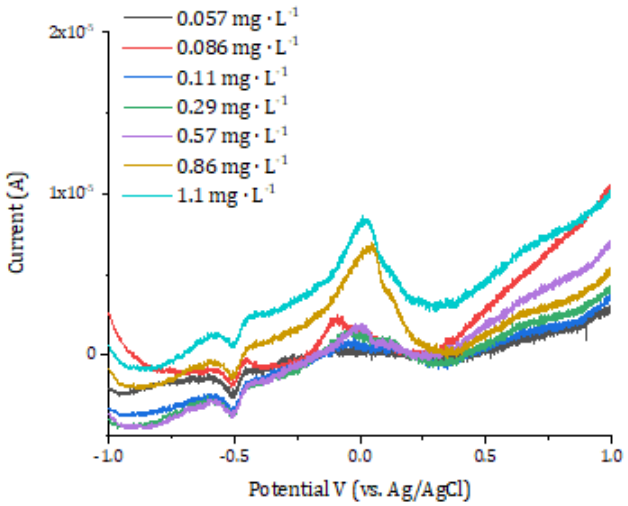

Figure 32. SWASV results for Cu^{2+} analysis using 14% rGO + 1 % graphite composite electrode.

4.1.6. Concluding remarks

In **Figure 33**, there is a graphical summary of the experimental work done.

20% graphite composite electrode presents the higher performance for 2 of 3 metals analyzed (Cd^{2+} and Pb^{2+}), even the 15% graphite composite electrode is the optimum composition (S/N ratio criterium). In consequence, SWASV seems to have a better performance when the electroactive area is bigger.

14% rGO composite electrodes dopped with graphite (1%) do not have suitable performance in the use of the SWASV technique to metal analysis.

CNTs composite electrodes based on different CNTS batch, old and new, we found that their properties are not the same. Furthermore, the morphology of the material has a significant impact on the sensor's electrochemical response. For that reason, we conclude that the composition of the corresponding prepared composite electrodes must be studied and optimized using percolation curves before its use.

Finally, glassy carbon is the most suitable electrode to analyzed Cu^{2+}, followed by the 20% graphite electrode.

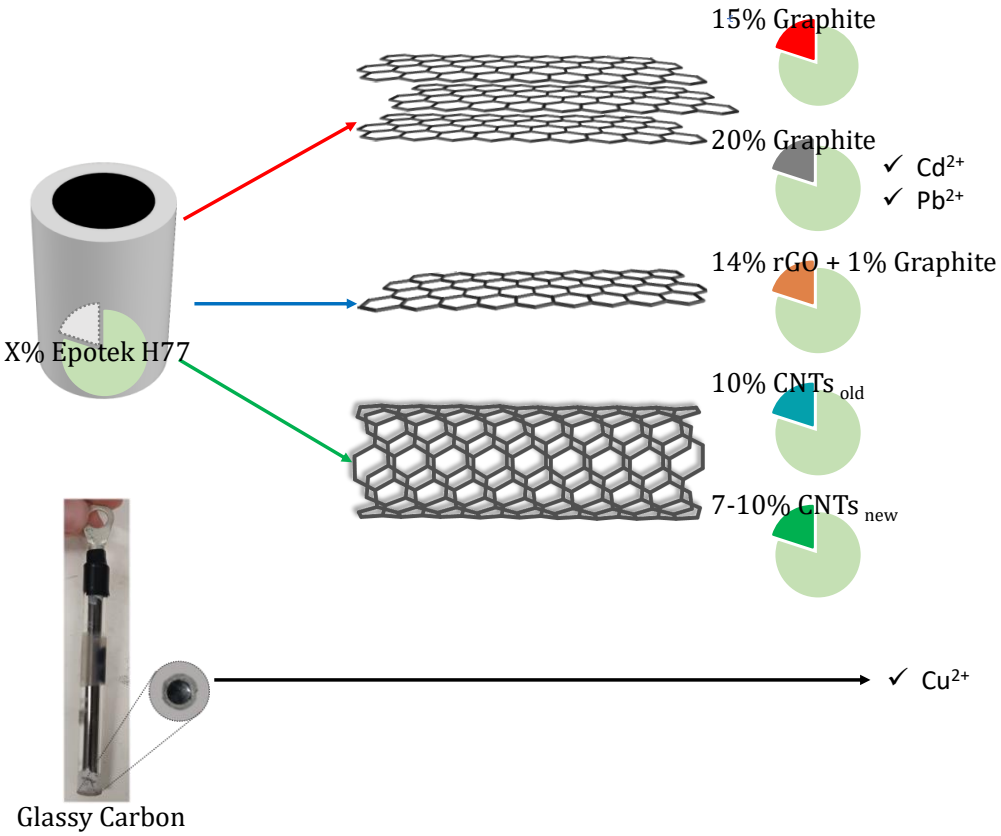

Figure 33. Graphical summary of test performed in Chapter IV — Part I.

Part II

Composite electrodes modified with mercury nanoparticles

This chapter is a modification of the paper «Composite Electrodes Based on Carbon Materials Decorated with Hg Nanoparticles for the Simultaneous Detection of Cd(II), Pb(II) and Cu(II)» (https://doi.org/10.3390/chemosensors10040148)

‡

4.2. Why using mercury nanoparticles?

Since old times mercury and its compounds have generated curiosity in human being. Greeks, Romans, Egyptians, Hindus, and Chinese knew the existence of this silver metal liquid at room temperature, and each civilization had its own legends about it. The symbol of mercury (Hg) comes from the Greeks, they named it "*hydrargyrum*" which means liquid silver. Mercury was named in honour to the Roman god, who was known to be the gods messenger because his speed and mobility. Furthermore, Mercury is the closest planet to the sun, and the symbol of the planet (☿) was used by the alchemist as a symbol for the mercury [100].

Mercury has three oxidation states: 0, I and II. Mercury(I) presents a dimeric cation (Hg_2^{2+}) that can present dismutation into 0 and II in basic media (NH_3, for example), so there are relatively few mercury (I) compounds. Its compounds had many uses in the past: cinnabar (mercury (II) sulphide, HgS) was used as a red pigment to decorate caves from Spain and France in the megalithic [101]. Mercury(II) chloride ($HgCl_2$) is extremely toxic, colourless, odourless and have a wide variety of applications, for example as fungicide in agriculture, as topical antiseptic (very low concentration), as catalyst in the synthesis of vinyl chloride[12] and as starting reagent of other mercury compounds [102]. Calomel is mercury(I) chloride (Hg_2Cl_2) and can be found in nature as a colourless, grey, or brown solid. It was used as a remedy for some diseases like syphilis, bronchitis, cholera, teething, gout, tuberculosis, influenza, fungicide etc. until the 20th century. Calomel now, it is a well-known standard in electrochemistry used in the manufacture of calomel reference electrodes (Saturated Calomel Electrode, SCE) [103]. SCE response is based on the following redox reaction **Equation 15**.

$$Hg_2Cl_{2\,(s)} + 2\,e^- \leftrightarrows 2Hg_{(l)} + 2\,Cl^-_{(aq)} \qquad \mathbf{E°=}\ +0.2415\ \text{V} \qquad \textbf{(Equation 15)}$$

Besides the medical use of Hg and its components, it was also used in the gold extraction due to its properties of "dissolve" the gold [104]. So, mercury properties of forming alloy with other metal were known long time ago.

Mercury(II) oxide, (HgO), which is a red or yellow crystalline solid is helpful in the preparation of various organic mercury compounds and some inorganic mercury salts.

[12] Vinyl chloride is the monomer of polyvinyl chloride also known as PVC. PVC is used to fabricate pipes, wire coatings, vehicle upholstery, and plastic kitchen ware.

Moreover, it is also used as an electrode (mixed with graphite) in zinc-mercuric oxide electric cells and in mercury batteries [105].

Nowadays, the use of mercury is almost banned due to its hazardous properties. Elemental mercury and methylmercury are neurotoxins. In addition, the inhalation of mercury vapour can have harmful effects on the nervous system and as well in the respiratory, digestive, and immune systems. The inorganic salts of mercury are corrosive to the skin, eyes, and gastrointestinal tract, and can induce kidney toxicity if they are ingested [106].

Further its hazardous properties, mercury presents a good conductivity, and in the 20th century it was used in the chloralkaline industry, as a cathode in the electrolysis of brine (NaCl high concentration solution) for production of sodium hydroxide (NaOH) and chlorine gas (Cl_2), but in the 21st century the mercury-cell plants for manufacture these elements have mostly passed out [107]. On the other hand, in analytical chemistry, the most important application was in polarography, as an electrode or mercury drops.

4.2.1. Polarography

Polarography is a voltammetric technique that uses a drop of mercury as a working electrode (dropping mercury electrode, DME). This technique was invented in 1925 by the Nobel prize Jaroslav Heyroský (awarded in 1959) [108]. Because of the use of DME in the linear scan polarography, the limiting current is controlled only by diffusion, not by convection. The current is recorded as function of the potential reaching a peak, but every time the drop falls the current decreases and starts again the cycle. Due to the properties of mercury discussed before, such as its ability to form amalgams with other metals, polarography is useful for metal analysis.

This technique presents several inconveniences such as slowness and poor detection limits [98]. In the 60s, the appearance of the voltammetric pulse methods, differential pulse polarography and square wave anodic polarography, solved these problems. Furthermore, these techniques could be used by other electrodes than de DME, in which case the techniques are called differential and square wave voltammetry.

4.2.2. Mercury nanoparticles

The application of Hg nanoparticles in the functionalization of carbon electrodes represents a novel and viable strategy for the determination of metals, while minimizing the disadvantages of using Hg. Thus, the synthesis, the modification, characterization, and the analysis performed using the electrodes with mercury nanoparticles (HgNPs) will be presented.

4.2.2.1. Synthesis

Two routes were tested, and the only difference between them is the polymer used in the synthesis (see **Scheme 13**). Route A is a modification of the route established by G. V. Ramesh et al. [109], and it is called Route B, when the same polymer proposed by G. V. Ramesh et al. is used. In both cases, 78.5 mg of $Hg_2(NO_3)_2{\cdot}2H_2O$ (98%, purchased from Alfa Aesar by Thermo Fisher Scientific, Kandel, Germany) were weighted, then 1 mL of HNO_3 0.47 M (65% from VWR chemicals, Radnor, PA, USA) was added and stirred smoothly until the salt is solved. Poly(diallyldimethylammonium chloride) (PDDA, M_W 200 000-350 000, 20% wt. in water solution, from Sigma Aldrich, St. Louis, MO, USA) solution is prepared mixing 3.5 mL of the polymer in 16 mL of Milli-Q water. Poly(vinyl alcohol) (PVA, M_W 13 000-23 000, 87-89% hydrolysed, from Sigma Aldrich, St. Louis, MO, USA) solution is prepared solving 3.6 g of the polymer in 16 mL of Milli-Q water and heating softly in a water bath until the PVA is totally solved. After preparing each polymer solution, 0.5 mL of each prepared polymer solution is added and stirred 10 min at 25 °C in an incubator.

The nanoparticles synthesized were characterized by two techniques:

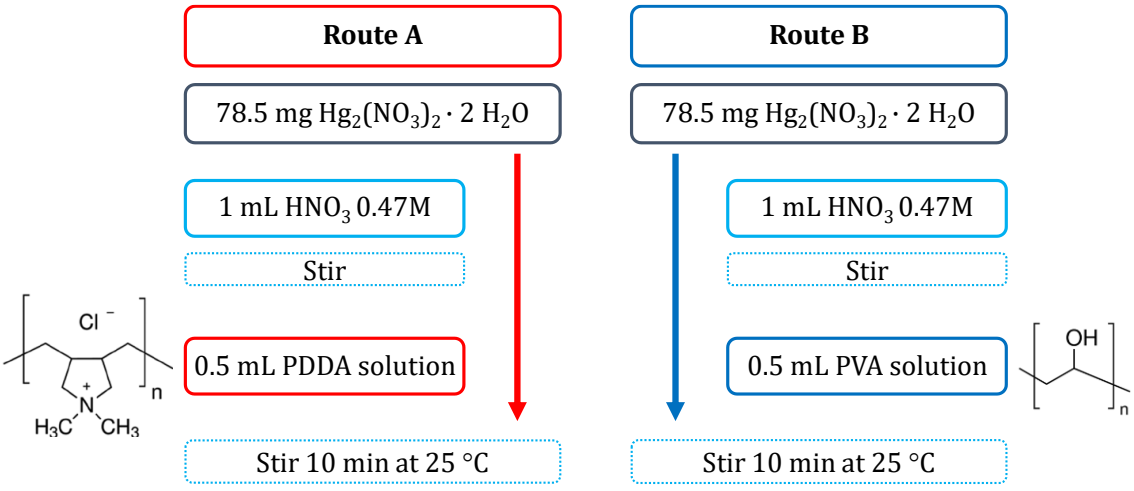

Scheme 13. Synthesis of the HgNPs: Route A and PDDA polymer structure and Route B and PVA polymer structure.

Transmission Electron Microscopy (TEM) is used to determine the particle size by measuring directly the images obtained. The results obtained are shown in **Figure 34**. The particle size of mercury nanoparticles synthesised by Route A ($HgNPs^{RouteA}$) was 2.7 ± 0.7 nm and for those synthesised by Route B ($HgNPs^{RouteB}$) was 18 ± 5 nm.

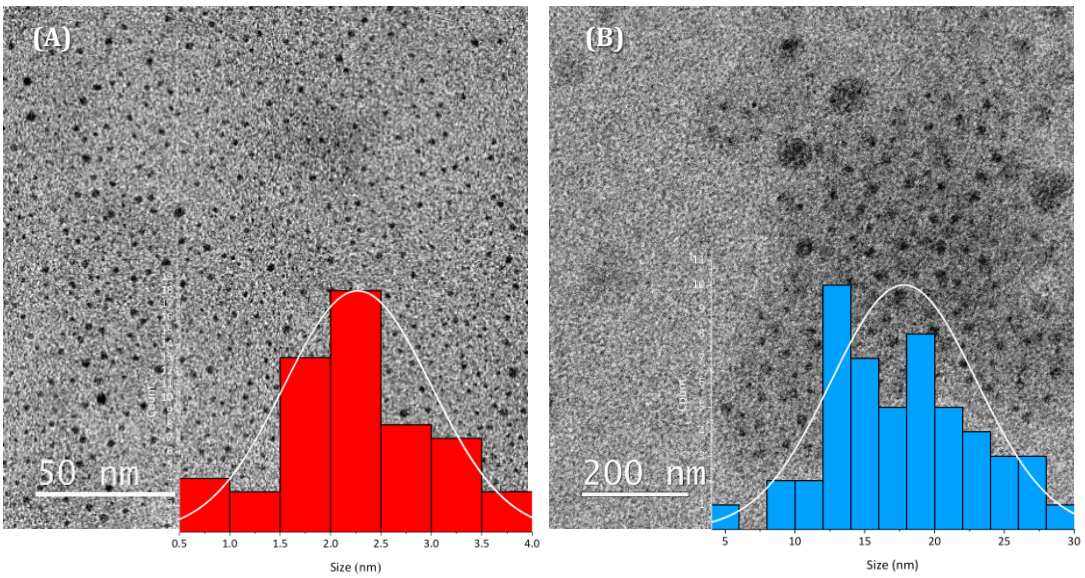

Figure 34. TEM images for (A) $HgNPs^{RouteA}$, and (B) $HgNPs^{RouteB}$. Inset histograms related.

The obtained results of ζ were +51.7 mV for $HgNPs^{RouteA}$ and +13.2 mV for $HgNPs^{RouteB}$. Which means that the $HgNPs^{RouteA}$ have less tendency to aggregation, and this is corresponded in HgNPs with higher stability.

4.2.2.2. Modification of the electrodes

Using the nanoparticles synthesized by the two routes mentioned above, the surface of the electrodes was modified by drop-casting (depositing an amount of the HgNPs solutions on the graphite composite electrode surface) to obtain three different electrodes, as can be seen in the scheme of **Figure 35**. The drop-casting consisted in 20 µL of each HgNPs solution, except for the third type of electrode, that first was submerged in a 10% wt. solution of PDDA in Milli-Q water in an ice bath for 10 minutes [110], followed by the drop-casting of the $HgNPs^{Route\ B}$ solution onto the PDDA layer. In all cases, the electrodes with the modified

surface were cured for 2 h at 80 °C. Obtained electrodes are namely as: HgNPs$^{Route\ A}$@graphite, HgNPs$^{Route\ B}$@graphite, and HgNPs$^{Route\ B}$/PDDA@graphite.

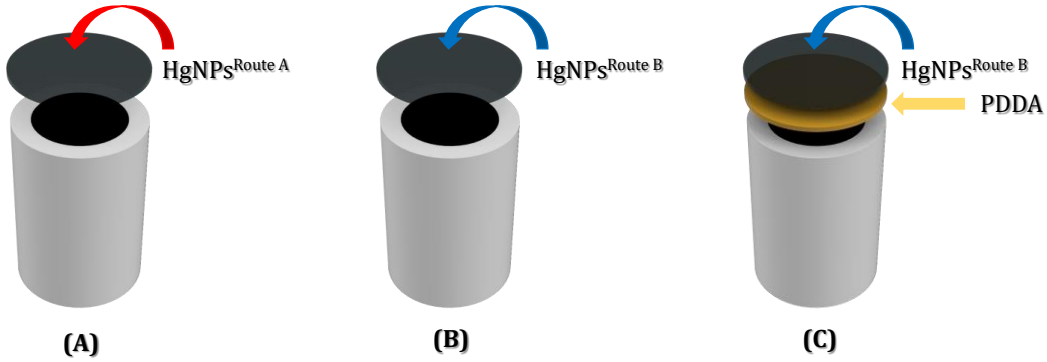

Figure 35. Different surface modifications of the composite electrode: (A) HgNPs^{RouteA}@graphite; (B) HgNPs^{RouteB}@graphite; (C) HgNPs^{RouteB}/PDDA@graphite.

4.2.2.3. Modified electrodes characterization

Once the composite electrode surfaces were modified (as indicated above) and after the thermal treatment (2 h at 80 °C), the differences between the two types of nanoparticles could be noticed at raw eye (as can be seen in **Figure 36**). The HgNPs^{RouteB}/PDDA@graphite electrodes looked like HgNPs^{RouteB} electrodes at raw eye, even they must be characterized by different means.

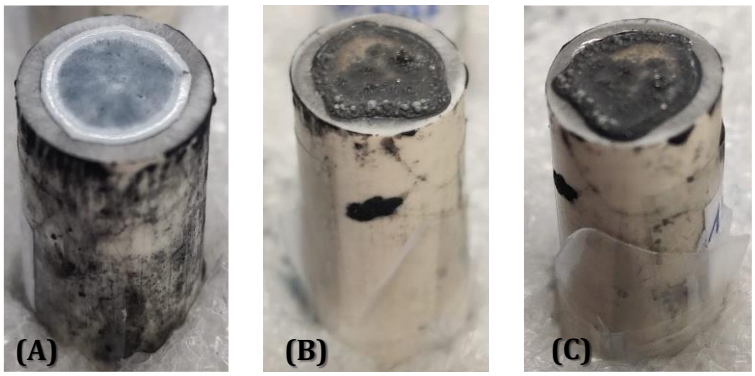

Figure 36. Modified electrodes images: (A) HgNPs^{RouteA}@graphite; (B) HgNPs^{RouteB}@graphite and (C) HgNPs^{RouteB}/PDDA@graphite

4.2.2.4. Morphological and chemical characterization

Optical microscope showed significant differences between the nanoparticles after the thermal treatment: HgNPs^{RouteA}@graphite surface looked like white fine powder (see **Figure 37.A**); on the other hand HgNPs^{RouteB}@graphite and HgNPs^{RouteB}/PDDA@graphite looked like shiny metal spheres (see **Figure 37.B** and **C**).

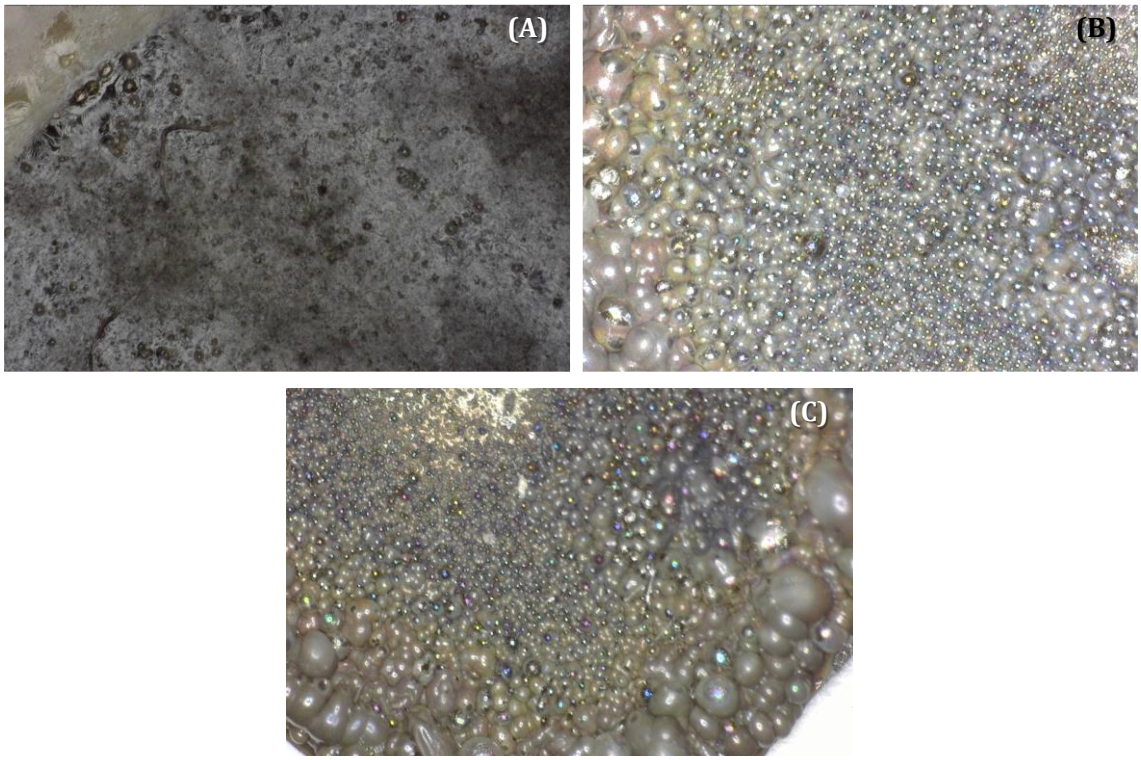

Figure 37. Digital microscope images (A)HgNPs^{RouteA}@graphite surface, (B) HgNPs^{RouteB}@graphite surface and (C) HgNPs^{RouteB} /PDDA@graphite surface. (1:120 augments).

X-Ray Photoelectron Spectroscopy (XPS) is used to obtain the oxidation number of the nanoparticles of mercury. The oxidation state of the Hg in the precursor salt, $Hg_2(NO_3)_2$ is Hg(I), after the addition of PDDA and the thermal treatment the oxidation state did not change, which is supported by the XPS results (**Table 16** and **Figure 38**). The binding energy value for $4f_{7/2}$ was quite similar with the reported one by NIST database of $Hg_2(NO_3)_2$. The difference between the binding energy of orbitals $4f_{7/2}$ and $4f_{5/2}$ is 4.01 eV [111]. On one hand, PDDA helps to stabilize the ions Hg_2^{2+} and NO_3^- instead of promoting the reduction of the Hg_2^{2+}. On the other hand, PVA is a stronger reductant agent than the PDDA, so it leads the reduction of the Hg_2^{2+} to metallic Hg and the aggregation of it, forming the characteristic mercury balls, as can be seen in **Figure 37.B**. The information about the oxidation state of the HgNPs^{RouteB} was reported in [109].

Table 16. Data obtained from the XPS adjustment using two components. Calibration was made by using carbon 1s at 284.8 eV.

Peak	Reported binding energy [eV]	Binding energy [eV]
Hg $4f_{7/2}$	101.2 [112]	101.32
Hg $4f_{5/2}$	105.21	105.35

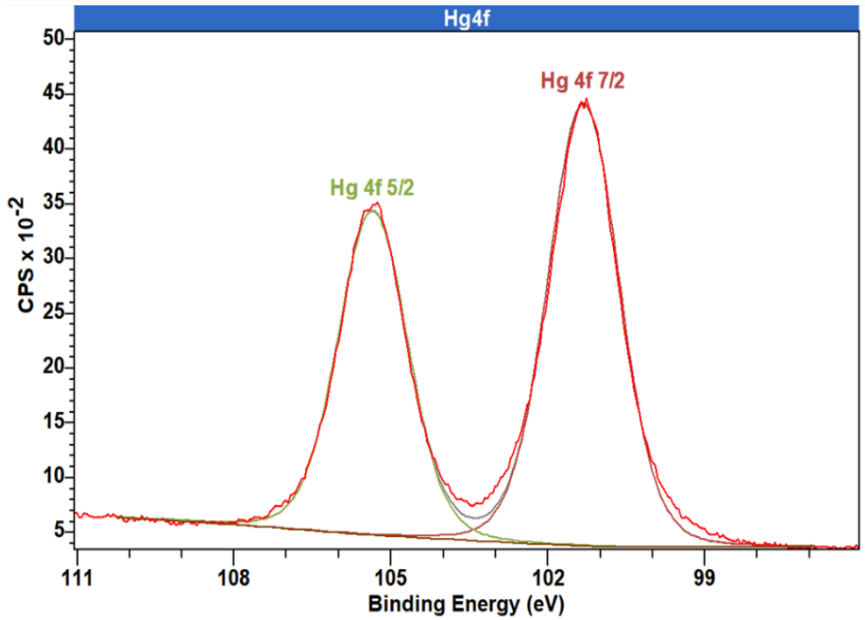

Figure 38. XPS analysis of HgNPs^{RouteA}@graphite: adjustment for Hg4f using two components: (green) Hg$4f_{5/2}$ and (red) for Hg$4f_{7/2}$.

The surface of raw electrode and the three types of modified electrodes were characterized by SEM (retro dispersive and secondary electron images) and EDX to determine the morphology and the elemental composition (qualitatively) of them. In

Figure 39 all these characterizations are shown. The amount of Hg varied depending on the type of modified electrode: the bare electrode (20% graphite) presented the C ≈ 69% and did not present mercury. The HgNPs^{RouteA}@graphite electrodes had the major amount of mercury: C ≈ 42% and Hg ≈ 27%. While the HgNPs^{RouteB}@ graphite and HgNPs^{RouteB}/PDDA@graphite electrodes had approximately the lower and similar quantity of Hg: C ≈ 61% and Hg≈ 7%, and C ≈ 64% and Hg ≈ 5%, respectively.

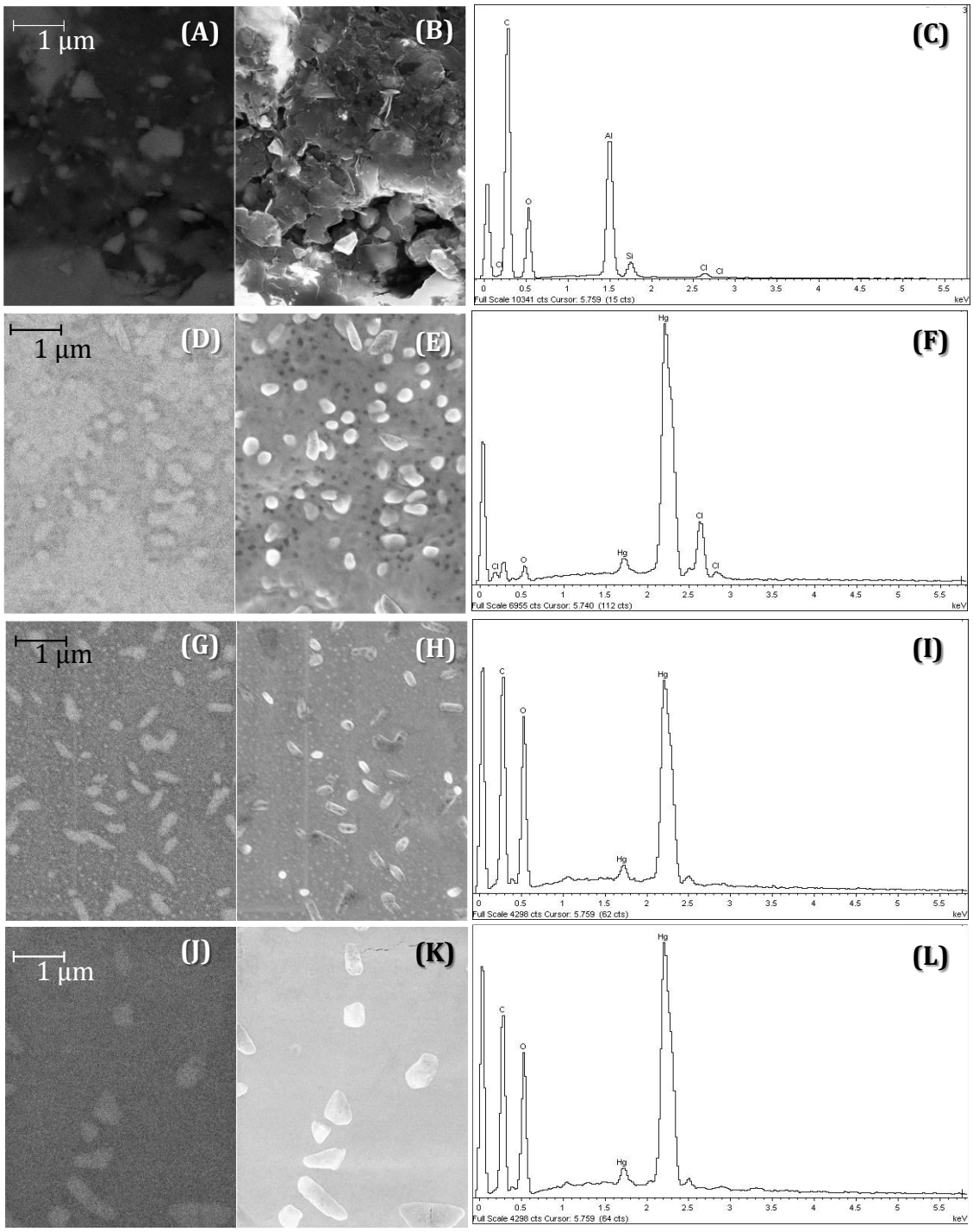

Figure 39. Retrodispersive (A, D, G, J), secondary electron SEM image (B, E, H, K) and EDX graphs (C, F, I L) for 20% graphite; $HgNPs^{RouteA}$@graphite electrode; $HgNPs^{RouteB}$@graphite electrode and $HgNPs^{RouteB}$/PDDA@graphite electrode, respectively. Both retrodispersive and secondary electron SEM images have the same scale: 1 µm.

4.2.2.5. Electrochemical characterization

Furthermore, the electrodes were characterized electrochemically, by CV and EIS in a 0.01 M $[Fe(CN)_6]^{3-}/[Fe(CN)_6]^{4-}$ (and 0.1 M KCl) solution.

CV showed different peaks depending on the electrode characterized (**Figure 40**), in these cases we had the peaks of the Fe(III)/Fe(II) solution and the ones corresponding to different Hg oxidation states. These differences in the Hg peaks are caused by the different oxidation state of the HgNPs used in each synthetic route used for the modification. In **Table 17** all the information is summarized.

Table 17. Assigned redox reaction with each potential for each electrode.

Electrode	Reaction	Potential [V vs. Ag/AgCl]
Raw(20% graphite)	$Fe^{2+} \rightleftarrows Fe^{3+}+e^-$	0.250
	$Fe^{3+}+e^- \rightleftarrows Fe^{2+}$	0.100
HgNPs^{RouteA}@graphite	$Fe^{2+} \rightleftarrows Fe^{3+}+e^-$	0.125
	$Fe^{3+}+e^- \rightleftarrows Fe^{2+}$	0.0
	$Hg_2^{2+} \rightleftarrows 2Hg^{2+}+2e^-$	0.125
	$2Hg^{2+}+2e^- \rightleftarrows Hg_2^{2}$	0.0
	$Hg^{2+}+2e^- \rightleftarrows Hg^0$	-0.500
HgNPs^{RouteB}@graphite	$Fe^{2+} \rightleftarrows Fe^{3+}+e^-$	0.125
	$Fe^{3+}+e^- \rightleftarrows Fe^{2+}$	0.0
	$Hg^0 \rightleftarrows Hg^{2+}+2e^-$	0.125
	$Hg^{2+}+2e^- \rightleftarrows Hg^0$	-0.500
HgNPs^{RouteB}/PDDA @graphite	$Fe^{2+} \rightleftarrows Fe^{3+}+é$	0.180
	$Fe^{3+}+e^- \rightleftarrows Fe^{2+}$	0.0
	$Hg^0 \rightleftarrows 2Hg_2^{2}+2e^-$	0.0
	$Hg_2^{2} \rightleftarrows 2Hg^{2+}+2e^-$	0.0
	$Hg^0 \rightleftarrows Hg2^{+}+2e^-$	0.180
	$Hg^{2+}+2e^- \rightleftarrows Hg^0$	-0.500

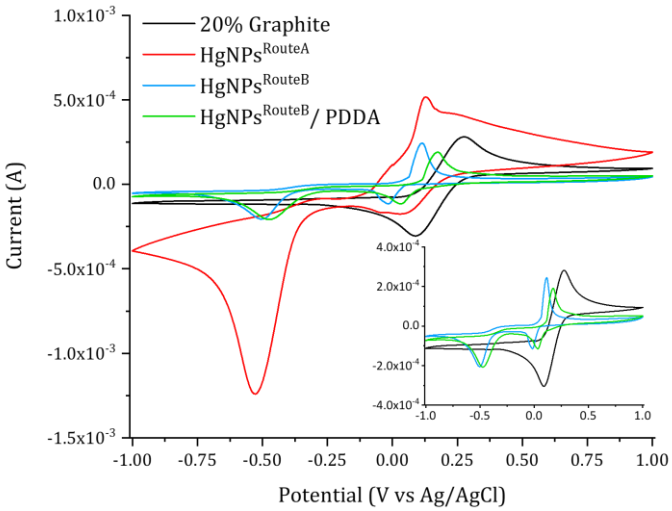

Figure 40. Cyclic voltammetry characterization for each type of electrode: 20% graphite (raw), HgNPs^{RouteA}@graphite, HgNPs^{RouteB}@graphite and HgNPs^{RouteB}/PDDA@graphite. Inset an extension of the raw and Hg-NPs$^{Route\ B}$ and Hg-NPs$^{Route\ B}$/PDDA electrodes. ν: 10 mV·s^{-1}.

There are a lot of redox reactions, that have been produced when the measurement is performed. To ensure the different potentials of the mercury reactions a CV was performed without the reference redox probe, Fe^{3+}/Fe^{2+}, just in KCl 0.1M. Moreover, the electroactive area of each modified electrode was calculated using the cathodic intensity and the first cycle of the cyclic voltammetry, which is the one that to minimizes the contribution of the mercury species. All these results appear in **Figure 41**, and as can be observed some potentials have shifted a little bit depending on the number of the cycle in the cyclic voltammetry. The electroactive area was calculated using Randles-Sevčik equation (**Equation 6**) and is shown in **Table 18**.

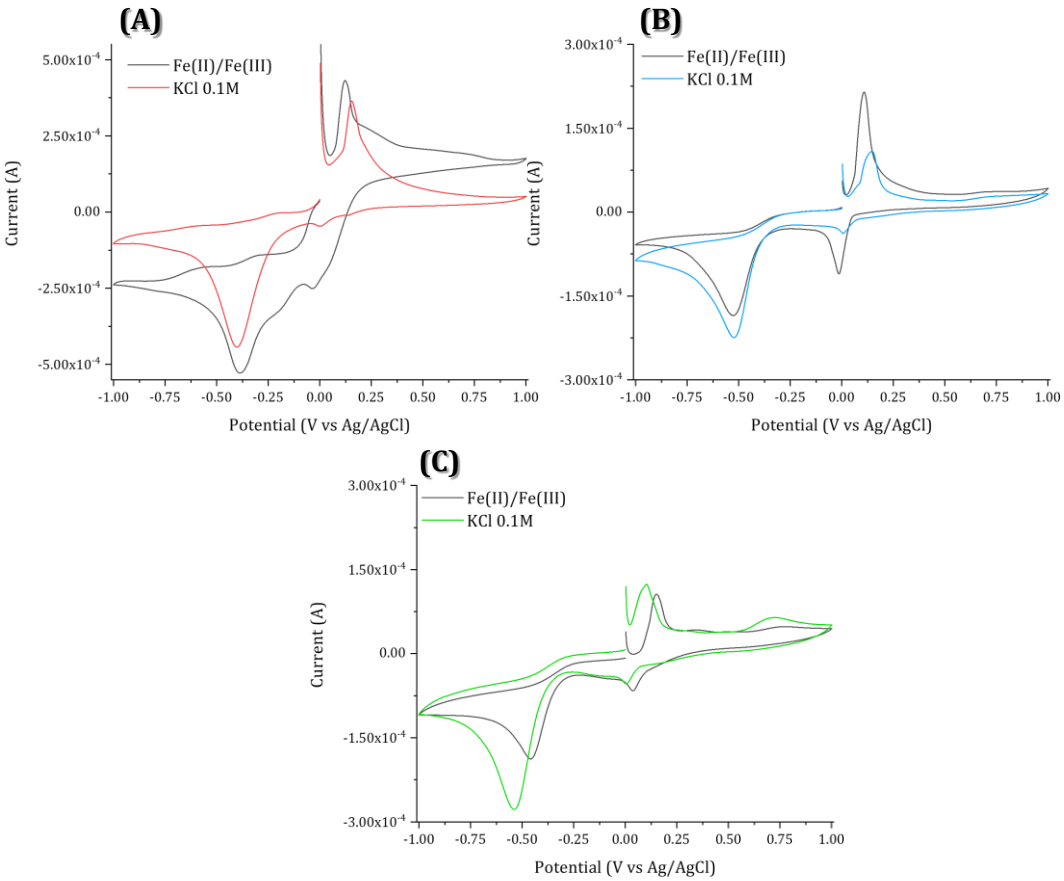

Figure 41. Comparison of the response in CV and in 0.01 M $[Fe(CN)_6]^{3-}/[Fe(CN)_6]^{4-}$, 0.1 M KCl and just KCL 0.1 M for electrodes (A) Hg-NPs^{RouteA}@graphite, (B) Hg-NPs^{RouteB}@graphite, and (C) Hg-NPs^{RouteB}/PDDA@graphite. ν: 10 mV·s^{-1}.

EIS gives information about the resistance of the electron to flow through the material. To achieve this information equivalent circuits for each modification were adjusted (**Figure 42**).

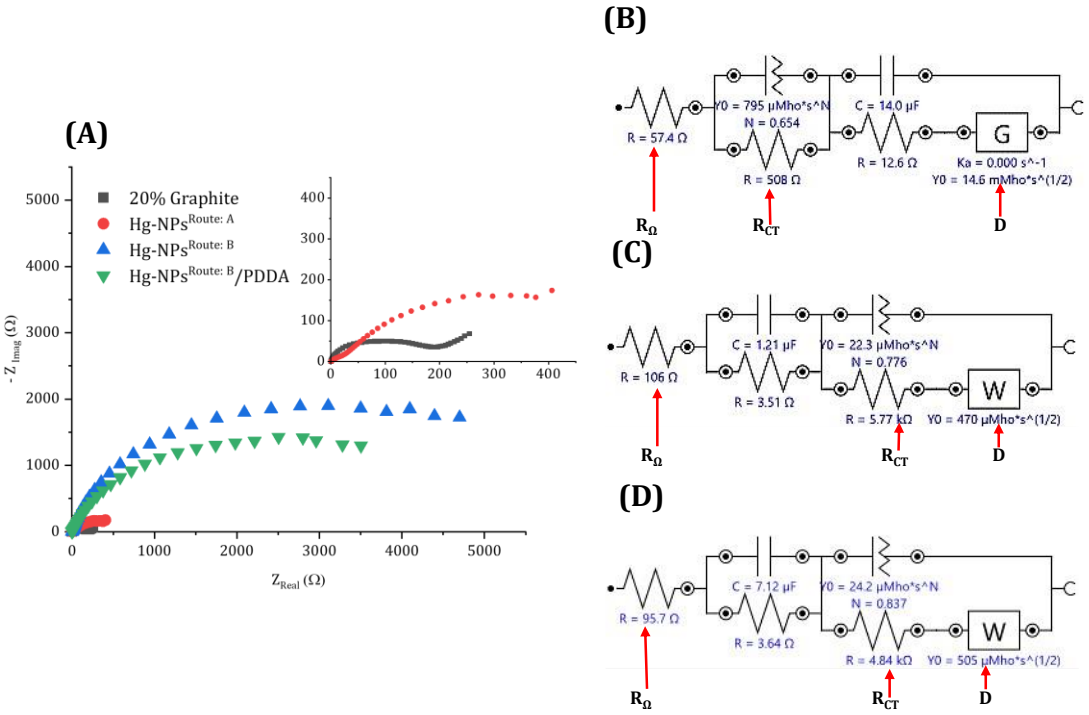

Figure 42. Representation of the components of the impedance by Niquist diagram (A) and adjusted circuits for electrodes: (B) HgNPs^{RouteA}, (C) HgNPs^{RouteB} and (D) HgNPs^{RouteB}/PDDA. Where R_Ω is the ohmic resistance; R_{CT} is the charge transfer resistance and D is the diffusion element chosen (G: Gerischer, W: Warburg)

In **Figure 42.A**, the representation of the elements of the electrochemical impedance (imaginary component and real component) is shown. In **Figure 42.B**, **C** and **D** each equivalent circuit has two parts that can be related to the graphite electrode and the HgNPs. The charge transfer resistance (R_{CT}) was considered the one with the Constant Phase Element (CPE) in parallel, in all the cases. In **Figure 42.B** the first part has the ohmic resistance (R_Ω) and in parallel a CPE and the charge transfer resistance. The second part of the circuit has in parallel a capacitor and a resistance and the element of diffusion, in this case a Gerischer. Gerischer was chose instead of the Warburg because this element gives information about the porosity of the material, so we consider that the nanoparticles of HgNPs^{RouteA} electrode were surrounded by a layer of the PDDA polymer that helps the stabilization, even the analyte need to cross this layer. In **Figure 42.C** and **D**, the first part of the circuits has the ohmic resistance and then in parallel a capacitor and a resistance, then the CPE element and another resistance that is considered the charge transfer resistance, and a pure diffusion element which is a Warburg in these two circuits.

All the results obtained by the electrochemical characterization using the CV and EIS were summarized in **Table 18**.

Table 18. Electroactive area (A) of each modified electrode, ohmic resistance (R_Ω) and charge transfer resistance (R_{CT}).

Electrode	A [cm^2]	R_Ω [Ω]	R_{CT} [Ω]
HgNPs^{RouteA}@graphite	0.27	57.4	508
HgNPs^{RouteB}@graphite	0.20	106	5771
HgNPs^{RouteB}/PDDA @graphite	0.19	95.7	4837

At the light of these results, the effect of the different polymers in the synthetic route must be remarked. PDDA is a quaternary amine polymer and the network that form could allow the charge migration that may enhance the electronic transfer. This can lead to a higher electroactive surface for HgNPs^{RouteA}@graphite, lower charge transfer resistance and higher ζ potential (+51.7 mV), which means higher stability and less aggregation for this synthetic route.

4.2.2.6. Electroanalytical performance of modified electrodes with HgNPs

The measurements were performed using SWASV technique, with a preconcentration step of 7 minutes, applying a potential of -1.4 V and bubbling N_2.

The first test was to determine if the mercury peak affects the metal analyzed. As can be observed in **Figure 43**, mercury peak (of all the modified electrodes) appears around 0.175 V and do not overlap any metal peak: Cd^{2+} appears at -0.7 V, Pb^{2+} at -0.5 V and Cu^{2+} at -0.2 V (all the potentials are vs Ag/AgCl).

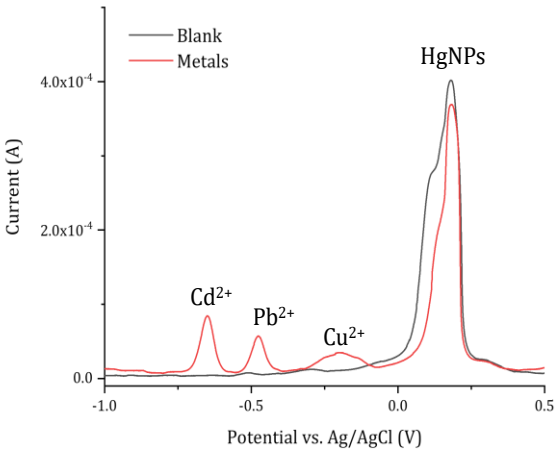

Figure 43. Evaluation of peak potential for HgNPs and the analyzed metals.

Each metal was quantified individually with the raw electrode (20% graphite) and the three types of electrodes modified with HgNPs. The corresponding calibration curves are shown in **Figure 44**.

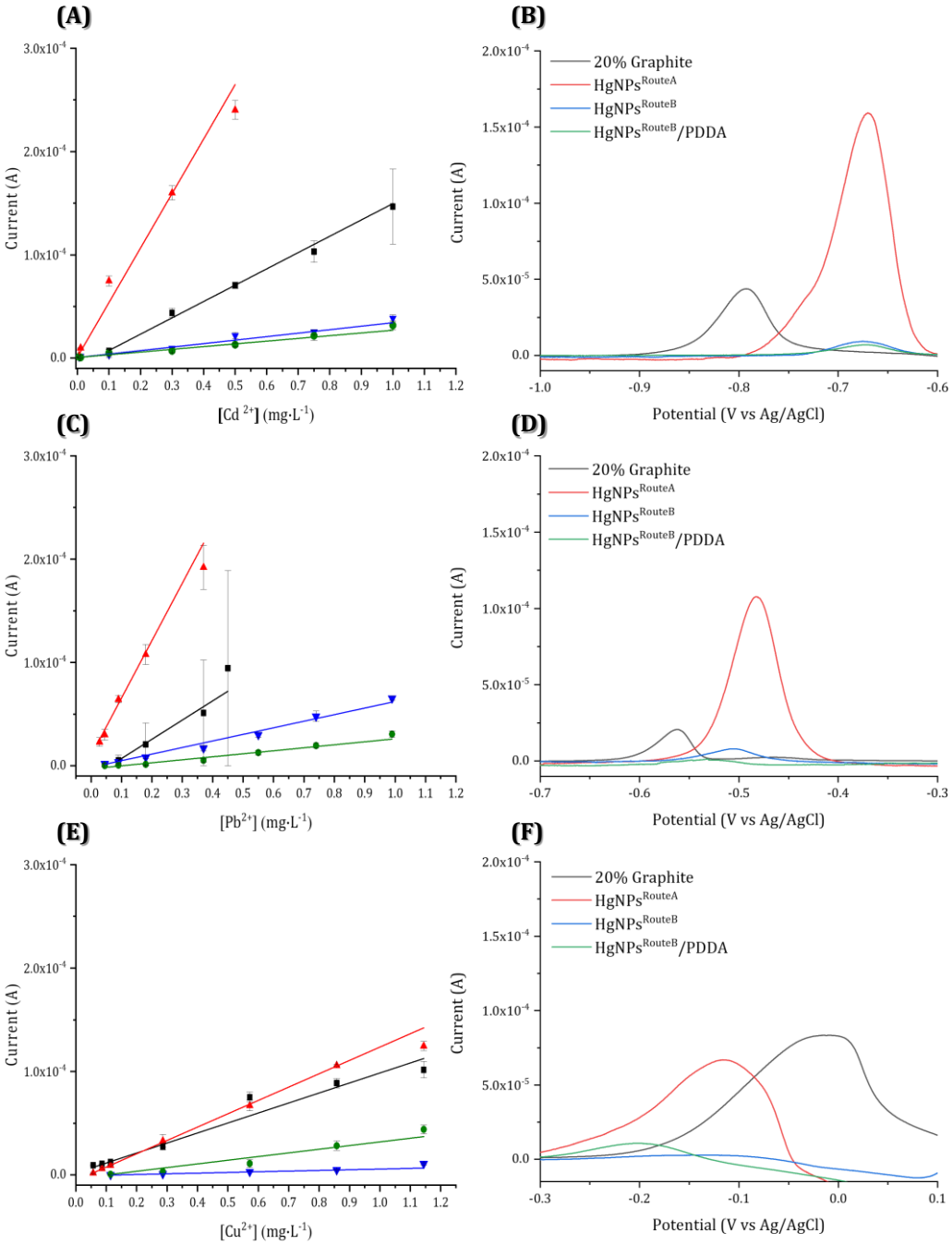

Figure 44. Calibration curves (A, C, E) and SWASV voltamperograms for one standard of the calibration curve (B) 0.3 mg·L^{-1} of Cd^{2+}, (D) 0.2 mg·L^{-1} of Pb^{2+} and (E) 0.6 mg·L^{-1}of Cu^{2+} using the different electrodes under study ■ 20% graphite; ▲ $HgNPs^{RouteA}$; ▼$HgNPs^{RouteB}$; ● $HgNPs^{RouteB}$/PDDA. The experimental error was estimated as the standard deviation (n = 3).

All the information from the calibration curves is summarized in **Table 19**.

Table 19. Calibration curves parameters of the three electrodes for all metal cations analysed separately. Experimental errors were calculated as standard deviation.

Cd^{2+}				
Electrode	**Sensitivity** [A·L·mg^{-1}]·10^5	**y- intercept** [A]·10^6	**R^2** (n = 5)	**Linear Range** [mg·L^{-1}]
Raw (20% Graphite)	(16 ± 1)	(-8 ± 1)	0.995	0.10–1.0
HgNPs^{RouteA}	(53 ± 7)	(1 ± 1)	0.930	0.0050–0.50
HgNPs^{RouteB}	(3.4 ± 0.2)	(0.6 ± 0.5)	0.980	0.050–1.0
HgNPs^{RouteB}/PDDA	(2.6 ± 0.3)	(0.6 ± 0.2)	0.940	0.050–1.0
Pb^{2+}				
Electrode	**Sensitivity** [A·L·mg^{-1}]·10^5	**y- intercept** [A]·10^6	**R^2** (n = 5)	**Linear Range** [mg·L^{-1}]
Raw (20% Graphite)	(19 ± 2)	(-12 ± 3)	0.95	0.090–0.45
HgNPs^{RouteA}	(56 ± 5)	(10 ± 5)	0.96	0.028–0.37
HgNPs^{RouteB}	(6.4 ± 0.3)	(-1.5 ± 0.7)	0.98	0.045–1.0
HgNPs^{RouteB}/PDDA	(2.9 ± 0.3)	(-3.0 ± 0.9)	0.93	0.045–1.0
Cu^{2+}				
Electrode	**Sensitivity** [A·L·mg^{-1}]·10^5	**y- intercept** [A]·10^6	**R^2** (n = 5)	**Linear Range** [mg·L^{-1}]
Raw (20% Graphite)	(9.7 ± 0.9)	(5 ± 5)	0.950	0.057–1.1
HgNPs^{RouteA}	(12.9 ± 0.2)	(-3 ± 3)	0.999	0.057–1.1
HgNPs^{RouteB}	(0.7 ± 0.1)	(-2 ± 1)	0.900	0.11–1.1
HgNPs^{RouteB}/PDDA	(3.6 ± 0.6)	(-8 ± 4)	0.900	0.11–1.1

Using HgNPs^{RouteA} comparing with the response of the raw electrode (20% graphite) it is found an improvement. A wider linear range for Cd^{2+} and Pb^{2+}, achieving a good quantification for lower concentrations levels, but decreasing the higher concentration levels able to be determined. Copper remains with similar values in quantification terms. All the sensitivities of the HgNPs^{RouteA} electrodes have improved compared to the bare, the HgNPs^{RouteB} and the HgNPs^{RouteB}/PDDA electrodes. These results indicated that this modification (HgNPs^{RouteA}) is the most suitable for a multi-metal sensor. For that reason, HgNPs^{RouteA}@graphite electrode will be used for further experiments. Moreover, detection limit (DL) for HgNPs^{RouteA} electrode was calculated following the **Equation 16**.

$$S_m = \bar{S}_{Blank} + 3sd_{Blank} \quad \textbf{(Equation 16)}$$

Where:

$\bar{S}_{Blank}$ = sum of the mean blank signal

sd_{Blank}= standard deviation of the blank

The detection limit obtained using the statistical approach for Cd^{2+} was 0.0015 mg·L^{-1} and for Pb^{2+} was 0.020 mg·L $^{-1}$. For Cu $^{2+}$, due to the observed displacement of the Cu peak (this will be deeply discussed in the real sample analysis), the statistic calculus cannot be followed, instead of that the detection limit was checked experimentally, measuring concentrations from 0.0010 to 0.057 mg·L^{-1}. Obtaining a positive current for 0.057 mg·L^{-1}, so this concentration was established as detection limit for Cu^{2+}. Using the HgNPs^{RouteA} electrode, the three metals were simultaneously determined, as can be observed in **Figure 45** and in all the information summarized in **Table 20.**

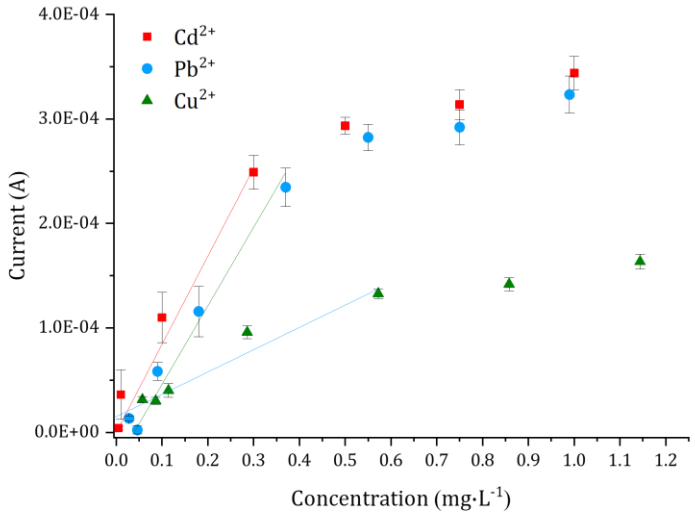

Figure 45. Simultaneous determination of Cd^{2+}, Pb^{2+} and Cu^{2+} using HgNPs^{RouteA} @graphite electrode.

Table 20. Calibration curve parameters and linear range obtained from the simultaneous detection of the three metals

Metal	Sensitivity [A·L·mg^{-1}]·10^5	R^2 (n = 4)	Linear Range [mg·L^{-1}]
Cd^{2+}	(84 ± 6)	0.99	0.0050–0.30
Pb^{2+}	(80 ± 10)	0.95	0.065–0.30
Cu^{2+}	(21 ± 3)	0.95	0.12–0.54

4.2.2.7. Reproducibility and repeatability

The reproducibility was evaluated by comparing the sensitivity obtained by using the same electrode (hence the same drop-casting) for three days, performing one calibration curve per day. Using the same $HgNPs^{RouteA}$@graphite electrode, in total, 45 measurements were performed.

The repeatability of the modification process was done by the evaluation of the sensitivity of two different drop-casting of $HgNPs^{RouteA}$ on the surface of the same electrode. In both cases, the range of concentrations studied was the linear range stablished in **Table 20** for each metal. The results are shown in **Table 21**.

Table 21. Reproducibility and repeatability of simultaneous detection of the metal cation studied by using $HgNPs^{RouteA}$@graphite electrode. The experimental error was calculated as standard deviation for their respective n.

Metal	**Reproducibility study** $[A \cdot L \cdot mg^{-1}] \cdot 10^5$ (n = 3)	**Repeatability study** $[A \cdot L \cdot mg^{-1}] \cdot 10^5$ (n = 2)
Cd^{2+}	(50 ± 10)	(40 ± 10)
Pb^{2+}	(60 ± 10)	(40 ± 10)
Cu^{2+}	(20 ± 10)	(8 ± 1)

In the reproducibility study the RSD of every measurement was below the 20% for Cd^{2+}, Pb^{2+} and Cu^{2+} except for the first point of the curve which is 30% for Cd^{2+} and 28% for Cu^{2+} due to the that they are the lowest concentrations level checked. The response of the sensors with the same drop-casting is comparable along time for Cd^{2+}, it does not change more than a 20% and for Pb^{2+} 16%. Comparing the behaviour of two different drop-casting, the RSD of each point measured is below the 30 % and the sensitivities do not change more than a 25% for all the metals.

4.2.2.8. Interference study

The evaluation of the selectivity of the sensor is a key point to apply this sensor in real samples. Due to the overlap of the CV peaks with the redox pair (**Figure 41**), $[Fe(CN)_6]^{3-}$ /$[Fe(CN)_6]^{4-}$, this overlapping can affect the selectivity towards the analytes. For that reason, Fe^{2+} and Fe^{3+} cations were the selected ones to perform the interference study. Furthermore, to emulate the maximum dissolved organic matter that is allowed by law in a treated urban wastewater, 125 $mg \cdot L^{-1}$ O_2 solution is measured [113].

In **Figure 46** the results of the measurements and the comparison of current intensity are shown. The comparison was performed with the concentration of interference and around 10 times lower concentrations of the analyte.

In **Figure 46.A**, **B** and **C** no peak corresponding to the interference was observed in the potentials of the metals analysed and the small differences in the intensities observed in the peaks could be related to the deterioration of the electrode modification for the use. In **Figure 46.D, E** and **F** the comparison of the response of the Cd^{2+} with the organic matter, Fe^{2+} and Fe^{3+}, are shown respectively. For Pb^{2+} are shown in **Figure 46 G, H** and **I** and for Cu^{2+} (**Figure 46.J, K** and **L**) the same comparison in the same order of interferences as before are presented. In all cases, the response to the interference is non-significant compared to the analyte one. These results show the good behaviour of the $HgNPs^{RouteA}$ electrode used for these three-metal analysis.

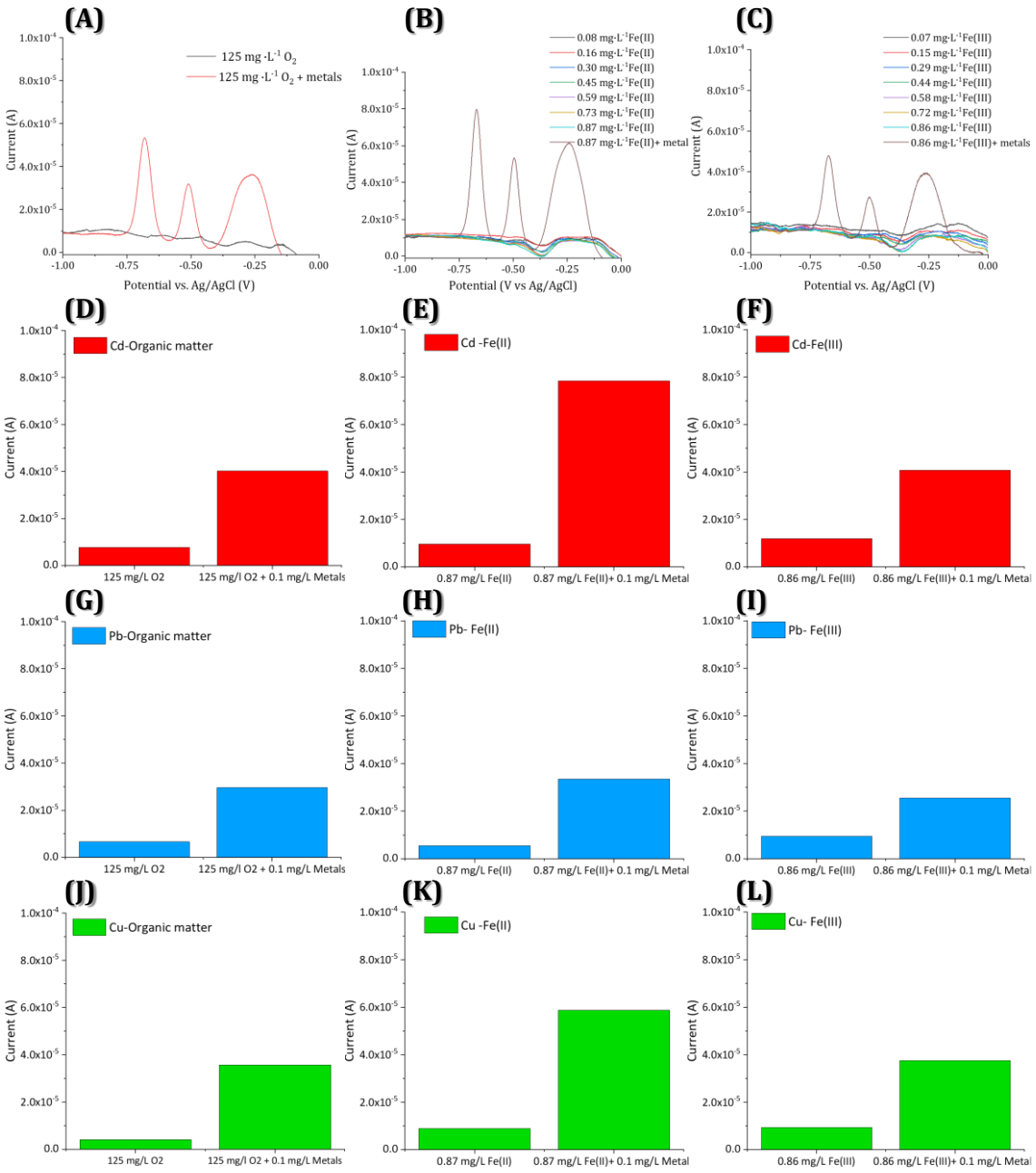

Figure 46. SWASV voltammograms of the addition of interferences: (A) Dissolved Organic Matter (O_2), (B) Fe^{2+} and (C) Fe^{3+}. Comparison of the current obtained for the maximum concentration of the interferences evaluated in the presence or not of the analyte: O_2: 125 mg·L^{-1} (D, G, J), Fe^{2+}: 0.87 mg·L^{-1}, (E, H, K) and Fe^{3+}: 0.86 mg·L^{-1}, (F, I, L) for Cd^{2+}: 0.11 mg·L^{-1}; Pb^{2+}: 0.09 mg·L^{-1} and Cu^{2+}: 0.08 mg·L^{-1} respectively.

4.2.3. Suitability for real sample analysis

Different samples were tested to check the suitability of these electrodes to analyse these metals in several matrices.

4.2.3.1. Spiked tap water

HgNPs^{RouteA}@graphite electrodes were checked with a spiked tap water sample, which is the simplest matrix to start testing these sensors for metal quantification purposes.

⌘ **Sample preparation**

This sample was prepared using 10 mL of tap water from the area of Barcelona (Spain) diluted in 90 mL of acetic acid/acetate buffer. The analysis was performed by standard addition calibration of all the metal simultaneously. All the points of the calibration curve were prepared individually.

⌘ **Results**

In **Figure 47.A** the SWASV voltammogram obtained from the spiked tap water analysis is shown. The double peak for Cu^{2+} observed probably can be explained as two origins: the high concentration of each metal addition and the weakening of the electrode due to the previous measurements. In **Figure 47.B** the calibration curves obtained for each metal are shown**.**

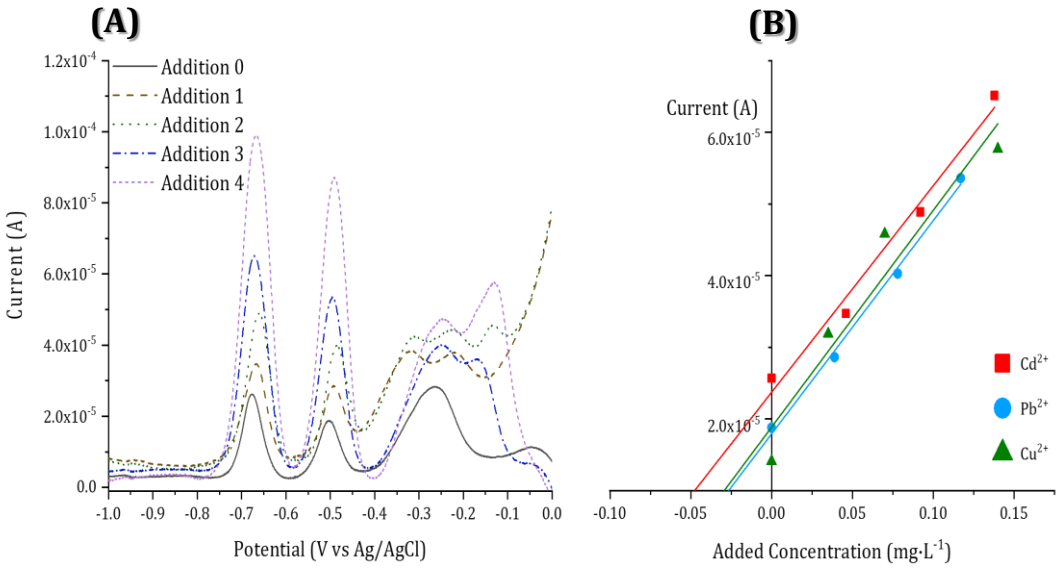

Figure 47. Spiked tap water analysis by standard addition method (A)SWASV voltammograms using HgNPs^{RouteA} sensors achieving the peaks of Cd^{2+} (-0.68 V), Pb^{2+} (-0.5 V) and Cu (-0.25 V). (B) Standard addition calibration curves for each metal.

The information from the calibration curves (sensitivity, y-intercept and R^2), the results obtained from extrapolation and the comparison with the selected reference method (ICP-MS) were summarized in **Table 22**.

Table 22. Summary of the calibration curve parameters obtained from the sample analysis by SWASV and comparison with the reference method (ICP-MS) and the recovery values. The recovery values were calculated from the quotient between the result of the proposed sensor and the ICP-MS results.

Metal	Sensitivity [A·L·mg^{-1}]·10^4	y-intercept [A]·10^5	R^2 (n=5)	$HgNPs^{RouteA}$ electrodes [mg·L^{-1}]	ICP-MS [mg·L^{-1}]	Recovery [%]
Cd^{2+}	(2.9 ± 0.3)	(2.4 ± 0.2)	0.98	2.06	1.9	108%
Pb^{2+}	(2.9 ± 0.1)	(1.8 ± 0.1)	0.99	1.51	1.6	94%
Cu^{2+}	(3.0 ± 0.6)	(1.9 ± 0.5)	0.93	1.56	1.5	104%

The recoveries have an error under the 10%, which we found suitable for these electrodes and samples with different matrix.

4.2.3.2. Sea water

Sea Water samples from Mar Menor (Spain) were provided by the Spanish project OPAL (Origin and Pathways of Anthropogenic solutes into coastal Lagoons: groundwater, sediments, and episodic events, Reference PID2019-110311RB-C21) to test the electrodes. This saltwater lagoon is the biggest in Europe, so due to its peculiar characteristics it has great biodiversity and ecological and geological importance. Nowadays, however, it is known for its periods of anoxia (massive dead fish appeared on the shore in 2019 and 2021 [114]) and pollution caused by some of the activities performed in the surroundings: metal mining, agriculture, and urbanism, mainly [115].

⌘ **Sample preparation**

When the measurements were performed, the data from the ICP-MS analysis were not accessible, so to obtain a suitable dilution to work with, several tests were done. Due to the difficult logistics of obtaining these samples, the tests could not be repeated. Several tests were performed to obtain a suitable dilution. The analysed sample was prepared using 10 mL of sea water diluted in 40 mL of buffer. The analysis was performed by standard addition calibration of all metal simultaneously. The additions were done from a mix metal solution of 4.1 mg·L^{-1} Cd^{2+}, 3.7 mg·L^{-1} Pb^{2+} and 4.8 mg·L^{-1} Cu^{2+}.

Hence, these high salinity samples give us a qualitative approach of the behaviour of the electrodes.

⌘ Results

Later, as mentioned, these samples were also analysed by ICP-MS and the obtained results are shown in **Table 23**.

Table 23. ICP-MS results from Mar menor samples.

Location	Cd^{2+} $[mg{\cdot}L^{-1}]{\cdot}10^{5}$	Pb^{2+} $[mg{\cdot}L^{-1}]{\cdot}10^{3}$	Cu^{2+} $[mg{\cdot}L^{-1}]{\cdot}10^{3}$
Los Urrutias	49	40	2.9
Carrasquilla	4.4	1.8	1.5
Playa Honda	5	3.5	1.6

These concentrations are below the quantification limits stablished previously for a multi-metal analysis, which are $5{\cdot}10^{-3}$ $mg{\cdot}L^{-1}$ for Cd^{2+}, $4.6{\cdot}10^{-2}$ $mg{\cdot}L^{-1}$ for Pb^{2+} and $8.6{\cdot}10^{-2}$ $mg{\cdot}L^{-1}$ for Cu^{2+}.

In **Figure 48** the SWASV voltammogram obtained from the Los Urrutias' sample is shown.

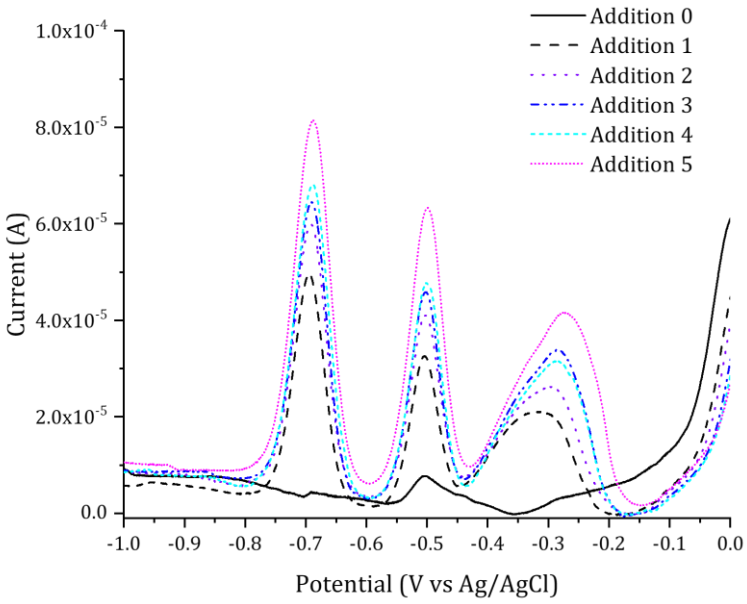

Figure 48. SWASV voltammogram obtained with the standard addition method of Los Urrutias' sample.

The concentration of Pb^{2+} is very close to the quantification limit established, but still under it. As the detection limit for Pb^{2+} was established at $2{\cdot}10^{-2}$ $mg{\cdot}L^{-1}$, so it is detected, but cannot be quantified.

The rest of the samples were all under the detection limits proved for this sensor.

4.2.3.3. Vineyard samples

These samples were provided by the project ReCuWINE (Characterization and Treatment of Contaminated Water, Sludge and Soil in the Wine Industry. A circular economy application of novel methodologies Reference: NJ700417). These samples came from a vineyard treatment plant in the D.O.P[13] Penedès Catalan region (Spain). $CuSO_4$ is widely used as fungicide in different types of vineyards [116], [117]. So, in this case, due to the origin of the sample, the concentration of copper is expected to be high. The process of the treatment plant has several steps including the wash of some parts of the grape and vine (sludge), the aerobic and anaerobic treatment of the sludge generated from the previous process, together with the recuperation of the remaining alcohol. As seen, in each step, a final sludge is generated, which will be our vineyard sample to be tested with our developed sensor (sludge, aerobic sludge and anaerobic sludge).

To analyse the sludges, they are dried and digested using an analytical microwave and concentrated nitric acid (HNO_3). This preparation was done by ReCuWINE investigators (**Annex I**). HNO_3 can affect the stability of the HgNPs, for that reason the amount of sample used is reduced to the minimum necessary to be in the linear range concentration of the $HgNPs^{RouteA}$ @graphite electrodes.

⌘ **Sample preparation**

The solution from the digestion of the sludges was measured directly by diluting 15 to 100 mL of acetic acid/acetate buffer. Then, the analysis was performed by standard addition calibration of all metals simultaneously. The additions were done from a mix metal solution of 4.1 $mg{\cdot}L^{-1}$ Cd^{2+}, 3.7 $mg{\cdot}L^{-1}$ Pb^{2+} and 4.8 $mg{\cdot}L^{-1}$ Cu^{2+}.

⌘ **Results**

First approaches to these samples were done blindside, so a first dilution 1 to 100 mL of the digested stock solution was done. As no signal was found, different dilutions were tested without any signal. Finally, the samples were analysed directly.

In parallel, the samples were analysed by ICP-MS and the obtained results are shown in **Table 24**. From the Cu values found, we confirmed that the concentrations values are high enough to be able to quantify them with $HgNPs^{RouteA}$ @graphite electrodes.

[13] D.O.P in Spanish *Denominación de Origen Protegida*. It is a form that has the Spanish Ministry of Agriculture, Fisheries and Food the regulate the quality of the foodstuff from a specific region.

Table 24. Summary of the samples analysed, the day of the sampling and the concentration of Cu^{2+} analysed by ICP-MS.

Sample	Date of sampling	Cu^{2+} [mg·L^{-1}]
Sludge	11/06/2022	0.663
Aerobic Sludge	14/11/2022	0.546
Anaerobic Sludge		0.719

From the ICP-MS analysis, the range of values of other metals that were found in these samples were: Fe (6.4-7.6 mg·L^{-1}), Mn (0.4-0.45 mg·L^{-1}) and Zn (0.28-0.36 mg·L^{-1}). Cd and Pb were not found.

Due to the complexity of the sample the peak of Cu^{2+} is not as clear as in previous water samples (tap water and sea water), some displacement in the potential where the Cu appears after each addition is observed (see **Figure 49.A, C** and **E**). This displacement can be attributed to the possible presence of Cu^{1+} due to the complex behaviour of the modified electrode ($HgNPs^{RouteA}$ @graphite). Furthermore, the mixed solution used in the standard addition calibration contained all three metals, but only copper is quantified. In **Table 25** all the calibration information of the sensor and the obtained Cu concentration is summarized.

Table 25. Summary of the calibration curves parameters with $HgNPs^{RouteA}$ @graphite electrode, the concentration found in the samples and the recovery compared with the ICP-MS results.

Sample	Sensitivity [A·L·mg^{-1}]·10^5	y-intercept [A]·10^6	R^2	$HgNPs^{RouteA}$ electrodes [mg·L^{-1}]	Recovery [%]
Sludge	(2.1 ± 0.1)	(7.2 ± 0.1)	0.98*	1.06	160%
Aerobic Sludge	(1.9 ± 0.4)	(3.6 ± 0.1)	0.81^x	0.646	118%
Anaerobic Sludge	(2.4 ± 0.5)	(6.5 ± 0.2)	0.83*	0.656	91%

*n=6; ^{x}n=5

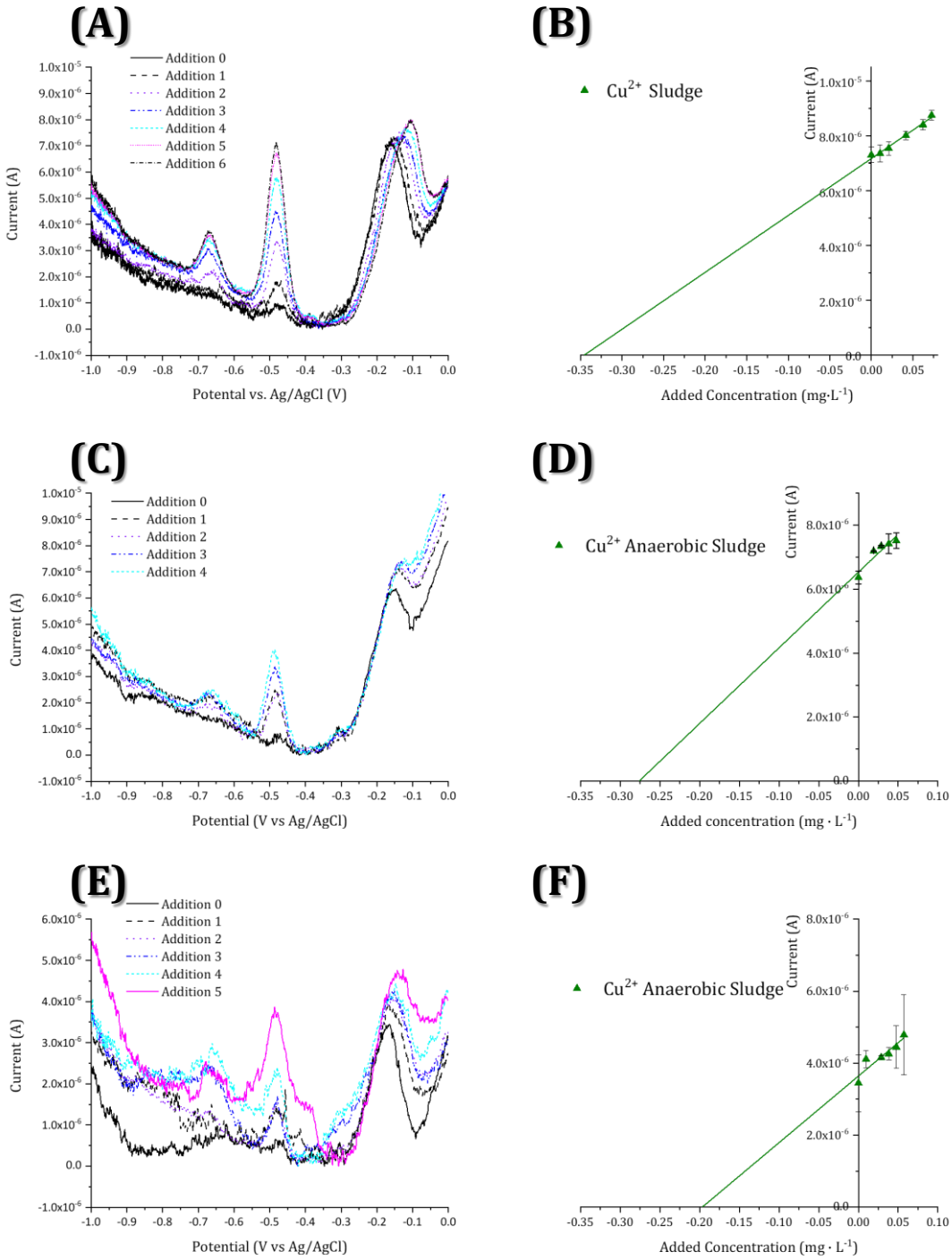

Figure 49. SWASV voltammogram obtained with the standard addition method (A, C, E) and calibration curve for Cu^{2+} (B, D, F); for sludge, aerobic sludge and anaerobic sludge, respectively.

The variation of the obtained results (from 160 to 91% recovery) could be related to different date of each sampling and/or the different treatment to the sample (non-treatment, aerobic or anaerobic). All these parameters: sampling date, also the season of the year when the sampling is performed, the treatment chosen, the bio-variability, etc. can affect the complexity of the matrix. The season of sampling is really important in agriculture because some treatments are performed only at a specific moment of the year, and these

treatments can change the composition of the sample matrix. The treatment of the sludge also can change the composition of the matrix. So, here we are analysing three different samples that cannot really be compared between them.

4.2.4. Concluding remarks

In **Figure 50**, the experimental work developed is a summarized. As seen, the modifications of the 20% graphite electrodes were done by means of two synthetic routes of HgNPs: Route A, using PDDA and Route B using PVA. In general, both HgNPs tested constitute a suitable strategy to modify the bare 20% graphite electrode for the three studied metal analysis.

Route A provides us with smaller and more stable nanoparticles. According to the XPS analysis the oxidation state of the $HgNPs^{RouteA}$ is I.

The performance of $HgNPs^{RouteA}$ @graphite electrode towards the metals analysis is better than the other options tested. But it has some issues for the Cu^{2+}.

These newly designed sensors allow the analysis in different aqueous matrices, such as tap water, sea water and digested samples from vineyard, with quite good results specially for tap water.

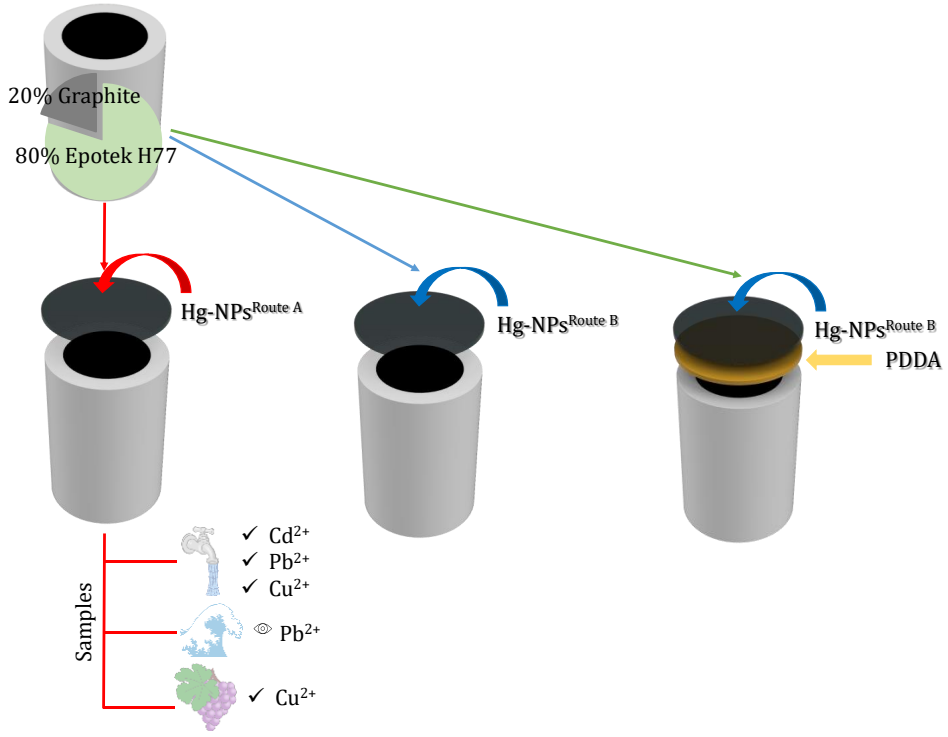

Figure 50. Graphical summary of test performed in Chapter IV —Part II

Part III

Composite electrodes modified using enzyme loaded polymersomes

This work has been done in collaboration with the Bioactive and Responsive Polymer department, from the Leibniz-Institut für Polymerforschung Dresden e.V.

Part of the content of this work has been submitted in the paper « *Multi-compartimentalized Electrochemical Sensing Platforms for Monitoring Cascade Enzymatic Reactions*» (under revision).

‡

4.3. Enzyme loaded polymersomes

Material science has evolved to develop some synthetic structures, called polymersomes (Psomes), for their similarity to the liposomes [118]. These structures were prepared by enabling the location of amphiphilic copolymers block until reach a (bi or mono) layer form. They can be very versatile, but the most known utility is as drug carriers, where the uptake and release can be modulated by different external stimulus that affected Psomes behaviour, such as pH change, target tissue, electrochemistry, light, ionic strength[119], [120], [121], [122], [123], [124]. Alternatively, Psomes can be loaded with enzymes, instead of drugs. Enzymes are well-known biologic catalysts that can be applied in biomedical, industrial, chemical, and biotechnological areas. However, these application fields can be limited for the stability of these catalysers to external parameters [125]. Psomes can help in the stabilization of the enzyme, protect them from the external parameters and give us the advantage of being able to encapsulate different enzymes (compartmentalization). Furthermore, these vesicles have channels that allow the diffusion of the substrates to produce enzymatic reaction and the diffusion of the enzymatic products into the environment [126]. Due to Psomes responsiveness to the surrounding environment, some enzymes, such as Horseradish Peroxidase, Alkaline Phosphatase, Ribitol Dehydrogenase, have been previously encapsulated in the Psomes and used in sensing applications [36].

Polymersomes can be added to multicomponent and multifunctional materials as nanocomposites. The incorporation of enzyme loaded Psomes (nanoscale material) onto the surface of composite electrodes will enable monitoring an enzymatic reaction using electrochemical techniques. However, Psomes are typically made with non-conductive block copolymers [118], which limits their applicability in electrochemical systems. On another hand, if the Psomes are incorporated as part of the composite matrix, their flexibility, and channels may be ineffective due to the rigidity of the matrix. For this reason, the use of carbon materials, such as CNTs or rGO represent an alternative solution to this issue, because they are well-known conductive materials and can be customized, to increase the affinity for these loaded vesicles to be anchored onto the surface of the electrode.

4.3.1. Polymersomes

The synthesis of the amphiphilic block-copolymer[14] (BCP, mPEG45-b-P(DEAEMA-co-DMIBMA)) was performed by Atom Transfer Radical Polymerization (ATRP), as previously

[14]According to IUPAC definition, a block copolymer is derivate from more than one species of monomer which are different or with different composition or sequence distributions of the constitutional units [154].

reported [127], [128]. The BCP has two parts a methoxy end group at the hydrophilic poly(ethylene glycol) (PEG) segment and the hydrophobic part (pH sensitive), 2-(diethylamino)ethyl methacrylate (DEAEM) and photo-crosslinker, 3,4-dimethyl maleic imidobutyl methacrylate (DMIBMA). Two BCPs were used with different relative compositions (**Table 26**) and characterized by ^{1}H Nuclear Magnetic Ressonance (^{1}H-NMR) and Size Exclusion Chromatography-MultiAngle Light Scattering (SEC-MALS). The synthesis and characterization were entirely done in the *Bioactive and Responsive Polymer* department (Dresden, Germany).

Table 26. Composition, block ratio, molecular weight, weight average molecular weight (M_w) and number average molecular weight (M_n) and dispersity (Đ) for both BCP used.

BCP	DEAEM	DMIBMA	PEG	Block ratio	M* [g·mol^{-1}]	M_w^x [g·mol^{-1}]	M_n^x [g·mol^{-1}]	Đ
CE 880-1	63	22	45	1:1:9	19700	36500	30800	1.19
AS 223	104	27	45	1:2:91	28600	53350	46850	1.14

*Determined by ^{1}H-NMR data.

^{x} Determined by SEC-MALS data.

In **Scheme** 14, the *in-situ* loading procedure of the Psomes is shown: where the crosslinkable block copolymer (BCP, 1 mg·mL^{-1}) and the enzyme Glucose Oxidase (GOx, 0.2 mg·mL^{-1}), were mixed at pH 5.0, both of them previously filtrated with a Nylon filter 0.2 µm. The formation and the loading of the Psomes is performed at the same time, a one pot reaction. After the self-assembly at pH 8.0, the solution remains 3 days in the dark with constant stirring, Then, the solution is filtrated with a 0.8 µm filter and the crosslinking process is performed by irradiating the sample with UV light (EXFO Omnicure 1000 from Lumen Dynamics Group Inc., Ontario, Canada, equipped with a high-pressure mercury lamp) for 30 s.

For the Empty-Psomes, the same procedure is followed just avoiding the addition of the enzyme.

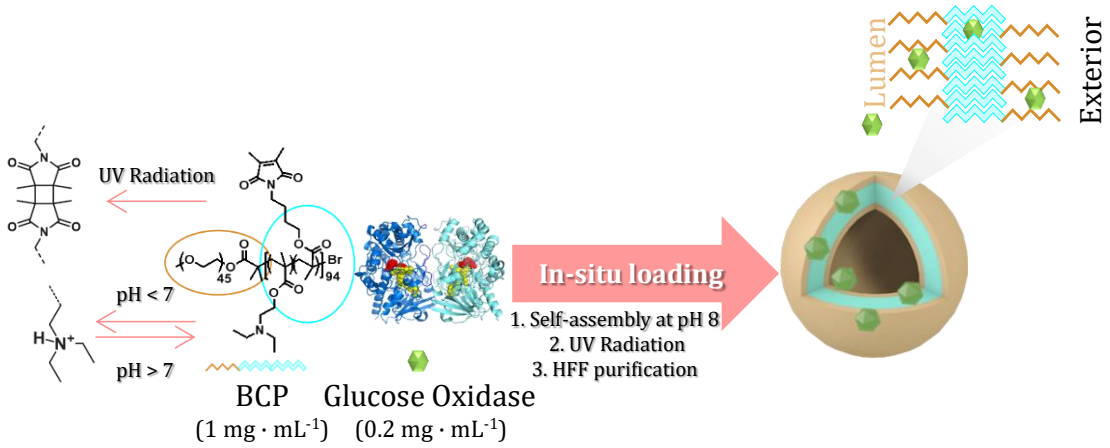

Scheme 14. Procedure for *In-situ* loading of GOx-Psomes.

The conditions to storage for months, all the loaded Psomes (GOx, CAT and $(\beta\text{-CD})_2$Hemin–Psomes) and the Empty-Psomes are at -19 °C [34].

The crosslinking, using UV radiation, avoid the disassembly of the membrane of the Psomes at acid pH (pH < 7), when the tertiary amine gets protonated the state of the Psome is swollen. On the contrary, in basic pH (pH > 7) the Psome is collapsed [33], [127]. As the assembly and loading were done simultaneously, the enzyme could be found in different places of the Psomes. The desired one is in the lumen (inner place) of the Psomes, others are trapped in the membrane and the rest remains in solution. To eliminate the last ones, that remains in solution, a Hollow Fiber Filtration (HFF) system using a 500 kDa membrane and NaCl 10 mM at pH as PBS buffer (flow = 15 mL·min^{-1}, TMP[15] = 130 mbar).

After all these processes, the Empty-Psomes (no cargo, just the membrane) and GOx-Psomes were characterized by different means: Dynamic Light Scattering (DLS) that gives information about the size and the polydispersity index[16] (PdI), and in the case of the GOx-Psome also by Transmission Electron Microscopy (TEM), which can provide morphological information.

The DLS studies can be divided in two types:

- ***pH cycles***: that consist in change the pH from 6.0 to 8.0, making the Psome open and close in cyclical way. Thus, the stability of the Psomes can be studied towards pH changes.

[15] TansMembrane Pressure (TMP) represents the driving force for transfer of material across the filter.
[16] Polydispersity index (PdI) based on the size, gives information about the heterogeneity of the sample (aggregation). PdI values go from 0, which is the ideal (uniform sample) to 1 (multiple particle size population). Values below 0.2 are acceptable.

⌘ ***pH**** (*pH star*): this value indicates at which pH the Psome is semi-swollen. It is done by titrating the vesicles from 8.0 to 5.0 and adjusting to a Boltzmann distribution.

4.3.2. Empty-Psomes characterization.

The two types of Empty-Psomes (depending on the BCP used) were characterized by the two methods previously mentioned. In **Figure 51.A**, and **C** the study of the pH cycles is shown. The Psomes keep their efficiency up to 5 pH cycles of pH for both BCPs, from pH 6.0 (open, size around 135-140 nm) to pH 8.0 (close, size around 65-110 nm). So, showing good stability towards the pH changes. The pH* for CE 880-1 is 6.87 and for AS 223 is 6.49, as is shown in **Figure 51.B**, and **D.** This differences in the size and pH* could be related to the BCP structure.

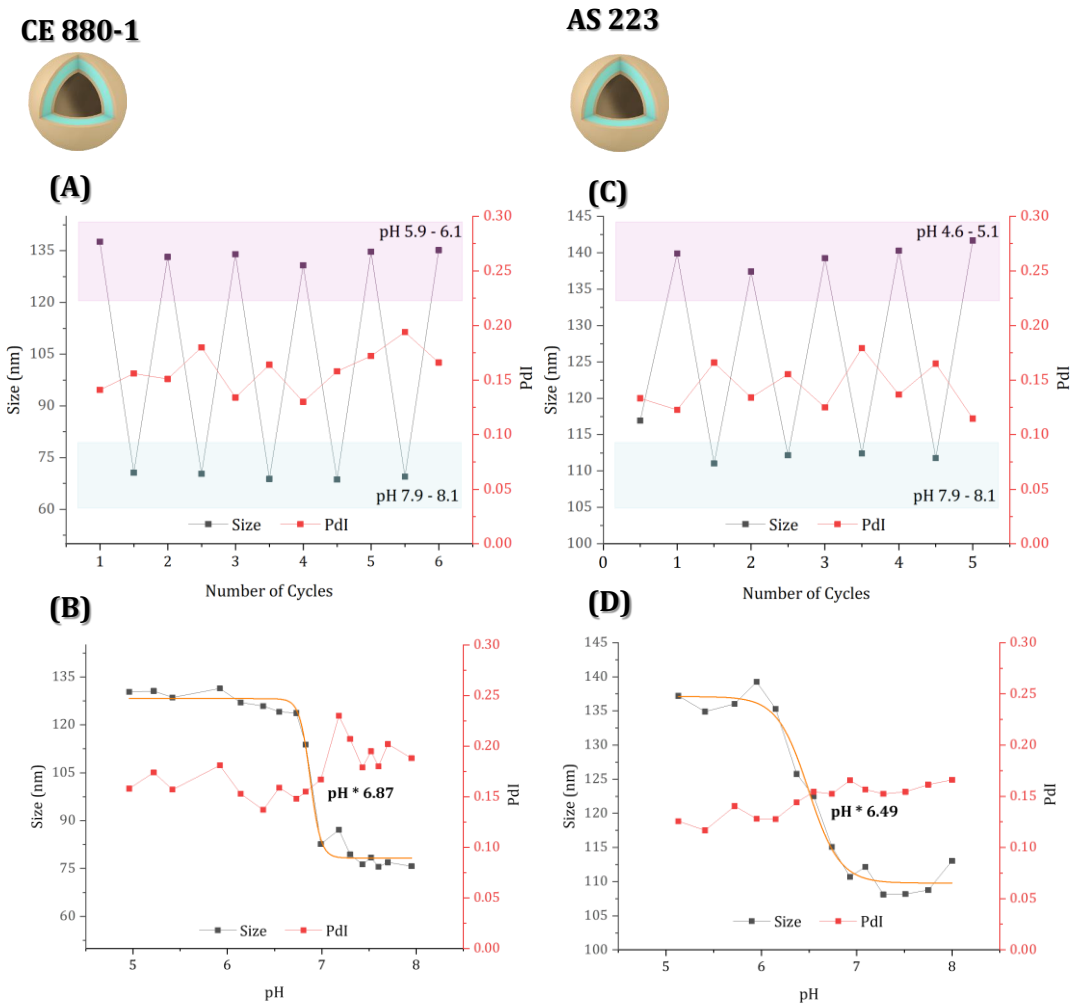

Figure 51. Empty-Psomes characterization by DLS. For 0.5 mg·mL^{-1} CE 880-1 (A) pH cycle in NaCl 10 mM, and (B) pH* study. For 0.5 mg·mL^{-1} AS 223 (C) pH cycle in NaCl 10 mM, and (D) pH* study.

4.3.3. GOx-Psomes characterization

The GOx-Psomes were prepared using both said BCPs and the loading was done following the procedure summarized in **Scheme 14.**

They were characterized by DLS In **Figure 52.A**, and **C** the study of the pH cycles is shown, and both presents good stability towards the pH changes. The pH* for CE 880-1 is 6.84 and for AS 223 is 6.88, as is shown in **Figure 52.B**, and **D**. Comparing with the Empty-Psomes, the loading process seems to affect the pH*, differently depending on the BCP: for the CE 880-1 the Empty-Psomes pH* is 6.87, while for the GOx-Psomes is 6.84, that it is not considered a remarkable difference; for the AS 223, the pH* for Empty and loaded Psomes is 6.49 and 6.88, respectively, that is a most notorious difference. But the pH* of both GOx-Psomes is alike, so they were used interchangeably when preparing GOx-Psomes due to these small differences between this response.

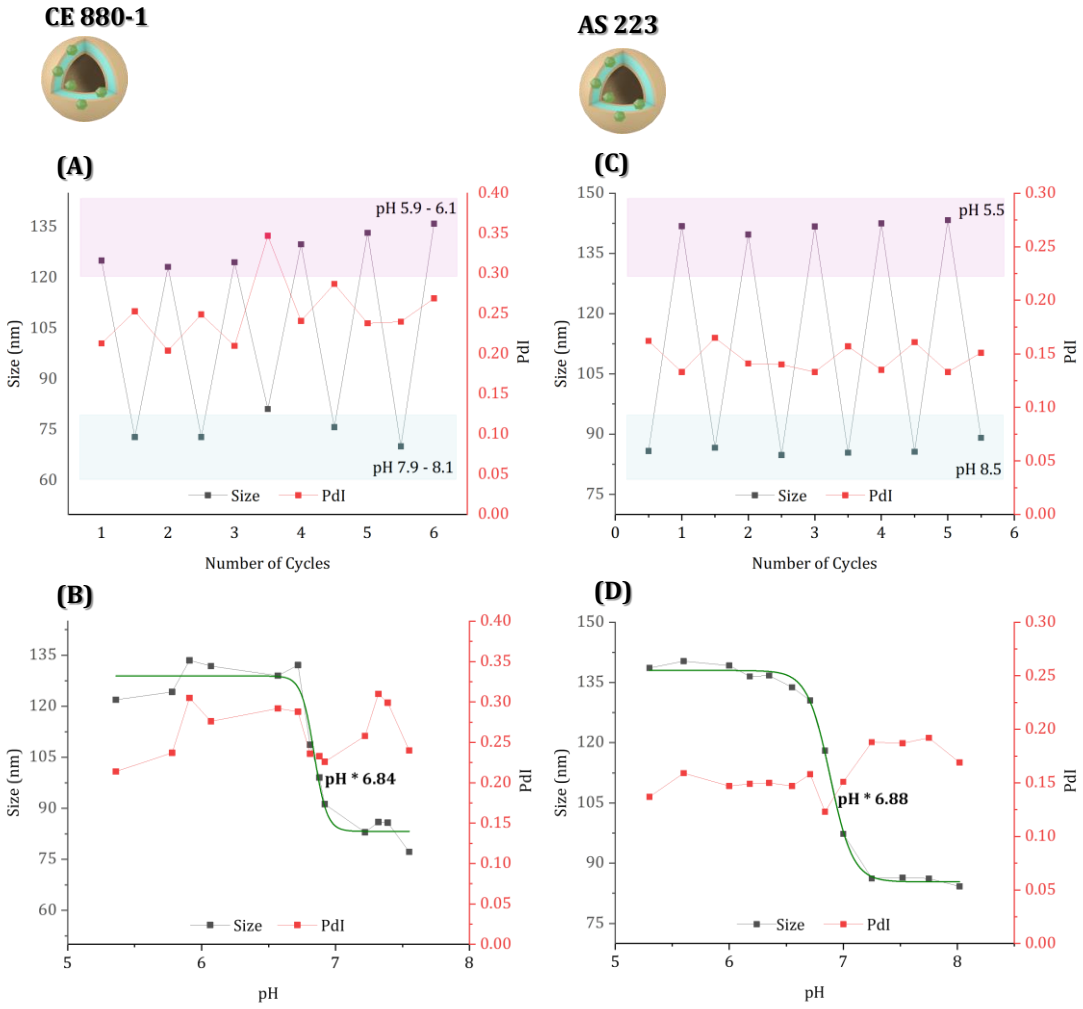

Figure 52. GOx-Psomes enssambled using the different BCP characterization by DLS. For 0.5 mg·mL^{-1} CE 880-1 (A) pH cycle in NaCl 10 mM, and (B) study of the pH*. For 0.5 mg·mL^{-1} AS 223 (C) pH cycle in NaCl 10 mM, and (D) study of the pH*.

Also, the GOx-Psomes (CE 880-1) were morphologically characterized by Cryo-TEM (see **Figure 53**, using 54 particles in 8 images). The diameter was 72 ± 15 nm and the membrane thickness was 18.9 ± 3.2 nm.

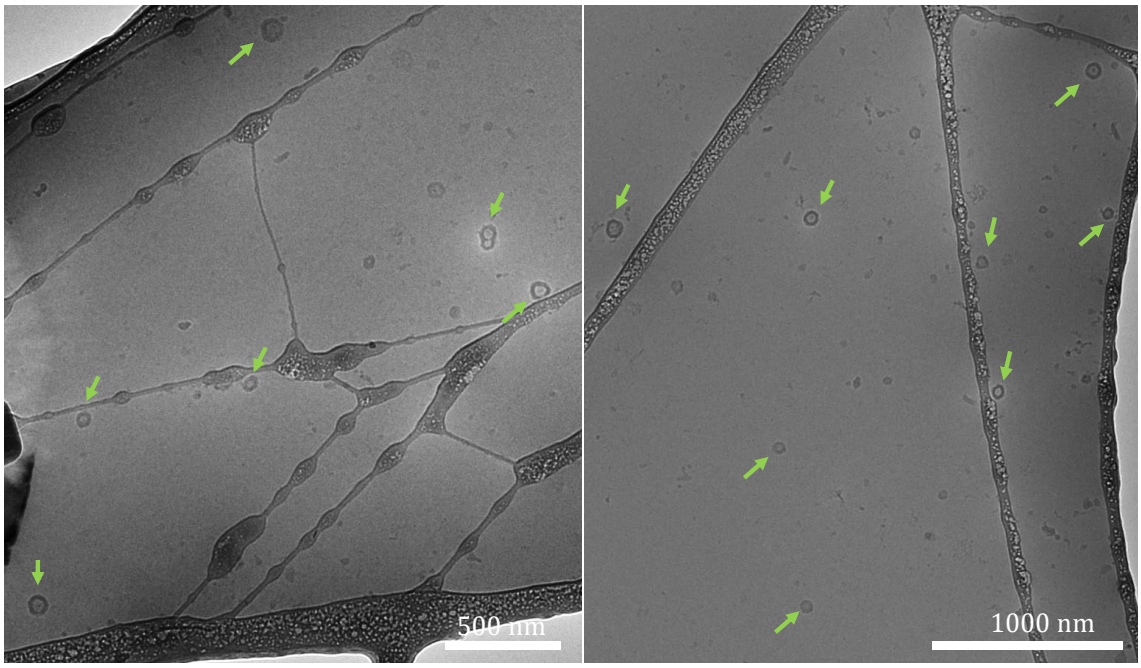

Figure 53. Cryo-TEM images of the GOx-Psomes (CE 880-1) (green arrows).

To calculate the Loading Efficiency (LE), the loading process of the Psomes described in **Scheme 14** was performed but instead of using GOx, labelled GOx (FITC[17]-GOx) was used. This FITC label allows to know where the enzyme is located, inside the Psomes or outside, in the media, because it is fluorescent. When the FITC-GOx is in the lumen of the Psomes the fluorescent signal will decrease compared when it is free in the medium. To eliminate the free enzyme in the media some Hollow Fiber Filtration (HFF) purification steps were done, and the purification is finished when the fluorescent intensity remains constant and near to zero F.I (counts). The purified solution and the waste solution were analyzed, and their responses are collected in **Figure 54.A** and **B**, respectively. Additionally, the size and the PdI of GOx-Psomes was determined, 135 nm and 0.191 before and 147 nm and 0.229 after HFF purification. The LE of the GOx-PSomes was calculated by fluorescence intensity after purification divided by fluorescence intensity before purification, and it is 27%, which is around ~0.05 μM.

[17] FITC is Fluorescein IsoThioCyanate.

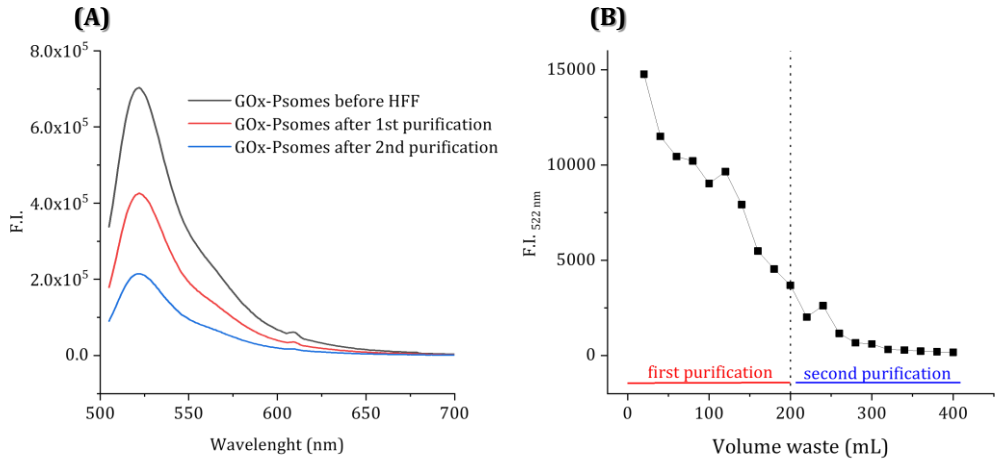

Figure 54. HFF purification steps monitoring: (A) before and after the several steps of HFF, and (B) waste solution analysis of the HFF purification.

Furthermore, the enzyme activity of GOx-Psomes was studied in solution by using the Amplex™ Red assay with glucose as target analysis. In **Figure 55.A** and **B** the activity of non-purified GOx-Psomes was studied at different pH. In **Figure 55.C**, the activity of the purified GOx-Psomes was studied at two pH where the Psomes state is swollen (pH 5.0) or closed (pH 8.0). Non-purified GOx-Psomes present higher activity than the purified ones, this is due the GOx that remains in solution. In **Figure 55.C** can be observed that higher activities can be achieved when the Psomes membrane is open (swollen state), due to the pass of the substrate through the membrane. However, when it is close (collapsed state), notable activities are also given. This, as was mentioned, gives information about where the enzymes are placed, from the mentioned results, it looks like some of the GOx molecules are in the membrane.

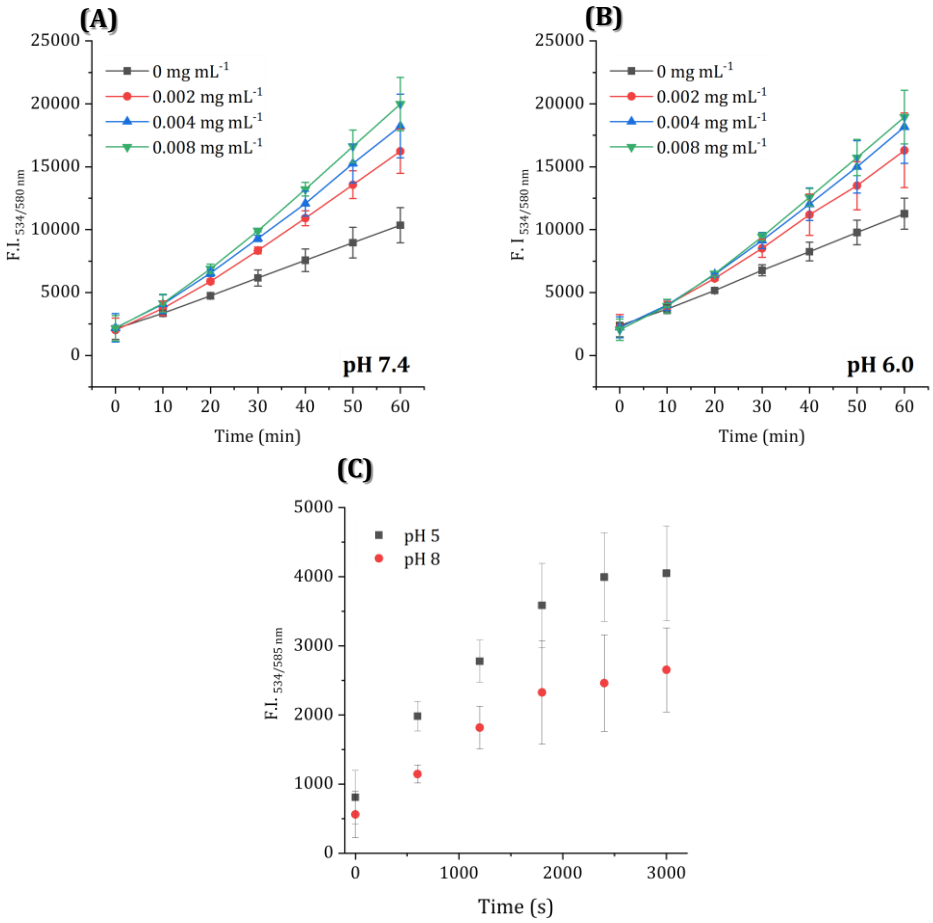

Figure 55. GOx activity study by a direct Amplex™ Red assay at different glucose concentrations of (A) non-purified GOx-Psomes at pH 7.4, (B) non-purified GOx-Psomes at pH 6.0, and (C) purified GOx-Psomes at pH 5.0 and 8.0 and glucose 0.001 mg·mL^{-1}.

4.3.4. Modification of the electrode surface

The first approach for anchoring the Psomes over the surface of the electrode were done at Bioactive and Responsive Polymer department of the *Leibniz Institut für Polymerschung e.V* (Dresden, Germany) directly onto the surface and using PDDA. Then, this works followed in the Chemistry department of the *Universitat Autònoma de Barcelona (*Bellaterra, Spain*)* using other polymers as pyrrole, chitosan, alginate, and physical anchors such as Al tape, Cu, tape, C tape and C stub. Initially, the easiest modification, directly placing the Psomes over the electrode surface was tested. Finally, the obtention of a hybrid nanomaterial to properly achieve the best modification was performed.

The graphite composite electrode selected was 15% graphite due the improved electrochemical performance and the best signal/noise ratio [91]. For that purpose, 15 new composite electrodes of this optimal ratio graphite/epoxy resin were constructed. The manufacturing process is described in **Chapter III: Materials & Methods**.

The results were characterized using the electrochemical redox pair $[Fe(CN)_6]^{3-}/[Fe(CN_6)]^{4-}$ and KCl 0.1M by cyclic voltammetry (CV) with a scan rate of 10 $mV \cdot s^{-1}$ and by electrochemical impedance spectroscopy (EIS) in a frequency range from 10^5 to 0.01 Hz. To obtain the values of R_{CT} the equivalent circuit adjusted was the Randles circuit (see **Figure 13** in **Chapter III: Materials & Methods**).

4.3.4.1. Directly onto the surface

The first approach was to drop-cast 20 µL of the Empty-Psomes onto the surface of the electrode. Then, dried 30 min at 40 °C and electrochemical characterized by CV and EIS. In **Figure 56**, the results of the characterization are shown.

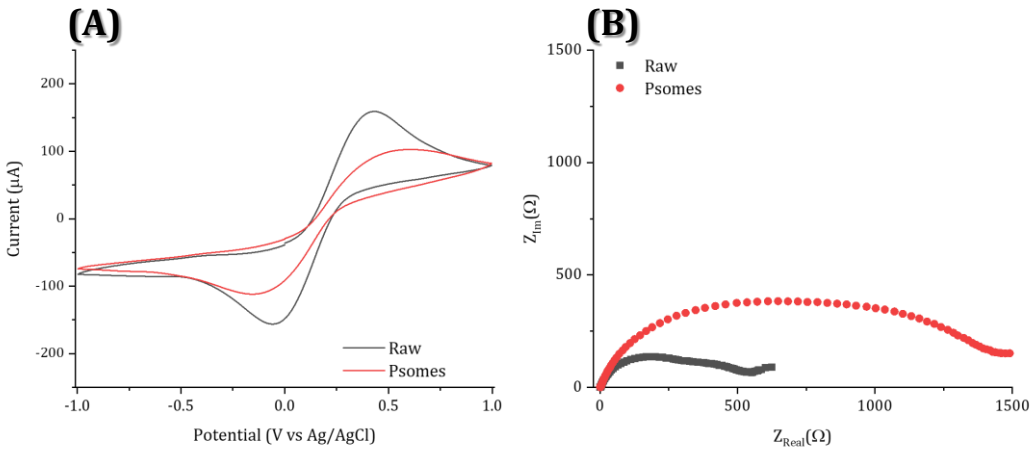

Figure 56. Electrochemical characterization of the raw composite electrodes and modified by directly drop-cast Empty-Psomes over the electrode surface: (A) CV (ν: 10 $mV \cdot s^{-1}$) and (B) EIS.

In **Figure 56.A**, it is shown a decrease in the response (lower current) of the electrodes due their modification and in **Figure 56.B**, an increase of the resistance to the charge transfer is shown, which is consistent with the low intensity recorded in the CV (**Figure 56.A**). The current decrease can be related to the increased resistance to electronic transfer caused by the presence of non-conductive Psomes on the electrode surface. Therefore, the problem with this kind of modification is the increase in the R_{CT} and the potential loss of the Psomes during the measurements. Next is focused to try to improve the stability of the Psomes in the electrode surface minimizing the R_{CT}.

4.3.4.2. Tapes and stubs modifications

Looking for a physical interaction between the electrode and the Psomes, some tapes (Al, Cu and C) and the carbon stub (C stub) were tested. All these materials were giving us by the *Servei de Microscopia de la Universitat Autònoma de Barcelona*. Usually, these kinds of tapes are used in electronic microscope sessions, due to their conductivity.

In **Scheme 15**, the process of modification using taps and stubs is graphically explained and consists in cut the tape (or stub) and place it over the raw composite electrode surface.

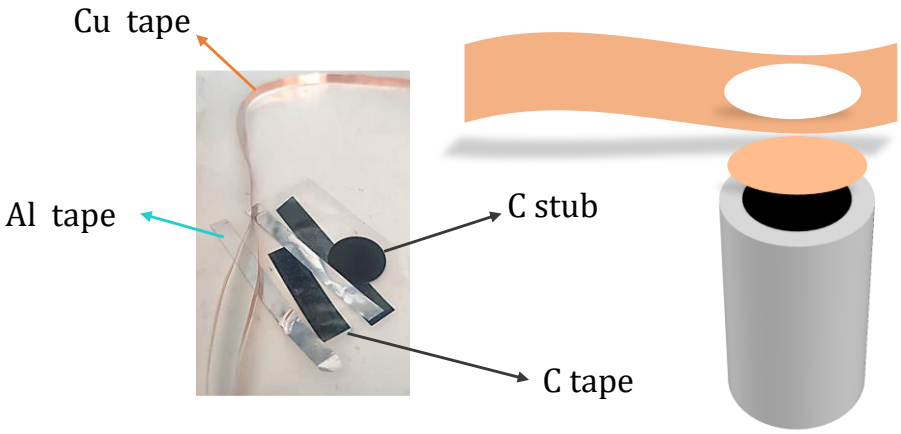

Scheme 15. Modification process using tapes and the stub.

These electrode modifications were characterized by CV.

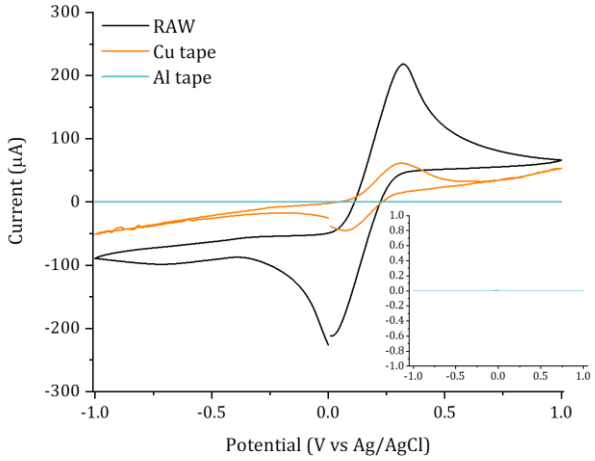

Figure 57. CV of Cu tape and Al tape modification over raw electrode. Inset extended CV for Al tape. (ν: 10 mV·s^{-1}).

In **Figure 57**, the response of the metallic tapes is presented. The Al tape modification does not present any current signal, which means this tape is not a good transducer. On the other hand, the Cu tape present a lower current, compared to the raw electrode, and at the end of the experiment was uncoupled of the electrode.

In **Figure 58,** the response of the C tape is showed. Compared to the raw composite electrode, placing the C tape over the electrode surface drastically reduces the current recorded, but not at zero. Also, the tape remains in its place at the end of the experiment. For that reason, an alternative C tape modification was tested. This is based on the drop-casting of 20 µL of 1 mg·mL^{-1} CNTs dispersion solution (in Milli-Q water) over the external C tape layer placed over the composite electrode and dried during 30 min at 40 °C. The response (Modified C tape) obtained was around 15 µA, and as can be observed in the inset of **Figure 58**, it has a microelectrode behaviour.

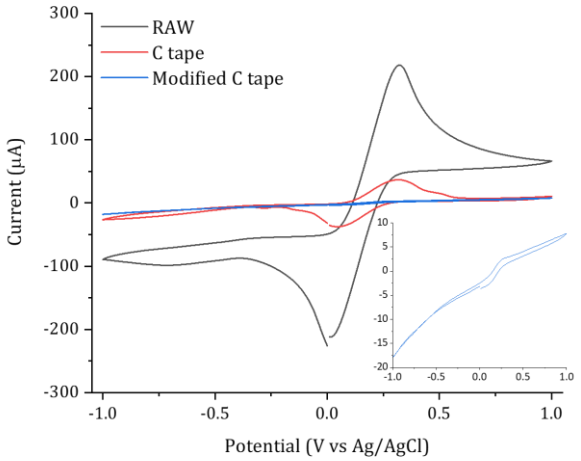

Figure 58. CV of C tape and its modification over raw electrode. Inset extended CV for modified C tape. (ν: 10 mV·s^{-1}).

Also, the response of other type of C tape, named C stub was also evaluated. The difference between the C tape and the C stub, is that the C stub has glue in both of its faces. As can be observed from **Figure 59**, the electrochemical response of the C stub is quite better than the C tape, because double the current obtained, but not improved over the raw composite electrode. When it was modified, in this case with 20 µL of 1 mg·mL^{-1} AuNPs@rGO dispersion solution (in Milli-Q water) and dried 30 min at 40 °C, the response also decreases near 0 µA.

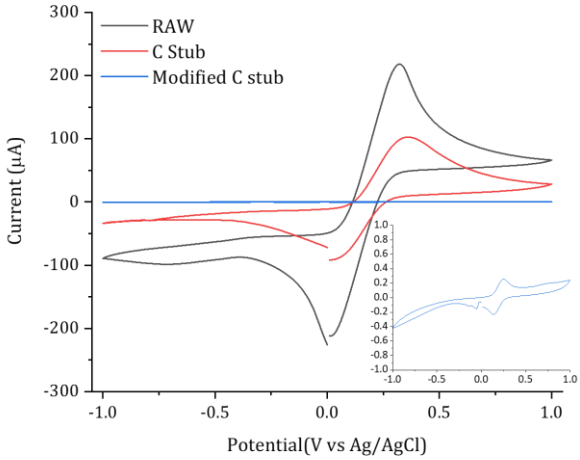

Figure 59. CV of the C stub and its modification over raw electrode. Inset extended CV for modified C stub (ν: 10 mV·s^{-1}).

Due the low responses obtained in these different conditions; all these modifications were discarded for further works.

4.3.4.3. Poly(diallyldimethylammonium chloride)

As it was said, the first approach was using Poly(diallyldimethylammonium chloride) (PDDA, 20% wt, from Sigma Aldrich) to anchor the Psomes over the electrode surface. Using a layer-by-layer protocol and due to its properties, specifically the positive charge of the PDDA, it was used as a molecular glue (see **Scheme 16**).

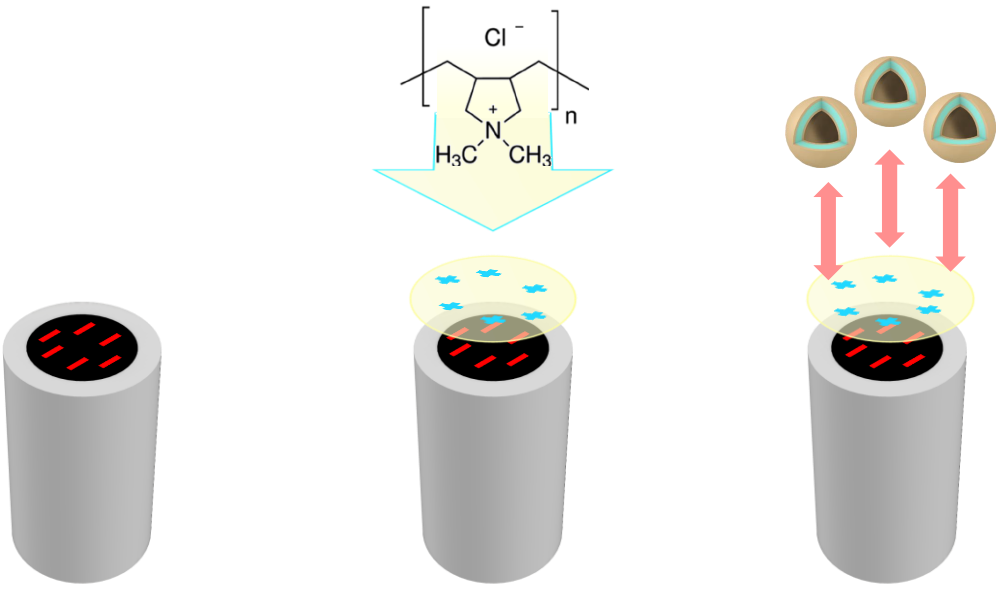

Scheme 16. Interactions between the layers in the modification process with PDDA. From left to right: raw electrode, PDDA layer and PDDA layer plus Psomes.

The modification protocol consists in two steps: first, the raw electrode was immersed for 20 minutes in a 10% PDDA solution, and second 20 µL of Empty- Psomes were drop-casted and dried for 30 min at 40 °C. The electrode modification was studied by CV and EIS, using the electrochemical reference redox pair $[Fe(CN)_6]^{3-}$/ $[Fe(CN_6)]^{4-}$. Results are collected in **Figure 60.**

In **Figure 60.A**, as the complexity in the modification is increase, and a layer with non-conductive materials are added a decrease in the current is observed comparing with the raw electrode. Highlight the peak of the oxidation of the PDDA at 0 V. In **Figure 60.B**, with the use of the PDDA in the system there is a reduction in the resistance to the charge transfer due to the charge of the PDDA itself, from 283.1 Ω of the raw electrode to 138 Ω of the

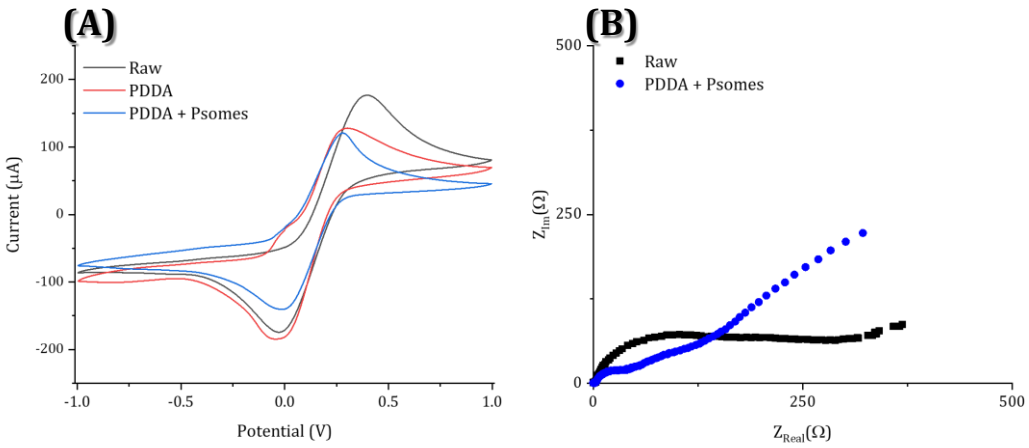

modified with PDDA + Psomes.

Figure 60. Electrochemical characterization of the composite electrodes modified by dopcasting with PDDA and Empty-Psomes/PDDA: (A) CV (ν: 10 mV·s^{-1}) and (B) EIS.

The inconvenience of this kind of modification was the loss of Empty-Psomes/PDDA when it is in contact with the measuring solution.

4.3.4.4. Pyrrole

To increase the adhesion of Psomes the electrodeposition of pyrrole on the electrode surface was studied. A solution of 0.1 M pyrrole (98%, C_4H_5N, Sigma Aldrich, St. Louis, MO, USA) and 0.035 M cesium bis(1,2-dicarbollide)cobaltate ($Cs[(C_2B_9H_{11})_2Co]$) (from KatChem, Czech Republic) was prepared in anhydrous acetonitrile (99.8%, Sigma Aldrich, St. Louis, MO, USA). Milli-Q water was added a posteriori to solubilize the cesium bis(1,2-dicarbollide)cobaltate, this salt helps to improve the charge transfer.

To electrodeposit this solution over the surface electrode, 25 cycles from -0.2 V to 1.1 V at a scan rate of 10 mV·s^{-1} were followed, as established previously [129].

The data obtained in these experiments is shown in **Figure 61.A** and **B** and indicates that the polypyrrole electrodeposited over the surface of the electrode do not present good conducting properties. Electrodeposition of polypyrrole drastically limits the electron transfer on the electrode surface (**Figure 61.A**) and increases the resistance to electron transfer (32220 Ω). The deposition of modified polypirrole with CNTs enhance the

conducting properties, presenting higher currents in the CV analysis and lower R_{CT} in the EIS analysis (191.7 Ω).

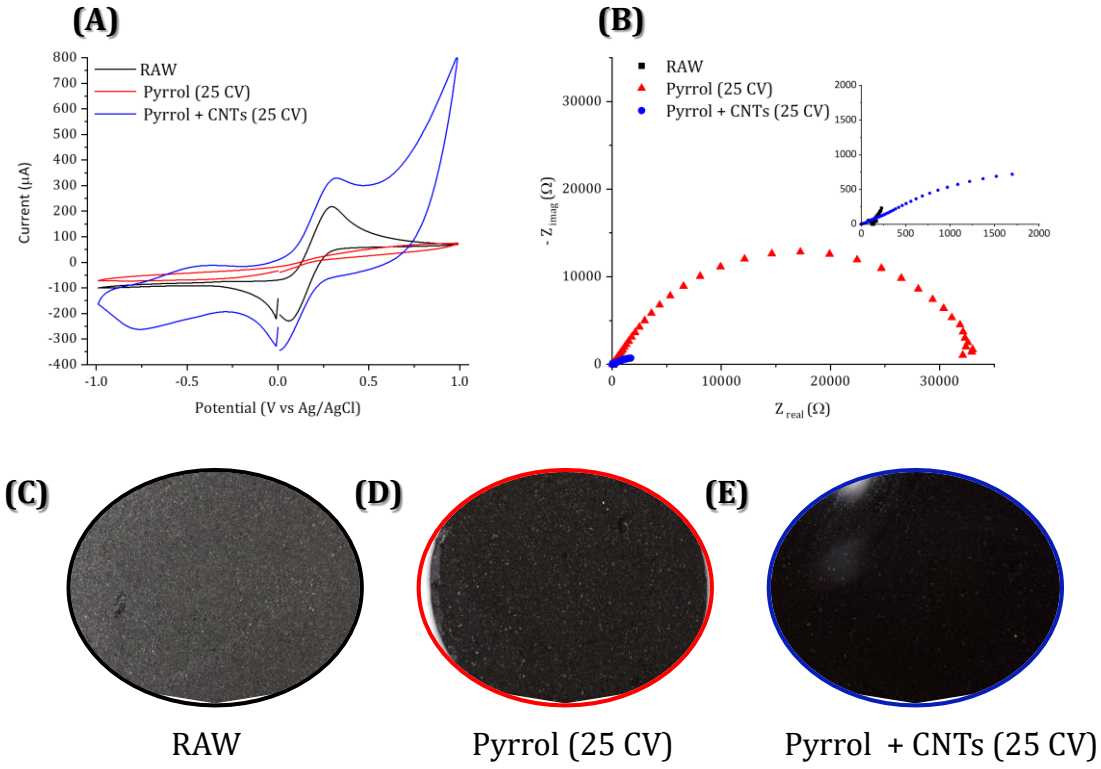

Figure 61. Electrochemical caracterization of composite electrode modificated with Pyrrole (A) CV (ν: 10 mV·s^{-1}) and (B) EIS. Microscope images (1:100 augments) (C) raw electrode surface, (D) electrode surface modified with electrodeposited polypyrrole, and (E) electrode surface modified with electrodeposited polypyrrole with 1% CNTs.

The evolution of the darkness of the electrode surface increase along with the modifications, as can be seen from **Figure 61.C**: with polypyrrole (**Figure 61.D**) and with polypyrrole plus CNTs (**Figure 61.E**).

As mentioned, there is an improvement of the electrochemical characteristics of the electrode with the electrodeposition of polypyrrole plus CNTs. However, the solvents used are not biocompatible with Psomes. So, due to the solvents used, this modification was discarded, and more bio-compatible polymers as chitosan and alginate were tested.

4.3.4.5. Chitosan

Chitosan is a polymer biocompatible with Psomes. It is used as immobilization agent in several studies [130]. A 10 mg·mL^{-1} solution of chitosan (Sigma Aldrich, St. Louis, MO, USA) was prepared in 0.1 M acetic acid/acetate buffer. Then, 100 µL of this chitosan solution were diluted in 900 µL of different solutions such as: PBS 10 mM, Milli-Q water, and a dispersion

of 1 mg·mL^{-1} AuNPs@rGO in water. 20 µL of each solution were drop-casted over the surface of different electrodes and dried during 30 min at 40 °C.

In **Figure 62.A**, a decrease in the current measured is observed compared with the raw electrode in all the modification tested. The same behaviour is observed for the chitosan in PBS and in the AuNPs@rGO dispersion. On another hand, modified chitosan with AuNPs@rGO (chitosan-AuNPs@rGO) and chitosan in Milli-Q have the same type of behaviour. In **Figure 62.B**, the raw electrode presents the lower R_{CT}, except chitosan in Milli-Q water, that presents the higher resistance to the charge transfer (1587 Ω), the rest of the electrode modifications present similar values of R_{CT}, 682.3, 785.1 and 816.8 Ω for chitosan PBS, AuNPs@rGO and modified chitosan respectively.

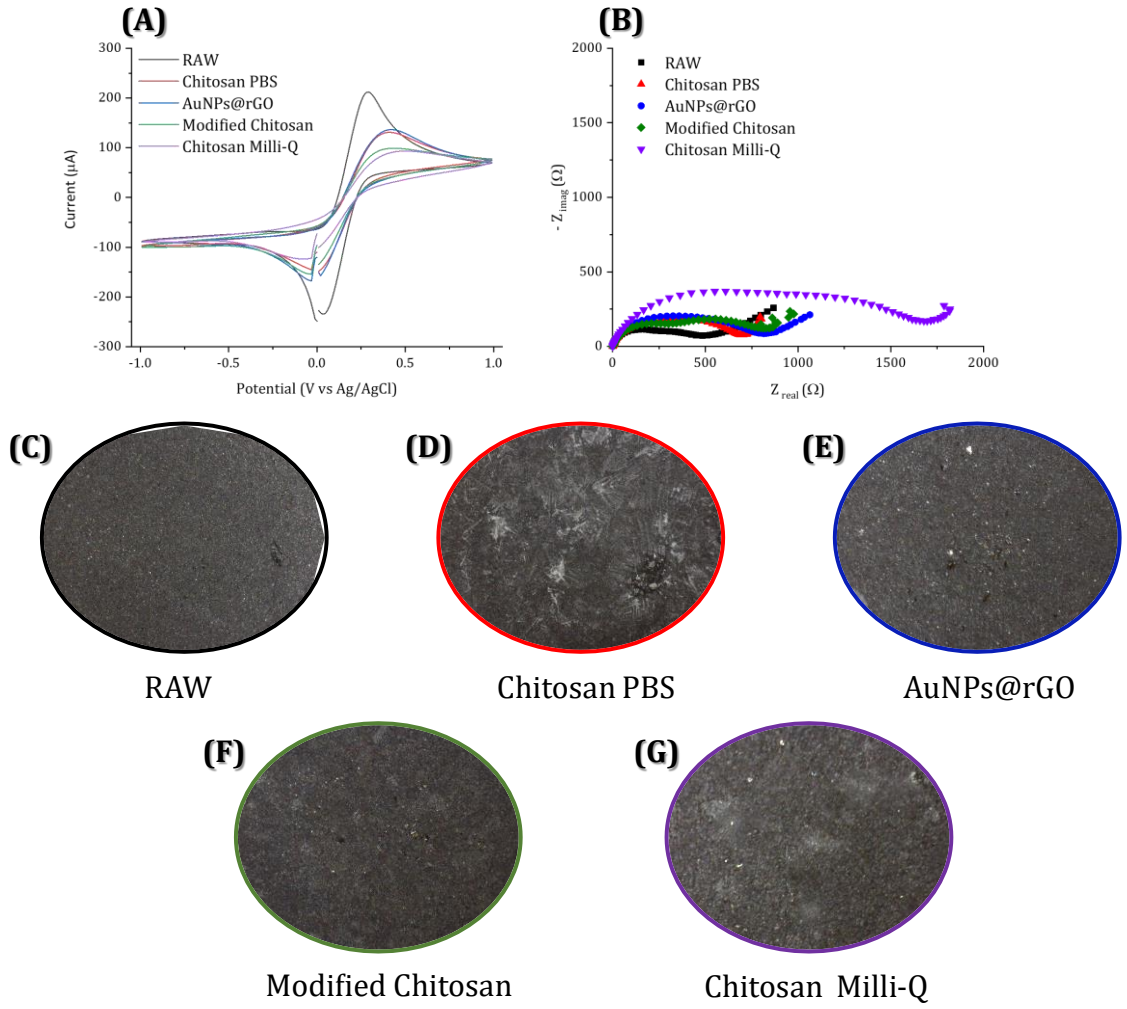

Figure 62. Electrochemical characterization of composite electrode modified with chitosan by (A) CV (v: 10 mV·s^{-1}) and (B) EIS. Optical microscope images (1:100 augments) (C) raw electrode surface, (D) Chitosan in PBS, (E) AuNPs@rGO dispersion, (F) Chitosan in AuNPs@rGO dispersion and (G) Chitosan in Milli-Q water.

Regarding the different aspects of the electrode modification in **Figure 62.D** up to **G,** this could be due the presence of salts, such as PBS or KCl.

4.3.4.6. Alginate

Alginate (AL) is also a compatible biopolymer with Psomes. It has been widely used in the immobilization of microorganisms [131]. To modify the composite electrode with alginate some solutions must be prepared: 4% Sodium Alginate (M: 10000-60000 g·mol^{-1} from Sigma Aldrich, St. Louis, MO, USA) and 1% $CaCO_3$ (≥99% from Fluka, Fisher Scientific SL, Madrid, Spain). The ratio of alginate:$CaCO_3$:PBS 10 mM pH 7.4, mixed for this test as 1:2:1, which was optimized in a previous work [132]. To the jellification step a potential of 1.5 V for different times, such as 90 s (1.5 min), 900 s (15 min), and 1800 s (30 min) were tested. Also, due to the viscosity of the alginate:$CaCO_3$:PBS solution, 20 µL was not possible to pipetting, and the volume was increased to 50 µL, which was the minimum amount able to be pipetted correctly. In **Figure 63.A** and **B** no differences in the response of the raw electrode and the one with the 90 s of jellification step were found. The electrodes with the 900 s and 1800 s of jellification step, also have similar electrochemical behaviour between them and both were better regard to raw electrode and modified with 90 s of jellification. For CV measurements of the 900 and 1800 s jellification time higher currents were obtained (**Figure 63.A**). These results are in accordance with a reduction of R_{CT} shown in **Figure 63.B**. The R_{CT} are 299.3 Ω for the raw electrode, 409.2 Ω for the Alginate PBS 90 s electrode, 124.1 Ω for the 900 s of jellification step electrode and 94.33 Ω for the 1800 s of jellification step electrode.

Alginate is a linear unbranched copolymer that contains different blocks of (1,4)-b-D-mannuronic acid, called block M and a-L-guluronic acid, named block G, which are covalently linked together in different sequences. The properties of the alginate gels depend on the jelling agent, which in this case is Ca^{2+}, that creates ionic bonds with G and M block increasing the conductivity [133].

At plain sight, as shown in **Figure 63.** from **C** to **F**, the surface of the electrode does not change significantly, except in the case of the **Figure 63.D**, that presents some salt crystals, probably from the PBS. In the other cases, the presence of salts it is not remarkable. According to these results, 900 s jellification time was selected for further experiments.

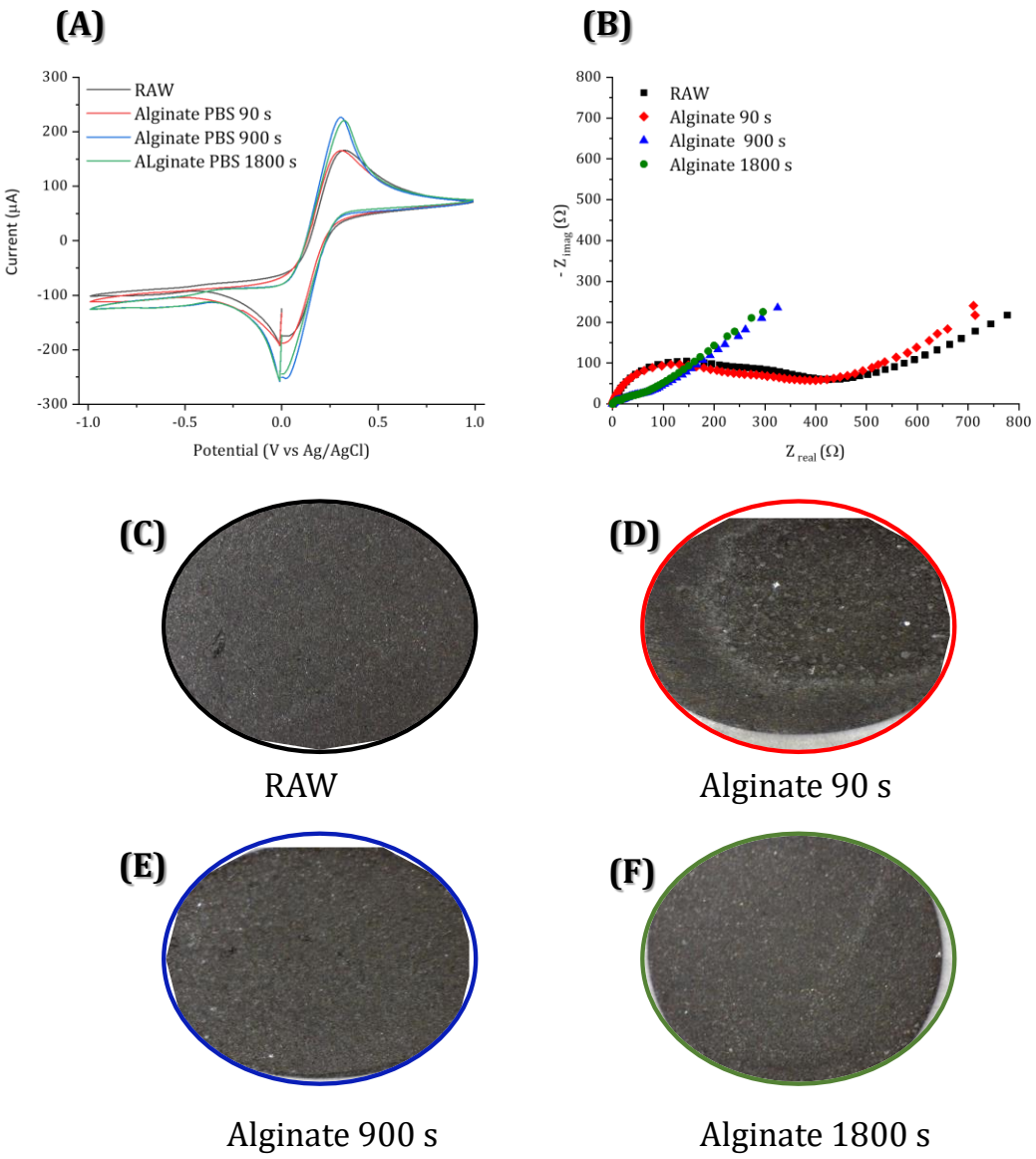

Figure 63. Electrochemical characterization of electrode modifications with alginate by (A) CV (ν: 10 mV·s^{-1}) and (B) EIS. Optical microscope images (1:100 augments) (C) raw electrode surface; and different times of jellification (D) 90 s, (E) 900 s, and (F) 1800 s.

The main difficulty of this modification with alginate was the assembly needed to perform the electrode jellification step (see **Figure 64**). This assembly was necessary, as even though the drop-casting was a viscous solution, when it contacts the deionized water (which has a higher concentration of ions than the Milli-Q water) the drop-casting was lost. So, to avoid that, some Teflon tape was wrapped around the electrode. The electrode is placed in a custom-made hole. The tape helps to seal the contents of the vessel from leaking. Slowly, the distilled water was added to the vessel with a pipette, trying to avoid the direct contact with the drop-casting.

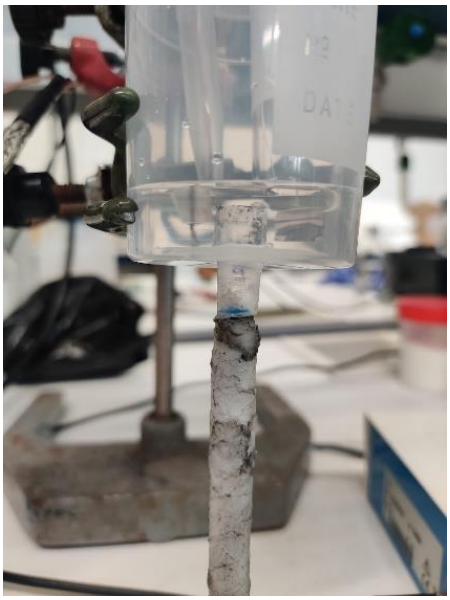

Figure 64. Assembly for the jellification step by applying 1.5 V.

To evade those troubles, a previous jellification step was added using a 1% $CaCl_2$ (>97%, from Panreac Química S.L.U.,Barcelona, Spain) [134]. Hence, when the drop-casting is done it is immersed in the $CaCl_2$ solution for 30 s and then the electrode is immersed and the jellification step using 1.5 V is followed.

As a summary, the modification procedure finally was done by using alginate, and following **Scheme 17**, where the jellification steps are properly included. So, alginate acts as supporting agent for capture and immobilize the elements necessary for the biosensor approaches.

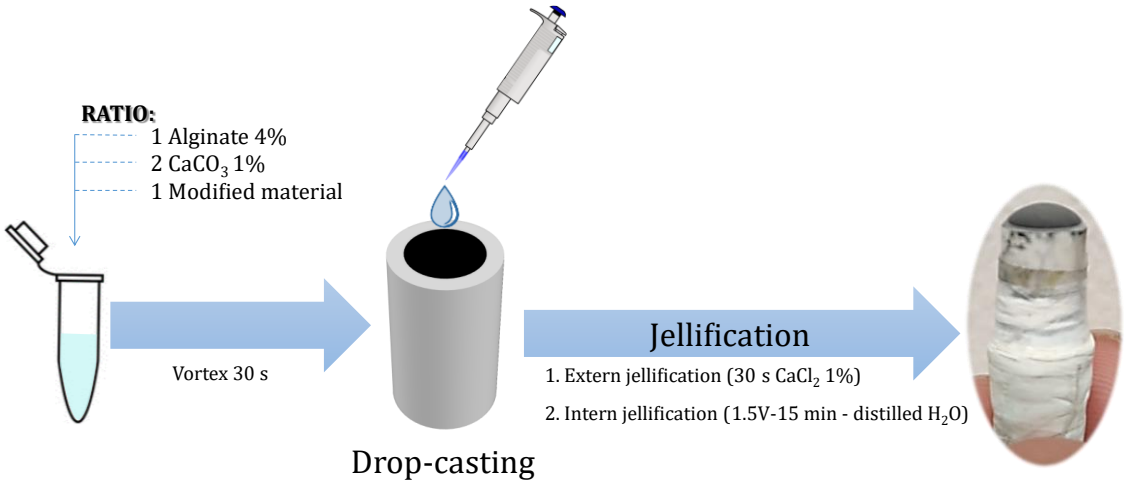

Scheme 17. Modification procedure of a composite electrode with alginate.

4.3.5. Synthesis of the complex hybrid nanomaterial

The next step was to prepare the hybrid material to modify the surface of the composite electrodes using alginate matrix. Many components were required, having all of them its function. The alginate is needed to improve the immobilization efficiency of the hybrid nanomaterial on the raw electrode surface; the thiol-β-Cyclodextrin (β-CD-SH) helps to enhance the interaction between the electrode's surface and Psomes by physical interaction [135]. AuNPs@rGO to anchor the β-CD-SH and to enhance the low conductive properties of the Psomes.

4.3.5.1. AuNPs@rGO synthesis and modification with β-Cyclodextrine

To enhance the low conductivity properties of the hybrid nanomaterial by Psomes presence, AuNPs@rGO was used. In **Chapter IV — Part I**, the synthesis of reduced Graphene Oxide (rGO) was explained at length, even now the reduction of the graphene oxide and the gold salt used to get the gold nanoparticles (AuNPs) is done simultaneously, following the next steps: 250 mL of 1 mg·mL^{-1} GrO/GO dispersion was prepared and sonicated for 1 h. Then, 0.709 g $HAuCl_4 \times 3H_2O$ (≥99.9%, Sigma Aldrich, Sat Louis, MO, USA) were added. After that, 250 mL Milli-Q water were also added, the final concentration of the $HAuCl_4$ is 0.0036 M. Gently and drop by drop, 250 mL of $NaBH_4$ 0.1 M (Analytical grade from Labkem, Labbox Labware, S.L., Barcelona, Spain) were added, and the solution is stirred for 1 h. To end, the final product was centrifuged at 3500 rpm and washed with Milli-Q water until neutral pH was obtained. The resulting solid was dried at 80 °C for 24 h [136], [137]. The complete process is summarized in **Scheme 18**.

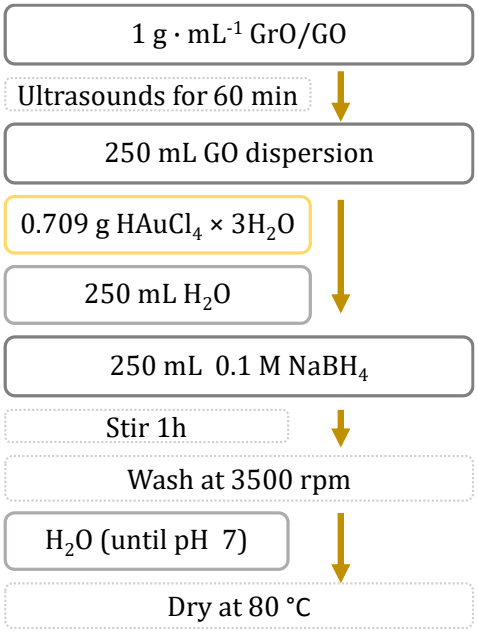

Scheme 18. Synthesis of AuNPs@rGO.

To anchor the Psomes on the electrode's surface, the prepared AuNPs@rGO were modified with β-CD-HS. It helps to enhance the interaction between the Psomes and the AuNPs@rGO [138].

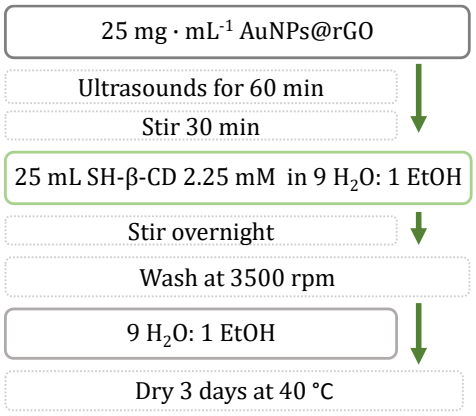

Scheme 19. Modification of the AuNPs@rGO with HS-β-CD.

First, 25 mL of 1 mg·mL^{-1} AuNPs@rGO dispersion in Milli-Q water was prepared using the ultrasound probe for 4 h. 25 mL of a 2.25 mM Heptakis-(6-deoxy-mercapto)-β-cyclodextrin (SH-β-CD, from AraChem, Tilburg, Netherlands) solution in 10% EtOH (≥99.8% Sigma Aldrich St, Louis, MO, USA) was prepared. The 25 mL prepared of each reagent were mixed and stirred overnight. Then the washing step was done by centrifuging and using a 10% EtOH solution. The solid is dried at 40 °C for 3 days [137]. The complete process is summarized in **Scheme 19**.

4.3.5.2. Modification of the β-CD-S-AuNPs@rGO with the Psomes

To prepare the hybrid nanomaterial used in the electrode modification, the one that contains the Psomes: a dispersion of 3.1 mg · mL^{-1} β-CD-S-AuNPs@rGO in Milli-Q water is prepared sonicating for 10 min. Then the solution of the Loaded Psomes was added in equal volume (500 µL of each solution) and were in contact for 24 h with constant stirring (the final volume was 1 mL). In **Table 27** there is a list of the electrode's modifications used.

Table 27. Summary of different modifications of the prepared β-CD-AuNPs@rGO material (500 µL). The percentages are given according to the volume contribution of GOx-Psomes (respect to 500 µL) and Empty-Psomes used in the modification. Total volume: 1 mL.

Name of the electrode	% GOx-Psomes	GOx-Psomes [µL]	Other [µL]
100% GOx-Psomes	100	500	-
75% GOx-Psomes	75	375	125 Empty-Psomes
50% GOx-Psomes	50	250	250 Empty-Psomes

In **Scheme 20**, the modification of the 100% GOx- Psomes is shown, and in the other modification cases, just it is needed the addition of the Empty-Psomes in the proportion indicated in **Table 27**.

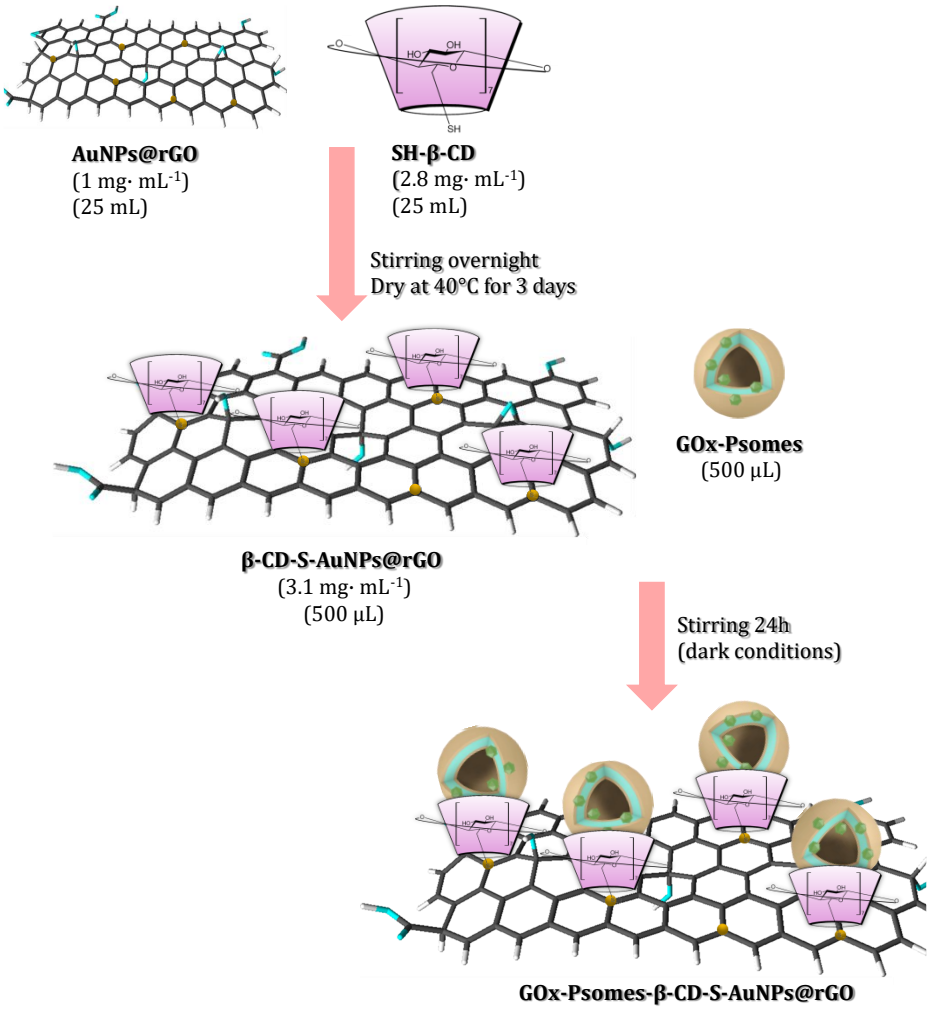

Scheme 20. Summarized hybrid nanomaterial preparation containing GOx-Psomes.

At the end the electrodes were modified following the **Scheme 17**, using the solution prepared before with the Psomes instead of PBS in the ratio 1:2:1 of alginate:$CaCO_3$:PBS. Then, an improved conductive hybrid nanomaterial, Psomes-β-CD-S-AuNPs@rGO/Alginate was obtained.

4.3.5.3. Morphological characterization of the GOx-Psomes electrode

After preparing the hybrid nanomaterial to modify the surface of the composite electrodes, this novel nanomaterial was characterized by different techniques to achieve an properly understanding its properties. The mapping of Au of the synthesized nanomaterials indicates a high presence of this metal, that is confirmed with the ICP-OES results: AuNPs@rGO presents 49 ± 15% (**Figure 65.A**) while in the hybrid nanomaterial, GOx-Psomes-β-CD-S-AuNPs@rGO, was 7.0 ± 0.7% of Au (**Figure 65.B**). The SEM reveals that alginate (AL) (**Figure 65.C**) presents a rugose surface after all the jellification steps. The presence of alginate seems to increase the difficulty of finding AuNPs as is shown in **Figure 65.D** and **G**,

due to the layers that are formed. The retrodispersive (**Figure 65.E** and **H**) and the EDX (**Figure 65.F** and **I**) both confirmed the presence of Au in both cases (see red circle in **Figure 65. E** and **H**).

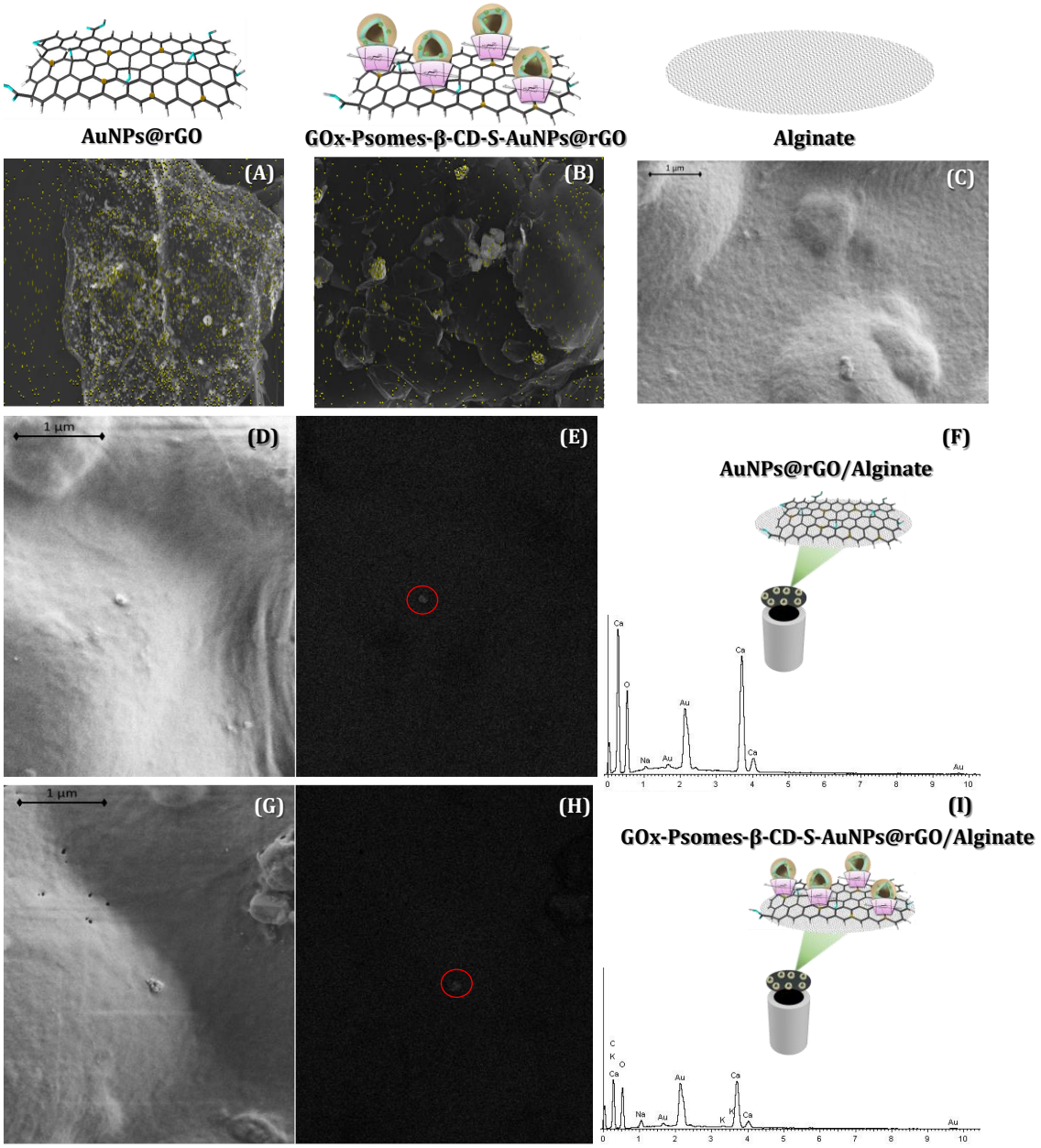

Figure 65. SEM images: mapping of Au (yellow) of (A) AuNPs@rGO material and (B) GOx-Psomes-β-CD-S-AuNPs@rGO material, (C) Secondary electron SEM image of alginate. Secondary electron SEM image(D) and (G) retrodispersive(E) and (H), and EDX graph(F) and (I) of AuNPs@rGO/AL electrode and GOx-Psomes-β-CD-S-AuNPs@rGO/AL electrode, respectively.

4.3.5.4. Electrochemical characterization of the GOx-Psomes-β-CD-S-AuNPs@rGO/AL electrode

The electrochemical characterization was firstly carried out by means of CV using $[Fe(CN)_6]^{3-}/[Fe(CN)_6]^{4-}$ redox probe. The method provided information about the

electroactive area (A) of the sensor and the charge transfer resistance (R_{CT}) was estimated using the *Randles-Sevčik* equation (**Equation 6**) which is appropriate for the electron-transfer controlled process (see **Figure 66**). The contribution of all the nanomaterials in the hybrid material to the electrochemical response were studied separately. Different raw electrodes were modified only one component at time. In all materials studied, the ratio of AuNPs@rGO was kept constant to prevent it from affecting the response of the modified composite electrode.

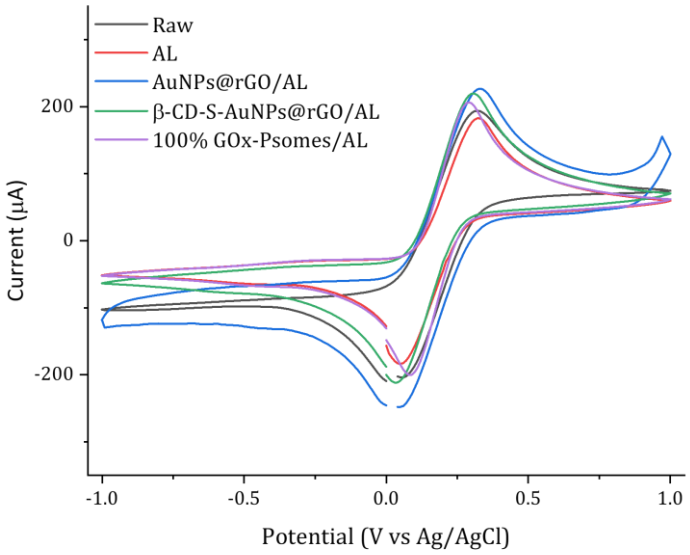

Figure 66. Electrochemical characterization by CV of each component in the hybrid nanomaterial (ν: 10 mV·s^{-1}).

The R_{CT} was calculated using the Tafel diagrams because is related to the exchange current (i_0) (**Equation 7**), in **Chapter III: Materials & Methods**) which give information about the reversibility of the process. i_0 can be determined using this diagram (see **Figure 67**).

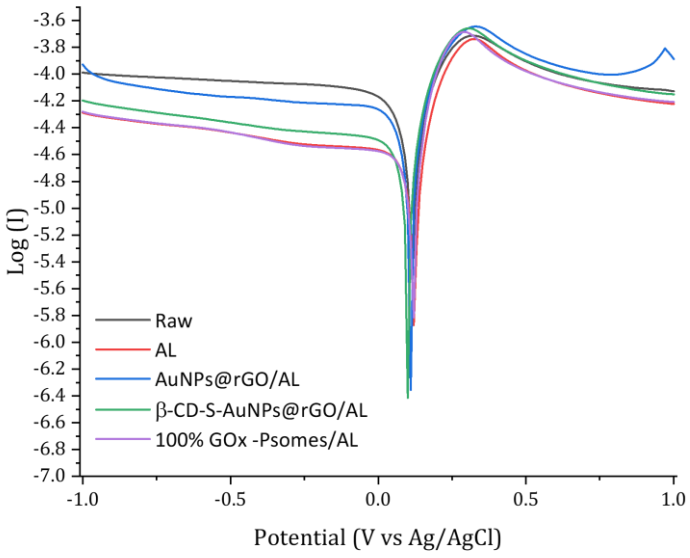

Figure 67. Tafel diagrams of each component in the hybrid nanomaterial.

The electroactive area (A) of each modification of the raw electrode with individual components of the hybrid nanomaterial and R_{CT} was calculated and collected in **Table 28**.

Table 28. Electroactive electrode areas (A) and charge transfer resistance (R_{CT}) determined of each component material used in the functionalization of the composite electrode.

Electrode	A [cm^2]	R_{CT} [Ω]
Raw (15% graphite)	0.36	6707.82
Alginate (AL)	0.34	8564.09
AuNPs@rGO/AL	0.43	8216.39
β-CD-S-AuNPs@rGO/AL	0.40	8324.94
100% GOx-Psomes/AL	0.38	9357.96

All electrode modifications with different components of the hybrid nanomaterial present similar electroactive areas, except for the AuNPs@rGO/AL modified electrode (0.43 cm^2). This difference and the lower R_{CT} (8216.39 Ω) could be related to the increasing of non-modified conductor (AuNPs@rGO) which seems that increases the roughness of the electrode surface and improves the electronic transference of the composite material. But when the modification goes further with β-CD-SH, the resistance to the charge transfer increases, since it is not as good conductive material. Also, comparing the raw electrode (15% graphite) with just the AL gel as modification, it seems that the presence of AL in the surface of the electrode does not significantly modify the electroactive area, but it gets worse as the electronic' transference and R_{CT} increases. Furthermore, the total modification with the complete hybrid nanomaterial (100% GOx-Psomes/AL) also increase the R_{CT} that means that the modification slightly affects the flow of electrons through the nanomaterial. In summary, the R_{CT} of the composite electrode increase after the modification procedure with each component of the nanomaterial respect the raw electrode. Except, for the modification only of AuNPs@rGO/AL which presents the lowest R_{CT} of the modified composite electrodes. In addition, an increase of the R_{CT} in the complete modification with the GOx-Psomes is observed probabl, due to the addition of non-conductive material.

4.3.6. Chronoamperometry

Chronoamperometry is one of the voltammetric techniques most applied in the field of electrochemical sensors. It is a time-dependant technique, and it consists in the study of the current generated along time at a potential applied (working potential) previously fixed (see **Figure 68**).

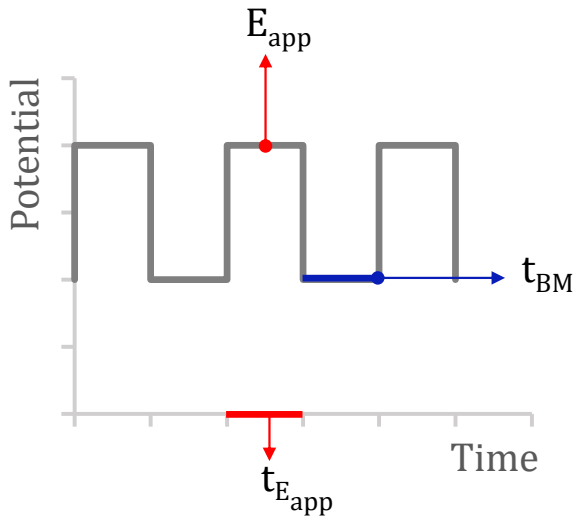

Figure 68. Excitation potential signal of the chronoamperometry technique applied. Where E_{app} is the potential applied, t_{Eapp} is the time which the potential applied and t_{BM} is the time between measurements.

To fix this potential a CV in the presence of the analyte is performed in a suitable medium. Usually, chronoamperometry is performed with no stirring, and the main matter transport mechanism is by diffusion, where the movement is done by the chemical potential gradient, and by migration, which is the effect of the electric concentration gradient. In presence of a support electrolyte the effects of the migration may be bypassed. This behaviour follows *Cottrell* equation (**Equation 17**). So, the current decays according to the inverse of the square root of time.

$$i = nFAC_a\sqrt{D_\alpha/\pi t} \qquad \textbf{(Equation 17)}$$

Where:

i: current (A)

n: mols of electrons transferred per mol of analyte.

F: Faraday constant (96485 C·mol^{-1})

A: electroactive area (cm^2)

C_a: electroactive specie concentration (mol·cm^3)

D_α: diffusion coefficient of the electroactive specie (cm^2·s^{-1})

π: number pi (3.1416)

t: time (s)

Otherwise, in a well-stirred solution it always will be substrate to produce the reaction and maintain the current of the electrode because of a constant diffusion layer is fixed [98], which will be helpful to detect the low analyte concentration. In **Figure 69**, there is an example of the measurement using 100% GOx-Psomes/AL sensor performed by the consecutive addition of glucose $6{\cdot}10^{-3}$ M to PBS 10 mM pH 7.4 with gentle stirring, the E_{app} is 1.4 V, the t_{Eapp} is 60 s and the time between measurements is 5 min. The data treatment is performed by doing the average of the values from the ten points between the seconds 29 and the 30, where the current is stable. The potential applied and the stirring will be studied in more detail.

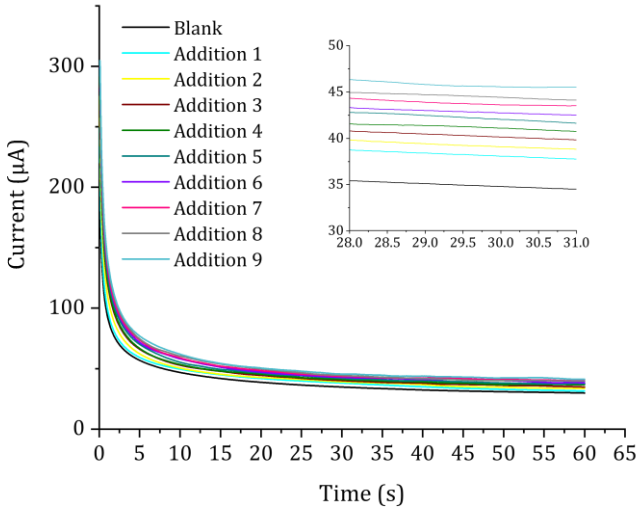

Figure 69. Chronoamperometry measurement using 100% GOx-Psomes/AL sensor performed by the consecutive addition of glucose $6{\cdot}10^{-3}$ M to PBS 10 mM pH 7.4. Experimental conditions: gentle stirring; E_{app}= 1.4 V, t_{Eapp}= 60 s and t_{bm}= 5 mins.

4.3.7. Optimization of the measurement's conditions

For the electroanalytical measurements several parameters were optimized, such as working potential, diffusion layer control (stirring), pH medium, response time, repeatability, reproducibility and % GOx-Psomes in the hybrid nanomaterial.

4.3.7.1. Potential applied

To optimize the potential applied, several CV in different conditions were performed to determine the response of the sensor modified with all the components of the hybrid nanomaterial. The first measurement in 10 mM PBS at pH 7.4 media (as a blank) and then in the presence of glucose $7{\cdot}10^{-5}$ M, which is the substrate of the enzyme and therefore the target analyte. In **Figure 70.A** the response of the system in PBS was checked as blank signal for all sensors. This signal corresponds to the residual current and the H_2O oxidation.

AuNPs@rGO/AL sensor presents the highest response, due to the highest electroactive area (0.43 cm^2) and the lowest charge transfer resistance (8216.39 Ω), compared to the rest of modified electrodes (see **Table 28**). On the other hand, in **Figure 70.B** the higher response in presence of glucose was given by the 100% GOx-Psomes/AL (GOx-Psomes-β-CD-S-AuNPs@rGO/Alginate) sensor because of the oxidation produced by the enzymatic reaction obtaining H_2O_2.

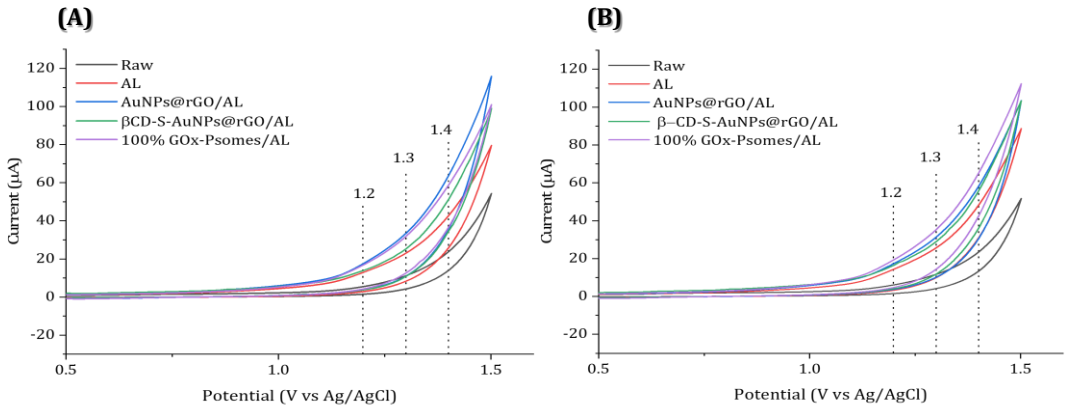

Figure 70. Cyclic voltammetry for the different electrode modifications tested in (A) PBS 10 mM at pH 7.4, and (B) $7 \cdot 10^{-5}$ M Glucose in PBS 10 mM at pH 7.4 (ν: 10 $mV \cdot s^{-1}$).

Furthermore, the maximum current differences between the blank (**Figure 70.A**) and the glucose measurements (**Figure 70.B**) were observed at 1.2 V, 1.3 V and 1.4 V (dotted line). In **Figure 71** it can be seen the response obtained for the100% GOx-Psomes/AL sensor in PBS (blank) and the PBS with glucose. At potentials applied higher than 1.2 V differences were observed.

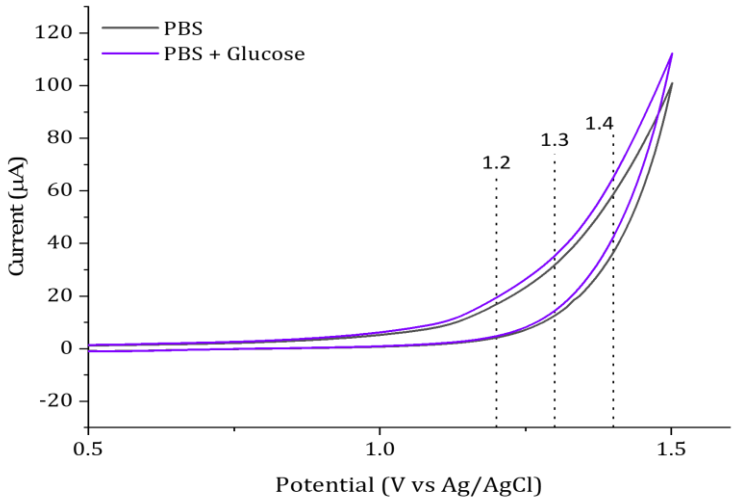

Figure 71.Comparative CV of the 100% GOx-Psomes/AL sensor in absence of glucose (black) and in presence of glucose (purple). (ν: 10 $mV \cdot s^{-1}$)

To ensure the response at each potential selected before, some calibration curves were performed using the 100% GOx -Psomes sensors. In **Figure 72**, differences in the response at different potentials can be noticed. At 1.2 V non-significant differences were observed when the concentration of glucose increased. At 1.3 V a slight slope is observed. At potential 1.4 V, the best performance and higher currents were achieved. Moreover, for all potential studied, the signal presents a saturation zone around $2 \cdot 10^{-4}$ M of glucose. Therefore, the potential 1.4 V was selected for chronoamperometry experiments.

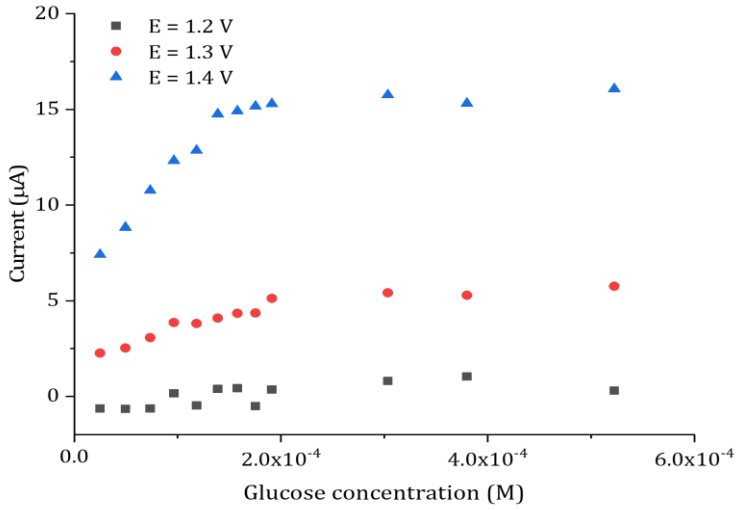

Figure 72. Study of the potential applied: 1.2 V (■); 1.3V (●) and 1.4 V(▲) using 100% GOx-Psomes/AL sensor performed by the consecutive addition of glucose $6 \cdot 10^{-3}$ M to PBS 10 mM at pH 7.4. Experimental conditions: gentle stirring, E_{app}= 1.4 V, t_{Eapp}= 60 s, and t_{bm}= 5 mins.

4.3.7.2. Chronoamperometry conditions

As was explained, chronoamperometry can be used without or with stirring while the measurement is performing to control the diffusion layer. In **Figure 73** is shown that a constant gentle stirring resulted in a better analytical response, as expected because of the thickness of diffusion layer was constant during the measurement time.

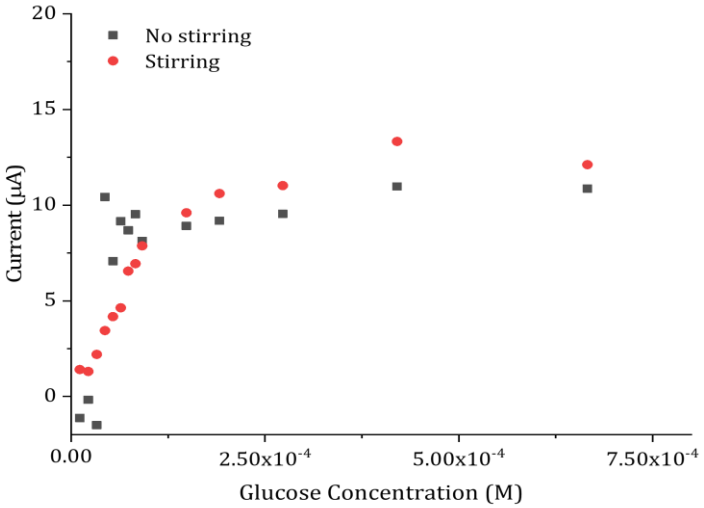

Figure 73. Diffusion layer study (stirring or not) using 100% GOx-Psomes/AL sensor performed by the consecutive addition of glucose $6 \cdot 10^{-3}$ M to PBS 10 mM at pH 7.4. Experimental conditions: gentle stirring, E_{app}= 1.4 V, t_{Eapp}= 60 s, and t_{bm}= 5 mins.

4.3.7.3. pH and time of measurement

To study the effect of the pH, the PBS solution was adjusted to different pH: 5.5, 6.0, 7.4 and 8.0 and experiments were running at two different concentrations solutions of glucose. The first one at low level ($4 \cdot 10^{-5}$ M of glucose) and another with a higher amount ($7 \cdot 10^{-5}$ M of glucose). Usually, in the Amplex ™ Red assay the samples were measured every 10 minutes. To reduce the analysis time spent in this assay, the product of the enzymatic reaction, hydrogen peroxide, was measured every 5 minutes until it reached the saturation response of the sensor. For the lower concentration 120 min were necessary until the saturation was reached, and 90 minutes for the higher concentration of glucose. As can be observed in **Figure 74.A**, for the lower concentration, there are two groups of results with two different behaviour: on one hand pH 5.5 and 6.0 results show similarities, and on the other hand, pH 7.4 and pH 8.0 have also similarities. At higher glucose concentrations (**Figure 74.B**), the response at pH 5.5 and pH 6.0 were significantly different from previous one and in contrary pH 7.4 and 8.0 a similar behaviour as at low glucose concentration is observed. At pH 5.5 the saturation is reached immediately.

Thus, pH 7.4 was the selected one due to its proximity to the physiologic pH. Furthermore, 5 min, is time enough for the enzymatic reaction to be produced, so to be able to detect the increase of the hydrogen peroxide that gets accumulated.

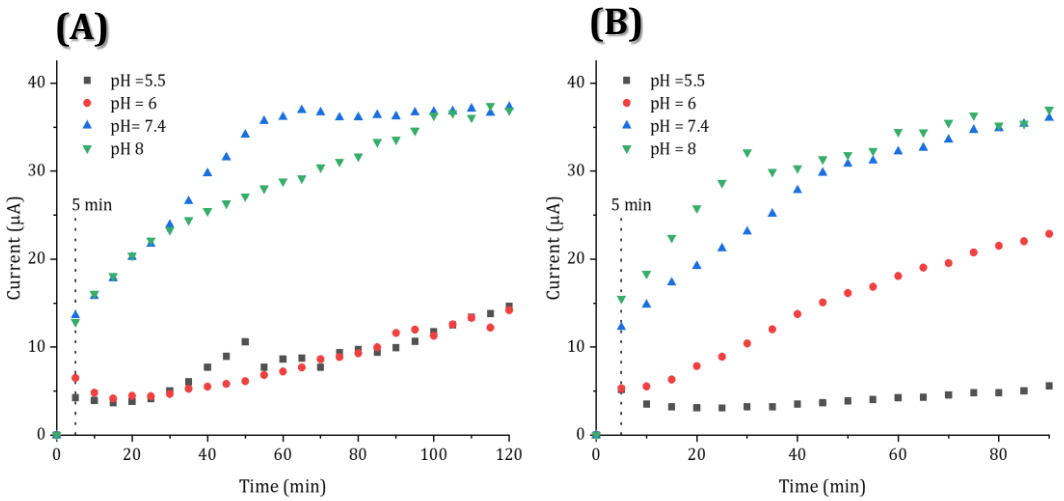

Figure 74. Chronoamperometric measurements every 5 min of (A) low ($4 \cdot 10^{-5}$ M) and (B) high ($7 \cdot 10^{-5}$ M) concentration of glucose at different pH using 100% GOx-Psomes/AL sensor in PBS. Experimental conditions: gentle stirring, E_{app}= 1.4 and V, and t_{Eapp}= 60 s.

Once the parameters of the measurements were settled, several calibration curves with the modified sensors with different compositions (see **Table 27**) were performed at 1.4 V, smooth stirring and at pH 7.4. All the data is summarized in **Table 29.**

Table 29. Summary of the calibration curves parameters using GOx-Psomes sensors: sensor composition, sensitivity and R^2.

Sensor [% GOx-Psomes]	% Empty Psomes	Sensitivity [µA·M^{-1}]	R^2	y- intercep [µA]
100	-	119641.02	0.999	0.61
		91453.70	0.970	-0.22
		113270.13	0.990	0.08
		181181.71	0.998	-0.09
		110789.68	0.995	0.20
Average		123267 ± 34040		0.12±0.32
75	25	49023.92	0.980	
		45153.76	0.990	
		44217.01	0.910	
Average		46132 ± 2548		
50	50	19297.69	0.980	
		15816.10	0.990	
		16550.23	0.920	
Average		17221 ± 1835		

Although this study is presented as a proof of concept and not as a glucose (bio)sensor, some analytical parameters were determined based on the test performed using 100% GOx-Psomes/AL sensor.

The detection limit (DL) was $6 \cdot 10^{-6}$ M and it was calculated using **Equation 18.**

$$DL = {}^{3 \cdot sd_y}/_{m} \qquad \textbf{(Equation 18)}$$

Where:

sd_y: standard deviation of the y-intercept

m: the slope of the calibration curve

The quantification limit (QL) was $3 \cdot 10^{-5}$ M and it was calculated using **Equation 19.**

$$QL = {}^{10 \cdot sd_y}/_{m} \qquad \textbf{(Equation 19)}$$

Where:

sd_y: standard deviation of the y-intercept

m: the slope of the calibration curve

The linear range of the 100% GOx-Psomes/AL sensor was verified experimentally, and it includes from $3 \cdot 10^{-5}$ to $2 \cdot 10^{-4}$ M as the first (QL) and last concentration of the linear response.

4.3.7.4. Reproducibility in the electrode fabrication

To evaluate the reproducibility of the modification strategy, a new batch of hybrid nanomaterial (using 100% GOx-Psomes), was prepared, and then four different electrodes customized with it (100% GOx-Psomes/AL sensors). Then a solution of $7 \cdot 10^{-5}$ M of glucose was measured for 1 hour and for the four electrodes tested similar response was obtained. In **Figure 75**, the average of the sensor's measurements (n=4 sensors) for every measurement at each time is represented, giving an average slope of 0.37 ± 0.05 $\mu A \cdot min^{-1}$. It can be proven that the experimental uncertainty of the measurements is maintained over time and is of the order of ± 5 μA.

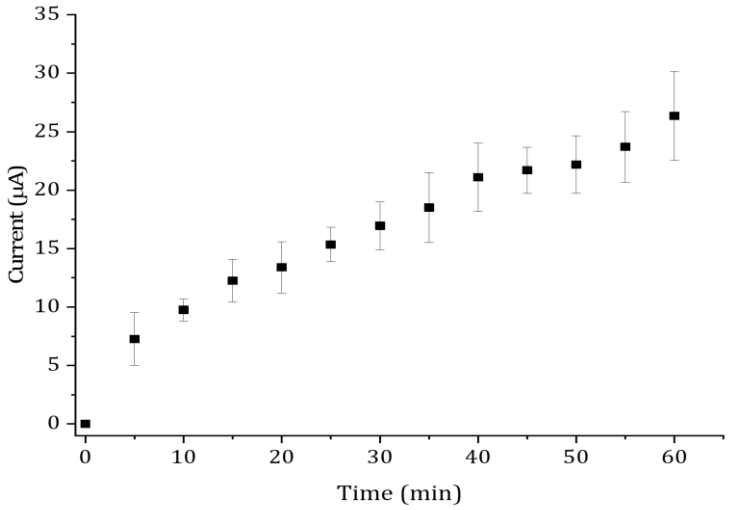

Figure 75. Reproducibility study (n = 4) using 100% GOx-Psomes/AL sensor measured in a solution of glucose $7 \cdot 10^{-5}$ M in PBS 10 mM pH 7.4. Experimental conditions: gentle stirring, E_{app}= 1.4 V, t_{Eapp}= 60 s, and t_{bm}= 5 mins.

4.3.7.5. Composition effect on the hybrid material

Different ratios of GOx-Psomes in the hybrid nanomaterial were tested (100, 75 and 50%) (see **Table 27** for the preparation). The % Response enables the comparation of the sensitivities obtained by several sensors modified with different amounts of GOx-Psomes (n=5 for 100% and n=3 for 75 and 50%). It is calculated by normalizing the sensitivities by the average obtained using the 100% GOx-Psomes/AL sensors (which is 123267 ± 34040 $\mu A \cdot M^{-1}$). As was expected, a decrease in the sensitivity of the sensors was observed when the % of GOx-Psomes in the hybrid nanomaterial decreased (**Figure 76**). This fact can be used to modulate the response of the modified sensors.

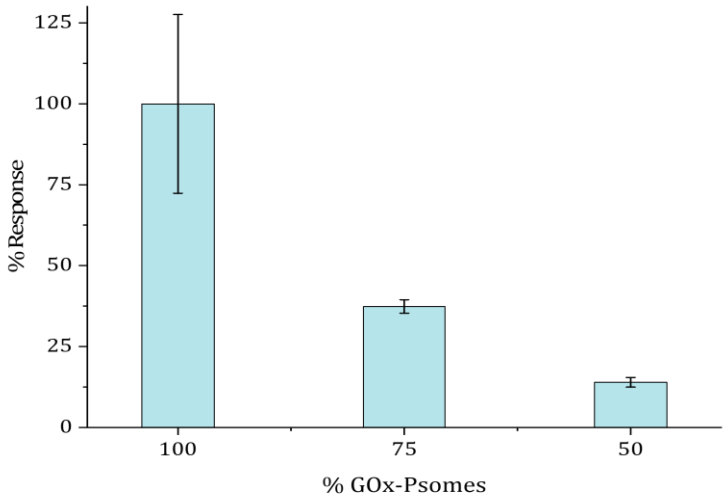

Figure 76. Comparison in the sensitivities for different % of GOx-Psomes in the electrode's modification (n = 5 for 100% GOx and n = 3 for 75 and 50%).

4.3.7.6. AuNPs outcome

Nanozymes are nanomaterials with enzyme-like behaviour. AuNPs can act as a nanozyme, whose behaviour is influenced by pH. The nanozyme presents oxidative-like behaviour in acid media, otherwise in basic media presents peroxidase-like activity. So, changing the pH of the media, the catalytic activity of the AuNPs can be modulated. Furthermore, the size, shape, composition, and modification of AuNPs must be controlled, otherwise it can lead to the loss of their catalytic activity [76].

Some electrodes modified using the synthesized AuNPs@rGO (0.3 $mg \cdot mL^{-1}$) and the alginate (AuNPs@rGO/AL sensors) were tested This modification was done to achieve the maximum response, because when the AuNPs are modified a decrease in the catalytic activity was notice [76]. The results were summarized in **Figure 77**, in any case there is a saturation zone, like the previous results found, which includes the electrodes modified with the hybrid nanomaterial.

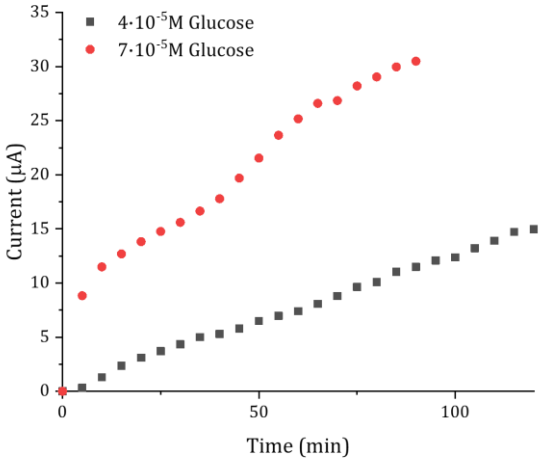

Figure 77. AuNPs effect in PBS 10 mM pH 7.4 and two different concentration of glucose using AuNPs@rGO/AL sensor. Experimental conditions: gentle stirring, E_{app} = 1.4 V, t_{Eapp}= 60 s, and t_{bm}= 5 min.

4.3.7.7. Real samples

Additionally, some sample analyses were followed by using the 100% GOx-Psomes/AL sensors and the results were compared with the ones provided by the bioanalyzer YSI 2700 Select. The recovery values were calculated from the quotient between the result obtained using the 100% GOx -Psomes /AL electrode and the one obtained using the commercial equipment method (see **(Equation 20)**.

$$\% \text{ Recovery} = {[C]_{100\%GOx-Psomes/AL}}/{[C]_{Bioanalyzer\ YSI\ 2700}} \cdot 100 \qquad \textbf{(Equation 20)}$$

Where:

$[C]$ = concentration obtained from different methods.

⌘ Synthetic samples

First, the analysis of synthetic samples prepared on PBS tampon spiked with glucose (**Figure 78**) was performed by triplicated using the optimal operation conditions and three different electrodes: 1.4 V, soft stirring, and performing each addition every 5 minutes.

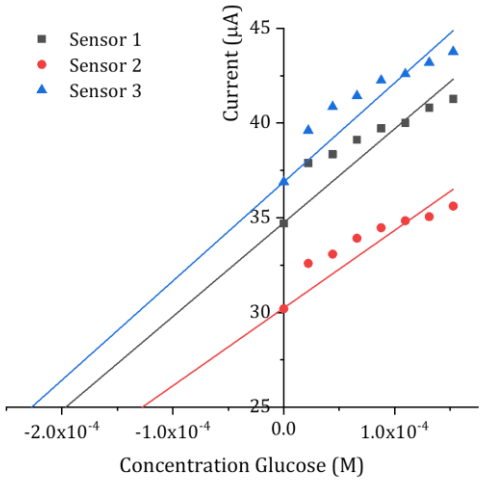

Figure 78. Calibration curve by standard addition method for three different electrodes for spiked samples analysis using 100% GOx-Psomes/AL sensor. Experimental conditions: 1.4 V, 5 min between additions, stirring, and PBS 10 mM at pH 7.4.

The results and the recovery were gathered in **Table 30** and compared (recovery) with the result obtained from the average of the three measurements of the commercial method. As can be seen, using the 100% GOx-Psomes/AL sensor good results are obtained, comparing with the method used here as reference (bioanalyzer YSI 2700 Select).

Table 30. Results of the standard addition method to analyze the spiked samples using three different sensors of the 100% GOx-Psomes/AL. Comparison with the method use as reference. The recovery values were calculated from the quotient between the average result of our sensors and the commercial method result. Experimental error is calculated as standard deviation.

Measured glucose [M]·10⁴	**Reference method** [M]·10⁴	**Recovery** [%]
1.56	1.50 ± 0.2	106 ± 3
1.64		
1.57		

⌘ Hypertonic glucose serum sample

40% Hypertonic glucose serum was analyzed using AuNPs@rGO/AL and 100% GOx-Psomes/AL sensors. The results of the calibration curves of three replicates are shown in **Figure 79** for each analysis, and the concentration obtained using different sensors were summarized in **Table 31**.

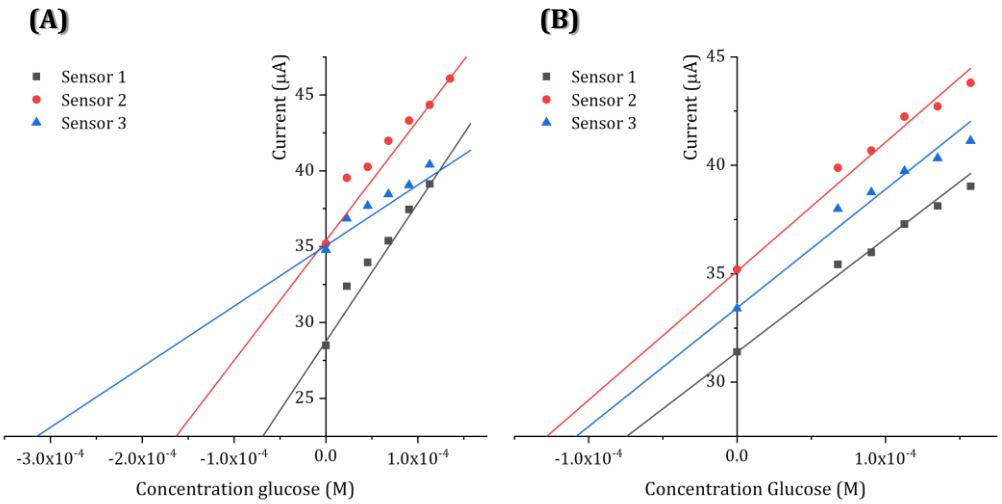

Figure 79. Real sample analysis of hypertonic glucose serum by standard addition method using three different electrodes (A) AuNPs@rGO/AL electrodes and (B) 100% GOx-Psomes/AL sensors. Experimental conditions: 1.4 V, 5 min between additions, stirring, and PBS 10 mM at pH 7.4

Table 31. Results of the sample analysis by standard addition method, comparison with a reference method and the recovery values. The sample was measured three times with two type of electrodes. Experimental error is calculated as standard deviation.

Sensor	Measured glucose [M]·10⁴	Reference method [M]·10⁴	Recovery [%]
AuNPs@rGO/AL	0.722	1.53±0.03	73 ± 30
	1.63		
	1.02		
100% GOx-Psomes	1.37		89 ± 2
	1.40		
	1.31		

As was mentioned before, at pH 7.4 AuNPs present nanozymatic behavior on the oxidation of the glucose, but the response of the sensors with only these nanoparticles in same operational conditions looks like had not sufficient catalytic effect [76], [81], probably due to the size and shape of the NPs and the non-optimal pH. This could be observed in the recovery values collected in **Table 31**, which presents random performance, with a 30%

variation between the three measurements. On the contrary, the 100% GOx-Psomes/AL sensor shows enhanced response compared with the reference method and also compared with AuNPs modified electrode.

4.3.8. Concluding remarks

In **Figure 80**, there is a graphical summary of the studies performed in this chapter. Several tests were performed over the previously optimized 15% graphite electrode. Some tapes and polymers of different nature were tested to immobilise Psomes, and the one chosen was alginate. Alginate is a natural polymer, which can be tuned with the Psomes properties following several steps to achieve the successful modification of the electrode surface.

AuNPs may have nanozymatic effect, which could contribute to the better performance of sensor. When checked, it was found that they are not effective enough on their own, at the conditions selected.

The optimization of the parameters to perform the measurements using chronoamperometry was performed. The optimum experimental conditions were: 1.4 V as potential applied, PSB 10 mM medium at pH 7.4, measurements under gentle stirring and perform a measurement every 5 min after the substrate addition, which is time enough for the enzymatic reaction to take place.

This developed sensor is a proof of concept as can be used as biosensor and was not designed to perform analytical measurements as glucose sensor, which was only used as target molecule to proof the effectiveness of the developed hybrid nanomaterial. So, the hybrid nanomaterial allows the effective modification of composite electrodes. Furthermore, open a way to real samples analysis based on enzymatic reactions.

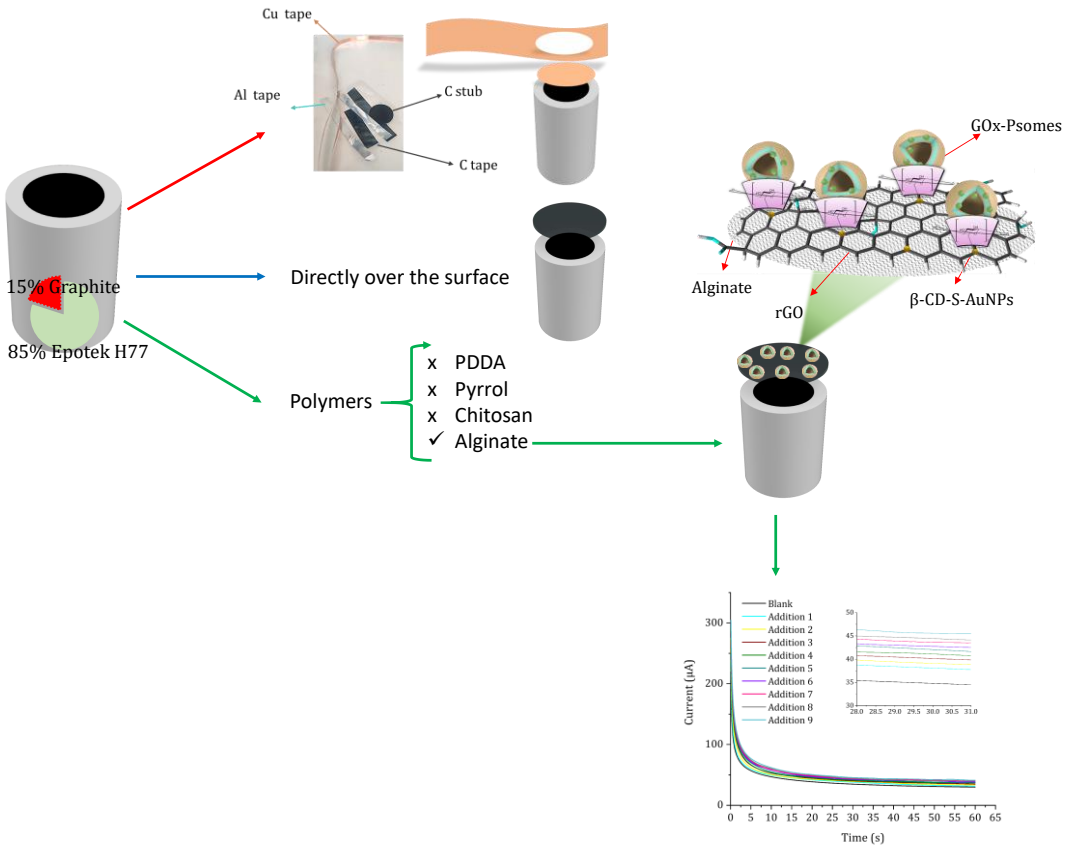

Figure 80. Graphical summary of the main results of Chapter IV — Part III.

Chapter IV

Cascade reaction over the modified composite electrodes

This work has been done in collaboration with the Bioactive and Responsive Polymer department, from the Leibniz-Institut für Polymerforschung Dresden e.V.

Part of the content of this work has been submitted in the paper « *Multicompartimentalized Electrochemical Sensing Platforms for Monitoring Cascade Enzymatic Reactions*» (Under Revision)

‡

4.4. Cascade reaction

A cascade reaction, also known as tandem or domino reaction, implicates two or more reactions that are subsequent, and each reaction can only start when the previous reaction step is completed [139].

It is important to distinguish between the cascade mode and the cascade reaction. The cascade mode is defined as how the reactions steps are organized, if all the enzymes are since the beginning, if they are added or if it is needed to isolate the product to continue the reaction. The cascade type reaction gives information about the interconnexion between the reactions, for example if the product of one reaction is the substrate of the next one or the cofactor, etc. In **Figure 81** a schematic summary of every cascade mode and type reaction is shown [139], [140], [141].

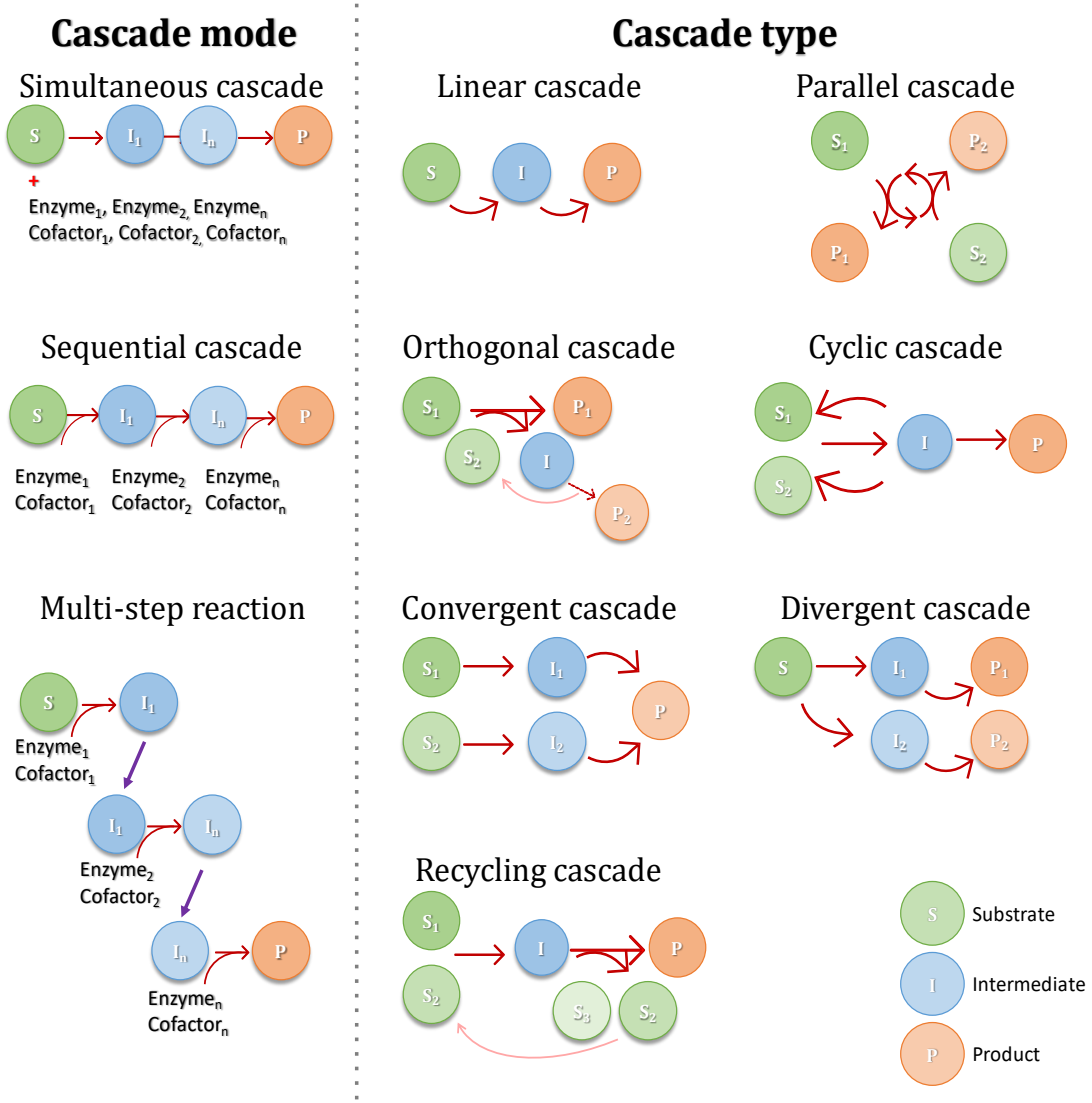

Figure 81. Cascade *modes* and *types* of reaction.

Mostly, there three types of cascade *mode*:

- **Simultaneous cascade**: all the reaction components are added at the same time in the reaction vessel and after reaching the end point the final product is isolated.
- **Sequential cascade**: the reaction steps are separated either in time or space, but only the final product is separated.
- **Multi-step reaction**: more than one isolation step is required.

There can be different interconnexion between the catalytic steps (cascade *types*).

- **Linear cascade**: a single product is synthetized via one or more catalytic steps.
- **Parallel cascade**: two enzymatic reactions are coupled through cofactors.
- **Orthogonal cascade**: product formation is coupled with cofactor regeneration or with the destructive removal of products.
- **Cyclic cascade**: combination of substrates is transformed into product and intermediate, while the intermediate is converted back to the substrates.
- **Convergent cascade**: two intermediates are formed in a linear way, then they are combined to one product.
- **Divergent cascade**: two intermediates are converted into two different products.
- **Recycling cascade**: a product can be used as substrate for a previous reaction step.

In this work, the target analyte is glucose, which is electrochemically detected indirectly, as H_2O_2, which is an electroactive specie. In cascade reaction, the first reaction is catalysed by Glucose Oxidase (GOx) and H_2O_2 is produced (**Equation 21**), shows the free enzyme reaction**).** The second step of the cascade is the consumption of H_2O_2 (free enzyme reaction in **Equation 22**) by Catalase (CAT).

$$C_6H_{12}O_6(Glucose) + O_2 + H_2O \rightarrow C_6H_{12}O_7(Gluconic\ Acid) + \boldsymbol{H_2O_2} \quad \text{GOx} \quad \textbf{(Equation 21)}$$

$$2\,\boldsymbol{H_2O_2} \rightarrow 2\,H_2O + O_2 \quad \text{CAT} \quad \textbf{(Equation 22)}$$

As was explained before, this is a simultaneous linear cascade, all the reagents are added at the beginning in the same pot (one pot reaction) and the product of the first reaction is the substrate of the second one. But, in the application as an electrochemical sensor, the one that is going to be measured is not the final product, it is the H_2O_2, which is an intermediate.

These enzyme cascade reactions are widely used in electrochemical biosensors in different areas, in **Table 32** there are some examples.

Table 32. Examples of electrochemical biosensors based on cascade reactions.

Analyte	Technique	Electrode	Immobilization	Enzymes	Application	Ref.
Proteins	Conductimetry	Au IDE[18]	In a membrane	Proteinase + Pronase	Biological research	[142]
	Amperometry	Pt electrode	In a membrane	Trypsin + Leucine aminopeptidase	Investigation of bioprocesses	[143]
Sucralose	Conductimetry	Au IDE	In a membrane	Invertase + Mutarotase + GOx	Food quality control	[144]
Lactose	Conductimetry	Au IDE	In a membrane	β-Galactosidase + Mutarotase + GOx		[145]
Maltose	Conductimetry	Au IDE	In a membrane	α-Galactosidase + GOx		[145]
L-Malic Acid	Amperometry	Au disk electrode	Deposition and immobilization using a dialysis membrane	L-Malate dehydrogenase + Diaphorase	Malolactic fermentation monitoring for winemaking	[146]
L-Lactic Acid	Amperometry	Au disk electrode	Deposition and immobilization using a dialysis membrane	L-Lactate oxidase + Horseradish peroxidase (HRP)		[146]

[18] Inter Digitated Electrode

Table 32(continue). Examples of electrochemical biosensors based on cascade reactions.

Analyte	Technique	Electrode	Immobilization	Enzymes	Application	Ref.
Glycerol	Amperometry	Au disk electrode	Deposition and immobilization using a dialysis membrane	Glycerol dehydrogenase + Diaphorase	Wine quality control	[147]
			Deposition and immobilization using a dialysis membrane	Glycerol dehydrogenase + HRP		[147]
Phosphate	Amperometry	Pt disk electrode	Deposition using laponite	Maltose phosphorylase + Mutarotase	Ecological monitoring	[148]
Creatine	Potenciometry	NH_4^+ ISE	In a membrane	Creatinase + Urease	Medical diagnosis	[149]
Arginine	Potentiometry	NH_4^+ ISE	In a membrane	Arginase+ Urease	Medical diagnosis	[149]
NH_4^+	Potentiometry	Prussian blue-carbon electrode	In a film	L-glutamate oxidase + L-Glutamate dehydrogense	Investigation	[150]
Tumor cells	Amperometry	Glassy carbon electrode	Cascade in two steps.	GOx+HRP	Diagnosis and clinical analysis	[151]

4.4.1. Cascade reaction based on natural enzyme loaded polymersomes

In **Scheme 21**, the *in-situ* loading process of the Psomes is shown: where the block copolymer (BCP, 1 mg·mL^{-1}) and Catalase (0.2 mg·mL^{-1}) are mixed at pH 5.0, both of them previously filtrated with a Nylon filter 0.2 µm. The formation and the loading of the Psomes is performed at the same time. After the self-assembly the solution is filtrated with a 0.8 µm syringe filter and irradiated for 30 s with UV light. In this way, two BCPs were used to prepared CAT-Psomes, one is CE 880-1 and the other one is AS223.

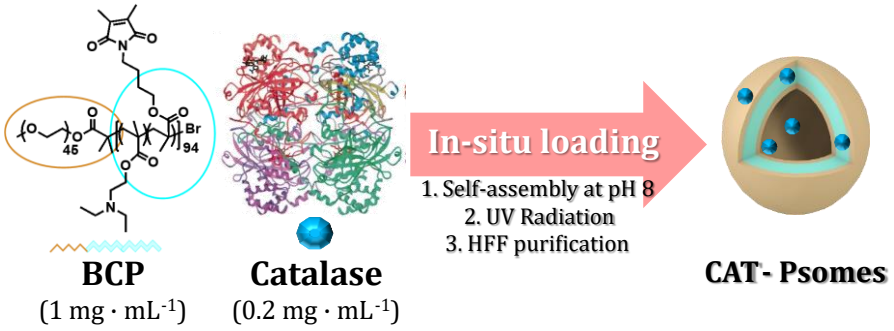

Scheme 21. Procedure for *In-situ* loading of CAT-Psomes.

The CAT-Psomes were prepared using both said BCPs and the loading was done following the procedure summarized in **Scheme 21**. They were characterized by DLS In **Figure 82.A**, and **C**. The study of the pH cycles is shown, and both presents good stability towards the pH changes. The pH* for CE 880-1 is 6.83 and for AS 223 is 6.66, as is shown in **Figure 82.B**, and **D**. Due to the small differences observed in their response when checking the pH* (pH where the Psomes is semi-closed) both were used interchangeably.

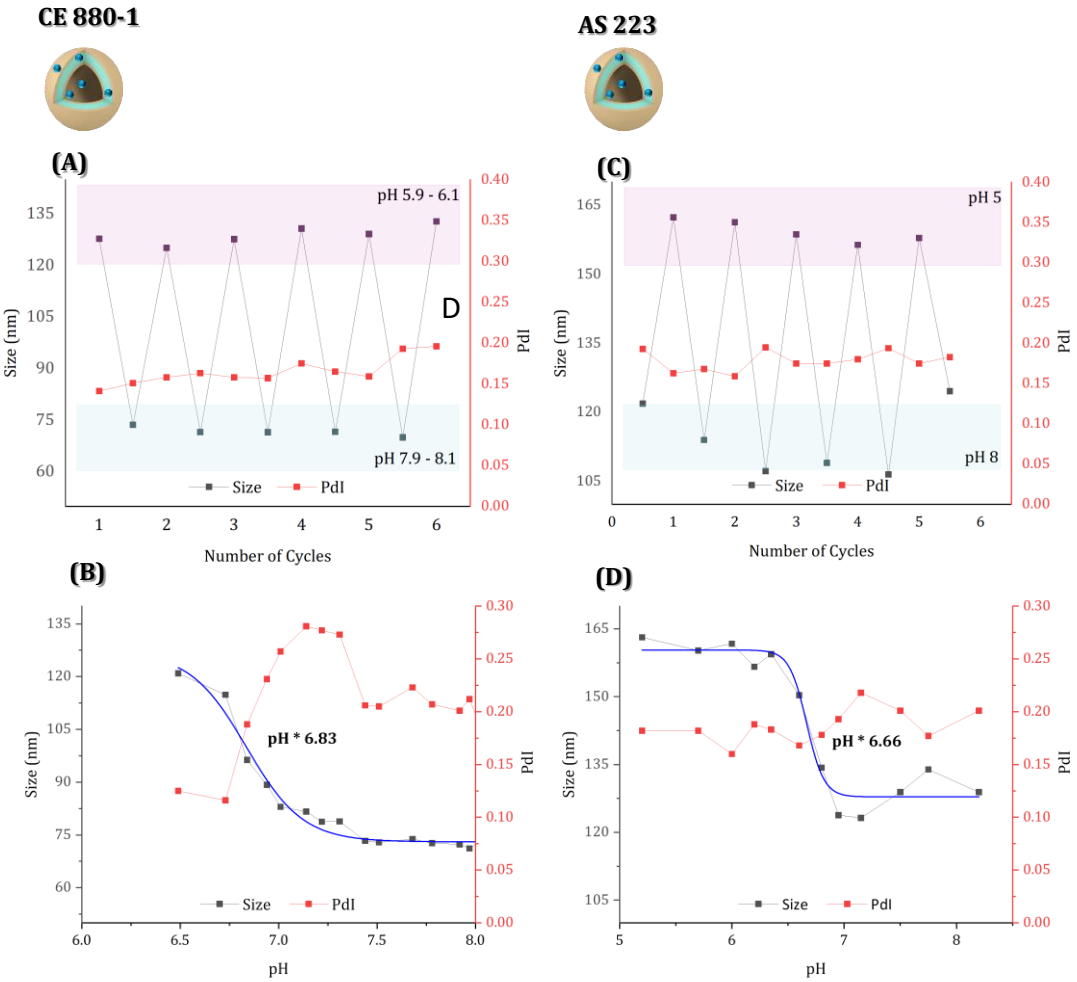

Figure 82. Characterization by DLS of CAT-Psomes enssambled using the different BCP. For 0.5 mg·mL^{-1} CE 880-1 (A) pH cycle in NaCl 10 mM, (B)pH titration. For 0.5 mg·mL^{-1} AS 223 (C) pH cycle in NaCl 10 mM, and (D) pH titration.

Further, the CAT-Psomes (CE 880-1) were morphologically characterized by Cryo-TEM (see **Figure 83**, using 67 particles in 7 images). The average diameter was 70 ± 16 nm and the membrane thickness was 16.7 ± 3.3 nm. Experimental uncertainty was standard deviation for both dimensions.

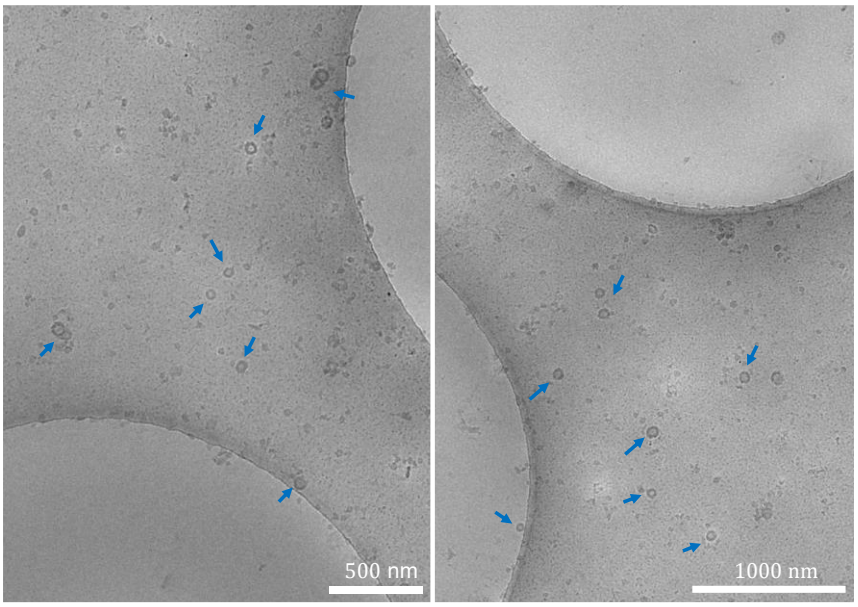

Figure 83. Cryo-TEM images of the CAT-Psomes (CE 880-1), indicated with blue arrows.

To calculate the loading efficiency (LE), the loading process of the Psomes described in **Scheme 21** was followed but instead of using CAT, labelled CAT (FITC[19]-CAT) was used. This FITC label allow to know where the enzyme is located, inside the Psomes or outside, in the media, because it is fluorescent. When the FITC-CAT is in the lumen (inner side) of the Psomes the fluorescent signal will decrease compared when it is free in the medium. To eliminate the free enzyme in the media some HFF[20] purification steps were done. The purification is finished when the fluorescent intensity remains constant and near to zero F.I (counts). The purified solution and the waste solution were analyzed, and their responses are collected in **Figure 84.A** and **B**, respectively. Additionally, the size and the polydispersity index (PdI) were analyzed, 118 nm and 0.169 before and 121.2 nm and 0.166 after HFF purification, respectively. The LE of the CAT-Psomes was calculated by fluorescence intensity after purification divided by fluorescence intensity before purification (using FITC-CAT-Psomes), and it is 24%, which is around~ 0.05 μM.

[19] Fluorescein IsoThioCyanate
[20] Hollow Fiber Filtration

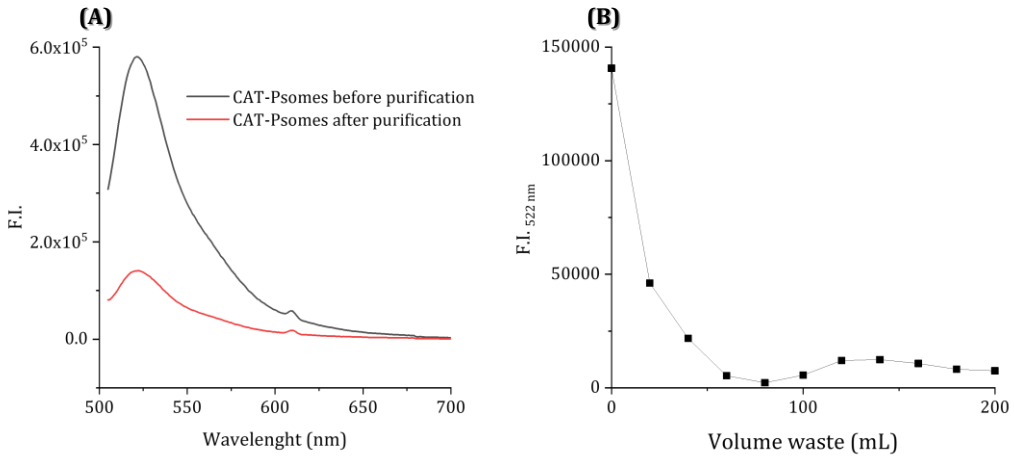

Figure 84. HFF purification steps monitoring: (A) Before and after the several steps of HFF, and (B) waste solution of the HFF purification.

Furthermore, the enzyme activity of CAT-Psomes were studied in solution by using the Amplex™ Red assay. **Figure 85.A** and **B** show the activity of non-purified CAT-Psome checked at different pH (7.4 and 6.0, respectively). In **Figure 85.C**, the activity of the purified CAT-Psomes were studied at two pH where the Psome state is swollen (pH 5.0) or closed (pH 8.0). Comparing with the non-purified CAT-Psomes, the higher activity is probably due the CAT that remains in solution. It can be observed that higher activities can be achieve when the Psomes membrane is in an open state (swollen state at pH 5.0), but, when it is in a close state (collapsed state pH 8.0), notable activities are also given. This, as was mentioned before, gives information about where the enzyme is placed, and it seems that some of enzyme molecules are in the membrane.

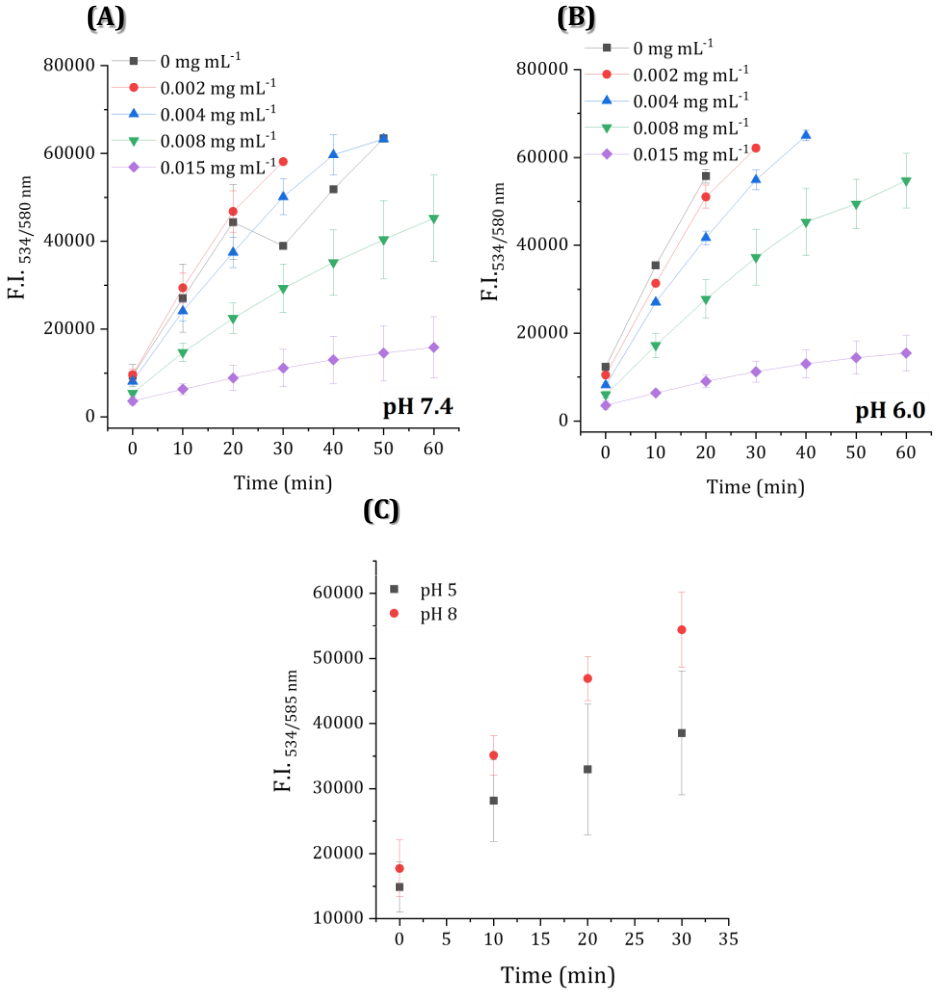

Figure 85. CAT activity study by a direct Amplex Red assay of (A) non-purified CAT-Psomes in PBS at pH 7.4, (B) non-purified CAT-Psomes in PBS at pH 6.0; and (C) purified CAT-Psomes in PBS at pH 5.0 and 8.0 and H_2O_2 4 μM.

4.4.1.1. Composite electrode modification to cascade reaction approach

In addition, the modification of the 15% graphite composite electrode surface to implement the cascade material was made in the same way as was explained previously, just changing the modification of the β-CD-S-AuNPs@rGO material with a mixture of CAT- Psomes and GOx-Psomes simultaneously (see **Scheme 22**), and following the volume proportion 2:1:1, respectively.

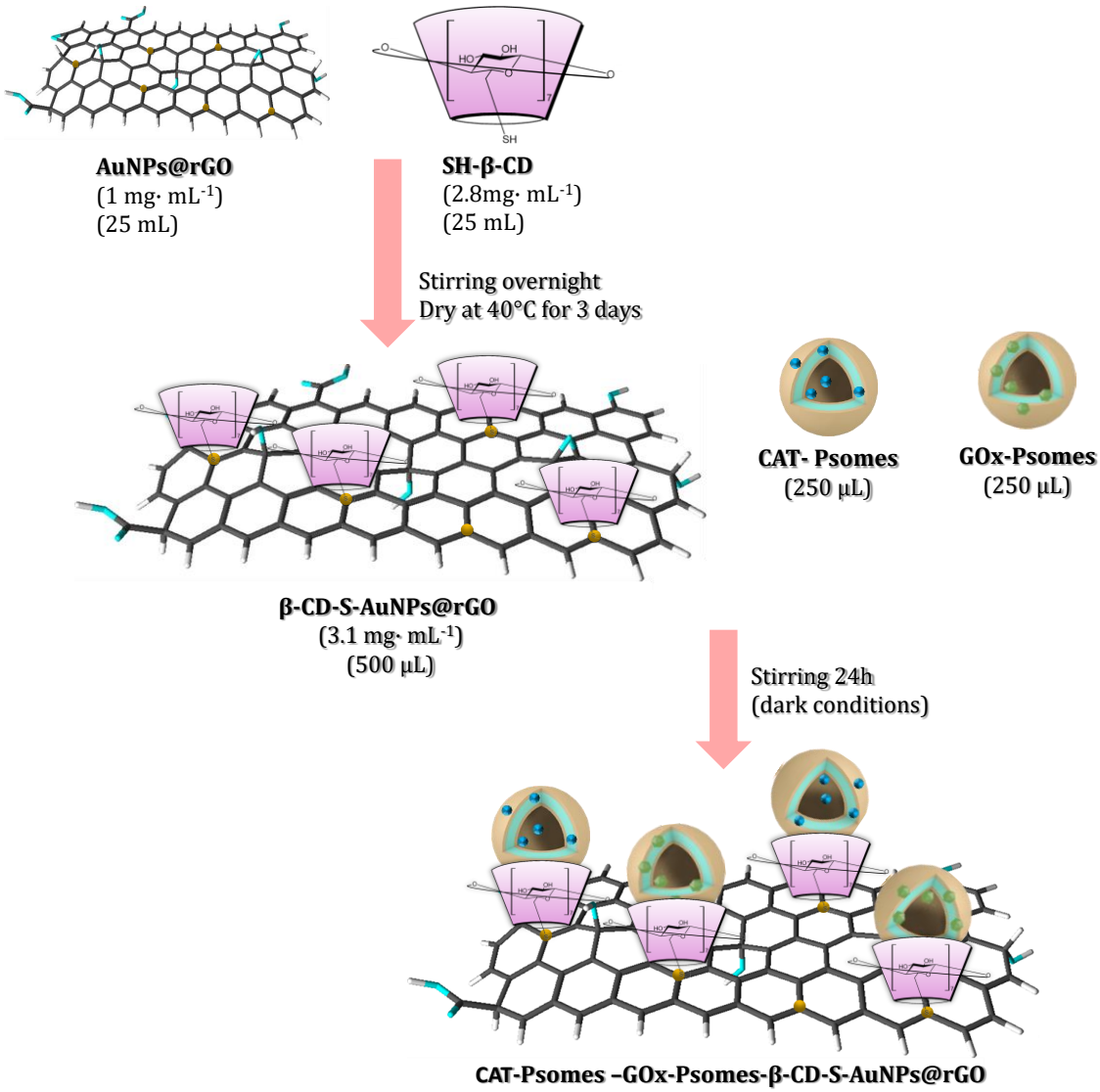

Scheme 22. Nanomaterial preparation using GOx and CAT loaded Psomes to cascade approach.

For the modification of the electrodes surface the hybrid nanomaterial was prepared and drop-casted over the electrode surface, following the same steps explained in **Scheme 17** (from **Chapter IV — Part III**), such as mixing the hybrid nanomaterial (125 µL) with

alginate 4% (125 µL), adding 250 µL $CaCO_3$ 1% , using external jellification with $CaCl_2$ 1% and internal jellification applying a potential (1.5 V) for 15 min.

Using this procedure, the 50% GOx-Psomes-50% CAT-Psomes electrodes were obtained (short name 50% CAT-Psomes).

4.4.1.2. Electrochemical evaluation of the cascade reaction approach

The cascade reaction was characterized electrochemically using the conditions optimized for the 100 % GOx- Psomes sensor and, comparing them with 50 % GOx-Psomes (50% GOx-Psomes-50% Empty-Psomes) and with 50% CAT-Psomes sensors by using the % Response (see **Figure 87** and **Table 33** for raw data). That is calculated by normalizing the sensitivities respect to the 100% GOx-Psomes sensor sensitivity.

Table 33. Summary of the calibration curves parameters using GOx-Psomes and CAT-Psomes sensors sensors with sensitivity and R^2.

% GOx-Psomes	% Other Psomes	Sensitivity [µA·M^{-1}]	R^2
100	-	119641.02	0.999
		91453.70	0.970
		113270.13	0.990
		181181.71	0.998
		110789.68	0.995
Average		123267 ± 34040	
50	50 Empty Psomes	19297.69	0.98
		15816.10	0.99
		16550.23	0.92
Average		17221 ± 1835	
50	50 CAT-Psomes	16068.00	0.95
		13021.80	0.92
		14924.40	0.96
Average		14671 ± 1539	

Using $4 \cdot 10^{-5}$ M and $7 \cdot 10^{-5}$ M glucose solutions, the response of the modified electrodes was characterized, the result is shown in **Figure 86**.

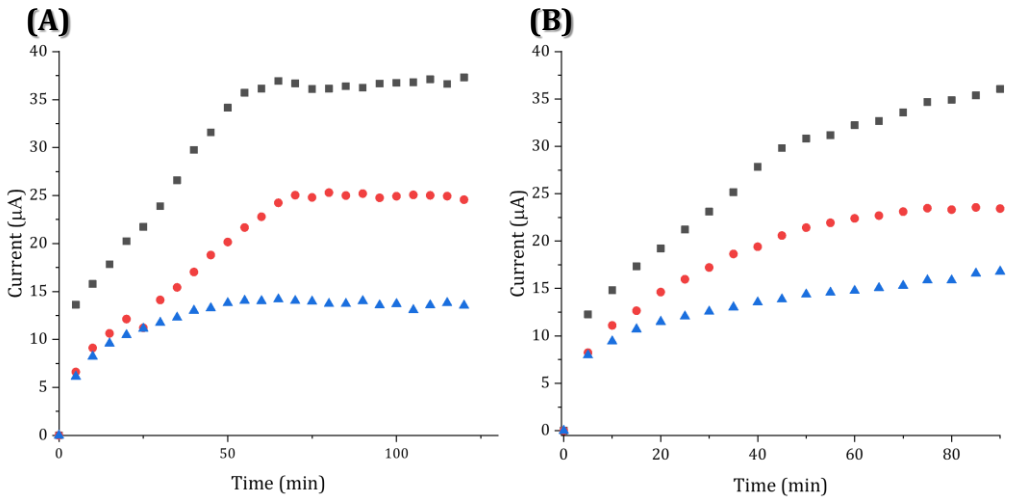

Figure 86. Signal evolution over time for a constant concentration of glucose at two different values (A) $4 \cdot 10^{-5}$ M, and (B) $7 \cdot 10^{-5}$ M. Where ■ 100% GOx-Psome sensor, ● 50% GOx-Psomes sensor and ▲ 50% CAT-Psomes sensor. Error in the measurements ≤ 5 µA.

In both glucose concentrations, the 100% GOx electrodes presented the higher response, followed by the 50% GOx-Psomes sensor (50% GOx-Psomes and 50% Empty-Psomes) and the last one is the one with CAT-Psomes (50% GOx-Psomes and 50% CAT-Psomes). This behaviour was expected due to the reduction of the amount of GOx in the hybrid nanomaterial and the consumption of the intermediate product, H_2O_2 by CAT enzyme. However, the effect of the CAT in both concentration levels is not observed until around the 20 mins for the highest concentration (**Figure 86.A**) and 10 min for the lowest concentration (**Figure 86.B**). For that reason, when the average of sensitivities obtained of all sensors in the calibration curves are compared, the. response between the 50% Empty-Psomes sensor and the 50% CAT-Psomes sensor is very similar (see **Figure 87** and **Table 33**), since the time is 5 min in calibration procedure.

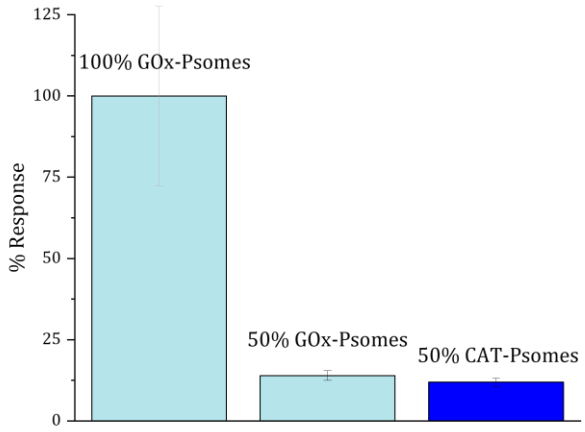

Figure 87.Comparison of the sensitivities of the calibration curves for 100% GOx sensor (n= 5), 50% GOx-Psomes (n=3) and 50% CAT-Psomes sensor (n= 3).

4.4.2. Cascade reaction based on nanozymes loaded polymersomes

Natural enzymes are biocatalyst with remarkable specificity even in mild conditions (for example room temperature, ambient pressure aqueous solutions, etc.). Even they are widely used in industrial, medical, and biological fields, they have several inconveniences such as denaturalization, high cost, difficult preparation that limited their practical applications [81].

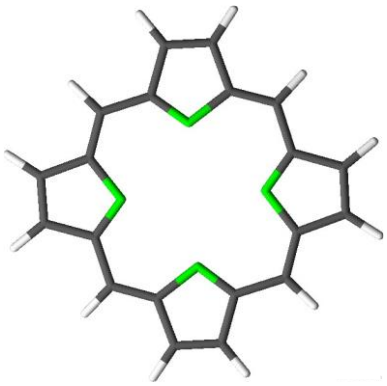

Figure 88. Basic structure of porphyrin ring.

Porphyrins are a group of heterocyclic macrocycle organic compounds. As is shown in **Figure 88**, it is composed of four modified pyrrole subunits. A well-known porphyrin with an iron core is the group Heme, whose functions include carrying oxygen in the blood torrent, also presents enzyme-like activity. Fe^{3+}-protoporphyrin[21] can catalyse the reduction of the H_2O_2 and compare to Fe^{2+}-porphyrins is cheaper, stabler and easier to obtain.

[21] Protoporphyrin is a derivate of the porphyrin with propionic acid groups.

4.4.2.1. Hemin loaded Psomes

Hemin chloride is an iron content Fe^{3+}-protoporphyrin, concretely the protoporphyrin IX[22]. Hemin chloride (**Figure 89**)can catalyse the reduction of the H_2O_2. Thus, for further comparison, the selected porphyrin to continue this work was Hemin chloride, even it presents several issues, especially its low solubility.

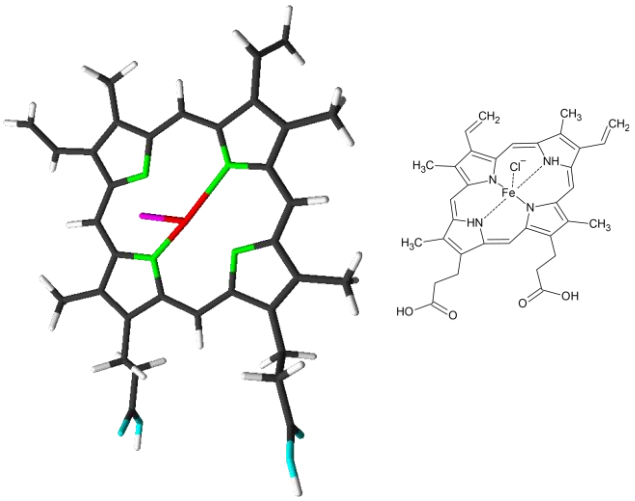

Figure 89. Hemin chloride structure.

This type of reaction is called Fenton like reaction and Fe-Porphyrins present this behaviour. In the case of Fe^{3+}, it was postulated that the oxidation is also produced to Fe^{4+} and the same mechanism explained in **Chapter I: Introduction** [152].

4.4.2.2. (β-Cyclodextrine)-Hemin complex solubility study

Initially, the solubilization of the Hemin chloride (≥ 96% purchased from Cayman Chemicals, MI, USA) was prepared by using NaOH 0.1 M and stirring minimum for 1 h.

After that, the solution obtained must be filtered using a 0.2 µm Nylon filter. The Hemin chloride solubility was checked in front of the pH. A stock solution 1 mg·mL -1 of Hemin chloride was prepared, and then 1.25 mL of this stock solution was diluted in PBS until reach 5 mL. After that, aliquots of the diluted Hemin chloride solution of 1 mL were placed in a centrifuge tube and the pH was adjusted to 5.0, 6.0, 7.0, 8.0 and 12.0, respectively. In **Figure 90**, a qualitative evolution of the supernatant of the solutions at these pH values was followed for 60 min (every 10 min a centrifugation step was done, and the aliquots were taken).

[22] Protophorpyrin IX is a precursor of the Heme group present in blood.

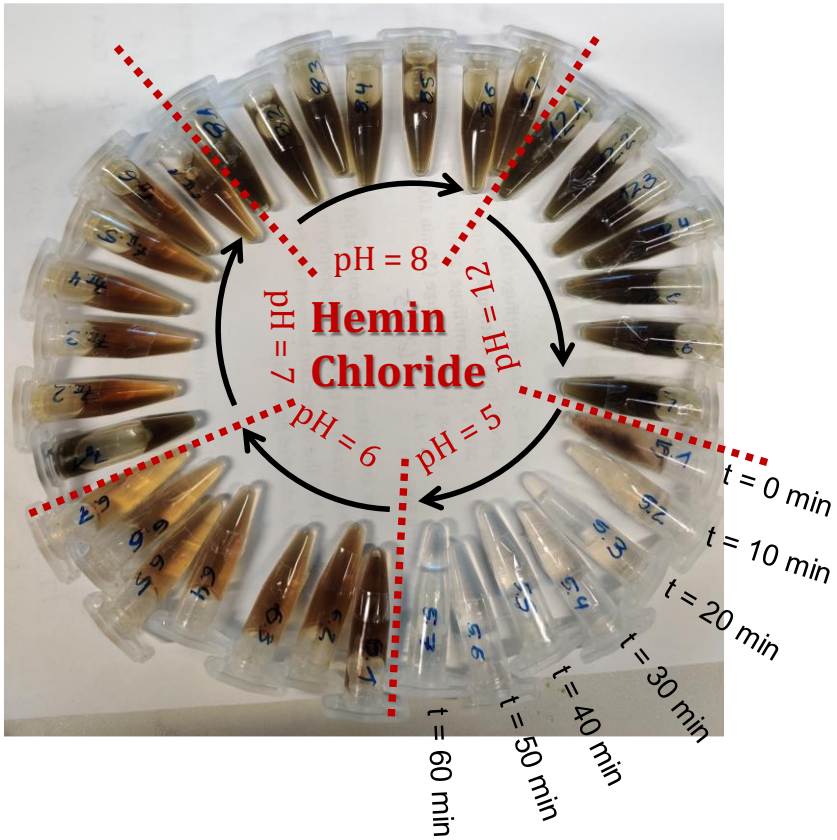

Figure 90. Qualitative evolution over time of the pH effect in the precipitation of the Hemin Chloride.

Then, due to the fact that the Hemin chloride molecule absorbs in the UV-Vis zone between 300 to 500 nm, these aliquots were analyzed using the Microplate Reader in absorbance mode. The reading at the wavelength (λ) of the maximum absorbance was represented in **Figure 91**. A decrease in the absorbance is observed in acid pH compared with basic pH, that can be related to a decrease in the amount of Hemin chloride in the solution leading to its precipitation at acidic pH.

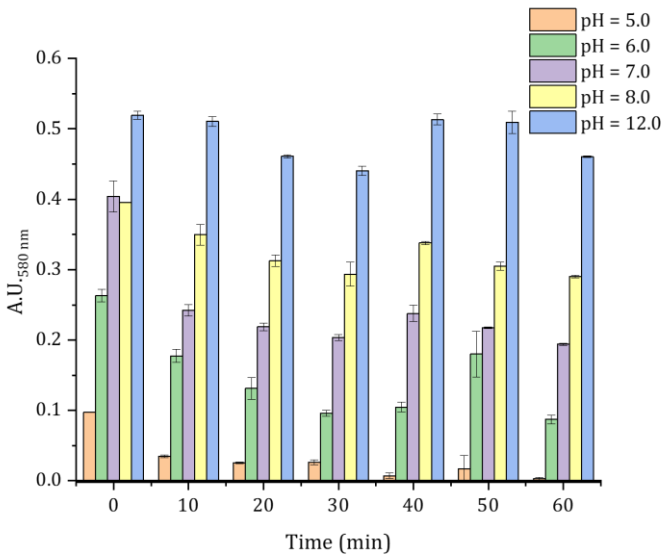

Figure 91. Absorbance evolution of the aliquots of the free Hemin Chloride at different pH. Error calculated as standard deviation of the measurements.

To evaluate the effect of the Psomes over the Hemin chloride, some approaches using a *post-loading* process of the Psomes were checked. This loading method is quite different than the previous one (*in-situ* loading). Due to the low stability of the Hemin chloride solution against the pH changes, *post-loading* process was the approach here chosen to overcome the difficulties of Hemin chloride solution preparation. The *post-loading* process consist in first the assembly of Empty-Psomes and then the charge of them with the porphyrin.

The first approach (**Scheme 23**) was using a stock solution of Hemin chloride 5 mg·mL^{-1} (in NaOH 0.1 M) prepared and diluted in PBS 10 mM to obtain two solutions: one of 2.5 mg·mL^{-1} and another of 1 mg·mL^{-1}. Then, for both the *post-loading* applied methods, the final concentration of Hemin chloride when the Empty-Psomes (1 mg·mL^{-1}) were in the media was at different levels: 0.15, 0.25, 0.50 and 1.0 mg·mL^{-1}. The differences between the methods tested are summarized in **Scheme 23**. The inconvenience of the Method 1 was that the pH switched to basic when the Hemin Chloride solution was added to the Empty-Psomes solution, and over.of pH 8.0 the Psomes are closed. Due to this inconvenience, method 2 from **Scheme 23** was the method selected to keep studying the *post-loading* process.

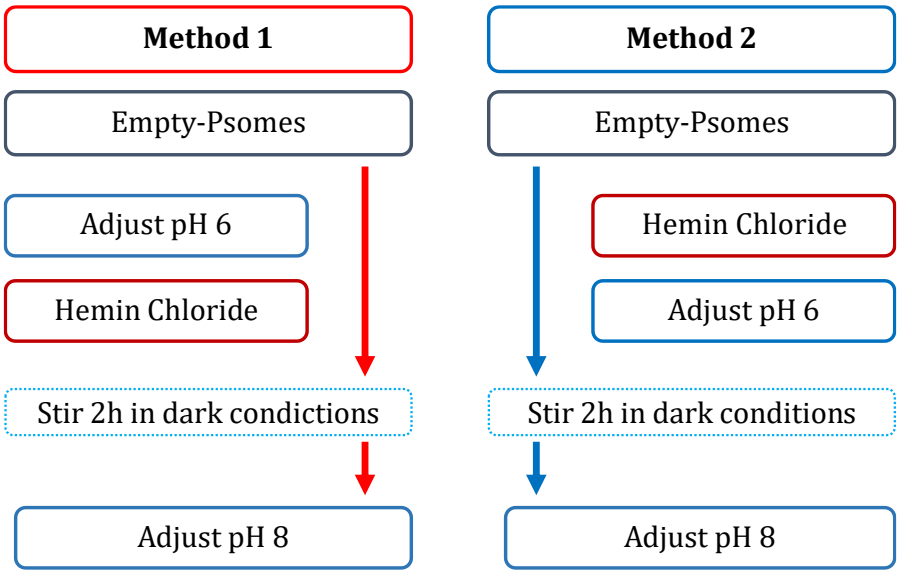

Scheme 23. Post-loading methods that were tested initially.

As was explained before, at acidic pH Hemin chloride precipitates. In order to check if this precipitation still occurs when the *post-loading* method 2 is used, the same qualitative previous experiment was performed. In **Figure 92** can be observed that at acid pH the precipitation does not occur in that case, compared to the free Hemin chloride case, shown in **Figure 90.**

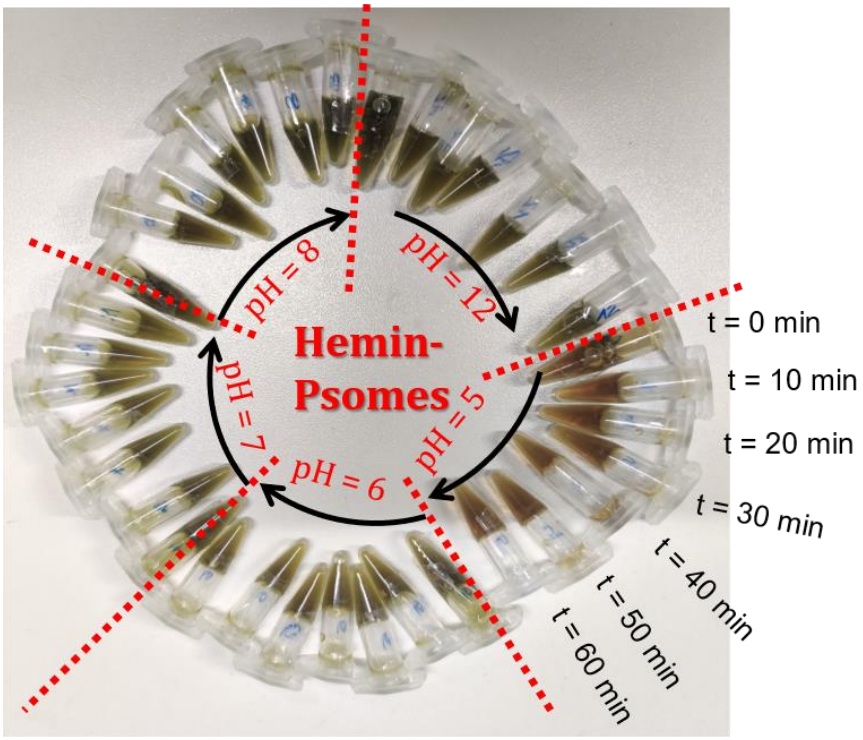

Figure 92. Qualitative evolution over time of the precipitation of the Hemin chloride after *post-loading* process by method 2 when the pH is changed.

Then, these aliquots were also analyzed using the Microplate Reader in absorbance mode in the UV-Vis zone between 300 to 500 nm, and the reading at wavelength of maximum in absorbance was represented in **Figure 93**. Even changing the pH the absorbance remains constant, highlighting pH 8.0, which is slightly superior in, almost, all times checked (up to 60 min)

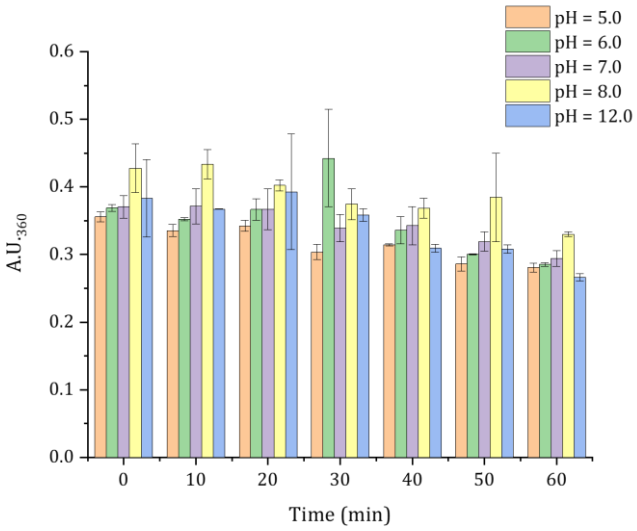

Figure 93. Absorbance evolution of the aliquots of the Hemin- Psomes with *post-loading* process by method 2 at different pH. Error was calculated as standard deviation of the measurements.

To use milder conditions and trying to avoid the precipitation at acidic media, and still with the purpose of increasing the solubility of the Hemin chloride, its complex formation with β-Cyclodextrin (β-CD from Sigma Aldrich, Germany) was evaluated and optimized [153]. The use of β-CD could help to increase the solubility due to the different behaviour of its parts, a hydrophobic cavity, and the hydrophilic outer surface. The set of experiments followed for the characterization of the β-CD-Hemin-complex (following the improvement of the solubility of Hemin chloride) was undergone in *Bioactive and Responsive Polymer department*, from the L*eibniz-Institut für Polymerforschung Dresden e.V*. [84].

To optimize the stoichiometry of the β-CD-Hemin complex, a titration using β-CD was performed. First, a stock solution of 4.5 mg·mL^{-1} of β-CD in NaOH 0.1 M is prepared. Then, in different containers, a 1 mg·mL^{-1} Hemin chloride is prepared and adding different quantities of β-CD (getting different Hemin chloride and β-CD ratios), and all of them are filled with NaOH 0.1 M until reach 1 mL, shaken in a vortex and incubated for 1 h at 37 °C (with stirring). In **Table 34** there are the different ratios and amounts of compounds used.

Table 34. Titration of Hemin chloride using different β-CD concentrations. From [84] with permission under Creative Commons Attribution-NonCommercial-No Derivatives Licence.

$Eq_{β\text{-}CD}$: Eq_{Hemin} [mols]	Hemin chloride [mg]	β-CD [μL]
0	1.07	0.00
0.5	0.93	173
1	0.99	392
1.5	1.15	793
2	1.10	968
2.5	1.00	1000

In **Figure 94**, the absorbance of the complex formed in each case was checked, being the $(β\text{-}CD)_2$-Hemin (ratio 2 of $Eq_{β\text{-}CD}$:Eq_{Hemin}), the one that has highest absorbance and therefore less rate of precipitation. That means the $(β\text{-}CD)_2$-Hemin in the complex formed and gives the highest solubility of the complex tested.

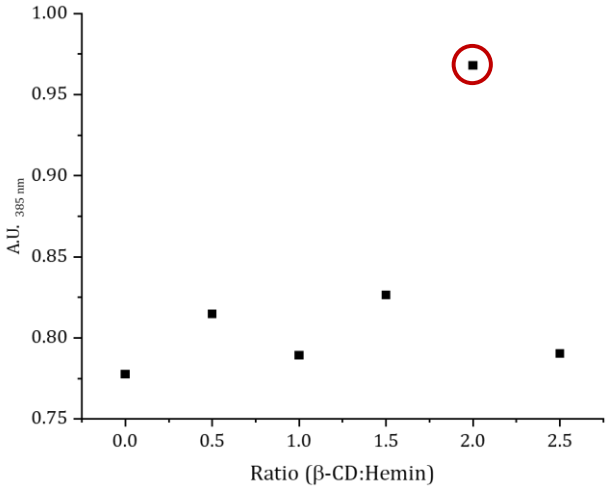

Figure 94. Absorbance at 385 nm of the proposed complex of $(β\text{-}CD)_n$-Hemin. From [84] with permission under Creative Commons Attribution-NonCommercial-No Derivatives Licence.

For further applications, the complex $(β\text{-}CD)_2$-Hemin was prepared by dissolving 4 mg of Hemin Chloride, 13.9 mg of β-CD in 2 mL of NaOH 0.1 M and shaking 1h at 37 °C.

All $(β\text{-}CD)_2$-Hemin-Psomes post-loading preparation process is summarized in **Scheme 24**.

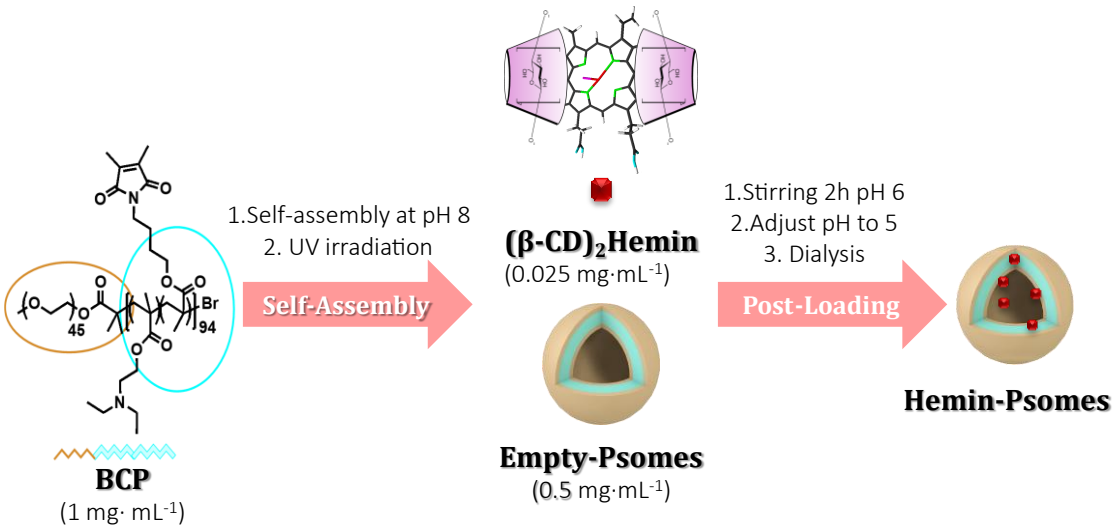

Scheme 24. (β-CD)$_2$Hemin-Psomes *post-loading* process. BCP: Block copolymer

After the assembly of the Empty-Psomes, the post-loading process consist in mixing and stir for 2 h the complex (β-CD)$_2$Hemin (150 µL, 2 mg·mL^{-1}), the Psome solution (5.00 mL, 1 mg·mL^{-1}) and PBS (5.85 mL, 2mM) at pH 6.0. After 1h, the pH was adjusted to 5.0. Then, the centrifugation step was carried out twice at 6000 rpm for 4 min. After that, the pH is adjusted to 8.0 using NaOH 0.1 M and the sample is purified by dialysis for 4 days; using a membrane MWCO of 100kDa against 1 mM PBS at pH 7.4 in constant stirring and under dark conditions (the buffer was changed daily) [84].

4.4.2.3. Characterization of the (β-CD)$_2$Hemin-Psomes

The (β-CD)$_2$Hemin-Psomes were characterized by DLS to obtain the pH* (pH star) of 6.85 (see **Figure 95**). This loaded Psomes were prepared using the BCP AS 223. The loading efficiency was ~1.5 µM, and the study of the enzyme-like behaviour in different medias is published in [84].

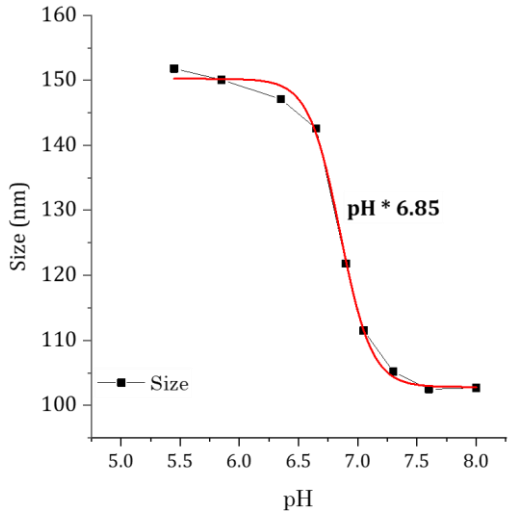

Figure 95. The $(\beta\text{-CD})_2$Hemin-Psomes titration. From [84] with permission under Creative Commons Attribution-NonCommercial-No Derivatives Licence

The $(\beta\text{-CD})_2$Hemin-Psomes were characterized by cryo-TEM, in **Figure 96**. The diameter of the $(\beta\text{-CD})_2$Hemin-Psomes is 90 ± 25 nm and membrane thickness 28 ± 8 nm (70 particles measured in 7 pictures). Comparing the size and the PdI reported by the Empty-Psomes, 104.2 nm and 0.147, respectively. Due to the type of loading used, the $(\beta\text{-CD})_2$Hemin-Psomes do not significantly differ this size and the PdI, being 102.2 nm and 0.157, respectively.

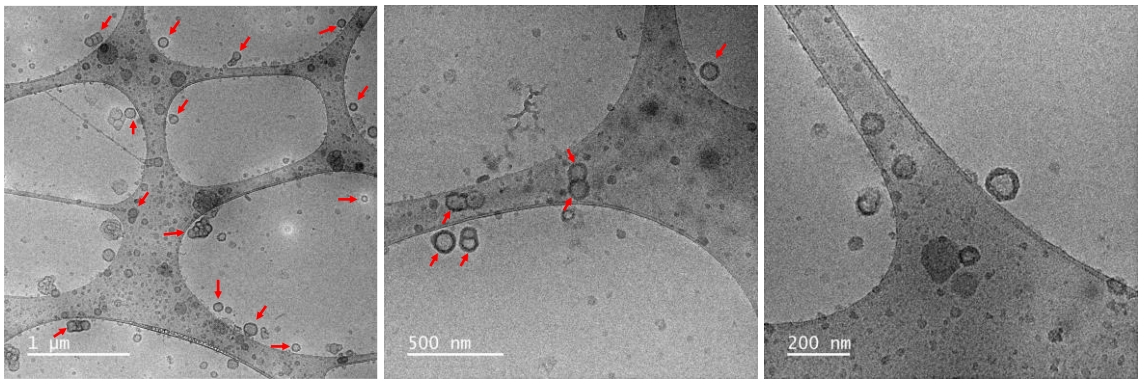

Figure 96. Cryo-TEM pictures of $(\beta\text{-CD})_2$Hemin-Psomes, indicated with red arrows.

4.4.2.4. Electrochemical approach in nanozyme-cascade reactions using modified composite electrodes

In addition, the modification of the composite electrodes was made in the same way as the 100% GOx-Psomes electrode and the other types of electrodes, just changing the modification of the β-CD-S-AuNPs@rGO material (**Scheme 17** from **Chapter IV—Part III**), with different percentages of loaded Psomes now with GOx and $(\beta\text{-CD})_2$Hemin. In the following **Scheme 25,** the modification procedure of the nanomaterial is summarized, and

the amounts of the loaded Psomes used for the construction of all the electrodes for this study of cascade reaction are summarized in **Table 35**.

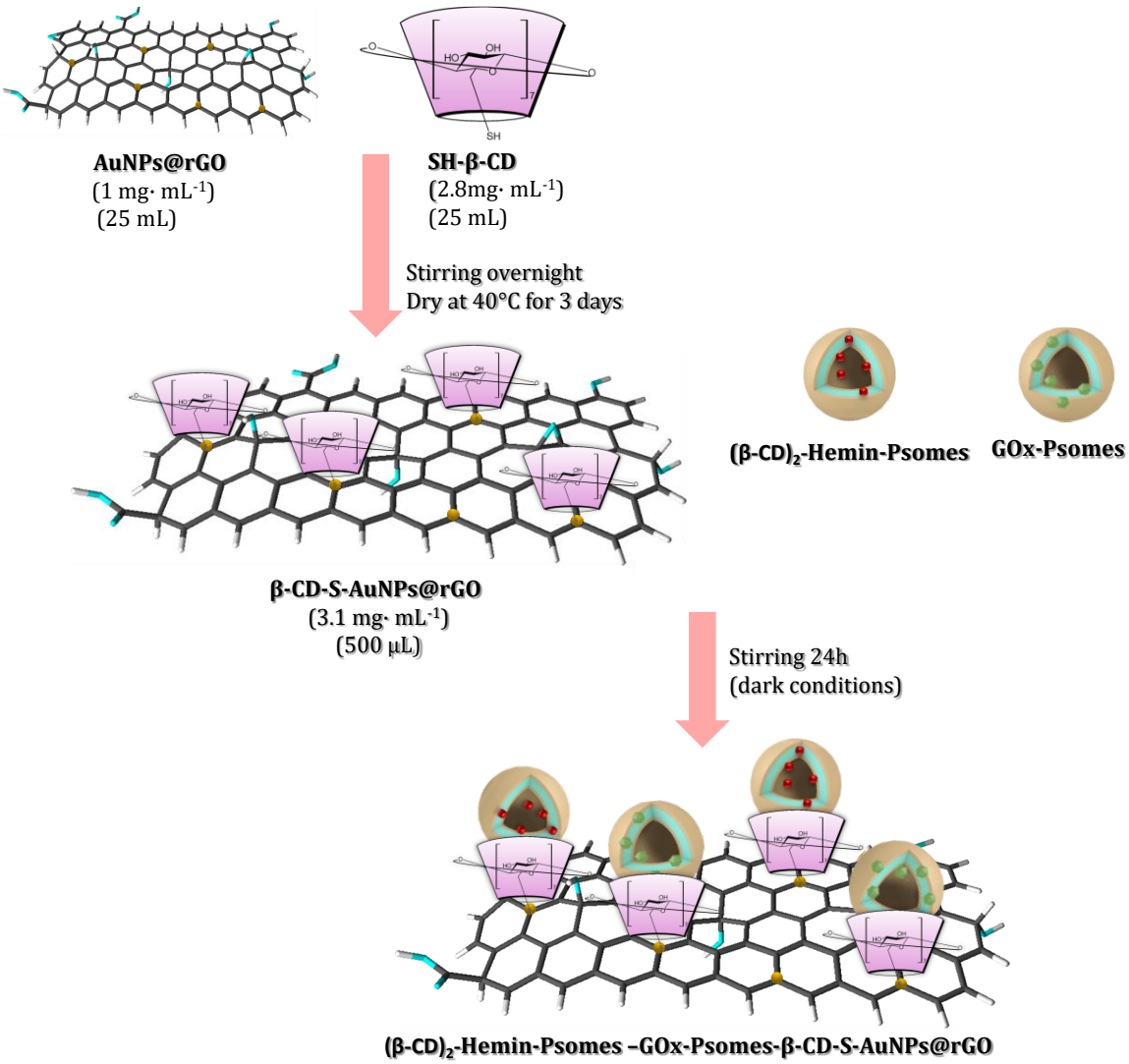

Scheme 25. Cascade approach to nanozyme hybrid nanomaterial preparation for the composite electrode modification.

Table 35. Summary of the preparation of different modifications of the β-CD-AuNPs@rGO material for the cascade reaction using enzymes and nanozymes. The percentagess are given according to the contribution of the 500 μL(total volume) used in the modification.

Name of the electrode	% GOx-Psomes	GOx-Psomes [μL]	Other [μL]
50% CAT-Psomes	50	250	250 CAT-Psomes
50% Hemin-Psomes			250 $(\beta\text{-CD})_2$Hemin-Psomes
90% Hemin-Psomes	10	50	450 $(\beta\text{-CD})_2$Hemin-Psomes

4.4.2.5. Electrochemical response of the cascade reaction using nanozymes

The response of the cascade reaction using natural enzyme was studied previously. At $4\cdot10^{-5}$ M glucose (lowest concentration) the differences between the electrodes were more evident than at $7\cdot10^{-5}$ M glucose (see previous **Figure 86**), for that reason the further studies were done using the lower concentration, $4\cdot10^{-5}$ M glucose. To test the current modified electrodes two pH conditions were selected: pH 7.4 and 6.0. pH 6.0 was chosen because in [84] was found that the enzyme-like activity is higher than at pH 7.5.

In **Figure 97.A** a comparison of all the electrodes tested at the optimized pH (pH 7.4) is shown. The 100% GOx-Psomes sensor has the higher signal, because there is a greater production of H_2O_2, followed by 50% Empty-Psomes. Both 50% CAT-Psomes electrode and 50% $(\beta\text{-CD})_2$Hemin-Psomes electrode have the same lower response, since part of the hydrogen peroxide produced is consumed by the enzyme CAT and the nanozyme Hemin, respectively. As can be seen from **Figure 97.B**, at pH 6.0 the behaviour of the enzyme and the nanozyme is very similar. It should be noticed that the performance of the nanozyme when changing the pH remain similarly, being the same in both pH under study (pH 7.4 and 6.0). In both cases, with the enzyme CAT and the nanozyme $(\beta\text{-CD})_2$Hemin, at pH 6.0 the measured current is practically constant, it can be hypothesized that at pH 6.0 the H_2O_2 produced by GOx is consumed by the enzyme or nanozyme, in addition to electrochemically, without accumulating. Under these conditions, CAT enzyme and Hemin nanozyme demonstrate enhanced catalytic activity. On the contrary for GOx enzyme, it does not seem to be the optimum conditions.

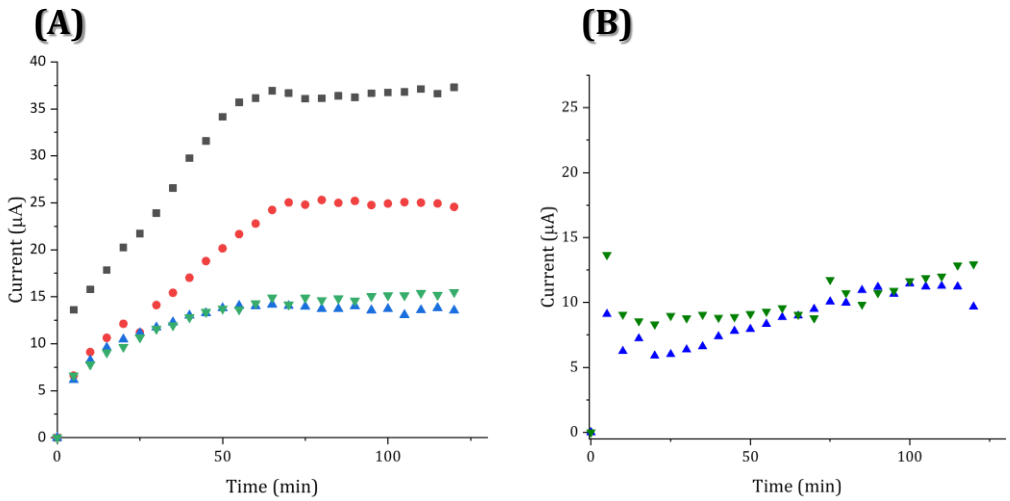

Figure 97. Evolution of the measurement for a constant concentration of glucose $4 \cdot 10^{-5}$ M (A) pH 7.5, and (B) pH 6; where ■ 100% GOx sensor, ● 50% Empty-Psomes sensor and ▲ 50% CAT-Psomes sensor and ▼ 50% $(\beta\text{-CD})_2$Hemin-Psomes. Error in the measurements ≤ 5 μA.

Due the adjacent properties of the nanozyme (cost-effective, higher stability, etc.) another percentage, 90% $(\beta\text{-CD})_2$Hemin-Psomes, was also tested. In **Figure 98**, the comparison of the performance of the corresponding sensor response at different pHs is shown and the difference in the response is remarkable. At pH 6 the Hemin activity is greater than at pH 7.5, because a lower current is obtained. It can be attribute to two factors: first, the optimum pH of GOx is 7.5 then a pH 6 less H_2O_2 was produced; and second, the H_2O_2 produced is consumed by Hemin and not consumed electrochemically. Consequently, a decrease in current was observed.

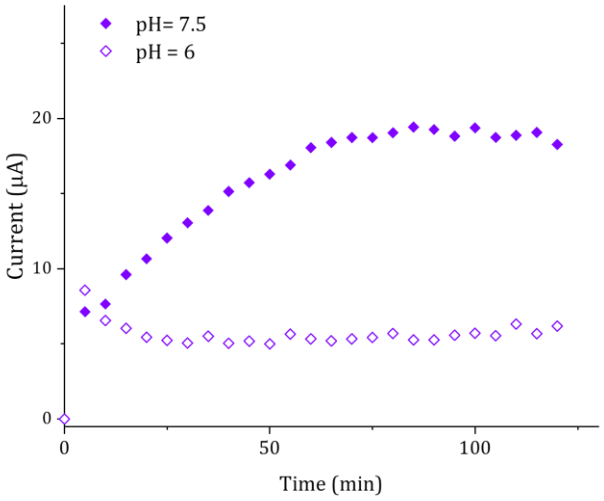

Figure 98. Response at different pH: ♦ 7.5 and ◇ 6 of the 90% $(\beta\text{-CD})_2$Hemin-Psomes composite electrode. Error in the measurements ≤ 5 μA.

Furthermore, in **Figure 99** the sensitivities of the calibration curves obtained at different pHs were compared using the 100% GOx-Psomes sensor at the different studied pH as references (% Response). An average sensitivity of 32974 ± 7927 $\mu A \cdot M^{-1}$ at pH 6, but 123267 ± 34040 $\mu A \cdot M^{-1}$ at pH 7.4 for the 100% GOx electrodes was found (there is a summary of the obtained values in **Table 36**). This difference in sensitivities is related to the optimum pH of GOx 7.4 in which more H_2O_2 is produced. Thus, more H_2O_2 must be enzymatically degraded by CAT enzyme and Hemin nanozyme.

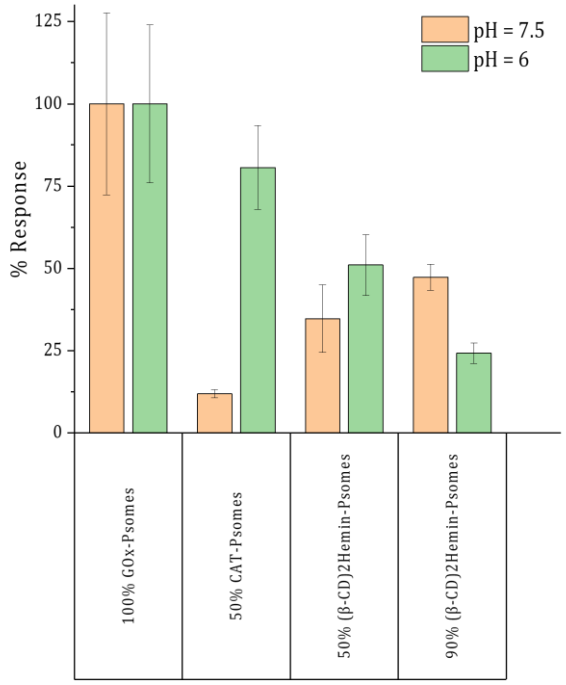

Figure 99. Comparison of the sensitivities of the calibration curves: 100% GOx sensor (n= 5), 50% CAT-Psomes sensor (n= 3), 50% $(\beta\text{-CD})_2$Hemin-Psomes sensor (n= 3) and 90% $(\beta\text{-CD})_2$Hemin-Psomes sensor (n= 3).

Table 36. Summary of sensitivities obtained from calibrations curves of the different % GOx-Psomes in modified sensors tested.

pH	% GOx-Psomes	% Other Psomes	Sensitivity [$\mu A \cdot M^{-1}$]	R^2
7.4	100	-	119641.02	0.999
			91453.70	0.970
			113270.13	0.990
			181181.71	0.998
			110789.68	0.995
	Average		123267 ± 34040	
	50	**50 Empty-Psomes**	19297.69	0.98
			15816.10	0.99
			16550.23	0.92
	Average		17221 ± 1835	
	50	**50 CAT-Psomes**	16068.14	0.95
			13021.79	0.92
			14924.44	0.96
	Average		14671 ± 1539	
	50	**50 (β-CD)$_2$Hemin-Psomes**	43312.27	0.98
			30020.87	0.96
			55266.32	0.99
	Average		42866 ±12629	
	10	**90 (β-CD)$_2$Hemin-Psomes**	63631.72	0.89
			54139.99	0.90
			57165.54	0.996
	Average		58312 ±4849	
6.0	100	-	24169.00	0.88
			39545.02	0.93
			35208.22	0.93
	Average		32974 ±7928	
	50	**50 CAT-Psomes**	22410.64	0.95
			26600.45	0.92
			30856.94	0.96
	Average		26623 ±4223	

Table 36 (continue). Summary of sensitivities obtained from calibrations curves of the different % GOx-Psomes in modified sensors tested.

pH	% GOx-Psomes	% Other Psomes	Sensitivity [$\mu A \cdot M^{-1}$]	R^2
6	50	**50 (β-CD)$_2$Hemin-Psomes**	20268.44	0.98
			15644.87	0.96
			14572.28	0.99
	Average		16829 ±3027	
	10	**90 (β-CD)$_2$Hemin-Psomes**	9199.64	0.81
			7404.48	0.90
			7388.55	0.996
	Average		7998 ±1041	

At pH 7.4, the % response of the 50% (β-CD)$_2$Hemin-Psomes sensor is comparable to the one obtained with the 50% CAT-Psomes sensor at the same pH, both containing the same amount of GOx-Psomes. Independent of the loading efficiency calculated for each type of Psome, the disposition of them is important. At pH 6, due to the type of loading, some of the natural enzyme used could be integrated in the membrane of the Psome, and this can help the feeding of the enzyme. On the contrary, for the (β-CD)$_2$Hemin-Psome, very few nanozyme are in the membrane, mostly are in the lumen of the Psome, so this can difficult the feeding for the reaction to be produced. In general, the results of the enzymatic cascade reaction show that nanozyme could be a good option to substitute natural enzyme in this type of vesicles. Moreover, further experiments will be needed to understand the slightly contrary results of 50% and 90% (β-CD)$_2$Hemin)-Psomes at pH 7.4.

4.4.3. Concluding remarks

In **Figure 100**, there is a summary of the main results obtained.

Polymersomes offer the possibility to perform heterogenous bioactive surface modification for composite electrodes. This sensing approach, open us a new possibility of an alternative strategy to the electrodes' customization *ad hoc*. Psomes are reservoir that stabilize either natural enzymes or nanozymes. Highlighting that Psomes allow the diffusion of substrates and products necessary to carry out the enzymatic cascade reaction.

The viability of this proof of concept has been demonstrated with the amperometric measurements carried out. In which a decrease in signal has been obtained in the sensors with GOx-Psomes and 50 % CAT-Psomes and 50 % (β-CD)$_2$Hemin-Psomes.

So, the use of a nanozyme, such as (β-CD)$_2$Hemin, offers us a complementary way to solve the problems that presents the use of natural enzyme, as low cost, stability to changes of temperature or pressions among others.

However, more experiments and research are needed to understand the obtained results regarding the (βCD)$_2$Hemin)-Psomes and its catalyst effect, when different amounts of this nanozyme is used.

An additional optimization of the (βCD)$_2$Hemin)-Psomes material used in the modification of the electrode for the cascade reaction is mandatory and the future work can be directed in this direction.

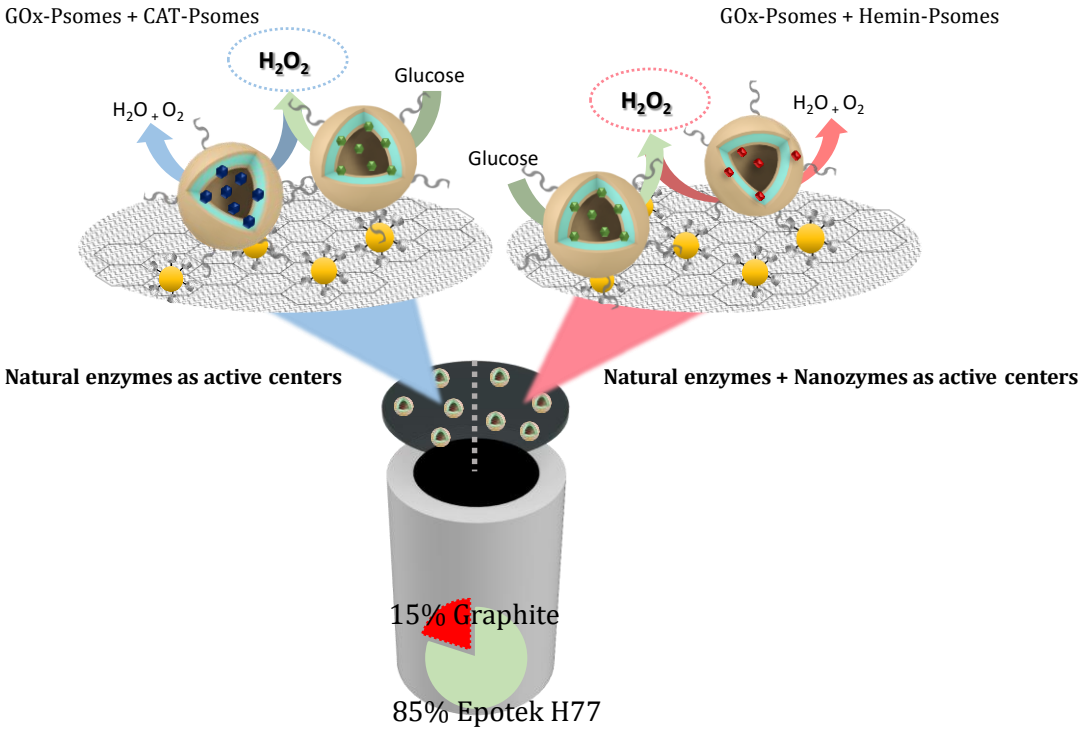

Figure 100. Graphical summary of the main results of Chapter IV —Part IV.

Chapter V

Conclusions

5.1. Conclusions

In this thesis different composite electrodes based on carbon materials and several composition ratios have been tested in the manufacturing of the voltametric sensors. The ratios used are the optimum and the maximum carbon material (conductor material) allowed by the epoxy resin (isolating material) used. The purpose of these composite electrodes is to achieve a surface modification enable to sense the target analytes.

As a general conclusion, based on the results obtained in this thesis it has been shown that a variety of modifications can be performed on the surface of the composite electrode. Firstly, inorganic modification with HgNPs, which is performed by drop-casting over the 20% graphite composite electrode and applied for metal sensing; and secondly, a biological modification with an intricate hybrid-nanomaterial formed by loaded Psomes, and β-CD-S-AuNPs@rGO, which was used to modify the surface of the 15% graphite composite electrode and applied in that case for glucose sensing.

In the specific case of the modification with HgNPs as metal sensor, the detailed conclusions obtained are as follows:

- The preconcentration time for Square Wave Anodic Stripping Voltammetry was optimized for each metal, and a compromise was reached by selecting 7 minutes, balancing the concentration measured for each metal cation with the total time required for simultaneous detection in a single measurement.
- Regarding the carbon ratio used for the fabrication of the composite electrodes: the 20% graphite electrodes, representing the maximum graphite content supported by the resin Epotek H77, exhibited superior performance for Cd^{2+} and Pb^{2+} sensing compared to the previously 15% graphite composite electrode with a higher signal-to-noise ratio. Notably, this improvement can be attributed to the increase of the number of sites available for the preconcentration of metals ions onto the electrode surface during the SWASV technique.
- Each batch of carbon nanotubes used for composite electrode preparation has its proper electrochemical behavior. Therefore, each series of electrodes manufactured with a composite electrode from different CNTS batch must be optimized using the percolation curves approach to evaluate the optimum CNTs ratio to work with.
- The conductivity of the reduced graphene oxide is along its axis. Accordingly, the conductivity of the composite material containing rGO depends on its orientation. So, due to the random orientation of the rGO sheets in the composite material was

necessary dopped it with graphite (14% rGO +1% graphite), but the sensing of Cu^{2+} was not achieved.

- ⌘ Glassy carbon electrode presents a good performance just for Cu^{2+} sensing, but due to the superior performance of the 20% graphite composite electrodes for Cd^{2+} and Pb^{2+} detection, this composite composition is selected to carry out further analysis.
- ⌘ To modify the surface of the 20% graphite composite electrode with HgNPs two synthetic routes were followed by using two different polymers giving different HgNPs. Poly(diallyldimethylammonium) chloride for Route A and polyvinyl alcohol for Route B. The $HgNPs^{RouteA}$ where Hg has an oxidation state of I, and these nanoparticles shows less aggregation and smaller particle size than the $HgNPs^{RouteB}$. These differences lead to a better behavior of $HgNPs^{RouteA}$ in both its electrochemical characterization and in the metals' measurement analysis.
- ⌘ Analysis of a mixed cation metal solution using the $HgNPs^{RouteA}$ modified composite electrode results in a decreased linear range for all metals, comparing to analyzing each metal individually. This narrowing of the linear range is likely caused by the complete occupation of the electrodes' electroactive area by each reduced metal during the SWASV preconcentration step.
- ⌘ The performance of the sensors was good enough for the analysis of synthetic samples (dopped tap water). Regarding other real samples, different difficulties were found. In the case of the Mar Menor samples, it was not possible to repeat the measurements to be able to verify the obtained results due to the difficulty obtaining the samples. In the case of the digested samples from vineyards, due to the variations of the data sampling, stations, biological variability, composition sample etc. the obtained results with the developed method compared to the ICP ones (which is used as a reference method) were not entirely suitable.

In the subsequent modification using β-CD-S-AuNPs@rGO and polymersomes for glucose sensing, the suitable ratio of graphite in the composite to have a proper biosensor was 15% (based on previous results and due to the optimized signal-noise ratio). The detailed conclusions obtained are as follows:

- ⌘ The previous loading of the enzyme was done by an *in-situ*, loading that means the Psomes assembling, and the loading is performed simultaneously, and the enzymes (GOx and CAT) can be found inside the Psomes but forming part of the wall or the external membrane. A *post-loading* where the Psomes are formed, and the cargo is trapped inside the Psomes. The optimization of the *post-loading* process of the nanozyme (Hemin chloride) and its derivates

has several difficulties which includes the precipitation of the free Hemin to the pH changes and with solubility problems at acidic pH. The precipitation towards pH changes was solved using Psomes to protect Hemin group by load on the Psomes, which is proved to enhance the stability. Also, the solubility problem was solved by forming a complex with $(\beta\text{-CD})_2$Hemin, which have been proved to have better solubility than other ratio complexes studied.

- The use of a hybrid nanomaterial composed by loaded Psomes-β-CD-S-AuNPs@rGO, to modify the surface of the composite electrode where each element has its proper function, seems to be a good option. Some components of this hybrid nanomaterial can mitigate the non-conductor effects of the Polymersomes.
- Among all the materials tested, such as pyrrole, PDDA, tapes and stubs etc., the use of alginate as a support matrix of the hybrid nanomaterial seems to be a good choice even a disadvantage is that it is required a very complex procedure, starting with a drop-casting and the subsequent jellification manufacturing process.
- The behavior of two block copolymers (BCP 880-1 and AS223) were check for the Psomes assembly. Comparing their properties in the Empty-Psomes (pH star and pH cycles and size) were found to be equivalent and used interchangeably.
- Psomes can be loaded with natural enzymes for the glucose analysis purpose. When Glucose Oxidase loaded Psomes (GOx-Psomes) composite electrodes are prepared, the technique selected for the measurements is chronoamperometry in phosphate buffer saline 10 mM. In these conditions, the obtained results lead to an optimum measurement.
- In the optimization of the chronoamperometry measurements for GOx-Psomes electrodes in PBS 10 mM buffer the results lead to an optimum measurement at pH of 7.4. In addition, the application a of constant smooth stirring to get control of the diffusion layer and working potential of1.4 V applied each 5 min to perform the measurements were used.
- Using Catalase-Psomes (CAT-Psomes) together with GOx-Psomes in the corresponding modified sensors a decrease on the measured current is found, which means that all the loaded Psomes can achieve communication between them. So, probably, the decrease of the current is a result of the fact

that part of the H_2O_2 generated by GOx, is consumed by CAT before to the detection stage.

- ⌘ The results of $(\beta\text{-CD})_2$-Hemin-Psomes modified composite electrodes and the CAT-Psomes composite electrodes have the same behavior, when the equivalent activity loads are used in the modification of the hybrid nanomaterial. The use of nanozymes, which are nanomaterials that have enzyme like behavior, have some advantages, such as its stability, compared to the natural enzymes. The obtained results confirmed that the use of CAT and $(\beta\text{-CD})_2$-Hemin, have a mimetic behavior and equivalent performance, when they are in the same activity effective inside the hybrid nanomaterial. Consequently, these natural enzymes and nanozymes can be used indistinctively.
- ⌘ The compartmentalization of Psomes proved to be a key point in monitoring the cascade reaction. Consequently, noticeably lower current intensities were observed when CAT or $(\beta\text{-CD})_2$-Hemin-Psomes were incorporated into the hybrid nanomaterial at a percentage of 50% respect to 50% GOx-Psomes compared to the 50% GOx-Psomes sensors (containing only GOx). There, the compartmentation of natural enzymes (H_2O_2-producing and consuming enzymes) and nanozymes (H_2O_2-consuming nanozymes) in cascade reaction offers the possibility to modify the composite electrode using heterogeneously bioactive cargos in the alginate matrix.

Future research will explore the modification of other electrode types and the utilization of additional Psomes cargos, including other natural enzymes and nanozymes. This novel approach to biosensor fabrication could pave the way for demand-driven sensor development with improved selectivity.

Chapter VI

References

6.1. References

[1] "Analytical Chemistry - American Chemical Society." Accessed: Sep. 21, 2023. [Online]. Available: https://www.acs.org/careers/chemical-sciences/areas/analytical-chemistry.html

[2] A. Hulanicki, S. Geab, and F. Ingman, "Chemical sensors definitions and classification," 1991.

[3] C. M. A. Brett, "Electrochemistry," in *Reference Module in Chemistry, Molecular Sciences and Chemical Engineering*, Elsevier, 2014. doi: 10.1016/B978-0-12-409547-2.10742-5.

[4] F.-Gabriel. Banica, *Chemical sensors and biosensors : fundamentals and applications*. John Wiley & Sons Inc, 2012.

[5] D. A. Skoog, F. James Holler, and T. A. Nieman, "Douglas A. Skoog & F. James Holler & Timothy A. Nieman - Principios de análisis instrumental (5ed, McGrawHill).pdf." pp. 1–856, 2001.

[6] T. J. Roussel, D. J. Jackson, R. P. Baldwin, and R. S. Keynton, "Amperometric Techniques," in *Encyclopedia of Microfluidics and Nanofluidics*, D. Li, Ed., Boston, MA: Springer US, 2008, pp. 39–47. doi: 10.1007/978-0-387-48998-8_26.

[7] M. Gimeno and F. M. Zanotto, "LEARNING about EDGE EFFECTS and ULTRAMICROELECTRODES in ELECTROCHEMISTRY: SYNERGY between EXPERIMENTS and SIMULATIONS," *Quim Nova*, vol. 43, no. 8, pp. 1172–1175, Sep. 2020, doi: 10.21577/0100-4042.20170587.

[8] J. Muñoz, J. Bastos-Arrieta, M. Muñoz, D. Muraviev, F. Céspedes, and M. Baeza, "CdS quantum dots as a scattering nanomaterial of carbon nanotubes in polymeric nanocomposite sensors for microelectrode array behavior," *J Mater Sci*, vol. 51, no. 3, pp. 1610–1619, Feb. 2016, doi: 10.1007/s10853-015-9484-0.

[9] J. Muñoz and M. Baeza, "Customized Bio-functionalization of Nanocomposite Carbon Paste Electrodes for Electrochemical Sensing: A Mini Review," *Electroanalysis*, vol. 29, no. 7. Wiley-VCH Verlag, pp. 1660–1669, Jul. 01, 2017. doi: 10.1002/elan.201700087.

[10] K. K. Chawla, *Composite materials: Science and engineering, third edition*. Springer New York, 2012. doi: 10.1007/978-0-387-74365-3.

[11] W. I. King, "The Annals of Mathematical Statistics," *The Annals of Mathematical Statistics*, vol. 1, no. 1, pp. 1–2, 1930, doi: 10.1214/aoms/1177733256.

[12] J. Muñoz, "Advanced amperometric nanocomposite sensors based on carbon nanotubes and graphene : Characterization , Optimization , Functionalization and Applications," no. September, p. 345, 2015.

[13] R. Montes, J. Bartrolí, F. Céspedes, and M. Baeza, "Towards to the improvement of the analytical response in voltammetric sensors based on rigid composites," *Journal of Electroanalytical Chemistry*, vol. 733, pp. 69–76, 2014, doi: 10.1016/j.jelechem.2014.09.022.

[14] C. M. A. Brett, A. Maria, and C. F. Oliveira Brett, "SURFACE MODIFIED ELECTRODES-REASONS AND ADVANTAGES."

[15] S. Bayda, M. Adeel, T. Tuccinardi, M. Cordani, and F. Rizzolio, "The history of nanoscience and nanotechnology: From chemical-physical applications to nanomedicine," *Molecules*, vol. 25, no. 1. MDPI AG, 2020. doi: 10.3390/molecules25010112.

[16] I. I. Khan, K. Saeed, and I. I. Khan, "Nanoparticles: Properties, applications and toxicities," *Arabian Journal of Chemistry*, vol. 12, no. 7, pp. 908–931, 2019, doi: 10.1016/j.arabjc.2017.05.011.

[17] S. K. Kulkarni, *Nanotechnology - Principles and Practices 3rd ed (Springer, CP, 2015).pdf*. 2014.

[18] G. Speranza, "Carbon nanomaterials: Synthesis, functionalization and sensing applications," *Nanomaterials*, vol. 11, no. 4, 2021, doi: 10.3390/nano11040967.

[19] J. Y. Lim, N. M. Mubarak, E. C. Abdullah, S. Nizamuddin, M. Khalid, and Inamuddin, "Recent trends in the synthesis of graphene and graphene oxide based nanomaterials for removal of heavy metals — A review," *Journal of Industrial and Engineering Chemistry*, vol. 66, pp. 29–44, 2018, doi: 10.1016/j.jiec.2018.05.028.

[20] T. D. Nguyen, M. T. N. Nguyen, and J. S. Lee, "Carbon-Based Materials and Their Applications in Sensing by Electrochemical Voltammetry," *Inorganics*, vol. 11, no. 2. MDPI, Feb. 01, 2023. doi: 10.3390/inorganics11020081.

[21] N. Martín, M. M. Haley, and R. R. Tykwinski, "Aromaticity: A web themed issue," *Chemical Communications*, vol. 48, no. 85, pp. 10471–10471, Oct. 2012, doi: 10.1039/c2cc90288e.

[22] J. Rodríguez Rodríguez, "Síntesis y caracterización de óxido de grafeno reducido funcionalizados con nanopartículas metálicas. Aplicación en el desarrollo de sensores amperométricos basados en materiales nanoestructurados."

[23] Z. L. Chen, F. Y. Kam, R. G. S. Goh, J. Song, G. K. Lim, and L. L. Chua, "Influence of graphite source on chemical oxidative reactivity," *Chemistry of Materials*, vol. 25, no. 15, pp. 2944–2949, Aug. 2013, doi: 10.1021/cm304123s.

[24] I. H. Cho, D. H. Kim, and S. Park, "Electrochemical biosensors: Perspective on functional nanomaterials for on-site analysis," *Biomaterials Research*, vol. 24, no. 1. BioMed Central Ltd., Feb. 04, 2020. doi: 10.1186/s40824-019-0181-y.

[25] D. Feldman, "Polymer history," *Des Monomers Polym*, vol. 11, no. 1, pp. 1–15, Feb. 2008, doi: 10.1163/156855508X292383.

[26] S. Koltzenburg, M. Maskos, and O. Nuyken, "Polymer Chemistry."

[27] N. Nazeer and M. Ahmed, "Polymers in medicine," in *Polymer Science and Nanotechnology: Fundamentals and Applications*, Elsevier, 2020, pp. 281–323. doi: 10.1016/B978-0-12-816806-6.00013-3.

[28] S. Trombino, F. Curcio, and R. Cassano, "Polymersomes as a promising vehicle for controlled drug delivery," in *Stimuli-Responsive Nanocarriers*, Elsevier, 2022, pp. 351–366. doi: 10.1016/b978-0-12-824456-2.00017-5.

[29] P. Pallavi, K. Harini, P. Gowtham, K. Girigoswami, and A. Girigoswami, "Fabrication of Polymersomes: A Macromolecular Architecture in Nanotherapeutics," *Chemistry (Switzerland)*, vol. 4, no. 3. MDPI, pp. 1028–1043, Sep. 01, 2022. doi: 10.3390/chemistry4030070.

[30] X. Zhang and P. Zhang, "Polymersomes in Nanomedicine - A Review," *Curr Nanosci*, vol. 13, no. 2, pp. 124–129, 2016, doi: 10.2174/1573413712666161018144519.

[31] S. Trombino, F. Curcio, and R. Cassano, "Polymersomes as a promising vehicle for controlled drug delivery," in *Stimuli-Responsive Nanocarriers*, Elsevier, 2022, pp. 351–366. doi: 10.1016/b978-0-12-824456-2.00017-5.

[32] M. V. Dinu, I. A. Dinu, S. S. Saxer, W. Meier, U. Pieles, and N. Bruns, "Stabilizing Enzymes within Polymersomes by Coencapsulation of Trehalose," *Biomacromolecules*, vol. 22, no. 1, pp. 134–145, Jan. 2021, doi: 10.1021/acs.biomac.0c00824.

[33] S. Moreno *et al.*, "Avidin Localizations in pH-Responsive Polymersomes for Probing the Docking of Biotinylated (Macro)molecules in the Membrane and Lumen," *Biomacromolecules*, vol. 21, no. 12, pp. 5162–5172, 2020, doi: 10.1021/acs.biomac.0c01276.

[34] R. Ccorahua, S. Moreno, H. Gumz, K. Sahre, B. Voit, and D. Appelhans, "Reconstitution properties of biologically active polymersomes after cryogenic freezing and a freeze-drying process," *RSC Adv*, vol. 8, no. 45, pp. 25436–25443, 2018, doi: 10.1039/c8ra03964j.

[35] P. Wen *et al.*, "Construction of Eukaryotic Cell Biomimetics: Hierarchical Polymersomes-in-Proteinosome Multicompartment with Enzymatic Reactions Modulated Protein Transportation," *Small*, vol. 2005749, 2020, doi: 10.1002/smll.202005749.

[36] M. El Idrissi, C. E. Meyer, L. Zartner, and W. Meier, "Nanosensors based on polymer vesicles and planar membranes: A short review," *J Nanobiotechnology*, vol. 16, no. 1, Aug. 2018, doi: 10.1186/s12951-018-0393-7.

[37] L. Zartner, M. S. Muthwill, I. A. Dinu, C. A. Schoenenberger, and C. G. Palivan, "The rise of bio-inspired polymer compartments responding to pathology-related signals," *Journal of Materials Chemistry B*, vol. 8, no. 29. Royal Society of Chemistry, pp. 6252–6270, Aug. 07, 2020. doi: 10.1039/d0tb00475h.

[38] L. Quan, H. Ding, C. Pan, Y. Wei, and Z. Xie, "Revealing membrane permeability of polymersomes through fluorescence enhancement," *Colloids Surf B Biointerfaces*, vol. 161, pp. 156–161, Jan. 2018, doi: 10.1016/j.colsurfb.2017.10.058.

[39] X. Chen, H. Jiang, Y. Wang, G. Zou, and Q. Zhang, "β-Cyclodextrin-induced fluorescence enhancement of a thermal-responsive azobenzene modified polydiacetylene vesicles for a temperature sensor," *Mater Chem Phys*, vol. 124, no. 1, pp. 36–40, Nov. 2010, doi: 10.1016/j.matchemphys.2010.07.015.

[40] S. Seo *et al.*, "Fluorescence resonance energy transfer between polydiacetylene vesicles and embedded benzoxazole molecules for pH sensing," *React Funct Polym*, vol. 73, no. 3, pp. 451–456, Mar. 2013, doi: 10.1016/j.reactfunctpolym.2012.11.016.

[41] C. Edlinger, T. Einfalt, M. Spulber, A. Car, W. Meier, and C. G. Palivan, "Biomimetic Strategy to Reversibly Trigger Functionality of Catalytic Nanocompartments by the Insertion of pH-Responsive Biovalves," *Nano Lett*, vol. 17, no. 9, pp. 5790–5798, Sep. 2017, doi: 10.1021/acs.nanolett.7b02886.

[42] J. Madsen *et al.*, "Nile blue-based nanosized pH sensors for simultaneous far-red and near-infrared live bioimaging," *J Am Chem Soc*, vol. 135, no. 39, pp. 14863–14870, Oct. 2013, doi: 10.1021/ja407380t.

[43] X. Chen *et al.*, "Photo-controlled molecular recognition of α-cyclodextrin with azobenzene containing polydiacetylene vesicles," *Chemical Communications*, no. 11, pp. 1356–1358, 2009, doi: 10.1039/b820894h.

[44] G. Ma and Q. Cheng, "A nanoscale vesicular polydiacetylene sensor for organic amines by fluorescence recovery," *Talanta*, vol. 67, no. 3, pp. 514–519, Sep. 2005, doi: 10.1016/j.talanta.2005.06.032.

[45] C. Wang and Z. Ma, "Colorimetric detection of oligonucleotides using a polydiacetylene vesicle sensor," *Anal Bioanal Chem*, vol. 382, no. 7, pp. 1708–1710, Jul. 2005, doi: 10.1007/s00216-005-3345-7.

[46] C. Jia, J. Tang, S. Lu, Y. Han, and H. Huang, "Enhanced Sensitivity for Hydrogen Peroxide Detection: Polydiacetylene Vesicles with Phenylboronic Acid Head Group," *J Fluoresc*, vol. 26, no. 1, pp. 121–127, Jan. 2016, doi: 10.1007/s10895-015-1691-1.

[47] T. Huang, Z. Hou, Q. Xu, L. Huang, C. Li, and Y. Zhou, "Polymer vesicle sensor for visual and sensitive detection of SO2 in water," *Langmuir*, vol. 33, no. 1, pp. 340–346, Jan. 2017, doi: 10.1021/acs.langmuir.6b03869.

[48] S. H. Jung *et al.*, "Chromatic biosensor for detection of phosphinothricin acetyltransferase by use of polydiacetylene vesicles encapsulated within automatically generated immunohydrogel beads," *Anal Chem*, vol. 87, no. 4, pp. 2072–2078, Feb. 2015, doi: 10.1021/ac501795x.

[49] J. H. Duffus, "'HEAVY METALS'-A MEANINGLESS TERM? (IUPAC Technical Report)," W. A. Temple, 2002.

[50] K. Jomova *et al.*, "Essential metals in health and disease," *Chemico-Biological Interactions*, vol. 367. Elsevier Ireland Ltd, Nov. 01, 2022. doi: 10.1016/j.cbi.2022.110173.

[51] K. Jomova *et al.*, "Essential metals in health and disease," *Chemico-Biological Interactions*, vol. 367. Elsevier Ireland Ltd, Nov. 01, 2022. doi: 10.1016/j.cbi.2022.110173.

[52] World Health organization, "Guidelines for drinking water quility," 2017.

[53] THE EUROPEAN PARLIAMENT AND THE COUNCIL OF THE EUROPEAN UNION, "DIRECTIVE (EU) 2020/2184 OF THE EUROPEAN PARLIAMENT AND OF THE COUNCIL on the quality of water intended for human consumption," 2020.

[54] X. Li, L. Wang, D. Du, L. Ni, J. Pan, and X. Niu, "Emerging applications of nanozymes in environmental analysis: Opportunities and trends," *TrAC - Trends in Analytical Chemistry*, vol. 120, p. 115653, 2019, doi: 10.1016/j.trac.2019.115653.

[55] Y. Wei *et al.*, "SnO 2/reduced graphene oxide nanocomposite for the simultaneous electrochemical detection of cadmium(II), lead(II), copper(II), and mercury(II): An interesting favorable mutual interference," *Journal of Physical Chemistry C*, vol. 116, no. 1, pp. 1034–1041, Jan. 2012, doi: 10.1021/jp209805c.

[56] S. Chaiyo, E. Mehmeti, K. Žagar, W. Siangproh, O. Chailapakul, and K. Kalcher, "Electrochemical sensors for the simultaneous determination of zinc, cadmium and lead using a Nafion/ionic liquid/graphene composite modified screen-printed carbon electrode," *Anal Chim Acta*, vol. 918, pp. 26–34, Apr. 2016, doi: 10.1016/j.aca.2016.03.026.

[57] C. Pérez-Ràfols, N. Serrano, J. M. Díaz-Cruz, C. Ariño, and M. Esteban, "A screen-printed voltammetric electronic tongue for the analysis of complex mixtures of metal ions," *Sens Actuators B Chem*, vol. 250, pp. 393–401, 2017, doi: 10.1016/j.snb.2017.04.165.

[58] B. Feier, D. Floner, C. Cristea, E. Bodoki, R. Sandulescu, and F. Geneste, "Flow electrochemical analyses of zinc by stripping voltammetry on graphite felt electrode," *Talanta*, vol. 98, pp. 152–156, Aug. 2012, doi: 10.1016/j.talanta.2012.06.063.

[59] R. Nasraoui, D. Floner, and F. Geneste, "Analytical performances of a flow electrochemical sensor for preconcentration and stripping voltammetry of metal ions," *Journal of Electroanalytical Chemistry*, vol. 629, no. 1–2, pp. 30–34, Apr. 2009, doi: 10.1016/j.jelechem.2009.01.024.

[60] X. Gao, W. Wei, L. Yang, and M. Guo, "Carbon nanotubes/poly(1,2-diaminobenzene) nanoporous composite film electrode prepared by multipulse potentiostatic electropolymerisation and its application to determination of trace heavy metal ions," *Electroanalysis*, vol. 18, no. 5, pp. 485–492, 2006, doi: 10.1002/elan.200503409.

[61] K. S. Selvan and S. S. Narayanan, "Synthesis and characterization of carbon nanotubes/asymmetric novel tetradentate ligand forming complexes on PIGE modified electrode for simultaneous determination of Pb(II) and Hg(II) in sea water, Lake water and well water using anodic stripping voltammetry," *Journal of*

Electroanalytical Chemistry, vol. 810, pp. 176–184, Feb. 2018, doi: 10.1016/j.jelechem.2017.12.074.

[62] P. Gupta *et al.*, "Parts per trillion detection of heavy metals in as-is tap water using carbon nanotube microelectrodes," *Anal Chim Acta*, vol. 1155, Apr. 2021, doi: 10.1016/j.aca.2021.338353.

[63] X. C. Fu, J. Wu, L. Nie, C. G. Xie, J. H. Liu, and X. J. Huang, "Electropolymerized surface ion imprinting films on a gold nanoparticles/single-wall carbon nanotube nanohybrids modified glassy carbon electrode for electrochemical detection of trace mercury(II) in water," *Anal Chim Acta*, vol. 720, pp. 29–37, Mar. 2012, doi: 10.1016/j.aca.2011.12.071.

[64] A. U. Alam, M. M. R. Howlader, N. X. Hu, and M. J. Deen, "Electrochemical sensing of lead in drinking water using B-cyclodextrin-modified MWCNTs," *Sens Actuators B Chem*, vol. 296, Oct. 2019, doi: 10.1016/j.snb.2019.126632.

[65] H. Xing *et al.*, "Highly sensitive simultaneous determination of cadmium (II), lead (II), copper (II), and mercury (II) ions on N-doped graphene modified electrode," *Journal of Electroanalytical Chemistry*, vol. 760, pp. 52–58, Jan. 2016, doi: 10.1016/j.jelechem.2015.11.043.

[66] S. Muralikrishna, D. H. Nagaraju, R. G. Balakrishna, W. Surareungchai, T. Ramakrishnappa, and A. B. Shivanandareddy, "Hydrogels of polyaniline with graphene oxide for highly sensitive electrochemical determination of lead ions," *Anal Chim Acta*, vol. 990, pp. 67–77, Oct. 2017, doi: 10.1016/j.aca.2017.09.008.

[67] M. B. Gumpu, M. Veerapandian, U. M. Krishnan, and J. B. B. Rayappan, "Simultaneous electrochemical detection of Cd(II), Pb(II), As(III) and Hg(II) ions using ruthenium(II)-textured graphene oxide nanocomposite," *Talanta*, vol. 162, pp. 574–582, Jan. 2017, doi: 10.1016/j.talanta.2016.10.076.

[68] M. Baghayeri, H. Alinezhad, M. Fayazi, M. Tarahomi, R. Ghanei-Motlagh, and B. Maleki, "A novel electrochemical sensor based on a glassy carbon electrode modified with dendrimer functionalized magnetic graphene oxide for simultaneous determination of trace Pb(II)and Cd(II)," *Electrochim Acta*, vol. 312, pp. 80–88, Jul. 2019, doi: 10.1016/j.electacta.2019.04.180.

[69] Y. L. Xie, S. Q. Zhao, H. L. Ye, J. Yuan, P. Song, and S. Q. Hu, "Graphene/CeO2 hybrid materials for the simultaneous electrochemical detection of cadmium(II), lead(II),

copper(II), and mercury(II)," *Journal of Electroanalytical Chemistry*, vol. 757, pp. 235–242, Nov. 2015, doi: 10.1016/j.jelechem.2015.09.043.

[70] J. Yukird, P. Kongsittikul, J. Qin, O. Chailapakul, and N. Rodthongkum, "ZnO@graphene nanocomposite modified electrode for sensitive and simultaneous detection of Cd (II) and Pb (II)," *Synth Met*, vol. 245, pp. 251–259, Nov. 2018, doi: 10.1016/j.synthmet.2018.09.012.

[71] D. R. Gough and T. G. Cotter, "Hydrogen peroxide: A Jekyll and Hyde signalling molecule," *Cell Death and Disease*, vol. 2, no. 10. Oct. 2011. doi: 10.1038/cddis.2011.96.

[72] J. E. Giaretta, H. Duan, F. Oveissi, S. Farajikhah, F. Dehghani, and S. Naficy, "Flexible Sensors for Hydrogen Peroxide Detection: A Critical Review," *ACS Applied Materials and Interfaces*, vol. 14, no. 18. American Chemical Society, pp. 20491–20505, May 11, 2022. doi: 10.1021/acsami.1c24727.

[73] V. B. Juska and M. E. Pemble, "A critical review of electrochemical glucose sensing: Evolution of biosensor platforms based on advanced nanosystems," *Sensors (Switzerland)*, vol. 20, no. 21. MDPI AG, pp. 1–28, Nov. 01, 2020. doi: 10.3390/s20216013.

[74] D. Petrović, D. Frank, S. C. L. Kamerlin, K. Hoffmann, and B. Strodel, "Shuffling Active Site Substate Populations Affects Catalytic Activity: The Case of Glucose Oxidase," *ACS Catal*, vol. 7, no. 9, pp. 6188–6197, Sep. 2017, doi: 10.1021/acscatal.7b01575.

[75] J. A. Bauer, M. Zámocká, J. Majtán, and V. Bauerová-Hlinková, "Glucose Oxidase, an Enzyme 'Ferrari': Its Structure, Function, Production and Properties in the Light of Various Industrial and Biotechnological Applications," *Biomolecules*, vol. 12, no. 3. MDPI, Mar. 01, 2022. doi: 10.3390/biom12030472.

[76] M. Sharifi *et al.*, "Antioxidant properties of gold nanozyme: A review," *Journal of Molecular Liquids*, vol. 297. Elsevier B.V., Jan. 01, 2020. doi: 10.1016/j.molliq.2019.112004.

[77] N. J. Lang, B. Liu, and J. Liu, "Characterization of glucose oxidation by gold nanoparticles using nanoceria," *J Colloid Interface Sci*, vol. 428, pp. 78–83, Aug. 2014, doi: 10.1016/j.jcis.2014.04.025.

[78] C. J. Yu, C. Y. Lin, C. H. Liu, T. L. Cheng, and W. L. Tseng, "Synthesis of poly(diallyldimethylammonium chloride)-coated Fe3O4 nanoparticles for

colorimetric sensing of glucose and selective extraction of thiol," *Biosens Bioelectron*, vol. 26, no. 2, pp. 913–917, Oct. 2010, doi: 10.1016/j.bios.2010.06.069.

[79] F. Manea, F. B. Houillon, L. Pasquato, and P. Scrimin, "Nanozymes: Gold-nanoparticle-based transphosphorylation catalysts," *Angewandte Chemie - International Edition*, vol. 43, no. 45, pp. 6165–6169, Nov. 2004, doi: 10.1002/anie.200460649.

[80] Y. Huang, J. Ren, and X. Qu, "Nanozymes: Classification, Catalytic Mechanisms, Activity Regulation, and Applications," *Chemical Reviews*, vol. 119, no. 6. American Chemical Society, pp. 4357–4412, Mar. 27, 2019. doi: 10.1021/acs.chemrev.8b00672.

[81] X. Wang, W. Guo, Y. Hu, J. Wu, and H. Wei, "Nanozymes: Next Wave of Artificial Enzymes," 2016, doi: 10.1007/978-3-662-53068-9.

[82] X. Hu *et al.*, "The construction of Fe-porphyrin nanozymes with peroxidase-like activity for colorimetric detection of glucose," *Anal Biochem*, vol. 675, Aug. 2023, doi: 10.1016/j.ab.2023.115224.

[83] M. Alfonso-Prieto, X. Biarnés, P. Vidossich, and C. Rovira, "The molecular mechanism of the catalase reaction," *J Am Chem Soc*, vol. 131, no. 33, pp. 11751–11761, Aug. 2009, doi: 10.1021/ja9018572.

[84] S. Moreno *et al.*, "Peroxidase-mimicking activity of nanozymes-loaded polymeric artificial organelles potentially active in acidic environment," *Journal of Polymer Science*, 2023, doi: 10.1002/pol.20230100.

[85] J. I. Goldstein *et al.*, "Scanning Electron Microscopy and X-Ray Microanalysis."

[86] "Transmission Electron Microscopy A Textbook for Materials Science."

[87] K. Rudnicki *et al.*, "A Sensitive Sensor Based on Single-walled Carbon Nanotubes: Its Preparation, Characterization and Application in the Electrochemical Determination of Drug Clorsulon in Milk Samples," *Electroanalysis*, vol. 32, no. 2, pp. 375–383, Feb. 2020, doi: 10.1002/elan.201900387.

[88] Y. Lu, C. Kreller, and S. B. Adler, "Measurement and Modeling of the Impedance Characteristics of Porous La[sub 1−x]Sr[sub x]CoO[sub 3−δ] Electrodes," *J Electrochem Soc*, vol. 156, no. 4, p. B513, 2009, doi: 10.1149/1.3079337.

[89] "Why Do They Put Sand on New Asphalt? | A-Rock Asphalt." Accessed: Jun. 01, 2023. [Online]. Available: https://arockasphalt.com/why-do-they-put-sand-on-new-asphalt/

[90] K. Benaboud, M. E. Achour, F. Carmona, and L. Salome, "Electrical properties of carbon black-epoxy resin heterogeneous materials near the percolation threshold," *Annales de Chimie Science des Matériaux*, vol. 23, no. 1–2, pp. 315–318, Jan. 1998, doi: 10.1016/S0151-9107(98)80082-2.

[91] R. Montes Martínez, "Caracterización de (Bio)compósitos en función de la proporción de grafito y optimización de la composición para su aplicación en el desarrollo de (Bio)sensores amperométricos," Universitat Autònoma de Barcelona, Barcelona, 2014.

[92] J. Muñoz, "Advanced amperometric nanocomposite sensors based on carbon nanotubes and graphene : Characterization , Optimization , Functionalization and Applications," no. September, p. 345, 2015.

[93] R. K. Gautam and A. Verma, "Electrocatalyst materials for oxygen reduction reaction in microbial fuel cell," *Biomass, Biofuels, Biochemicals: Microbial Electrochemical Technology: Sustainable Platform for Fuels, Chemicals and Remediation*, pp. 451–483, Jan. 2018, doi: 10.1016/B978-0-444-64052-9.00018-2.

[94] "El grafeno y sus derivados | Todo lo que necesitas saber." Accessed: May 22, 2023. [Online]. Available: https://www.phi4tech.com/es/blog_es/el-grafeno-y-sus-derivados/

[95] V. Uskoković, "A historical review of glassy carbon: Synthesis, structure, properties and applications," *Carbon Trends*, vol. 5. Elsevier Ltd, Oct. 01, 2021. doi: 10.1016/j.cartre.2021.100116.

[96] P. A. JENKINS and K. R. SHEPHERD, "IDENTIFICATION OF ABSCISIC ACID IN YOUNG STEMS OF PINUS RADIATA D. DON," *New Phytologist*, vol. 71, no. 3, pp. 501–511, 1972, doi: 10.1111/j.1469-8137.1972.tb01950.x.

[97] P. J. F. Harris, "Fullerene-like models for microporous carbon," *Journal of Materials Science*, vol. 48, no. 2. pp. 565–577, Jan. 2013. doi: 10.1007/s10853-012-6788-1.

[98] D. Skoog, F. Holler, and S. Crouch, *Principios de análisis fundamental*. 2008.

[99] S. L. Dropsens, "Serie: Prácticas de laboratorio Ref.: DRP-PL4, 'Determinación de cobre en agua de grifo .'" Accessed: Sep. 13, 2020. [Online]. Available: https://www.dropsens.com/pdfs_productos/new_brochures/pl1_pl2_pl3_pl4_pl5_pl6_pl7.pdf

[100] J. Sloane, "Mercury, element of the ancients," https://sites.dartmouth.edu/toxmetal/mercury/mercury-element-of-the-ancients/.

[101] P. Bueno-Ramirez, R. maría Barroso bermejo, and R. de Balbin Behrmann, "Funerary red (cinnabar versus ochre) and megalithic rituals in the central Iberian peninsula. The hypogean necropolis of Valle de las Higueras, Huecas, Toledo, Spain," *Bulletin de la Société préhistorique française*, vol. 116, no. 1, pp. 73–93, 2019, doi: 10.3406/bspf.2019.14983.

[102] V. S. Vaidya and H. M. Mehendale, "Mercuric Chloride (HgCl2)," in *Encyclopedia of Toxicology: Third Edition*, Elsevier, 2014, pp. 203–206. doi: 10.1016/B978-0-12-386454-3.00330-4.

[103] K. N. Thakore, "Calomel," in *Encyclopedia of Toxicology: Third Edition*, Elsevier, 2014, pp. 625–626. doi: 10.1016/B978-0-12-386454-3.00266-9.

[104] B. Verbrugge and S. Geenen, *Global Gold Production Touching Ground: Expansion, Informalization, and Technological Innovation*. Springer International Publishing, 2020. doi: 10.1007/978-3-030-38486-9.

[105] "Batteries - Zero Mercury." Accessed: Aug. 28, 2023. [Online]. Available: https://www.zeromercury.org/about-mercury/mercury-in-products/batteries/

[106] "Mercury and health." Accessed: Aug. 19, 2022. [Online]. Available: https://www.who.int/news-room/fact-sheets/detail/mercury-and-health

[107] "mercury - Principal compounds | Britannica." Accessed: Aug. 19, 2022. [Online]. Available: https://www.britannica.com/science/mercury-chemical-element/Principal-compounds

[108] "News and Views," *Nature*, p. 1271, Oct. 24, 1959.

[109] G. V. Ramesh, M. D. Prasad, and T. P. Radhakrishnan, "Mercury nanodrops and nanocrystals," *Chemistry of Materials*, vol. 23, no. 23, pp. 5231–5236, 2011, doi: 10.1021/cm2022533.

[110] P. B. Landon *et al.*, "Designing hollow nano gold golf balls," *ACS Appl Mater Interfaces*, vol. 6, no. 13, pp. 9937–9941, 2014, doi: 10.1021/am502519x.

[111] D. Briggs, "X-ray photoelectron spectroscopy (XPS)," *Handbook of Adhesion: Second Edition*, pp. 621–622, 2005, doi: 10.1002/0470014229.ch22.

[112] National Institute of Standards and Technology, "NIST X-ray Photoelectron Spectroscopy Database," NIST Standard Reference Database Number 20, National Institute of Standards and Technology, Gaithersburg MD, 20899 (2000). Accessed: Feb. 27, 2022. [Online]. Available: https://srdata.nist.gov/xps/Default.aspx

[113] Boletín Oficial del Estado, *Real Decreto 509/1996 de 15 de marzo, de desarrollo del Real Decreto-ley 11/1995, de 28 de diciembre, por el que se establecen las normas aplicables al tratamiento de las aguas residuales urbanas.* Spain: BOE-A-1996-7159, pp. 1996–7159.

[114] A. Cerrillo, "¿Qué es la anoxia? Así muere el Mar Menor," *La Vanguardia*, Barcelona, Aug. 24, 2021. Accessed: Apr. 17, 2023. [Online]. Available: https://www.lavanguardia.com/natural/contaminacion/20210824/7677955/asi-muere-mar-menor-anoxia.html

[115] J. Heezen and L. Fernández López, *PETI Fact-finding visit to Mar Menor, Spain*. European Parliament: Policy Department for Citizens' Rights and Constitutional Affairs, 2022. Accessed: Apr. 17, 2023. [Online]. Available: https://www.europarl.europa.eu/RegData/etudes/BRIE/2022/729054/IPOL_BRI(2022)729054_EN.pdf

[116] B. Karimi *et al.*, "Ecotoxicity of copper input and accumulation for soil biodiversity in vineyards," *Environmental Chemistry Letters*, vol. 19, no. 3. Springer Science and Business Media Deutschland GmbH, pp. 2013–2030, Jun. 01, 2021. doi: 10.1007/s10311-020-01155-x.

[117] E. Besnard, C. Chenu, and M. Robert, "Influence of organic amendments on copper distribution among particle-size and density fractions in Champagne vineyard soils." [Online]. Available: www.elsevier.com/locate/envpol

[118] S. Moreno, B. Voit, and J. Gaitzsch, "The chemistry of cross-linked polymeric vesicles and their functionalization towards biocatalytic nanoreactors", doi: 10.1007/s00396-020-04681-w/Published.

[119] E. G. Graham-Gurysh *et al.*, "Delivery strategies for cancer vaccines and immunoadjuvants," in *Systemic Drug Delivery Strategies: Volume 2 of Delivery Strategies and Engineering Technologies in Cancer Immunotherapy*, Elsevier, 2021, pp. 359–408. doi: 10.1016/B978-0-323-85781-9.00014-2.

[120] S. Trombino, F. Curcio, and R. Cassano, "Polymersomes as a promising vehicle for controlled drug delivery," in *Stimuli-Responsive Nanocarriers*, Elsevier, 2022, pp. 351–366. doi: 10.1016/b978-0-12-824456-2.00017-5.

[121] X. Zhang and P. Zhang, "Polymersomes in Nanomedicine - A Review," *Curr Nanosci*, vol. 13, no. 2, pp. 124–129, 2016, doi: 10.2174/1573413712666161018144519.

[122] C. Misra, R. K. Paul, N. Thotakura, and K. Raza, "Biodegradable self-assembled nanocarriers as the drug delivery vehicles," in *Nanoparticle Therapeutics: Production Technologies, Types of Nanoparticles, and Regulatory Aspects*, Elsevier, 2022, pp. 293–325. doi: 10.1016/B978-0-12-820757-4.00007-7.

[123] O. Rifaie-Graham *et al.*, "Photoswitchable gating of non-equilibrium enzymatic feedback in chemically communicating polymersome nanoreactors," *Nat Chem*, Jan. 2022, doi: 10.1038/s41557-022-01062-4.

[124] P. Pallavi, K. Harini, P. Gowtham, K. Girigoswami, and A. Girigoswami, "Fabrication of Polymersomes: A Macromolecular Architecture in Nanotherapeutics," *Chemistry (Switzerland)*, vol. 4, no. 3. MDPI, pp. 1028–1043, Sep. 01, 2022. doi: 10.3390/chemistry4030070.

[125] M. V. Dinu, I. A. Dinu, S. S. Saxer, W. Meier, U. Pieles, and N. Bruns, "Stabilizing Enzymes within Polymersomes by Coencapsulation of Trehalose," *Biomacromolecules*, vol. 22, no. 1, pp. 134–145, Jan. 2021, doi: 10.1021/acs.biomac.0c00824.

[126] S. Moreno *et al.*, "Avidin Localizations in pH-Responsive Polymersomes for Probing the Docking of Biotinylated (Macro)molecules in the Membrane and Lumen," *Biomacromolecules*, vol. 21, no. 12, pp. 5162–5172, 2020, doi: 10.1021/acs.biomac.0c01276.

[127] S. Moreno *et al.*, "Light-Driven Proton Transfer for Cyclic and Temporal Switching of Enzymatic Nanoreactors," *Small*, vol. 16, no. 37, pp. 1–11, 2020, doi: 10.1002/smll.202002135.

[128] J. Gaitzsch, D. Appelhans, L. Wang, G. Battaglia, and B. Voit, "Synthetic bio-nanoreactor: Mechanical and chemical control of polymersome membrane permeability," *Angewandte Chemie - International Edition*, vol. 51, no. 18, pp. 4448–4451, Apr. 2012, doi: 10.1002/anie.201108814.

[129] M. Zea, R. Texidó, R. Villa, S. Borrós, and G. Gabriel, "Specially Designed Polyaniline/Polypyrrole Ink for a Fully Printed Highly Sensitive pH Microsensor," *ACS*

Appl Mater Interfaces, vol. 13, no. 28, pp. 33524–33535, Jul. 2021, doi: 10.1021/acsami.1c08043.

[130] Y. Zhang, Y. Li, W. Wu, Y. Jiang, and B. Hu, "Chitosan coated on the layers' glucose oxidase immobilized on cysteamine/Au electrode for use as glucose biosensor," *Biosens Bioelectron*, vol. 60, pp. 271–276, Oct. 2014, doi: 10.1016/j.bios.2014.04.035.

[131] A. Márquez-Maqueda *et al.*, "Enzymatic Biosensors Based on Electrodeposited Alginate Hydrogels," in *Procedia Engineering*, Elsevier Ltd, 2016, pp. 622–625. doi: 10.1016/j.proeng.2016.11.229.

[132] E. Forner *et al.*, "Electrochemical biosensor for aerobic acetate detection," *Talanta*, vol. 265, p. 124882, Dec. 2023, doi: 10.1016/j.talanta.2023.124882.

[133] G. Kaklamani, D. Kazaryan, J. Bowen, F. Iacovella, S. H. Anastasiadis, and G. Deligeorgis, "On the electrical conductivity of alginate hydrogels," *Regen Biomater*, vol. 5, no. 5, pp. 293–301, Oct. 2018, doi: 10.1093/rb/rby019.

[134] A. Schmitt *et al.*, "Calcium alginate gels as stem cell matrix -making paracrine stem cell activity available for enhanced healing after surgery," *PLoS One*, vol. 10, no. 3, Mar. 2015, doi: 10.1371/journal.pone.0118937.

[135] F. Rajabasadi *et al.*, "Multifunctional 4D-Printed Sperm-Hybrid Microcarriers for Assisted Reproduction," *Advanced Materials*, vol. 34, no. 50, Dec. 2022, doi: 10.1002/adma.202204257.

[136] P. Sánchez-Peña, J. Rodriguez, D. Gabriel, J. A. Baeza, A. Guisasola, and M. Baeza, "Graphene functionalization with metallic Pt nanoparticles: A path to cost-efficient H2 production in microbial electrolysis cells," *Int J Hydrogen Energy*, vol. 47, no. 34, pp. 15397–15409, Apr. 2022, doi: 10.1016/j.ijhydene.2022.03.078.

[137] J. Muñoz *et al.*, "Amperometric thyroxine sensor using a nanocomposite based on graphene modified with gold nanoparticles carrying a thiolated β-cyclodextrin," *Microchimica Acta*, vol. 183, no. 5, pp. 1579–1589, 2016, doi: 10.1007/s00604-016-1783-x.

[138] C. Karakasyan, M. Taverna, and M. C. Millot, "Determination of binding constants of hydrophobically end-capped poly(ethylene glycol)s with β-cyclodextrin by affinity capillary electrophoresis," *J Chromatogr A*, vol. 1032, no. 1–2, pp. 159–164, Apr. 2004, doi: 10.1016/j.chroma.2003.11.021.

[139] E. Ricca, B. Brucher, and J. H. Schrittwieser, "Multi-enzymatic cascade reactions: Overview and perspectives," *Advanced Synthesis and Catalysis*, vol. 353, no. 13. pp. 2239–2262, Sep. 2011. doi: 10.1002/adsc.201100256.

[140] R. Siedentop, C. Claaßen, D. Rother, S. Lütz, and K. Rosenthal, "Getting the most out of enzyme cascades: Strategies to optimize in vitro multi-enzymatic reactions," *Catalysts*, vol. 11, no. 10. MDPI, Oct. 01, 2021. doi: 10.3390/catal11101183.

[141] E. T. Hwang and S. Lee, "Multienzymatic Cascade Reactions via Enzyme Complex by Immobilization," *ACS Catalysis*, vol. 9, no. 5. American Chemical Society, pp. 4402–4425, May 03, 2019. doi: 10.1021/acscatal.8b04921.

[142] B. KHADRO, P. NAMOUR, F. BESSUEILLE, D. LEONARD, and N. JAFFREZIC-RENAULT, "Validation of a conductometric bienzyme biosensor for the detection of proteins as marker of organic matter in river samples," *Journal of Environmental Sciences*, vol. 21, no. 4, pp. 545–551, Apr. 2009, doi: 10.1016/S1001-0742(08)62306-2.

[143] G. L. Radu and P. R. Coulet, "Amperometric Peptide Sensor for Protein Determination," *Anal Lett*, vol. 26, no. 7, pp. 1321–1332, Jul. 1993, doi: 10.1080/00032719308017415.

[144] O. O. Soldatkin, V. M. Peshkova, S. V. Dzyadevych, A. P. Soldatkin, N. Jaffrezic-Renault, and A. V. El'skaya, "Novel sucrose three-enzyme conductometric biosensor," *Materials Science and Engineering C*, vol. 28, no. 5–6, pp. 959–964, Jul. 2008, doi: 10.1016/j.msec.2007.10.034.

[145] O. O. Soldatkin *et al.*, "Development of conductometric biosensor array for simultaneous determination of maltose, lactose, sucrose and glucose," *Talanta*, vol. 115, pp. 200–207, 2013, doi: 10.1016/j.talanta.2013.04.065.

[146] M. Gamella *et al.*, "Integrated multienzyme electrochemical biosensors for monitoring malolactic fermentation in wines," *Talanta*, vol. 81, no. 3, pp. 925–933, May 2010, doi: 10.1016/j.talanta.2010.01.038.

[147] M. Gamella, S. Campuzano, A. J. Reviejo, and J. M. Pingarrón, "Integrated multienzyme electrochemical biosensors for the determination of glycerol in wines," *Anal Chim Acta*, vol. 609, no. 2, pp. 201–209, Feb. 2008, doi: 10.1016/j.aca.2007.12.036.

[148] C. Mousty, S. Cosnier, D. Shan, and S. Mu, "Trienzymatic biosensor for the determination of inorganic phosphate," 2001.

[149] R. Koncki, I. Walcerz, F. Ruckruh, and S. Glab, "CHIMICA ACTA Bienzymatic potentiometric electrodes for creatine and L-arginine determination," 1996.

[150] K. Sasaki, H. Furusawa, K. Nagamine, S. Tokito, H. Furusawa, and S. Tokito, "Constructive Optimization of a Multienzymatic Film Based on a Cascade Reaction for Electrochemical Biosensors," *ACS Omega*, vol. 5, no. 50, pp. 32844–32851, Dec. 2020, doi: 10.1021/acsomega.0c05521.

[151] M. Dong *et al.*, "Ultrasensitive electrochemical biosensor for detection of circulating tumor cells based on a highly efficient enzymatic cascade reaction," *RSC Adv*, vol. 13, no. 19, pp. 12966–12972, Apr. 2023, doi: 10.1039/d3ra01160g.

[152] W. H. Koppenol, "THE CENTENNIAL OF THE FENTON REACTION," 1993.

[153] H. Zhang, B. Zhang, M. Zhu, S. M. Grayson, R. Schmehl, and J. Jayawickramarajah, "Water-soluble porphyrin nanospheres: Enhanced photo-physical properties via cyclodextrin driven double self-inclusion," *Chem Commun (Camb)*, vol. 50, no. 37, pp. 4853–4855, 2014, doi: 10.1039/c000000x/NIH.

[154] "Glossary of basic terms in polymer science (IUPAC Recommendations 1996)."

Annex

7.1. Annex I: Vineyard sample digestion

Sampling campaign involved the collection of the different wastes produced after the wine-making process at CADES , the plant in charge of treating wastes produced in wineries in Penedès area. Samples included grape pomace (composed of grape skin, stems, and seeds), wastewater and sludge.

Microwave (MW) acid digestion of solid samples is required before metals analysis. Samples of around 0.2 g were weighed in the digestion vessels, 10 mL of nitric acid (HNO_3) was added and left overnight as a pre-digestion step. The following day, the vessels were placed in the microwave and the samples were digested. The methodology followed is described in EPA 3051A about microwave assisted acid digestion of sediments, sludges, soils, and oils.

Acknowledgments

8.1. Acknowledgements

Estimado lector, si has llegado hasta aquí muchas gracias por el tiempo que te has tomado en hacerlo. A partir de este punto voy a dejar la ciencia a un lado y voy a agradecer a todas las personas que me han acompañado en este largo pero muy satisfactorio camino. Si, he dicho muy satisfactorio, no te sorprendas tanto, porque no solo han crecido mis conocimientos en ámbitos que jamás me lo hubiera imaginado (materiales, electroquímica…), sino que también he crecido como persona. Todo eso se lo debo en primer lugar a mis directoras de tesis Mireia y Cristina, que me han indicado la dirección en que caminar. Sin vosotras esto no habría sido posible, muchas gracias por la paciencia y el esfuerzo que me habéis dedicado. Mireia, muchísimas gracias por estar siempre ahí, por sacar siempre tiempo para discutir resultados o experimentos o simplemente para hablar. Cristina, muchas gracias por aportar ese pragmatismo, ese ojo al detalle y esa alegría que te caracterizan.

En segundo lugar, me gustaría agradecer a Julio Bastos y a Silvia Moreno, sois unos referentes para mí, tanto a nivel profesional como personal. Julio, desde la serendipia, te has convertido en una persona muy importante en este camino. Me siento muy afortunada de poder contar con alguien que transmite esas buenas vibras y que siempre tiene una palabra amable para decirte. También me gustaría agradecer especialmente a Silvia por adoptarme en Dresden; fueron unos meses con sus más y sus menos, pero muchas gracias por todo lo que me enseñaste, por ampliar mi mundo de química analítica, por tu inestimable ayuda, por esas charlas y risas durante el café y por abrirme tu casa en Navidad.

Me gustaría dar las gracias a todas las personas que han hecho que cada paso sea más llevadero, tanto de GTS como de GENOCOV, sois muchas como para poneros a todas aquí, pero me alegro de haber topado con compañeros como vosotros. Especialmente a mi *Solete*, Franc Paré, estos años no hubieran sido lo mismo sin ti. Gracias por estar ahí tanto para (y en) lo bueno como para (y en) lo malo; por hablarme en físico y en electroquímico (y por enseñarme sus entresijos), por esos cafés (en mi caso te) con croissant de chocolate en nuestro *spot*, por esas conversaciones tan variopintas, *random* e interesantes… podría seguir, pero la lista podría ser algo larga, así que lo dejo en un TIMO, que ya sabes que es y creo que engloba todo lo que pudiera escribir. También una mención especial a Elena Rodríguez, Iris Henríquez, Júlia Senyé, Lorena Ferrer, Pilar Sánchez, Sandra Pérez y Ghizlane el Korchi: a todas vosotras gracias por ayudarme, por escucharme y tener siempre palabras de ánimo.

A mis nenis; Anna de los Aire, Paula Doménech Helena Fuente, y Laura Ferré; por estar ahí y aguantar la chapa de cosas que os suena a chino, por ser ese "comodín del público" (lo que no sabe una igual lo sabe otra), por ayudarme a desconectar (que a veces es totalmente necesario), por las risas, por venirme a visitar a Alemania…podría seguir, pero la lista sería muuuy larga, así que me remito a la frase (perfeccionada del décimo aniversario):

"*Lo que la Química ha unido con enlace covalente, ni el tiempo lo rompe*".

A quien también tengo que agradecer muchísimo su apoyo, su compresión y empatía es a Miriam Pérez. Sin ti ya estaría rotita, ya te lo dije en su momento, pero eres mi persona vitamina, es hablar contigo y salir con las pilas cargadas. Mil gracias por estar ahí, por no tener tapujos en decirme las cosas, por ser mi compi de aventuras (y desventuras), de dulces y de planes improvisados o muy planeados.

Además, tengo que agradecer a Jesús Pérez su incondicional apoyo y su empatía, aunque a veces se pierda en mi mundo.

Y, por último, pero no menos importante, sin ellos no habría sido posible, ni empezar este camino, ni ninguna de las cosas que he logrado. Muchas gracias a mi familia; a mi madre, a mi padre y a mi iaia por estar ahí siempre; cuando me iba pronto a la uni y llegaba tarde del laboratorio, cuando no me daba tiempo a sacar a Joules…Gracias por apoyarme en todo momento y en cada decisión, aunque a veces no fuera la mejor.

Solo me falta añadir a esta lista a Joules, es mi sombra de cuatro patas. Ha estado conmigo en las largas noches de escritura, en los paseos para despejarme, en las reuniones (vía TEAMS) y siempre que ha podido. Su apoyo, aunque solo fuera descansando su cabeza en mi pierna, obligándome a parar a descansar o acurrucándose al lado de la silla durante las horas de escritura ha sido de gran valor para poder llevar a cabo este camino y llegar a buen puerto.

Ahora sí, aquí termina mi periplo estimado lector, como has podido comprobar no estoy yo sola detrás de esta aventura.